Implementing 3D Printing for the Long-Term Release of Biomacromolecules

Kristian Plender

Thesis submitted to The University of Nottingham in fulfilment of the requirements for the Degree of Doctor of Philosophy

University of **Nottingham**
UK | CHINA | MALAYSIA

June 2023

Abstract

The advancement of new biotherapeutics demands appropriate strategies that allow effective delivery to the body for the treatment of chronic diseases, which is of growing importance globally. This includes the development of implantable delivery systems with enhanced control over release at an intended site with the desired dosing. Additive manufacturing (AM), often referred to as three-dimensional (3D) printing, has been identified due to the potential advantages. This includes lower-cost initial formulation trials, geometric control and spatial location of bioactives to better modulate delivery in comparison to common manufacturing routes e.g. tabletting.

The use of inkjet printing (IJP) systems has well-documented success for producing delivery devices that allow release of small molecules (Da), but this is less reported regarding delivery of larger bioactives (kDa). This prompted the initial exploration in this thesis into IJP using poly(ethylene glycol) diacrylate (PEGDA) based formulations to assess encapsulation and delivery of biomacromolecules from 3D structures. Challenges encountered with this approach included increases in viscosity with increases in protein loading as well as precipitation during droplet ejection, residing as debris on the nozzle jet interface. This prevented reliable jetting and aligned with difficulties reported in previous literature attempts at processing biomacromolecules.

Digital light processing (DLP) was proposed as an alternative printing method that negated the requirement for formulations to pass through an orifice, which widens applicable materials selection. Samples were fabricated, allowing encapsulation of model proteins lysozyme (LYZ, 14 kDa), bovine serum albumin (BSA, 66 kDa) and alkaline phosphatase (ALP, 160 kDa). A range of PEGDA were selected from 575 to 10,000 Mn for formulation preparation in an effort to vary release from the printed polymer matrix. Key properties characterised included swelling ratio, swelling rate and theoretical matrix mesh size approximations, as determined by applying modified Peppas-Merrill equations. It was found that the respective values of each increased as Mn of the PEGDA selected increased. Limited release ($17.6 \pm 5.2\%$ and $13.3 \pm 1.2\%$) of LYZ and BSA was achieved from PEGDA Mn 10,000 20% (*w/v*) samples

with 1 mg/mL model protein loading. A separate study using BSA considered the influence of increasing loading to 5 mg/mL, whereby release was then achieved using formulations of PEGDA Mn 4000, 8000 and 10,000 at 20% (*w/v*). Increased availability of free protein allowed increased release, but this was still limited with maximum elution being 25.8 ± 1.4% occurring over 3 days before plateau. DLP enabled sample production, but the formulations utilised and reliance on swelling alone was unsuitable for achieving long-term release.

Finally, hydrolytically labile macromers were prepared through Michael addition modification of the previously used PEGDAs with an inexpensive thiol; dithiothreitol (DTT). Samples were fabricated by mixed-mode (MM) photopolymerisation, whereby increasing the thiol to acrylate ratio (SH:acrylate) increased areas of the polymer network that would hydrolytically degrade. Tuning the starting PEGDA Mn blend, macromer% (*w/v*) and SH:acrylate ratio allowed BSA release over 3 months+, fulfilling a main thesis aim. For example, samples using a PEGDA blend of Mn 575/4000 (1:1) 20% (*w/v*) and 0.25 SH:acrylate content with 5 mg/mL BSA loading led to release over 112 days with zero-order characteristics ($R^2 = 0.95$) observed from day 2 of release onwards. Release of ALP was achieved with 56.6 ± 1.6% eluted over 21 days; an improvement on the PEGDA only formulations where no significant release was detected. Associated matrix mesh size approximations acted as a comparative tool between sample sets and provided reasoning for why differences in release occurred. Structural changes were confirmed using cryo-SEM imaging and mechanical properties assessed through compression testing in the as-printed and swelled (degraded) sample state.

The results in this thesis suggest that kDa bioactives can be firstly encapsulated using simple scalable DLP printing processes and their elution controlled through changes in crosslinking mechanism, monomer selection, monomer%, SH:acrylate ratio, bioactive size and loading concentration. Throughout, emphasis has been placed on developing the understanding of the underlying principles associated with release of biomacromolecules from 3D printed structures. The information gathered could be applied to a further range of proteins in the development towards controlled delivery of protein therapeutics.

Acknowledgements

Declaration

Unless acknowledged otherwise, the work presented in this thesis is my own. No part of this work has been submitted for another degree at the University of Nottingham, or any other institute of learning, to my best knowledge.

Kristian Plender

June 2023

COVID-19 Impact Statement

My planned training on processes and laboratory equipment was scheduled for early 2020. On the 18th March 2020 the government closed all schools, swiftly followed by a nationwide lockdown on 23rd March. Before the lockdown, following guidance from the university halls of residence, I returned to my parental home. Working from home was not an ideal environment and it was difficult to plan each day's work. Uncertainty around when lockdown measures would end, when I would return to university and how this would influence my PhD also impacted my planning and ultimately ability to conduct any experimental work.

The first lockdown was detrimental to my plans and work timetable. It severely impacted my schedule at a critical time. I should have been able to complete training on equipment and start practical work. It became a desk-based writing period. These important early stages of my PhD, after training, had been outlined for testing proposed ideas. Reduced laboratory time has compromised my project's progression. Output potential and depth and breadth of work that could have been explored was hindered.

I returned to Nottingham in August, with access to laboratories restricted as part of a phased return. Post-doctoral staff and PhD students in the latter stages of research were prioritised. I did not resume experimental work until 21st September 2020 (6 months after the first lockdown). I required access to facilities that spanned different buildings, each adopting varied protocols and operating hours which added further complication. The phased access policy affected my ability to complete necessary experiments e.g. assessing long-term biological release requires multiple sample time points to be taken at set times. User demand and laboratory availability determined the possible experiments that could be conducted and made planning, at times, unmanageable. Issues were compounded by other laboratory users also wanting to make up for lost time and experiencing the same issues as myself.

Rearranging my training during this period became difficult due to increased demand from students and the trainer's own work commitments. University protocols aligned with government requirements adding constraints e.g.

limiting the number of trainees per session and using Perspex screens between trainees and the trainer. In a few cases my training had to be postponed. It was also apparent COVID-19 impacted global supply chains, leading to a lack of general consumables e.g. no stock of pipette tips. Delivery of materials, e.g. PEGDA, had significant delays. Again, this impacted my ability to prepare for and conduct experimental work effectively and timely. In-person meetings and conferences were replaced with online formats. Interaction with colleagues was more challenging in comparison to face-to-face conversation that being in a laboratory allows e.g. spontaneous discussion about project ideas and collaboration opportunities were restricted.

A 2nd lockdown took effect on 5th November 2020, planned to last a minimum of 4 weeks. The University remained open, allowing scheduled experimental work to continue. The "new way of working" still presented challenges and was coupled with more uncertainty making it difficult to foresee how my project would develop in the considerably diminishing timeframe. A 3rd lockdown from January to March 2021, meant no change in working procedure. This continued to exasperate my project ambitions.

To manage the difficulties I have alluded to in this statement, my proposed ideas were scaled back and prioritised. This has impacted the extent to which I could investigate concepts as part of the overall project scope intended and reduced the level of understanding that could be attained. For example, multiple formulation and printing trials were planned to run simultaneously but this had to be reduced. This reduction compromised the ability to gather a wider range of data to determine the governing factors dictating release.

This impact statement summarises the effect COVID-19 has had on me and my PhD course of study and should be taken into consideration during the assessment of my thesis.

Contents

List of Figures

List of Tables

List of Abbreviations and Equation Symbols

Abbreviations

(*v/v*)	Volume per volume
(*w/v*)	Weight per volume
(*w/w*)	Weight per weight
.STL	Stereolithography
^{1}H NMR	Proton nuclear magnetic resonance
2D	Two-dimensional
2PP	Two photon polymerisation
3D	Three-dimensional
ALP	Alkaline phosphatase
AM	Additive manufacturing
ANOVA	Analysis of variance
API	Active pharmaceutical ingredient
ASTM	American Society for Testing and Materials
BMP	Bitmap
BSA	Bovine serum albumin
BV	Bacterial vaginosis
CAL	Computed axial lithography
CAT-SEM	Cryogenic analytical and transfer scanning electron microscope
$CDCl_3$	Deuterated chloroform
CG	Chain-growth
d.p	Decimal places
D_2O	Deuterium oxide
Da	Dalton
DETX	2,4-diethylthioxanthone
diH_2O	Deionised water
dlogM	Differential log concentration
DLP	Digital light processing
DNA	Deoxyribonucleic acid
DOD	Drop-on-demand
DPI	Dots per inch
DSA	Drop shape analyser
DTT	Dithiothreitol

dW	Differential weight fraction
EDB	Ethyl 4-(dimethylamino) benzoate
EG	Ethylene glycol
EVA	Ethylene vinyl acetate
FDA	Food and Drug Administration
FEP	Fluorinated ethylene propylene
GelMA	Gelatin methacrylate
GI	Gastrointestinal
GLP-1RAs	Glucagon-like peptide-1 receptor agonists
GMP	Good manufacturing practice
GPC	Gel permeation chromatography
HME	Hot melt extrusion
HPLC	High-performance liquid chromatography
HRP	Horseradish peroxidase
ID	Intradermal
IJP	Inkjet printing
IM	Intramuscular
ISO	International Organisation for Standardisation
IV	Intravenous
kDa	Kilodalton
LAIs	Longer acting injections
LAP	Lithium phenyl-2,4,6-trimethylbenzoylphosphinate
LCD	Liquid crystal display
LDH	L-lactate dehydrogenase
LED	Light-emitting diode
LN_2	Liquid nitrogen
LYZ	Lysozyme
MCR	Modular compact rheometer
MHRA	Medicines and Healthcare products Regulation Agency
MM	Mixed-mode
Mn	Number average molecular weight
MQ	Milli-Q
mRNA	Messenger ribonucleic acid
MSCs	Mesenchymal stem cells
MW	Molecular weight

Mw	Weight average molecular weight
nAMD	Neovascular age-related macular degeneration
NB	Norbornene
NHS	National Health Service
NICE	National Institute for Health and Care Excellence
NIR	Near infrared
OVA	Ovalbumin
PBF	Powder bed fusion
PBS	Phosphate-buffered saline
PCL	Poly(caprolactone)
PDGFs	Platelet derived growth factor
PDI	Polydispersity index
PEG	Poly(ethylene glycol)
PEGDA	Poly(ethylene glycol) diacrylate
PEG-NB	Poly(ethylene glycol)-norbornene
PGA	Poly(glycolic acid)
pI	Isoelectric point
PLA	Poly(lactic acid)
PLGA	Poly(lactic-co-glycolic acid)
PMMA	Polymethyl methacrylate
PNP	Para-nitrophenol
PNPP	Para-nitrophenol phosphate
ppm	Parts per million
PTMC	Poly(trimethylene carbonate)
R^2	Coefficient of determination
rhBMP-2	Recombinant human bone morphogenetic protein 2
rhEPO	Recombinant human erythropoietin
RNA	Ribonucleic acid
RPM	Revolutions per minute
S.D.	Standard deviation
s.f	Significant figures
SA	Surface area
SA/V	Surface area to volume
SC	Subcutaneous
SEM	Scanning electron microscopy

SG	Step-growth
SH	Thiol
SLS	Selective laser sintering
TA	Triamcinolone acetonide
TC	Technical Committee
TD	Transdermal
T_g	Glass transition temperature
TGF-β 1	Transforming growth factor-beta 1
THF	Tetrahydrofuran
TPUs	Thermoplastic polyurethanes
UV	Ultraviolet
VEGFs	Vascular endothelial growth factors
VP	Vat photopolymerisation
VVC	Vulvovaginal candidiasis
WHO	World Health Organisation

Equation Symbols

$(r_0{}^2)^{1/2}$	Root mean square end-to-end distance of the polymer in the free state
$\overline{M_c}$	Average MW between two adjacent crosslinks
$\overline{M_n}$	Average MW of the oligomer
C_n	Polymer rigidity factor
M_r	MW of repeat units
$M_t/M\alpha$	Fraction of active released at time t
M_d	Dried mass
M_r	Relaxed mass
M_s	Swelled mass
Q_0	Amount of active quantified in solution prior to release
Q_t	Cumulative release at time t
$\overline{v}$	Specific volume
V_1	Molar volume of solvent
$V_{2,r}$	Polymer volume fraction (relaxed state)
$V_{2,s}$	Polymer volume fraction (swelled state)

$\rho_{Polymer}$	Polymer density
$\rho_{Solvent}$	Solvent density
χ_1	Flory-Huggins parameter
d	Diameter
E	Young's modulus
K	Release rate constant
l	Carbon-carbon bond length
n	Release exponent
Oh	Ohnesorge number
Q	Mass swelling ratio
Re	Reynolds number
t	Time
V	Velocity
We	Weber number
γ	Surface tension
δH	Chemical shift values (delta)
ε	Strain
η	Viscosity
ξ	Theoretical matrix mesh size
ρ	Density
σ	Uniaxial stress

Chapter 1 Literature Review

1.1 Biomacromolecule Structures and Associated Delivery Challenges

Biomacromolecules can be categorised as large biological polymer structures including proteins, nucleic acids, such as deoxyribonucleic acid (DNA) and ribonucleic acid (RNA), carbohydrate polysaccharides and lipids. Peptides and proteins have particularly seen increased interest in recent decades for their potential use as therapeutics. Complex biomacromolecule compositions can often offer high selectivity, specificity and potency with reduced side effects and toxicity, compared to small molecules [1].

However, due to their size, complexity and often unstable nature biomacromolecules are challenging to maintain or deliver effectively from a delivery device [2,3]. Complex biomacromolecule compositions are often susceptible to degradation and have reduced permeation across biological barriers [1]. Naturally this demands the development of methodologies that will ensure protection of these molecules throughout required manufacturing process stages, whilst still allowing for desired and controlled end release. In order to achieve this, the biomacromolecule structure and subsequent characteristics must be well understood in relation to pharmacological and therapeutic requirements.

1.1.1 Peptides and Proteins

1.1.1.1 Stages of Progressive Protein Folding and Conformation

The primary structure of a protein consists of a linear sequence of peptide bonding between amino acid residues that form a polypeptide chain, exhibiting both a carboxyl terminus and amino terminus dependant on the variable R group, shown in Figure 1.1(a)(b). The polypeptide chain folds into a specific conformation dependant on interactions between amino acid side chains [4]. This is dictated by size, shape, hydrophobicity and isoelectric point (pI) of an amino acid in relation to charge states such as protonated cation, neutral zwitterionic or deprotonated anion, shown in Figure 1.2.

Secondary structures consist of localised folding and hydrogen bonding stabilisation between the main chain peptide groups. Side chain interactions also have an impact by reducing hydration of the peptide group, known as

shielding effect, that further promotes protein folding [5]. This results in α-helix coiled structures and β-pleated sheets, shown in Figure 1.3(a)(b). Examples of α-helix structures include keratin and collagen that consist of a coiled backbone and side chains arranged in a helical array structurally stabilised by hydrogen bonding occurring between NH and CO groups. β-pleated sheets consist of lateral β-strands that are either parallel or anti-parallel in order [2,6].

Three-dimensional (3D) spatial arrangements of secondary structures that are conformed mainly by non-covalent bonding and intermolecular forces are called tertiary structures. Hydrophobic interactions contribute to protein folding, where the R group of an amino acid is either hydrophobic or hydrophilic which influences positioning and configuration [7]. In addition, hydrogen bonding within the polypeptide chain and interaction between the R side groups helps in stabilising the protein structure. Ionic bonding also occurs between positively and negatively charged R groups that are in close proximity. Another contributing factor to overall protein stability is van der Waals forces resulting from attraction and repulsion between molecules that are polarised [2,7]. In some cases, covalent bonding can happen through disulphide bridging (R-S-S-R) between cysteine residues. For example, in the case of insulin there are two bridges between the A and B chains and one within the A chain itself [8].

Quaternary structures represent what is seen as the highest level of protein organisation, comprised of multiple polypeptide chains (subunit structures) that are held by non-covalent bonds. An example of a quaternary structure comprised of two α subunits and two β subunits is haemoglobin, allowing for transportation of oxygen by binding to an iron-containing protein [2]. Figure 1.3 aids in illustrating secondary, tertiary and quaternary structures shown from (a-c) respectively. Further terminology to describe protein structures includes motifs and domains. Motifs are commonly part of a protein sequence with a biological function, whereas domains have a specific function and typically operate independently to that of the rest of the protein structure [9,10].
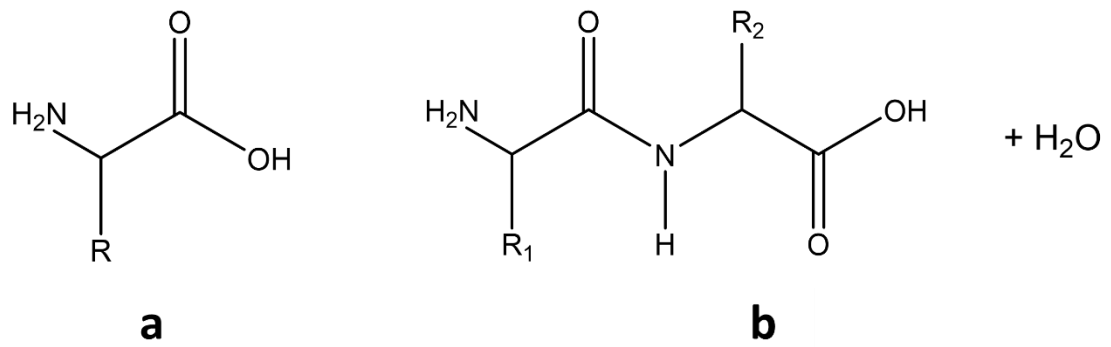
Figure 1.1: (a) Amino acid structure with variable R side chain and (b) peptide bonding between 2 amino acids.

Cation
(pH < pI, positive net charge)

Zwitterion
(Neutral pH/pI, no net charge)

Anion
(pH > pI, negative net charge)
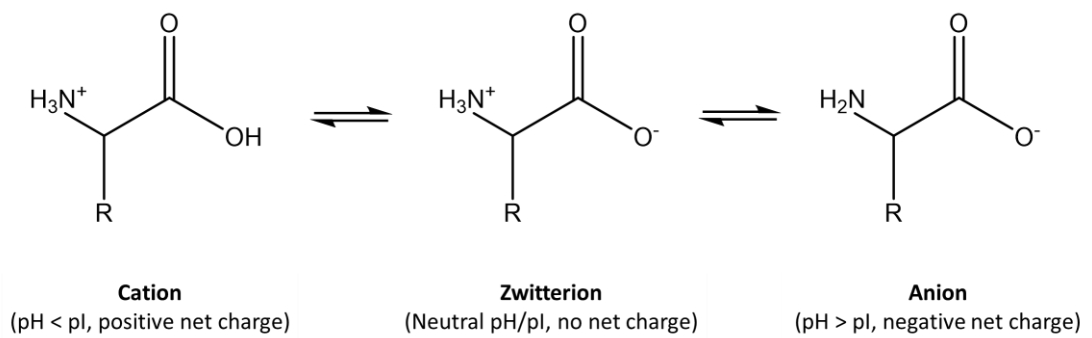
Figure 1.2: Schematic to show the effect of protonation and deprotonation of an amino acid from a zwitterionic state, influenced by the pH of a solution and pI of the amino acid.
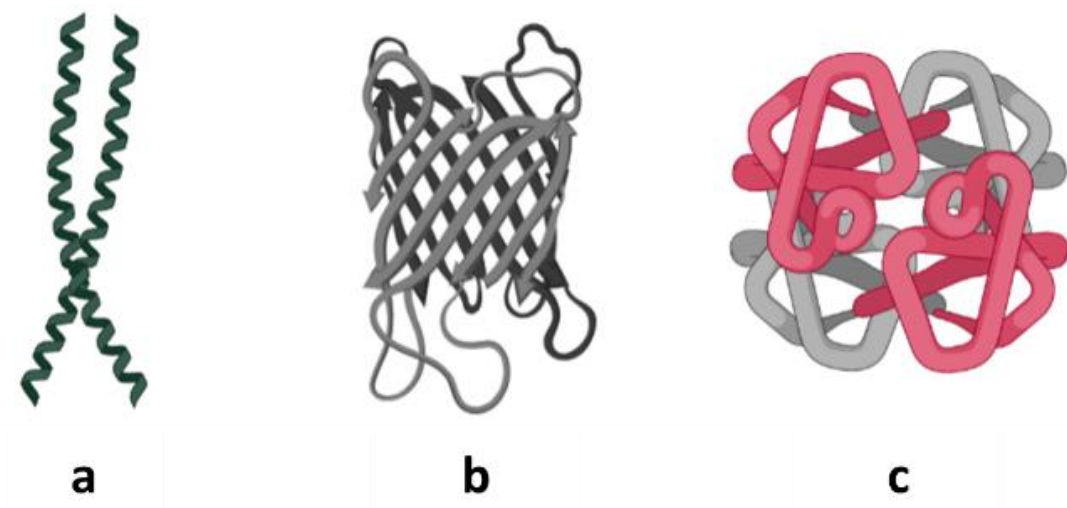
Figure 1.3: Example schematics of (a) α-helix coiled structures (b) anti-parallel β-strands and (c) tetramer quaternary structure representation of haemoglobin comprised of $\alpha_2\beta_2$ tertiary subunits. Created with BioRender.com

1.1.2 Biologics as Therapeutics for Global Population Health Needs

The development of biological therapeutics, such as peptides and proteins, have seen increasing interest and recognition for their potential in addressing requirements for disease therapy. The emergence and largely documented success stems from their distinct biochemical properties. Options available include natural hormones, growth factors and antibodies or manufactured therapeutics that mimic and harness similar characteristics [11,12].

Examples of applications where biological therapeutics have been approved for clinical use in revolutionary and transformative treatment methods include:

- Insulin and growth hormone glucagon-like peptide-1 receptor agonists (GLP-1RAs) for treating type II diabetes mellitus [12,13].
- Epoetin, an erythropoietin hormone used for treating anemia due to a lack of healthy red blood cells [11].
- Rituximab, a monoclonal antibody, used for treating non-Hodgkin lymphoma cancer [11].
- Messenger RNA (mRNA) for COVID-19 vaccine development [14].

Suitable biological therapeutic based treatments have also been widely researched for addressing chronic diseases encompassing cardiovascular, gastrointestinal (GI) and gastric disease [11–13].

The development of biological therapeutics, and understanding relevant delivery methods, could have potential benefits to serve a vast spectrum of patient healthcare needs across populations and thus highly beneficial to worldwide public health. For example, the treatment of prevalent chronic diseases, typically associated with ageing populations, that have a constant or reoccurring impact on patients [15].

This demands the advancement of treatment plans that are consistent, sustained and ideally autonomous. A Health Survey for England report, highlighted dependency on utilising prescribed medication increases with age, particularly when considering multiple medication with 3% of 16-24 year olds taking 3-4 medicines a week increasing to 82% for those aged 85 and over. This trend is also seen in the case of 5+ medicines a week, rising from 9% in

the 45-54 age category to 56% aged 85 and over [16]. If prescribed and taken correctly, these are predominantly effective and can manage the respective condition(s) the patient has been diagnosed with. However, it has been previously reported by the World Health Organisation (WHO) that patient compliance is a prevalent problem with approximately 50% of patients not taking their medication as prescribed [17].

It is also probable that the likelihood of medication errors could increase as the number of health conditions and medications taken increases [15]. The issue of accidental error or incorrect compliance to a medication plan may also be negatively impacted further if different medications are required to be taken at different times of the day/week. Hence, progression from single medication tablets towards multi-medication and longer acting delivery devices, such as depots or implants, in theory, presents a promising strategy to combat some of these issues. Furthermore, it can be postulated that accounting for different patient group needs (age, gender, ethnicity etc) in more efficient and targeted ways could lead to improved therapeutic outcomes with minimised side effects.

Working towards a patient-centred approach has also been emphasised by the UK National Health Service (NHS) and National Institute for Health and Care Excellence (NICE) Quality Standard for Medicines Optimisation. This considers four main principles covered under the overall aims of improved patient outcomes and an aligned strategy towards measurement and monitoring of medicines optimisation [18].

However, there are many potential barriers to the adoption and pace of these advancements regarding biological therapeutics, with clinically acceptable formulations and end integration into suitable delivery device systems still a largely unmet need. One dominating initial barrier to research with biological therapeutics, as is the case with many pharmaceutical related product developments, is that the complex multi-stage processes required for their production comes with high cost implications. Legislation and multi-phase clinical trial approval are lengthy mandatory processes that can take decades to complete before the emergence of an end delivery device product onto the

market. Safety, efficacy and quality are at the forefront for approval by agencies such as the United States Food and Drug Administration (FDA) or United Kingdom Medicines & Healthcare products Regulatory Agency (MHRA). Over the coming decades it is evident that biological therapeutics will continue to be explored. As a result, the understanding of processing these products into a final exemplar such as an injectable depot, scaffold or implantable release system must become better understood.

1.1.3 Biomacromolecule Encapsulation Considerations

The proposed concept of encapsulating biomacromolecules within delivery devices must consider necessary formulation stages and identification of an appropriate manufacturing method. This requires the adoption of protocols that maximise the protection of the incorporated biologic throughout all stages of fabrication, administration and delivery.

Partial disruptions to a protein structure can lead to loss of function through a sharp transition from a conformed folded to unfolded elongated state [2]. Stability of biologics in aqueous solution can be altered by additions of small organic molecules called cosolvents, that either aid or disrupt folding conformation. For example, denaturants shift the equilibrium towards the unfolded state whereas protecting osmolytes contribute to attaining a folded state [19,20]. Degradation can also occur by cleavage of peptide bonds through hydrolysis, with the breakdown rate increasing due to proteases within the human body [21]. Challenges in biomacromolecule delivery include relative insolubility in water and solvents compared to micromolecules. Attempts to improve solubility include the addition of charged amino acids to solutions to minimise aggregation [22–24].

Immunogenicity is an additional consideration that plays a role in dictating the success and delivery of a specified protein and relates to the ability of a substance to initiate a bodily (humoral or cellular) immune response in humans or animals [25]. For effective protein delivery, immunogenicity needs to be low and is dependent on factors such as chemical composition, heterogeneity, molecular size, solubility and degradation characteristics. In addition, patient

characteristics, dose quantity and the administration method selected can also determine the level of immunogenicity and thus delivery success [11].

Taking into account the factors highlighted, Section 1.2 considers administration route options for biologics with advantages and disadvantages of each presented in relation to effectiveness and ease of administration with examples of end applications. Fundamental release mechanisms, theories and modelling are evaluated in Section 1.3 followed by the appropriate selection of manufacturing methods to fabricate delivery devices covered in Section 1.4 and materials in Section 1.5.

1.2 Administration Routes for Delivery of Biologics

This section considers administration routes for delivery in respect to tablet dosage forms or implantable devices, outlining and assessing reasons for their selection in relation to end delivery requirements.

1.2.1 Oral

Oral delivery devices, such as tablets, often offer simple and immediate release at relatively low cost. Other benefits include compliance, low risk of infection and that they can be taken at home without medical assistance. However, problems associated with oral delivery of biomacromolecules include fast degradation, low bioavailability (~2%) and short half-lives (~30 minutes) [26,27]. A primary issue with this administration route is the epithelial barrier of the GI tract. The organised architecture of the epithelial layer acts as a physical and chemical barrier that controls absorption of biologics by passive diffusion defined by a concentration gradient. The first-pass metabolism effect also means that the concentration of a delivered biologic is greatly reduced prior to reaching systemic circulation [28]. Greater than 60% of small molecule drug products marketed are delivered orally, but this is not reflected for the delivery of peptides and proteins [27].

Oral administration route barriers for biologics are due to physiochemical properties (pH stability, hydrophobicity, size and ionisation constant) and susceptibility to degradation (stomach acid, digestive enzymes) [27,29]. Oral absorption is complex and influenced by a combination of factors including dose, solubility and epithelial permeability which may vary with patient age,

diet, GI transit time and medical needs. Approaches to improve bioavailability include use of absorption enhancers and enzyme inhibitors [30,31]. In addition, multi-layer core-based oral delivery systems have been designed to facilitate adjuvant release before biologic release [32].

1.2.2 Sublingual and Buccal

Sublingual (under the tongue) and buccal (against the cheek) administration of medication can offer benefits, such as bypassing the first-pass effect due to passive diffusion through venous blood in the oral cavity. For example, nitroglycerin is primarily metabolised and cleared in a single pass by the liver and therefore can instead be delivered via sublingual form [33]. Sublingual tissue is highly permeable due to underlying capillaries whereas buccal tissue is less permeable and exhibits slower absorption [34]. These self-administering routes act as a desirable option for patients with difficulties swallowing tablets. However, both are typically limited to low dose short-term release delivery applications due to patient discomfort maintaining the dose form position and inconvenience when eating and drinking [34].

1.2.3 Rectal

Rectal administration allows partial bypassing of first-pass metabolism, due to similar passive diffusion observed for sublingual and buccal routes. Rectal mucosa is highly vascularised and allows for rapid and efficient systemic absorption. This route is typically reserved for patients with GI motility issues that interfere with the intestinal tract [35].

1.2.4 Vaginal

Vaginal drug administration can be used to provide pain relief and treat infections e.g. bacterial vaginosis (BV), vulvovaginal candidiasis (VVC) and trichomoniasis [36]. This route also bypasses the GI tract and allows lower dosing over prolonged periods for continuous medication into highly vascularised vaginal tissue e.g. contraceptive hormone devices [37,38].

1.2.5 Parenteral Administration Examples

Parenteral administration is a term that relates to any administration route that does not involve drug adsorption via the GI tract. It is predominantly performed through direct injection into the body following aseptic precautions or

application to the skin and largely classified under five main categories: transdermal, intradermal, intravenous, subcutaneous and intramuscular shown in Figure 1.4(a-e) respectively. By avoiding the GI tract and first-pass metabolic effects, parenteral administration of biologics often leads to longer active effect associated with higher bioavailability [39]. Table 1.1 provides a summarised outline of different parenteral routes with the associated advantages, disadvantages and examples of delivery applications from previous literature.
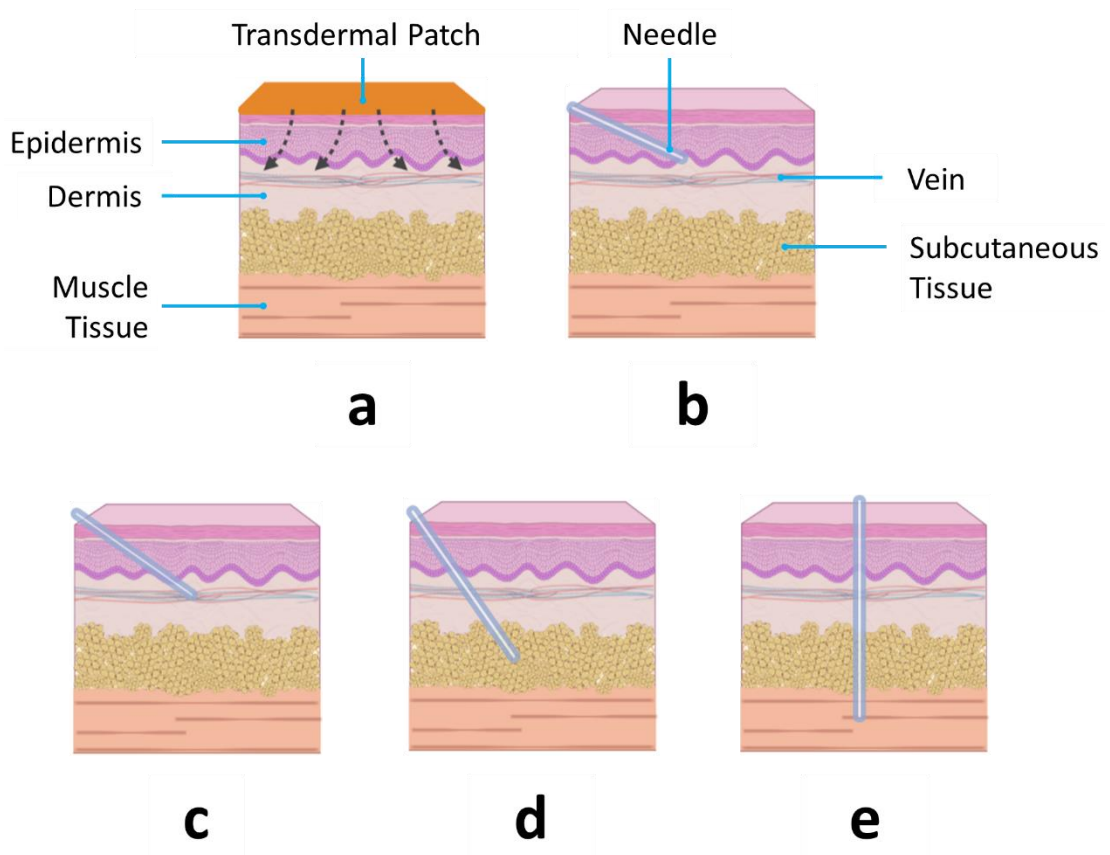
Figure 1.4: Simplified schematic to show parenteral administration routes of (a) transdermal, illustrated with a patch delivery device, and (b) intradermal, (c) intravenous, (d) subcutaneous and (e) intramuscular. Created with BioRender.com

Table 1.1: Summary of parenteral administration routes with associated advantages and disadvantages respective to end application examples.

Parenteral Administration		
Route	**Advantages (+)** **Disadvantages (-)**	**Examples**
Transdermal (TD) Delivery occurring across the skin [40].	+ Non-invasive and ease of self-administration [40,41]. − Limited to low molecular weight (MW) active pharmaceutical ingredients (APIs) below ~500 Da [39,42]. − Requires APIs with Lipinski properties such as high lipophilicity and potency [39,42].	Microneedle array patches and active devices e.g. stimulated by electrode signalling [40,43]. Delivery of nicotine (smoking cessation), fentanyl (pain relief) and nitroglycerin (angina pectoris chest pain relief) [43].
Intradermal (ID) Delivery within the dermis at a shallow angle [44].	+ Non-invasive TD delivery devices can be used for local and systemic administration needs [45]. − Requires highly trained personnel and can have poor consistency with injected volumes and risk of accidental subcutaneous injection [46].	Local anaesthetic and allergy testing [47]. Lidocaine delivery for rapid local anaesthesia [48]. Diagnostic skin testing for allergic rhinitis, asthma and/or otitis media with effusion [49].
Intravenous (IV) Delivery into a vein [39].	+ Fast and direct delivery for application needs requiring systemic circulation [39].	Nanoparticle delivery of anticancer drugs e.g. paclitaxel [52].

	+ High bioavailability due to bypassing of absorption barriers and metabolic mechanisms [39]. − Requires API to be in aqueous solution or fine suspension to prevent embolism [39,50]. − Requires trained personnel with long infusion periods with risk of infection [51].	Delivery of lung-targeted nanofibers for pulmonary hypertension [53]. Green light-triggered intraocular drug release of encapsulated doxorubicin for IV chemotherapy of retinoblastoma [54].
Subcutaneous (SC) Delivery into adipose tissues e.g. 45 or 90° angle [39].	+ Suitable for APIs exhibiting low bioavailability. API absorption is slow and sustained due to a lower number of blood vessels [55]. − Injection volumes up to 3 mL can prove problematic when trying to achieve therapeutically meaningful concentrations [51,56].	Long-term delivery requirements, where the pH of interstitial fluid within SC tissue is approximately 7.4 [57]. Self-administering autonomous insulin delivery devices [58]. Biodegradable implant for sustained antiretroviral and hormone delivery [59].
Intramuscular (IM) Delivery into muscle tissue e.g. 90° angle [39].	+ Increased vasculature compared to the SC layer and accommodates larger dose volumes (~0.5 – 3 mL) that are faster acting [47,60]. − Incorrect administration can cause inadvertent delivery into the SC tissue, reducing drug efficacy and absorption rate [60].	In-situ depots acting as API repositories, with absorption rate dependant on physiological factors [61].

1.3 Therapeutic Release Profiles and Mechanisms Adopted for Delivery Device Design

1.3.1 Release Rate Profiles and Condition Dependant Release

Figure 1.5(a-e) highlights five release rate profiles for delivery devices [62]. The following section outlines release kinetics and reasoning behind their possible selection in relation to examples of previous delivery applications, as documented in Table 1.2.
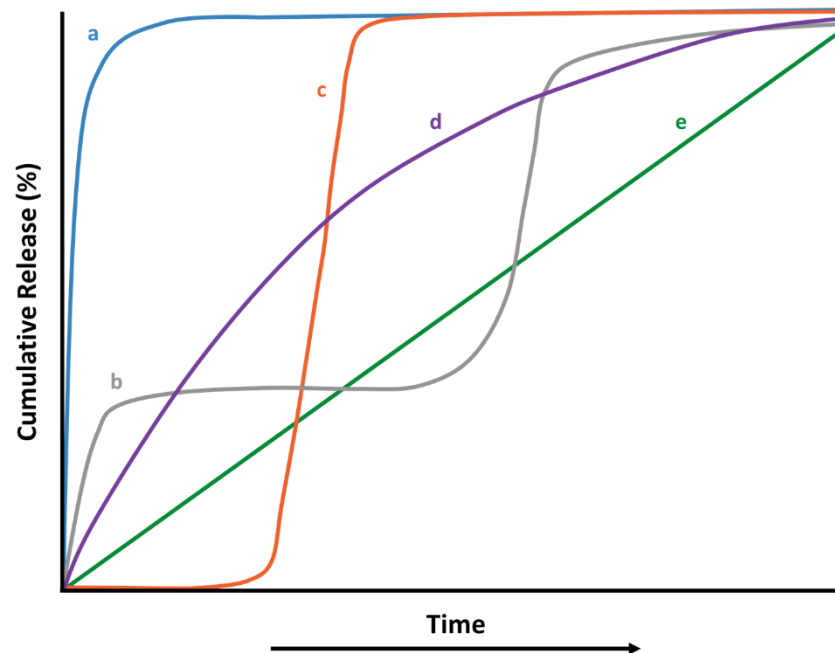
Figure 1.5: Example profiles of (a) immediate release, (b) pulsatile release,(c) delayed release, (d) first-order release and (e) zero-order release.

The desired release rate profile of a delivery device system is dictated by requirements that aim to achieve maximal therapeutic benefit, with minimised side effects, in relation to patient specific needs. This is dependent on the intended release of a specific dose(s) over a pre-determined time period. For example, treatment via sustained therapeutic release over 24 hours to maintain a steady concentration systemically. It is also important to account for the therapeutic window to minimise any significant adverse side effect in patients and ensure the required dose is achieved; i.e. the area of a concentration release profile situated between the level of minimum effective concentration to achieve therapeutic benefit and minimum toxic concentration [63].

12

Table 1.2: Summary of different release strategies with end application examples.

(1) Strategies for Timed Release		
Strategy	**Description**	**Examples**
Immediate/Burst Release	A rapid onset of API release experienced before a stable plateau release profile is reached, shown by Figure 1.5(a) [62].	Delivery of benzodiazepines for rapid anti-seizure epilepsy treatment [64].
Pulsatile Release	Release of a precise amount of API after a predetermined off period (lag time) for repeated cycles, shown in Figure 1.5(b) [62].	Diseases with symptoms that follow a circadian rhythm where administration at certain times may initiate or improve the therapeutic effect on the patient [62]. Delivery release of anti-inflammatory drugs to manage rheumatoid arthritis [65].
Delayed Release	API is not released immediately but instead after a set period of time, as observed in Figure 1.5(c) [62].	Enteric coatings for oral solid dosage forms to prevent API delivery until the small or large intestine [62,66].
(2) Strategies for Slow Continuous Release		
Strategy	**Description**	**Examples**
First-Order Release	Release following Fick's law of diffusion, where API dependent release occurs over an extended period as shown by Figure 1.5(d) [67,68].	Onset of API action is followed by a slower sustained release, minimising dosing frequency e.g. release occurring over 1 to 3+ months in duration [62].

	Release occurring at a constant rate, independent of API concentration and maintained within the therapeutic window, throughout the delivery period, as shown in Figure 1.5(e) [67–69].	Delivery of recombinant human erythropoietin (rhEPO), used to treat chronic nephropathy and anaemia over ~30 days from poly(lactic-co-glycolic acid) (PLGA) microparticles; $R^2 >$ 0.98 [70].
Zero-Order Release	Release occurring at a constant rate, independent of API concentration and maintained within the therapeutic window, throughout the delivery period, as shown in Figure 1.5(e) [67–69].	Delivery of recombinant human erythropoietin (rhEPO), used to treat chronic nephropathy and anaemia over ~30 days from poly(lactic-co-glycolic acid) (PLGA) microparticles; $R^2 >$ 0.98 [70].

(3) Strategies for Triggered and Targeted Release

Strategy	Description	Examples
Stimuli Sensitive Release	Release dependent on biological or external induced signalling triggers such as changes in temperature, pH range, chemical interactions and electrical impulse [71].	Insulin (5.7 kDa) release from the pancreas is triggered by glucose concentration and can be replicated via insulin pump delivery systems for management of diabetes [72].
Targeted Release	Increasing API concentration specifically in a designated area of the body relative to other areas [68].	API delivery to cancerous tumours through carriers accumulating in pathological sites (passive) or ligand attachment for carrier surface interaction with pathological cells (active) [73].

1.3.2 Overview of Delivery Device Release Mechanisms

Establishing the required release mechanisms to achieve a desired release rate profile can involve chemical or enzymatic degradation of the polymer-API matrix. Structural changes through swelling and diffusion can also be assessed over the period of intended release [68]. This section provides an insight into the different approaches in the context of their possible selection for delivery device design.

1.3.2.1 Dissolution-Controlled

APIs in principally dissolution-controlled delivery device systems can be either encapsulated within or coated with a polymeric membrane that breaks down over a pre-determined amount of time (t) [68]. For example, a low solubility coating that allows immediate release (reservoir) or a dissolvable matrix in which the API is dispersed (monolithic) shown in Figure 1.6(a)(b) respectively. Hence, this approach is typically associated with short-term release tablets (minutes/hours).
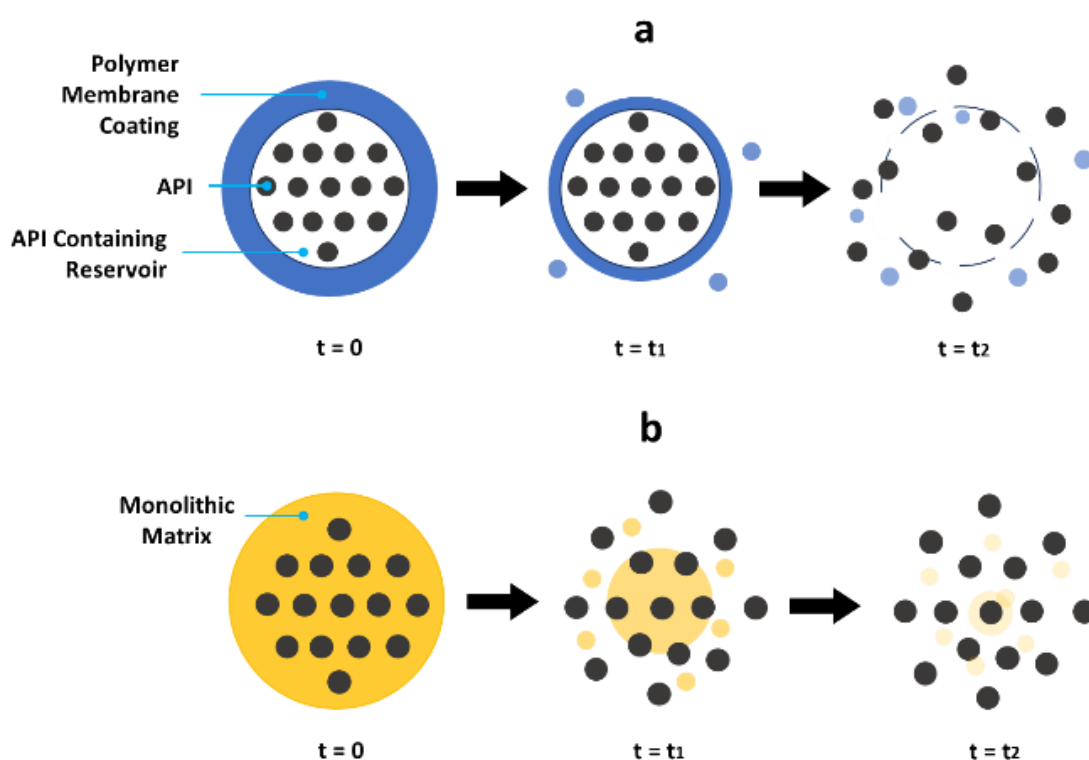
Figure 1.6: Simplified schematic representation of dissolution-controlled release via (a) reservoir system and (b) dissolving monolithic matrix.

1.3.2.2 Diffusion-Controlled

Diffusion-controlled delivery device systems require the API to transfer from a high concentration reservoir via pores in a rate-controlling membrane or a matrix itself, shown in Figure 1.7(a)(b) respectively. Differences in concentration gradient across this membrane boundary can also impact the rate of release, with diffusion categorised as Fickian or non-Fickian [68,74]. These mechanisms are commonly adopted for immediate release oral tablet forms (minutes/hours) but are also applicable to more sustained periods of release (days/weeks) if the rate can be tuned appropriately. One example of this could be whereby rate of release is dictated by the ability for encapsulated APIs to move from the central core through a membrane. Factors to consider include API molecular size and level of loading in relation to membrane thickness, porosity and solubility.

Release from a monolithic matrix, where the API is homogenously present throughout the structure, occurs when outside layers are exposed and with time dissolve, allowing for progressive diffusion [68,74]. Matrix characteristics to consider include composition, structure, porosity, swelling and degradation in relation to API solubility, stability, charge interactions and interaction with the matrix [74]. In addition, spatial locality of encapsulated APIs could influence release such as loading predominantly in the core versus at nearer the surface or equal distribution within the delivery device.
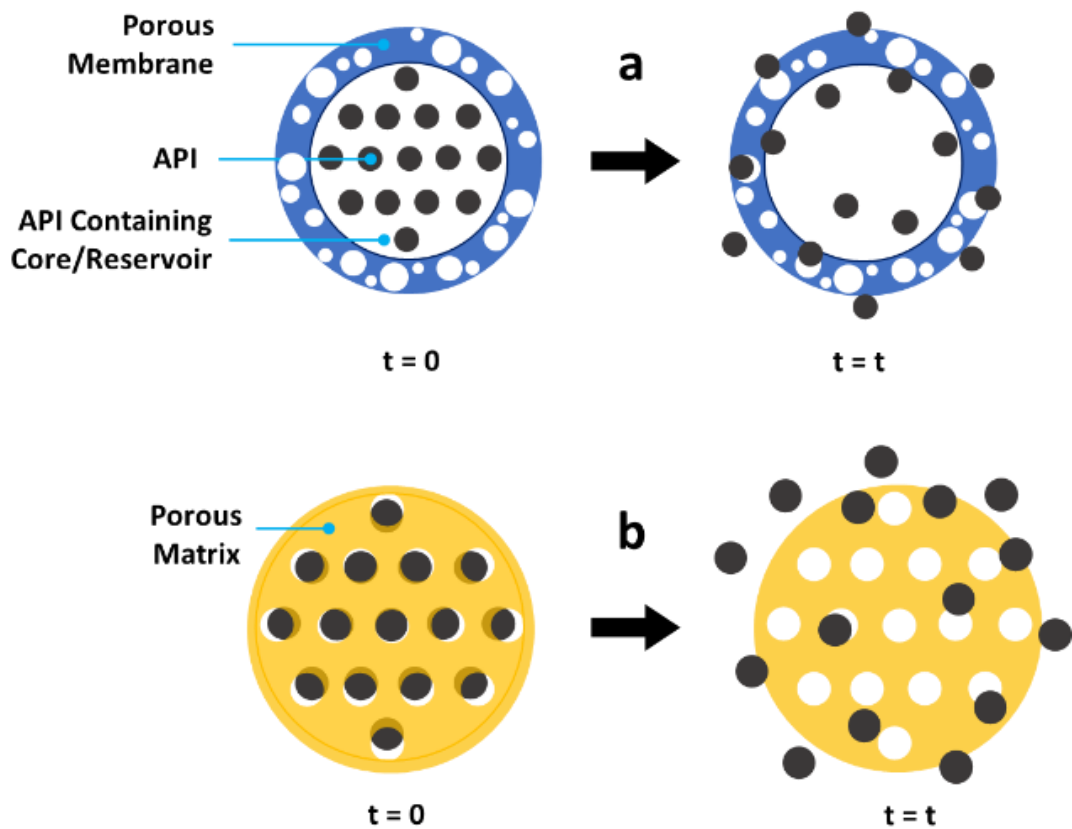
Figure 1.7: Simplified schematic of diffusion-controlled release from
(a) reservoir core with a porous membrane and (b) porous monolithic matrix.

1.3.2.3 Swelling-Controlled

Delivery through swelling has been exploited particularly in the case of hydrogel systems, where an API is initially dispersed within a hydrophilic polymer and eluted upon solvent penetration and retention over time [74]. Delivery devices utilising swelling as a principle mechanism for release are popular for biological actives. The hydrated state can aid in protecting and regulating function, such as enabling hydrophobic interactions that maintain protein tertiary structure [74,75]. Figure 1.8 provides a simplified schematic representation of swelling initiated release, which can be linked to a multitude of factors including polymer selection, crosslinking mechanism, polymer volume fraction and matrix mesh characteristics. A combination of these factors dictates if release will firstly occur and secondly the release rate. Degradable polymers could initially exhibit changes from swelling before subsequent matrix disruption.
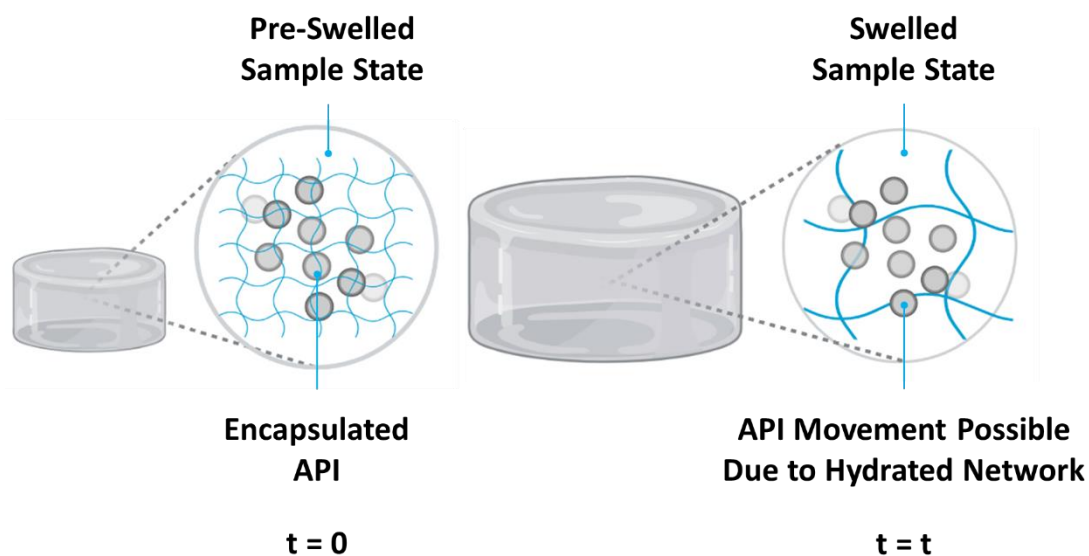
Figure 1.8: Simplified schematic showing swelling of a hydrogel matrix initiated by the penetration of a solvent at t = 0, leading to a more hydrated and open network allowing for API movement and release at t = t. Created with Biorender.com.

1.3.2.4 Chemically-Controlled

Selected stimuli or natural biological processes can trigger controlled release through changes in the chemical structure of a delivery device, related to composition and MW [68,76]. For example, progressive reduction in polymer MW through breakdown within a pH specific region within the body. Bulk eroding versus surface eroding systems are highlighted in Figure 1.9(a)(b) respectively. For both scenarios, the degradation mechanism that governs release can also be utilised to avoid the requirement for device removal after administration [68]. Another option includes API conjugation through chemical linkage to a polymer backbone, which during cleavage within physiological conditions leads to release, shown in Figure 1.9(c) [68]. Applications include polymer-protein conjugates involving pegaptanib sodium (Macugen®) for treatment of neovascular age-related macular degeneration (nAMD) [77,78].
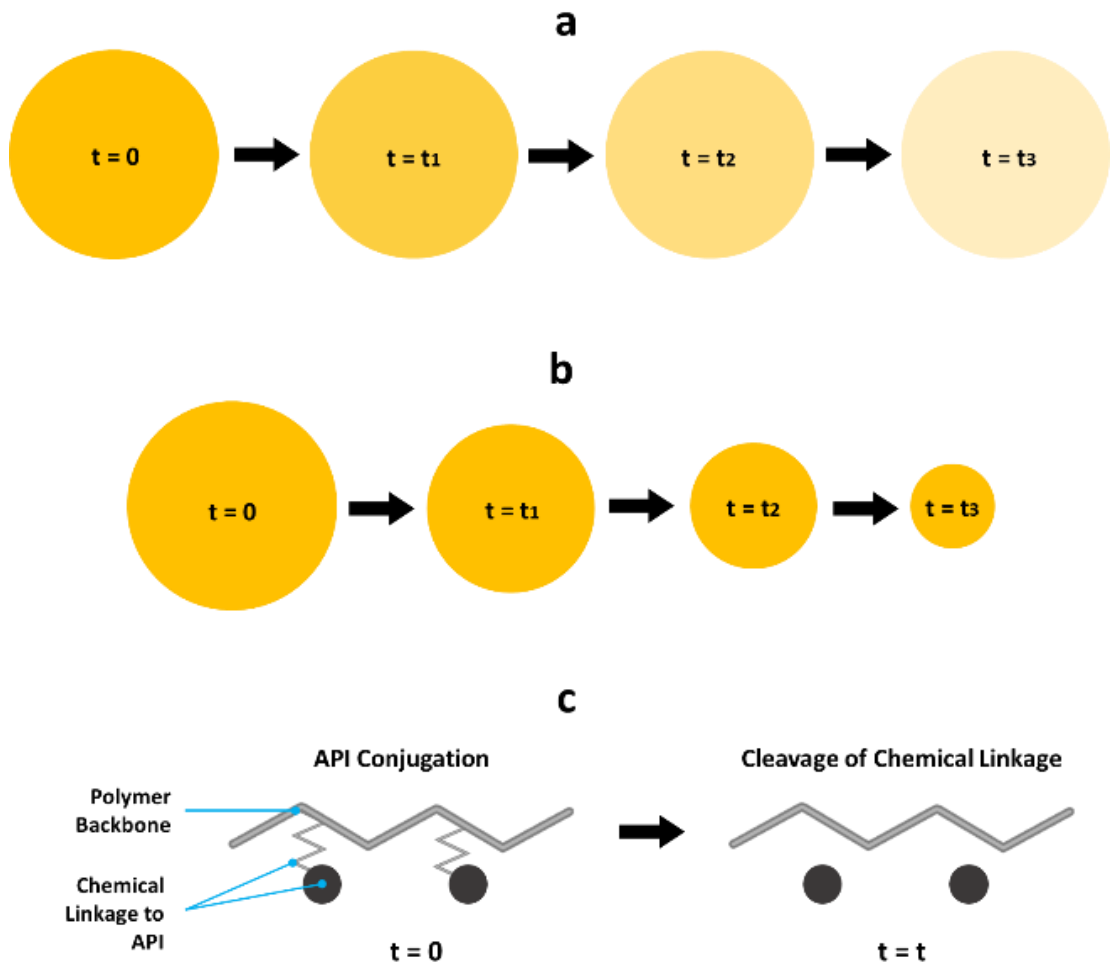
Figure 1.9: Simplified schematic of (a) bulk erosion, (b) surface erosion and
(c) API-polymer conjugation cleavage over time (t).

1.3.3 Matrix Mesh Size Considerations

Encapsulation of bioactives within a delivery device for controlled release applications must consider the influence of matrix mesh size and crosslinking density. Matrix mesh size, defined as the linear distance between two adjacent crosslinks that comprise a polymer network, is an important indicator to determine the likelihood of entrapment or release [60].

Previous literature has reported attempts to understand matrix properties, including the proposal of different theories and experimental analysis to determine key parameters such as changes in swelling ratio. Approximations for establishing a matrix mesh size value for hydrogels have largely been

calculated through applying the rubber elastic theory or equilibrium swelling theory, based upon Peppas-Merrill principles. Alternative suggestions to these models including the Mackintosh theory, blob model and scattering related analysis have been explored but are less reported [79–81].

1.3.3.1 Rubber Elastic Theory

The rubber elastic theory links structural properties to stiffness by estimating shear modulus under applied stress based on the number of chains in the network [82]. Corrections are often required to be practically applicable for a wider range of network scenarios, such as accounting for swollen state and junction functionality. Examples of junction models include affine and phantom which consider mobility of junctions with regard to elasticity [82,83]. However, the theory systematically neglects differences in hydrogel polymer chain length, molecular structure and interaction in a solvent [82,84].

1.3.3.2 Equilibrium Swelling Theory (Peppas-Merrill)

The Peppas-Merrill equation is a modified version of the Flory-Rehner equation regarding equilibrium swelling theory, which considers the state of a hydrogel immediately after crosslinking as "relaxed" prior to immersion in a solvent leading to its "swelled" state [82]. Changes in matrix mesh size are determined through comparisons of properties in these two states. This includes polymer attributes such as MW, volume fraction, network chain segments bounded by crosslinks and solvent interaction [82,84].

1.3.4 Influence of Crosslinking Mechanism on Polymer Matrix Formation

One common approach to tuning mesh properties is through changing the MW of the polymer chain, as this directly influences distance between adjacent crosslinks of the polymer network [84,85]. Furthermore, reducing the polymer fraction will result in a more open network, but mechanical requirements based on end application must be considered. Release rate and desired longevity of release must be considered in relation to bioactive size and concentration within the delivery device. Polymers consisting of predominantly hydrophilic aspects will also lead to increased solvent uptake and increase in swelling ratio [85]. For degradable materials, swelling ratio and matrix mesh size could

be expected to change over time, whereby entrapment of bioactives may occur until matrix mesh size becomes sufficient to allow release.

Formulation decisions will be dictated by associated crosslinking mechanisms required to form a 3D structure. In the case of AM this must be relative to the selected technique, such as ultraviolet (UV) light-initiated crosslinking. Increased crosslinking density will result in a stiffer and more tightly bound matrix, which will swell to a lesser extent compared to a more elastic matrix due to hindrance of polymer chain mobility [86]. Crosslinking mechanisms, such as chain-growth (CG), step-growth (SG) and mixed-mode (MM) polymerisation examples outlined in upcoming Sections 1.3.4.1 – 1.3.4.3 and represented in Figure 1.10(a-c) respectively, influence the formation of polymer networks.
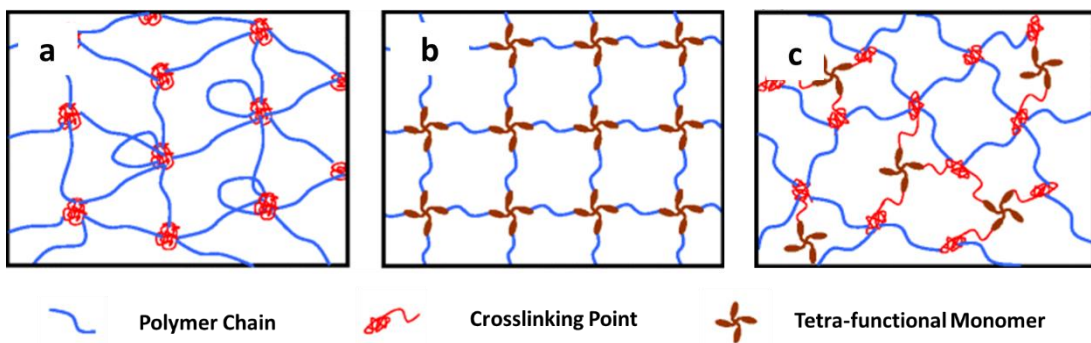
Figure 1.10: Simplified schematics of polymerisation via (a) chain-growth (CG), (b) step-growth (SG) and (c) mixed-mode (MM) mechanisms. Adapted from [85].

1.3.4.1 Chain-Growth (CG) Radical Polymerisation

Linear polymers, such as functionalised poly(ethylene glycol) (PEG), have been employed for CG polymerisation. Successive chain lengthening is achieved through the addition of monomer molecules onto the end of chain active sites one at a time via free radicals [85,87]. Non-ideal variation across the end crosslinked matrix can occur due to random entanglement, reflective of the heterogenous nature of the CG matrix mesh [85,88]. Whilst this could limit control over bioactive release it may still be possible to establish formulations that are suitable through appropriate polymer selection.

1.3.4.2 Step-Growth (SG) Polymerisation

SG crosslinking occurs when at least two multifunctional monomers are reacted, with the rate of crosslinking typically faster than CG systems through multiple independent reactions [85,87]. A particular benefit of SG polymerisation is the generation of comparatively more ordered and homogenous structures [85,88]. However, materials associated with this polymerisation mechanism can have higher associated costs and lower availability from commercial sources due to greater complexity during synthesis e.g. use of multi-arm norbornene terminated polymers and multi-arm thiols. This can present issues, particularly at an early-stage of development where end delivery device requirements are not clear.

1.3.4.3 Mixed-Mode (MM) Polymerisation

MM polymerisation approaches aim to act as a hybrid alternative to structural formation through entirely CG or SG dominated formulations, to harness the relative advantages of each [85,89]. This allows a level of flexibility including changing linkage selection between polymer chains and using stoichiometric imbalances to dictate end matrix mesh characteristics [89,90]. For example, increasing the ratio of thiol (SH) to acrylate groups leads the network to become more SG-like and can be tuned for polymerisation kinetics as well as degradation characteristics [85,91].

1.4 Manufacturing Methods for Producing Delivery Devices

1.4.1 Conventional Production Techniques

Well established, highly repeatable and scalable formative manufacturing methods include compaction, moulding and extrusion. This is attractive for pharmaceutical companies to ensure product efficacy and quality for safe patient use [92,93]. Delivery devices must adhere to stringent regulations related to pharmacokinetic analysis and clinical trials (*in vitro* and *in vivo*) as well as considerations of sustainability and good manufacturing practice (GMP) compliance [93]. However, restrictions dictated by pre-produced tooling limit design flexibility and optimisation trials. Changes to moulds or dies incur additional costs with machine downtime often leading to "one size fits all" approaches rather than optimising for different patient group needs.

1.4.1.1 Powder Compaction

For oral delivery devices, such as tablets, powder compaction is the most commonly adopted method of production [94]. This process involves combining the API and excipients through mixing and granulation to a desired particle size, distribution and morphology. The mix is then dried, compressed and coated (if required) as outlined in Figure 1.11.
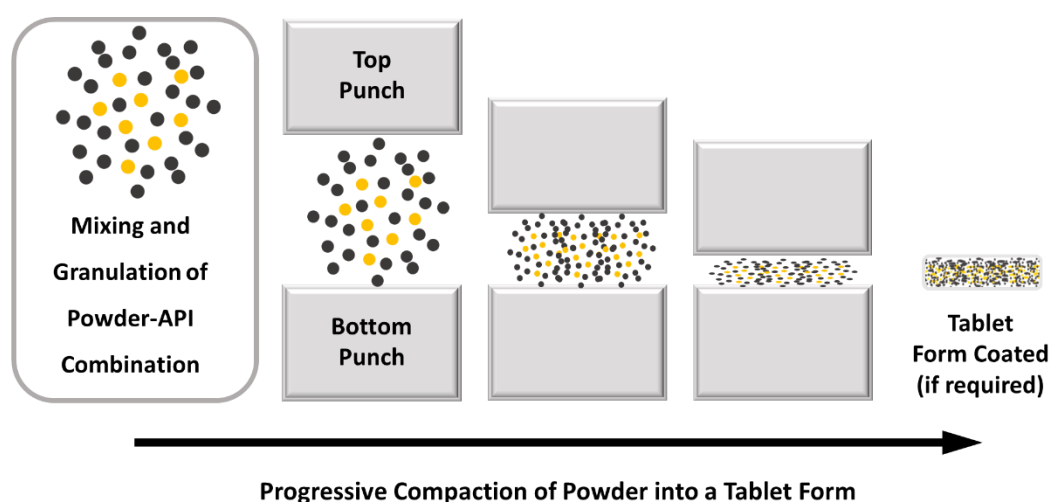
Figure 1.11: Simplified schematic of tablet production via powder compaction.

1.4.1.2 Injection Moulding and Hot Melt Extrusion (HME)

Granulated thermoplastic-API blends that are fed into a heated barrel, forming a molten liquid, can be injection moulded. Heated polymer is transferred by a rotating screw into a cavity. This is cooled to solidification prior to ejection of the completed part, shown in Figure 1.12. Multi-cavity moulds allow increased production rates, but rheological properties must ensure adequate filling of the mould per cycle [95,96]. Inadequate material preparation can lead to distortion, shrinkage, sink marks and voids [96].

HME is a continuous process, whereby polymer-API blends are similarly fed into a heated barrel to reach their glass transition temperature (T_g). The melt passes through a die of the desired geometry, is cooled and then sectioned as required [97]. HME is a solvent-free process with minimal compression of actives, allowing dispersion at a molecular level in the final dosage form which can lead to improved bioavailability [98]. However, it requires APIs to be thermally stable which poses degradation issues during processing [97,98].
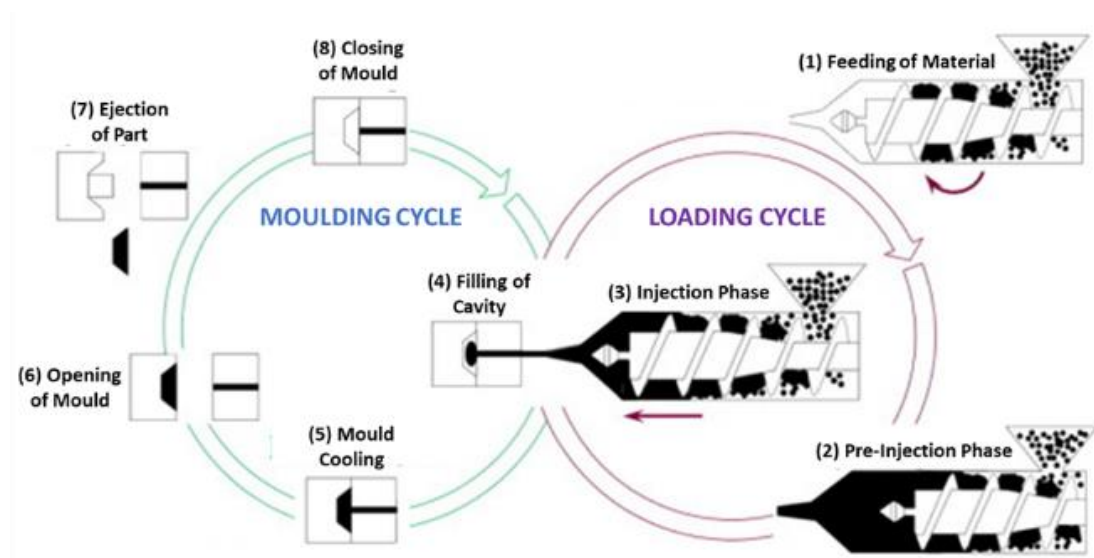
Figure 1.12: Flow diagram representing typical cycles of an injection moulding process. Adapted from [95].

1.4.2 Additive Manufacturing (AM) 3D Printing Techniques

1.4.2.1 Introduction to AM – Definition and Classifications

The International Organisation for Standardisation (ISO) Technical Committee (TC) 261 alongside the Committee F42 Additive Manufacturing (AM) Technologies as part of the American Society for Testing and Materials (ASTM) define AM as a method that uses 3D model data to produce physical objects in a layer-by-layer manner [99]. AM, also referred to as 3D printing, contrasts traditional tool-based techniques (subtractive or formative). The ASTM definition of AM can be categorised into seven classified processes [99]. Material extrusion, material jetting/inkjet printing (IJP), vat photopolymerisation (VP) and powder bed fusion (PBF) feature within previous literature regarding the production of pharmaceutical delivery devices. Table 1.3 provides an overview of these AM methods with advantages (+), disadvantages (−) alongside examples of use for pharmaceutical applications.

Table 1.3: Summary of AM/3D printing techniques with the associated advantages and disadvantages respective to end application examples.

AM/3D Printing Techniques Implemented for Pharmaceutical Delivery Device Production		
Printing Modality	**Advantages (+)** **Disadvantages (-)**	**Examples**
Material Extrusion	+ Allows deposition of higher viscosity materials to produce clinically relevant designs (µm – mm) [100]. + Multi-nozzle setups available for multi-material printing e.g. Cellink BioX™. − Print resolution sacrificed when a wider nozzle is	Segmented multi-active dosage form resulting in different API release profiles [101]. Medication consolidation to reduce errors in medication by improving patient compliance [101].

		required to allow suitable flow of material [100].
Material Jetting/Inkjet Printing (IJP)	+ Minimised contamination due to non-contact droplet deposition [102]. + High level of control over spatial location of ink, multi-material capability and μm scale features [102,103]. − Viscosity and particle additions can cause complications with the nozzle interface [104]. − IJP of biomacromolecules is less reported with no current documentation of an end 3D printed sustained delivery device.	Small molecule delivery device e.g. tablets for a poorly soluble drug, carvedilol [105]. Multi-material dosage forms for ibuprofen delivery [106]. Bespoke polydrug implants for pitavastatin and trandolapril delivery [107]. Piezoelectric jetting to print lysozyme and observe imparted effects via passing through a printhead [108]. Empirical studies of IJP proteins and cell-containing structures [109].
Vat Photopolymerisation (VP)	+ Ability to produce smooth, dimensionally accurate parts and feature resolution ~10 – 100 μm when printing parameters are optimised [110,111].	PEGDA-based oral dosage forms for 4-aminosalicylic acid (4-ASA) and paracetamol delivery [113].

		Lidocaine hydrochloride loaded bladder treatment device [114].
	+ Digital light processing (DLP) systems often have reduced printing times via crosslinking the entirety of each layer pattern at once [112]. − Resins must still adhere to viscosity limitations to adequately spread within the vat and able to be crosslinked e.g. UV light initiated [112].	Dissolvable active and passive microneedle patch [115]. 3D printed microneedle patches for intradermal insulin delivery [116].
Powder Bed Fusion (PBF)	+ PBF requires no support structures allowing geometrical complexity [117]. − Localised and high-powered laser beams for sintering pose significant thermal degradation concerns regarding some APIs [118].	Eudragit L100-55 tablets containing paracetamol at 5, 20 and 35% (*w/w*) [119]. Prosthetics and biopolymer scaffolds harnessing geometrical complexity [120,121].

1.5 Materials and Design Choices for Delivery Device Examples

Achieving desired functionalities for an end delivery device appropriate in accordance with an end application is a multi-factorial challenge. Important aspects involved include suitable manufacturing methods, dimensional requirements, release characteristics and mechanical properties as well as the ease of administration, maintenance and retraction of the device (if required). Appropriate material choices for a selected processing technique and delivery aim govern overall success. This section provides past examples from literature to give an overview of delivery device fabrication with reasoning for the materials selection.

1.5.1 Non-Biodegradable Materials

In recent times, the majority of available implantable delivery devices have been manufactured from non-biodegradable polymers [122]. Implants need to be mechanically capable throughout use and avoid breakage to prevent changes in intended release and for easy retrieval if required. This could suggest why non-biodegradable materials are favourable as there is less chance of unwanted variation over time compared to biodegradable systems where matrix dissolution is often utilised as a way of delivering an API.

Materials used for permanent drug delivery devices include materials such as silicones, thermoplastic polyurethanes (TPUs) or copolymers. For example, a 2 x 2 x 40 mm contraceptive rod device (Nexplanon®) was FDA approved in 2006 and is comprised of an ethylene vinyl acetate (EVA) copolymer containing 68 mg of etonogestrel (a progestin). A daily dose of 25 – 70 µg is delivered depending on the time period since implantation [123]. Insertion into the SC tissue is possible using a specifically designed preloaded applicator at a 30° angle and can remain in the body for up to 3 years to inhibit monthly ovulation [123,124]. The implant is also radiopaque, due to 3% (*w/w*) barium sulphate addition, making it easier to locate using X-ray imaging before extraction [125]. However, whilst EVA is biocompatible it is not biodegradable which means the implant requires surgical removal, often more painful than insertion, once it has served its purpose. This implant is designed to deliver for a prolonged period of up to 3 years, so arguably the compromise is outweighed. Other examples include osmotic pump type systems, such as the

4 x 44 mm cylindrical titanium alloy ITCA 650 implant, that provides subcutaneous delivery of exenatide. Extracellular fluid enters the semi-permeable membrane which expands an osmotic engine leading to a piston drive and expulsion of API containing biodegradable PLGA microspheres [126,127].

1.5.2 Biodegradable Materials

One prominent advantage of using biodegradable materials over non-biodegradable materials is that surgical removal of the delivery device is not required, minimising patient discomfort [122]. However, degradation kinetics across the entirety of the delivery device release must be well understood. This is particularly challenging with changes regarding pH, temperature and biological interactions that occur within the human body. Additionally, associated degradation by-products must be easily eliminated [122].

PEG has been well-studied for bioactive encapsulation due to its hydrophilic, non-toxic and non-immunogenic properties. It can be easily functionalised for crosslinking through acrylate ending and introduced as part of block copolymer chains [128,129]. Attempts at a sustained ocular delivery of small and large drug molecules, triamcinolone acetonide (TA) and ovalbumin (OVA), were achieved through photocrosslinked encapsulation. Poly(ethylene glycol) diacrylate (PEGDA) systems of two different MWs (250 and 700 Da) with pore forming agents were utilised to tune release. TA was fully released but OVA (43 kDa) showed limited elution with ~62% of the total loaded over the time period studied [130]. Once swelled, PEGDA/pore former samples had no further functionality or scope to allow release. Degradation of unmodified PEGDA chains through hydrolysis of ester linkages is a long process and indicates challenges with achieving sustained release of larger molecules.

Synthetic polyesters have also been utilised, harnessing the different degradation mechanisms and times with selection made in relation to application. Poly(caprolactone) (PCL) is semi-crystalline with degradation through random hydrolytic chain scission of ester bonds which can take from 2 to 4 years dependent on MW, degree of crystallinity and in-situ conditions [131,132]. Poly(lactic acid) (PLA) degrades via hydrolysis of ester linkages,

which over 6 to 12 months in media at 37°C can lead to mechanical properties dropping by ~50% [133]. PLGA is a copolymer of PLA and poly(glycolic acid) (PGA) that can display stimuli sensitive behaviour, dependent on acid or ester end groups, and degrades faster than PLA alone [134]. Amorphous poly(trimethylene carbonate) (PTMC) in contrast degrades *in vivo* via surface erosion. MW has a large influence on erosion rate and loss of mechanical properties, with degradation ranging from weeks to years [135]. Diluents and temperature can be necessary to ease polyester processing but may not be suitable for incorporating bioactives due to transition phases.

Natural polymers can be used as carriers for bioactive encapsulation including polysaccharides (e.g. chitosan, alginate) or protein-based (e.g. gelatin derivatives, collagen, elastin-like) [136]. Advantages of these materials include that they are biocompatible, biodegradable, non-toxic, exhibit low immunogenicity and often possess biomimetic properties [137–139]. Natural polymers can be combined with synthetic polymers for hybrid properties, such as injectable PEG-chitosan hydrogels for dual release of an ciprofloxacin (antibiotic) and BSA (acting as a growth factor decoy) for wound-healing applications [140]. Another example includes extrusion printing of PCL-chitosan based implants for release of ibuprofen over 120 hours, with release tuned through material ratio selection and the structural density of the end device fabricated [141].

Chapter 2 Hypothesis and Aims

2.1 Overarching Research Hypothesis

The selection of appropriate AM/3D printing approaches, along with changes in formulations, polymer matrix properties, and geometry will enable the encapsulation of biomacromolecules within a delivery device and facilitate subsequent controlled release. Release rate and delivery duration will be modulated through these factors relative to the incorporation of proteins with different physiochemical properties.

2.2 Model Protein (Enzyme) Selection

Model proteins (enzymes) are commonly inexpensive and easier to acquire in larger quantities. This allows for multiple repeat experiments and method development at relatively low cost early-stage delivery device development. Alkaline phosphatase (ALP), bovine serum albumin (BSA) and lysozyme (LYZ) were proposed in this thesis due to their contrasting characteristics (size, pI, optimum pH conditions and structural features) and the potential to model an end delivery application. For example, LYZ to model growth factor recombinant human bone morphogenetic protein 2 (rhBMP-2) for studying release rates from microparticles for regenerative applications [142]. Table 2.1 summarises the differences between three model proteins selected.

Table 2.1: Properties of the proposed model proteins ALP, BSA and LYZ.

Model Protein	MW (kDa)	pI (pH)	Structure
Alkaline Phosphatase (ALP) [143–145]	~ 140 – 160	~ 4.4 – 5.8	Dimeric, membrane-derived glycoprotein.
Bovine Serum Albumin (BSA) [146–148]	~ 66	~ 4.5 – 5.5	Globular structure comprised of both α-helices and β-sheets.
Lysozyme (LYZ) [149,150]	~ 14	~ 10.5 – 11.4	Single chain polypeptide (129 amino acid residues).

2.3 Identification of Industrial Aims

1. Develop ink formulations and designs appropriate for a selected AM process e.g. the use of DLP printing to produce exemplar samples for the encapsulation of model proteins and subsequent release from different polymer matrices.

2. Understand achievable release profiles relevant to an intended application, e.g. zero-order release with minimal initial burst.

3. Efficiently load and release proteins with minimal loss of function and to ensure the therapeutic window can be achieved for the lifetime of the device created. For example, a depot/implant capable of sustained release over 1 to 3+ months, whilst being able to incorporate relatively high levels of drug/biological loading.

4. Consider incorporating proteins with different physiochemical properties, including as combinations with potentially different intended delivery profiles, and relate to potential future work applications.

2.4 Additional Considerations for Delivery Device Development

- Establishing a mechanism of release consistent across *in vitro* and *in vivo* conditions leading to good *in vitro in vivo* correlations and predictions.

- Development of a delivery device capable of being manufactured from lab to commercial scale that is ideally able to be sterilised using conventional technologies.

- Fabrication of outcomes capable of being safely administered in the community by a nurse, pharmacist or by a patient themselves. For example, biocompatible implants with minimal invasiveness that will biodegrade and thus negate a removal stage once the drug/biological has been delivered. The 3D printed device must also maintain mechanical integrity and be easily retrievable if required.

Chapter 3 Materials and Methods

3.1 Materials

Tablets used to prepare a phosphate-buffered saline (PBS) solution were purchased from Sigma-Aldrich. 2,4-diethylthioxanthone (DETX), ethyl 4-(dimethylamino) benzoate (EDB), lithium phenyl-2,4,6-trimethylbenzoylphosphinate (LAP), tartrazine, DL-Dithiothreitol (DTT), glycerol, alkaline phosphatase (ALP) from bovine intestinal mucosa, bovine serum albumin (BSA) and lysozyme (LYZ) were also purchased from Sigma-Aldrich. Different PEGDA monomers of number average molecular weight (Mn) 575 and 700 were purchased from Sigma-Aldrich and 1000, 4000, 8000 and 10,000 purchased from Generon Ltd. For quantifying total protein release, a Pierce™ Coomassie (Bradford) Protein Assay Kit (catalogue no. 23200) was purchased from Thermo Fisher Scientific. ALP activity was assessed using a Pierce™ PNPP Substrate Kit (catalogue no. 37620), purchased from Thermo Fisher Scientific. Corning® Costar® 96-well Clear Flat Bottom Polystyrene Not Treated Microplates were used for both assays. For proton nuclear magnetic resonance (^{1}H NMR) analysis, deuterated chloroform ($CDCl_3$) (99.9+% atom D) or deuterium oxide (D_2O) (99.9+% atom D) from Sigma-Aldrich was used as a solvent and for gel permeation chromatography (GPC) high-performance liquid chromatography (HPLC) grade tetrahydrofuran (THF) (99.9+%) from Thermo Fisher Scientific was used as a solvent.

3.2 3D Printing Manufacturing Techniques

3.2.1 Inkjet Printing (IJP)

IJP was conducted using a commercial Dimatix DMP-2830 [Fujifilm, Corp.] material printer. The cartridge used (DMC-11610) consisted of 16 linearly aligned nozzles, each with a diameter of 21 μm. Nozzles are spaced 254 μm apart and can produce a ~10 pL drop volume. Approximately 1.5 mL of a prepared ink formulation was filtered using a 0.2 μm filter and injected into the cartridge reservoir. During this procedure, particular care was taken to minimise bubble formation and the cartridge was covered with tape to prevent ambient light from prematurely initiating crosslinking. A light-emitting diode (LED) UV lamp attachment (365 nm, 600 mW/cm^2) [Printed Electronics Ltd.]

was mounted in-line with the printhead path and was used to cure ink formulations during printing deposition.

Initial printability tests were conducted in the form of droplet arrays, lines and squares to optimise the required printing and cartridge settings within the Dimatix software. Once droplet spacing, related to dots per inch (DPI) and sabre angle, was established the required resolution for design files could be determined using Equation 3.1 [151].

$$Droplet\ Spacing\ (\mu m) = \frac{25400}{Resolution\ (DPI)} \ (\mathbf{Eq.\,3.\,1})$$

Bitmap (BMP) patterns for a desired design were prepared with the necessary resolution, relative to the loaded ink formulation, using Inkscape [Inkscape Project], an open-source vector graphics editor software. Where possible, individual layer height was established by printing 50 layers of each ink for a 5 x 5 mm square and measured using a micrometre. Three samples were printed to calculate an average layer height to then determine the number of layers that would be required to reach a desired print height, for example 2 mm. Figure 3.1 outlines the typical stages of the IJP process. To aid in the processing of ink formulations, printer system settings can be exploited including cartridge waveform pulse profile, voltage, temperature, distance from substrate, cleaning cycles as well as substrate type and temperature.
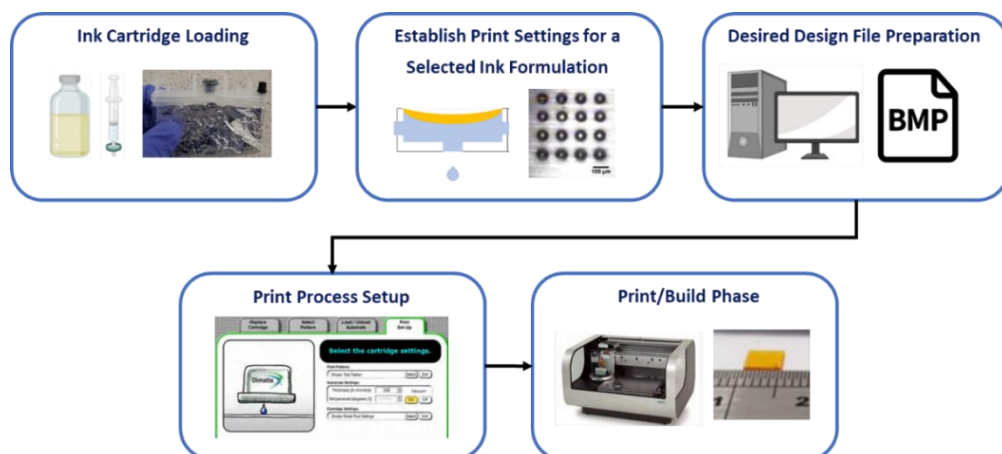
Figure 3.1: Schematic overview representation of the typical stages associated with an IJP process.

3.2.2 Digital Light Processing (DLP) Printing

The DLP printer selected for experimental work was a low-cost Anycubic Photon Mono, with a maximum build area of 130 x 80 x 165 mm. The system consists of a UV LED array matrix light source (approximately 1.2 to 1.4 mW/cm^2) that projects each layer pattern successively through a liquid crystal display (LCD) panel that the ink vat is positioned upon, as shown in Figure 3.2(a). Design patterns were created and exported as stereolithography (.STL) files and prepared within Chitubox V1.9.0 software to be recognised by the printer. Important parameter considerations that dictate the pattern file generated include bottom layer number and exposure time, general layer exposure time, speed of movement of the platform and delay periods between movement or exposure phases. Figure 3.2(b) shows an arrangement of an example .STL design positioned within the relative printer vat area and ready for the print cycle to commence.

a

b
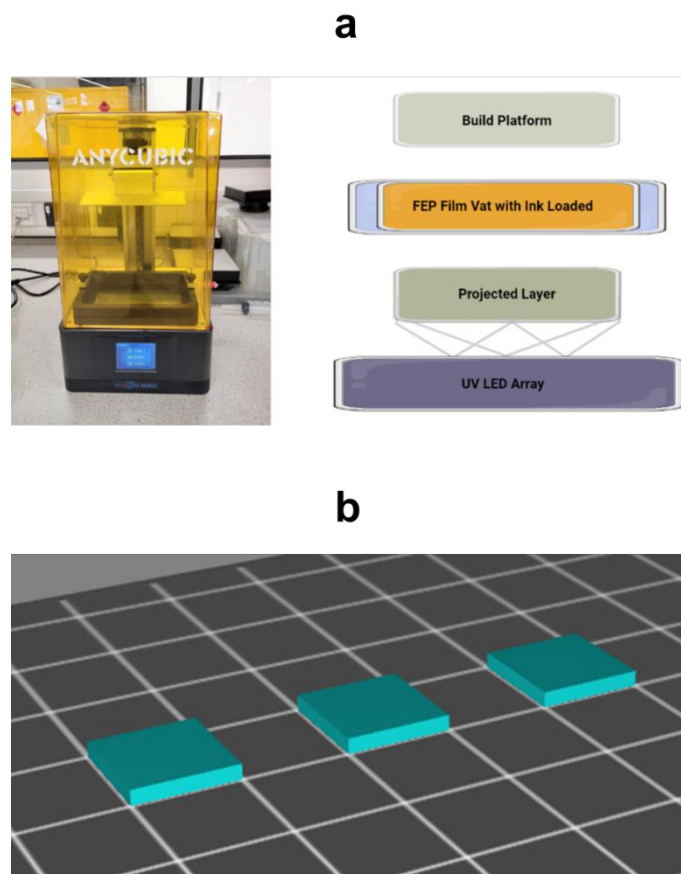
Figure 3.2: (a) Anycubic Photon Mono DLP printer with schematic of components and (b) .STL file patterns arranged on the build plate in the Chitubox V1.9.0 software.

3.3 Ink Formulation Preparation

3.3.1 Poly(ethylene glycol) Diacrylate (PEGDA) Based Formulations

3.3.1.1 IJP

When preparing formulations, the model protein to be incorporated was firstly added to a PBS solution at a desired concentration, for example 1 mg/mL with respect to the total end formulation volume, to aid with solubility of the protein. A photoinitiator, DETX, and an accelerator, EDB, were added in equal quantities, unless another photoinitiator was used e.g. LAP. Finally, the selected amount of PEGDA component was added incrementally to the solution of PBS or Milli-Q (MQ) water, photoinitiator and accelerator (if required). Glycerol was used as a humectant. Individual ink formulations were mixed with a magnetic stirrer bar on a stirrer plate for 15 minutes. Inks were prepared on the same day as printing and stored at room temperature until use.

3.3.1.2 DLP Printing

Selected model protein(s) to be incorporated were firstly added to a PBS solution at a desired concentration, with respect to total end formulation volume. The selected photoinitiator of LAP and photoabsorber tartrazine, if required, were then added to the solution at a desired weight percent of the formulations. For example, 0.5% (*w/v*) LAP in respect to total formulation volume and tartrazine at 0.1% (*w/w*) of PEGDA content. Following this, PEGDA of Mn 575, 700, 1000, 4000, 8000 or 10,000 was added until the content required with respect to % (*v/v*) or (*w/v*) in PBS solution. Individual ink formulations were mixed with a magnetic stirrer bar on a stirrer plate to aid in the dissolution and to ensure consistent and full mixing of constituents. Formulations with higher Mn PEGDA powders required longer mixing times and all inks were prepared on the same day as printing.

3.3.2 Preliminary Analysis of Formulation Preparation: Effect of Stirring

A concentration of 20 µg/mL of ALP, used as the model protein, in PBS was prepared, using 20 mL per beaker to replicate the minimum amount that would be prepared for an DLP process. A stirrer bar was added to each beaker and stirring speeds of 100, 200 and 300 revolutions per minute (RPM) were selected for durations of 5, 15 and 30 minutes using an RCT basic stirrer plate

[IKA®]. Samples were taken from each container, in triplicate, at the required interval for the associated activity assay.

3.3.3 Preliminary Analysis of Formulation Preparation: Effect of UV Exposure

A preliminary UV exposure test setup was used to indicate if UV impacted protein activity. A concentration of 20 µg/mL of ALP, used as the model protein, in PBS was prepared with 50 µL pipetted into a 1 mL syringe positioned underneath a Firefly 25x10 mm AC 345 – 385 nm, 1.5 W/cm² UV lamp [Phoseon Technology], as shown in Figure 3.3(a)(b). Two experimental conditions of continuous UV exposure and UV exposure with periods of 30 seconds irradiation followed by 30 seconds of rest, as an attempt to replicate DLP printing exposures, were compared up until 5 minutes had been elapsed. Samples were taken from the exposed ink, in triplicate, at the required interval for the associated activity assay.
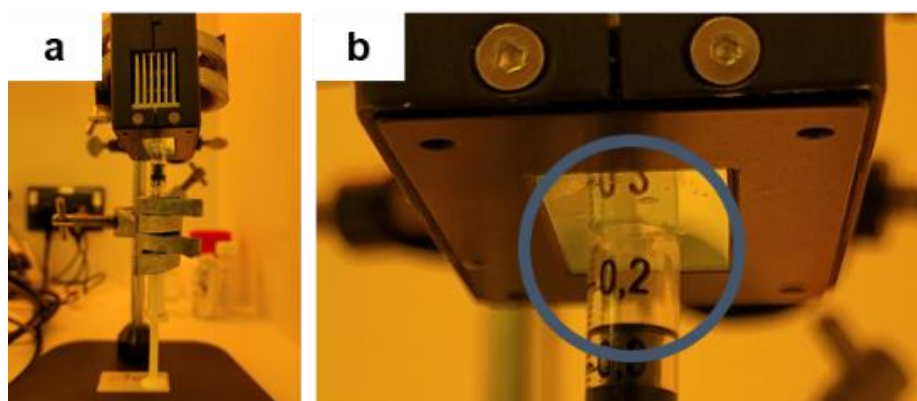
Figure 3.3: (a) UV lamp test setup and (b) positioning of syringe with 50 µL of ALP in PBS solution (20 µg/mL concentration) under the UV projection area.

A second UV study was conducted in-situ within the Anycubic Photon Mono printer vat, to better indicate the impact of UV irradiation during the printing process. The Anycubic Photon Mono DLP printing process utilises UV exposure at 405 nm. A concentration of 20 µg/mL of ALP in PBS was prepared, whereby 20 mL was then poured into the vat. A design file that covered the entirety of the vat (130 x 80 mm) was created for a 1-layer depth of 25 µm. Continuous exposure times of 1, 5, 10 and 30 minutes were selected, with samples taken from the exposed ink at the required interval for the associated activity assay and each condition repeated three times.

3.3.4 Synthesis of Poly(ethylene glycol) Diacrylate (PEGDA) and Dithiothreitol (DTT) to Produce PEGDA-DTT Macromers

Individual materials of PEGDA and DTT were prepared together to synthesise PEGDA-DTT macromers via the process of Michael addition. Combining these materials was achieved via mixing on a stirrer plate with a magnetic stirrer bar for one hour in PBS. Confirmation in previous literature has shown the kinetics of this specific Michael addition reaction occurs relatively fast, with the concentration of free SH groups typically reduced to near zero within 10 minutes [152,153]. To ensure acrylate-terminated PEGDA-DTT chains resulted from the reaction, the synthesis was designed with a stoichiometric imbalance in favour of PEGDA, the acrylate component. Synthesis of these macromers can be easily tuned via changes in the selected SH to acrylate molar ratio. Figure 3.4(a) outlines the chemical structures of the materials and stages involved to prepare the final PEGDA-DTT macromers, shown in Figure 3.4(b). Preparation of different PEGDA-DTT based formulations, for use in DLP printing, followed the same stages as outlined previously in Section 3.3.1.2.
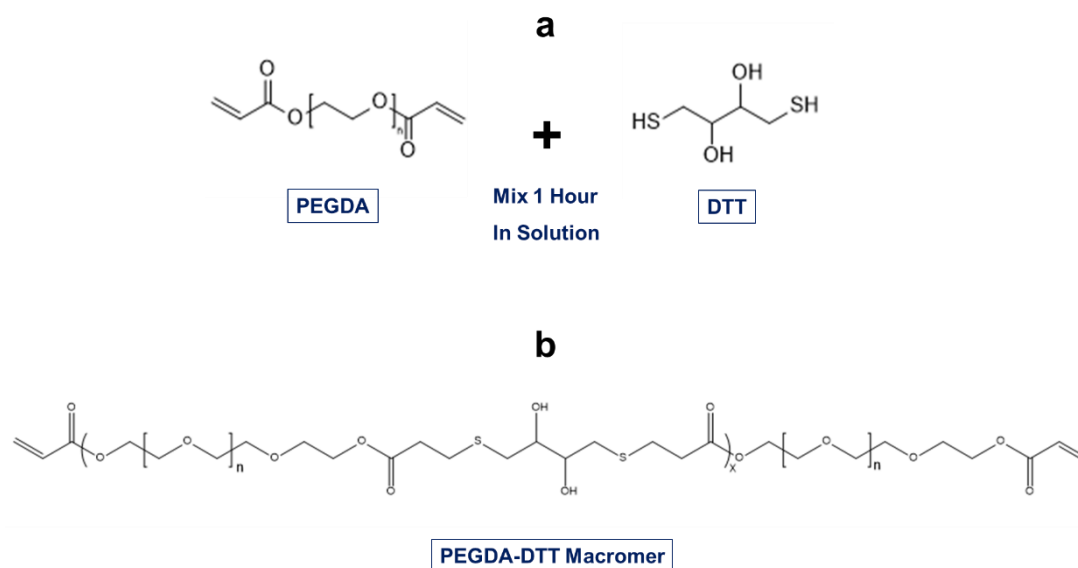
Figure 3.4: Chemical structures of (a) acrylate component (PEGDA) and SH component (DTT), which when mixed for 1 hour produced (b) PEGDA-DTT.

3.4 Characterisation Methods and Techniques

3.4.1 Rheology

To aid in the pre-print characterisation of ink formulations, a Physica modular compact rheometer (MCR) 301 [Anton Parr, GmbH] was used. Rheological properties, in particular viscosity, must be suitable for the selected printing technique. A rotational test setup was selected using a cone-and-plate probe geometry (CP25-1/S-SN15991) with diameter of 24.97 mm, 1.022° angle and 51 µm truncation. This was due to the well-defined shear rate application and the ability to use relatively small sample volumes. Other setup options include parallel plate and coaxial cylinder geometries. Each ink sample was pipetted onto the stationary base plate to ensure adequate filling when contacted by the probe. If required, the sample was trimmed to prevent over-filling. The viscosity value for each ink was determined using the average (n = 3) of all values recorded at shear rates between 1 to 1000 s^{-1} over a time period of 300 seconds with data points taken every second.

3.4.2 Surface Tension, Density and IJP Z Parameter

Preliminary droplet analysis was conducted using a drop shape analyser (DSA) 100S [KrÜss Scientific Instruments, Inc.]. To aid initial ink formulation characterisation, the surface tension was determined at room temperature, using the pendant drop method and Young-Laplace equation. A 1 mL syringe containing each ink formulation was used to consistently produce droplets from a Dimatix needle orifice of 1.25 mm. Surface tension values were determined using an average of 5 droplet measurements (n = 5). Ink density (g/mL) was determined by using an analytical balance and deposition of 1 mL of sample via a 1 mL syringe.

Values collected from density, surface tension and viscosity measurements were used to calculate the Z parameter, a printability indicator, shown in Equation 3.2. A Z value between 1 – 10 suggests that DOD IJP will be possible with that ink formulation [154].

$$ Z = \frac{1}{Oh} = \frac{Re}{\sqrt{We}} = \frac{\rho V d / \eta}{\sqrt{\rho V^2 d / \gamma}} = \frac{\sqrt{\gamma \rho d}}{\eta} \ (\mathbf{Eq. 3.2}) $$

Where Oh is the Ohnesorge number, Re is Reynolds number and We is Weber number. Density is represented by ρ, velocity by V, fixed nozzle diameter by d, viscosity by η and surface tension by γ.

3.4.3 Gel Permeation Chromatography (GPC)

GPC was used to characterise the distribution of MW and the polydispersity index (PDI). PEGDA and PEGDA-DTT macromers were dissolved in HPLC-grade THF at a concentration of approximately 2 mg/mL. A flow rate of 1 mL/min in THF at 35°C through a multi-column setup was used (one PLGel guard column and two PLGel Mixed-C columns 7.5 x 300 mm in series) [Agilent Technologies, Inc.]. For calibration of the differential refractive index detector [Agilent Technologies, Inc.], 12 narrow dispersity polymethyl methacrylate (PMMA) standards ranging from 540 – 2,210,000 g/mol were used. Chromatograms of retention time versus differential refractive index and logMW versus differential weight fraction were prepared in Astra 6.1.7 software [Wyatt Technology Corp.].

3.4.4 Proton Nuclear Magnetic Resonance (^{1}H NMR) Spectroscopy

^{1}H NMR spectroscopy was performed to determine the acrylate:ethylene glycol (EG) ratios of PEGDA polymers, which were dissolved in $CDCl_3$ at a concentration of 10 mg/mL and filtered through cotton wool to remove any insoluble material. PEGDA-DTT macromers were dissolved using D_2O. Spectra were recorded as an average of 16 scans at 400 MHz using an AV400 NMR Spectrometer [Bruker Corp.]. Residual $CDCl_3$ signal (7.26 ppm) acted as references for chemical shifts recorded in δ_H. Acrylate peaks were associated with peaks between 5.5 and 6.5 ppm, with peaks of repeating polymer units around 3.5 ppm. The number of hydrogen atoms per acrylate group (three per group and two groups per chain, for an acrylate terminated polymer) are constant. The signal-per-proton value was taken from the associated peaks and used to convert the integral of repeating unit peaks for the polymer being analysed. Each PEG unit has a MW of 44 g/mol and was used to convert the number of repeat units to the polymer MW. TopSpin 4.0.8 software [Bruker Corp.] was used to process the spectra datasets.

3.4.5 Optical Microscopy

Optical microscope imaging of printed samples was conducted using an Eclipse LV100ND Polarized Light/Dispersion microscope [Nikon UK Ltd.] with NIS Elements Software. ImageJ software [National Institutes of Health and the Laboratory for Optical and Computational Instrumentation, LOCI, University of Wisconsin] was used to add scale bars to images taken.

3.4.6 Cryo-Scanning Electron Microscopy (Cryo-SEM)

Cryo-SEM imaging was conducted using a Zeiss Crossbeam 550, a high resolution, cryogenic analytical and transfer scanning electron microscope (CAT-SEM) system, with a cryogenic stage capable of maintaining a sufficient cryogenic temperature below -150°C. Cryo-SEM enables imaging of samples with high water content through rapid freezing. This technique was selected to track changes in the structural morphology of 3D printed samples as a result of associated swelling, degradation or a combination of these two mechanisms. Selected samples were first sectioned, to expose an interior aspect, and positioned onto a sample holder stub prior to being plunged into liquid nitrogen slush (LN_2 slush technique) [155].

Once submerged, the samples were transferred to the cryo-vacuum chamber, coated in platinum to become conductive and positioned in the main SEM chamber. During sublimation of the water from the samples, the internal structure was revealed with preservation of the native state and true morphology at a macromolecular level.

3.4.7 Sample Swelling and Theoretical Matrix Mesh Size Calculation

Sacrificial samples were prepared alongside the samples dedicated for the release study, to allow for tracking of the swelling and degradation of printed samples over time. Sample sets (n = 3) were added to 3 mL of PBS (pH ~7.4) to ensure full coverage and swelled within an incubator at 37°C. At each selected time point interval, samples were firstly removed, blotted and weighed. This was conducted at days 0, 1, 2, 3, 7, 10, 14, 21 and 28. After weighing in the swelled state, samples were freeze dried and lyophilised to obtain their dried mass. This allowed for the calculation of mass swelling ratio (Q) in Equation 3.3.

$$Mass\ Swelling\ Ratio\ (Q) = \frac{M_s - M_d}{M_d} \quad (\textbf{Eq. 3.3})$$

Where swelled mass and dried mass at equilibrium after lyophilisation are denoted M_s and M_d respectively.

The Peppas-Merrill equation, a modification of the Flory-Rehner equation, was used to determine the network parameter $\overline{M_c}$, shown in Equation 3.4. This corresponds to the average MW between two adjacent crosslinks, related to the degree of crosslinking within a hydrogel network. Previous literature has implemented this model for similar hydrogel-based applications and material compositions, for example PEG polymers as contained in this thesis [130,156,157]:

$$\frac{1}{\overline{M_c}} = \frac{2}{\overline{M_n}} - \frac{\left(\frac{\bar{v}}{V_1}\right)\left[\ln\left(1 - V_{2,s}\right) + V_{2,s} + \chi_1 \cdot V_{2,s}^{2}\right]}{V_{2,r}\left[\left(\frac{V_{2,s}}{V_{2,r}}\right)^{\frac{1}{3}} - \frac{1}{2} \cdot \left(\frac{V_{2,s}}{V_{2,r}}\right)\right]} \quad (\textbf{Eq. 3.4})$$

Where $\overline{M_n}$ is the average MW of the oligomer (g/mol), in the case of this work PEG. $\bar{v}$ is the specific volume, inverse of polymer density, for PEGDA in its amorphous state (0.893 cm^3/g), V_1 is the molar volume of solvent (PBS, 18 cm^3/mol) and $V_{2,s}$ and $V_{2,r}$ represent polymer volume fraction in the swelled and relaxed state. The Flory-Huggins parameter, χ_1, accounts for the polymer-solvent interaction (0.426 for PEG-Water).

The polymer volume fraction of samples and swelling ratio was calculated for the swelled state and as printed state (proposed in this thesis as the relaxed state) using Equation 3.5, 3.6 and 3.7.

$$Polymer\ Volume\ Fraction = \frac{1}{Volumetric\ Swelling\ Ratio} \quad (\textbf{Eq. 3.5})$$

$$Volumetric\ Swelling\ Ratio\ _{Swelled} = \frac{\dfrac{M_s - M_d}{\rho_{Solvent}} + \dfrac{M_d}{\rho_{Polymer}}}{\dfrac{M_d}{\rho_{Polymer}}}\ \textbf{(Eq. 3.6)}$$

$$Volumetric\ Swelling\ Ratio\ _{Relaxed} = \frac{\dfrac{M_r - M_d}{\rho_{Solvent}} + \dfrac{M_d}{\rho_{Polymer}}}{\dfrac{M_d}{\rho_{Polymer}}}\ \textbf{(Eq. 3.7)}$$

Where PBS density (1.014 g/cm^3) was used as the solvent density, $\rho_{Solvent}$, and PEGDA density (1.12 g/mL) for the polymer density, $\rho_{Polymer}$. M_s, M_d and M_r refer to the mass of a sample in the swelled, dried and relaxed state respectively.

The theoretical matrix mesh size, ξ, of the prepared hydrogel samples was then obtained using Equation 3.8 and 3.9.

$$\xi = \left(\overline{r_0{}^2}\right)^{1/2} \cdot V_{2,s}{}^{-\frac{1}{3}}\ \textbf{(Eq. 3.8)}$$

$$\left(\overline{r_0{}^2}\right) = l^2 \cdot \left(2 \cdot \frac{\overline{M_c}}{M_r}\right) \cdot C_n\ \textbf{(Eq. 3.9)}$$

Where $\left(\overline{r_0{}^2}\right)$ is the root mean square end-to-end distance of the polymer in the free state. Carbon-carbon bond length (0.154 nm) is denoted with l, M_r is the MW of repeat units (44 g/mol in the case of PEG) and C_n is a known polymer rigidity factor (4 for PEG).

It must be noted that this proposed theoretical matrix mesh model was applied primarily as a comparative numeric tool between samples printed from different formulations, tracking changes in their respective properties over time.

3.4.8 *In Vitro* Model Protein Release Quantification

3.4.8.1 Sample Setup and Release Conditions

One PBS tablet per 200 mL deionised water (diH$_2$O) yielded 0.01 M phosphate buffer, 0.0027 M potassium chloride and 0.137 M sodium chloride, pH ~7.4. Printed samples prepared for a release study (n = 3) were placed into glass scintillation vials with 3 mL of PBS solution, to ensure full coverage, and swelled within an incubator at 37°C. A static setup was utilised rather than one requiring agitation due to the number of samples and shared equipment space available in the laboratory. Release conditions (pH 7.4 buffer at 37°C) were selected in an effort to best represent that of an intended implantation site (subcutaneous region). The pH of the PBS solution used was checked with a calibrated Accumet AE 150 benchtop pH meter [Thermo Fisher Scientific, Inc.].

Samples of PBS media were taken from the release study vials at pre-determined time intervals. This included more regularly at the initial stages of release on day one (hourly) and then at days 1, 2, 3, 7, 10 and 14 followed by weekly sampling until no significant release was detected. Samples were analysed the same day and PBS release media in the release study vials fully replaced.

3.4.8.2 Alkaline Phosphatase (ALP) Para-Nitrophenol Phosphate (PNPP) Activity Assay

To quantify ALP activity, a Pierce™ PNPP substrate kit was utilised. To form the assay substrate, one 5 mg PNPP tablet was dissolved per 5 mL of 20% 5X diethanolamine buffer and 80% diH$_2$O. 5 µL of each sample to be measured was pipetted into a microplate well before adding 195 µL of the prepared substrate. The well plate was incubated at room temperature, where a colour change from colourless to a yellow hue occurs when PNPP is catalysed to para-nitrophenol (PNP) by ALP. This was observed over a set time period by measuring absorbance at 405 nm, with 25 flashes, every minute for 30 minutes using an Infinite 200 PRO Microplate reader. A standard curve was first prepared using PNP product. This provided a calibration range for unknown samples to be referenced against, allowing protein activity to be quantified for a respective sample using the equation of the straight line.

3.4.8.3 Bradford Total Protein Release Assay

For quantifying protein release, PBS media from each release study vial containing a single individual implant was collected at each selected time point. This was then used for quantifying total protein release via a low-cost Pierce™ Coomassie (Bradford) total protein assay. Protein binding with the dye leads to a colour change from brown to blue, dependant on the concentration of protein in the sample [158]. In each well, 200 µL of sample and 100 µL of reagent was added and mixed thoroughly by repetitive pipetting. The well plate was then read at an absorbance of 595 nm, with 25 flashes, using an Infinite 200 PRO Microplate reader [Tecan Group Ltd.]. Preparation of a standard curve range was used to correspond unknown sample values with known concentration values using the equation of the straight line.

3.4.9 *In Vitro* Release Kinetics and Mathematical Modelling

Different release kinetics have been used in previous literature to indicate the associated mechanisms of release in relation to delivery devices. Mathematical models for these different scenarios have been applied in relation to experimental data gathered.

3.4.9.1 Zero-Order

Release that follows zero-order kinetics can be fitted using Equation 3.10.

$$Q_t = Q_0 + K_0 \cdot t \; (\textbf{Eq. 3.10})$$

Where Q_t represents cumulative release at time t, Q_0 is the amount of active being quantified in solution prior to release ($t = 0$). K_0 corresponds to a zero-order release rate constant.

3.4.9.2 First-Order

Release that follows first-order kinetics can be represented by Equation 3.11 and Equation 3.12.

$$\frac{dQ}{dt} = -K \cdot t \; (\textbf{Eq. 3.11})$$

$$Log Q_t = Log Q_O - \frac{K \cdot t}{2.303} \; (\textbf{Eq. 3.12})$$

Release is deemed concentration dependent and K, for this model, is a first order rate constant in time^{-1}.

3.4.9.3 Higuchi

Release that follows Higuchi kinetics can be represented by Equation 3.13.

$$Q_t = K \cdot \sqrt{t} \ (\textbf{Eq. 3.13})$$

Where K in this instance is the release rate constant of the Higuchi model, with graphical plotting of the amount of active released per square root of time.

3.4.9.4 Korsmeyer-Peppas

Release can be fitted to the Korsmeyer-Peppas model using Equation 3.14.

$$\frac{M_t}{M\alpha} = K \cdot t^n \ (\textbf{Eq. 3.14})$$

Where $M_t/M\alpha$ is fraction of active released at time, t. K in this instance is the release rate constant of Korsmeyer-Peppas and n the release exponent. The value of n is related to a mechanism of release through a polymer slab, as defined by Korsmeyer-Peppas [159]:

- Fickian diffusion, $n \leq 0.5$.

- Non-Fickian transport, $0.5 < n < 1$.

- Case-II transport, $n = 1$.

- Super Case-II transport, $n > 1$.

It must be noted, the model is plotted using log cumulative release (%) versus log time and is only applicable for the first 60% of cumulative release.

3.4.10 Texture Analyser Compression Testing

To provide a mechanical comparison for viscoelastic properties, printed samples were placed into a compression test fixture setup within a texture analyser, TA-HD plus [Stable Micro-Systems]. Samples were compressed using a 5 kg load cell in the Z direction at a speed of 0.1 mm/s until failure or a strain of 50% was registered. A suitable linear region from the collected

stress-strain curve for each sample set (n = 3) was then analysed to determine a compressive Young's modulus value using Equation 3.15.

$$E = \frac{\sigma}{\varepsilon} \ (\mathbf{Eq.\,3.\,15})$$

Where E was the Young's modulus, σ the uniaxial stress and ε the strain.

3.5 Statistical Analysis and Schematics

Quantitative data is expressed as the average ± standard deviation (S.D.), n = 3 unless otherwise stated, and analysed for statistical significance using an analysis of variance (ANOVA) test with post-hoc analysis to compare between 3 or more data sets. A corresponding p value of < 0.05 * represented a statistically significant difference. Further levels of statistical significance evaluated included p < 0.01 **, p < 0.001 ***, p < 0.0001 ****. GraphPad Prism 9 [GraphPad Software Inc., San Diego, USA] was used for the statistical analysis and graphical plotting of data (colour-blind safe palette). In most cases, schematics were prepared within BioRender.

Chapter 4 Optimisation of Inkjet Printing (IJP) for Encapsulation and Release of Model Proteins

4.1 IJP Introduction

Material jetting or inkjet printing involves non-contact droplet deposition of ink formulations that are then consolidated to form a layer via crosslinking e.g. UV initiated. Essential stages include droplet formation, ejection, flight and coalescence during droplet-substrate interaction. Droplet size and wettability upon deposition relate to droplet spacing required. Figure 4.1 represents a drop-on-demand (DOD) piezoelectric inkjet printer [160]. Actuation occurring from wave pulse deformation and volumetric changes induces pressure allowing droplet ejection, illustrated in Figure 4.2. Other systems use thermal actuation or continuous valve controlled droplet jet streams [161].

Figure 4.3(a-e) represents different examples of printed line behaviours including individual droplets, scalloped, uniform, bulging and stacked coins [162]. Suspension based formulations can also exhibit a "coffee ring" effect where solidified polymer tends to the perimeter of a droplet after solvent evaporation, shown in Figure 4.3(f) [163].
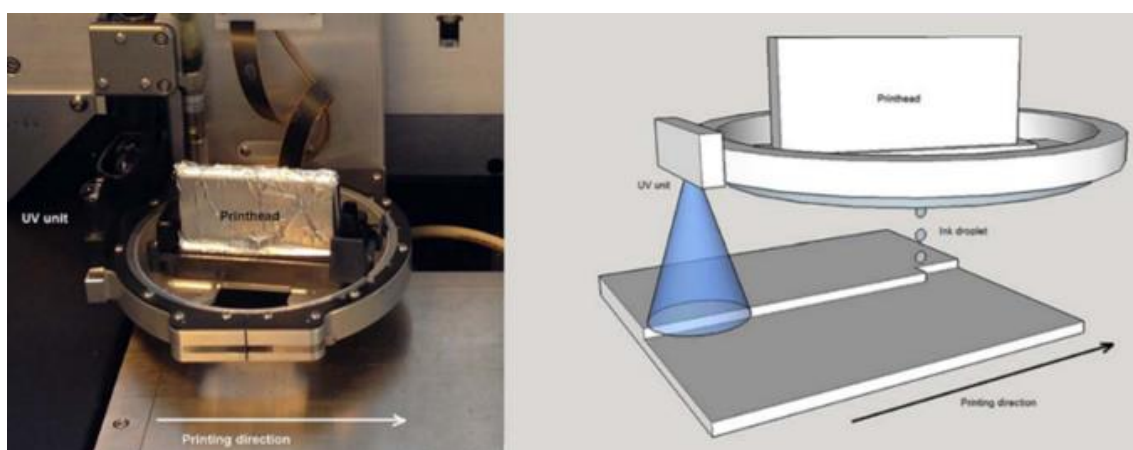
Figure 4.1: Dimatix DMP-2800 jetting setup and process schematic of UV light crosslinking consolidation of deposited droplets. Reproduced from [160].
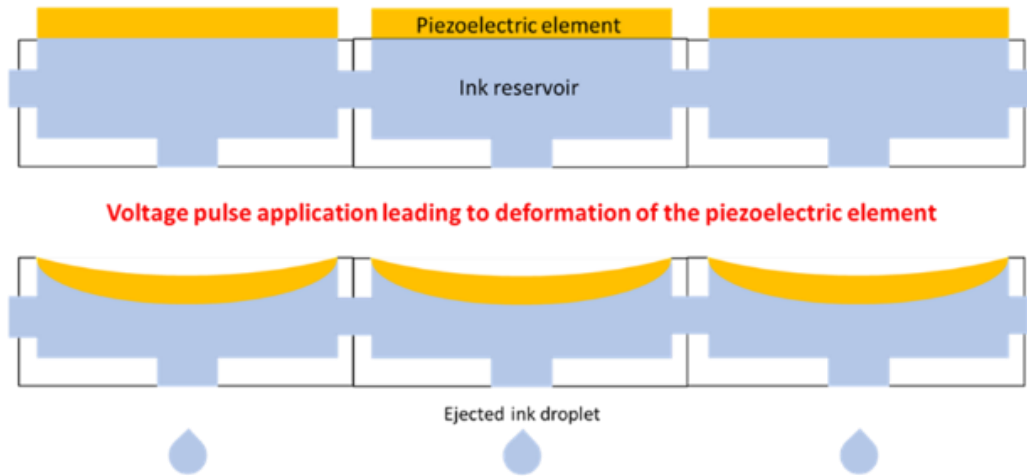
Figure 4.2: Schematic representation of piezoelectric deformation leading to droplet ejection due to volumetric changes from induced pressure.
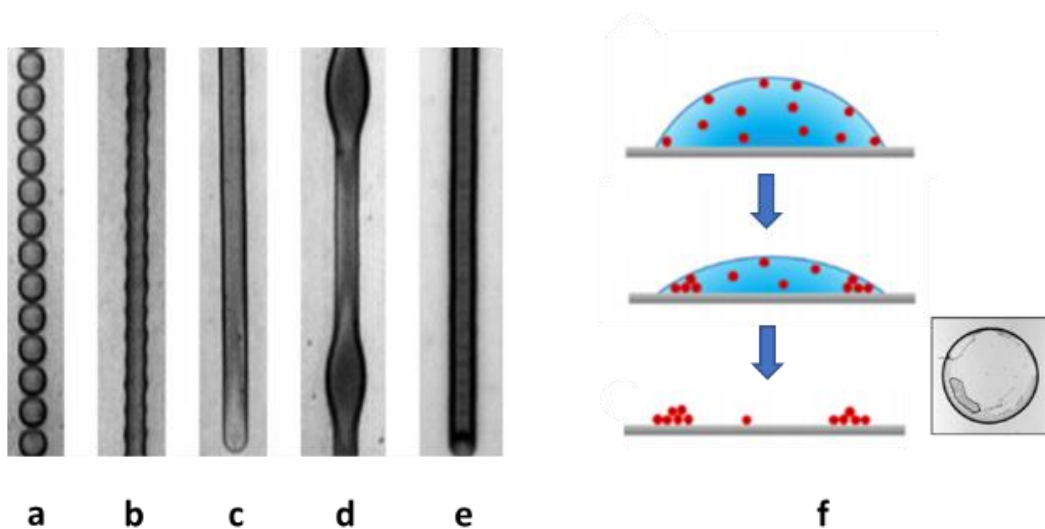
Figure 4.3: Printed line formations (a) individual droplets, (b) scalloped, (c) uniform, (d) bulging, (e) stacked coins. (f) a simplified schematic of solvent evaporation leading to solidified polymer at the perimeter termed the "coffee-ring" effect. (a-e) adapted from [162] and (f) adapted from [163].

Previous success has been reported in literature for the IJP of small molecule drugs. This includes IJP research into the processing and packaging of small molecule compounds contained within fabricated 3D delivery devices, such as microneedles and implants. Hence, this prompted the suggestion that IJP manufacturing techniques could also be, in theory, applicable for processing biomacromolecules (kDa). However, the encapsulation and controlled delivery of larger biomacromolecules from similar structures has been far less documented and explored to-date. For example, introductory research conducted by Biswas et al. observing the effect of jetting on LYZ activity and self-reported empirical work by Derby et al. was highlighted in IJP Table 1.3.

4.1.1 Chapter Hypotheses

1. IJP will be a suitable AM technique for the processing of biomacromolecule containing ink formulations e.g. PEGDA based.

2. IJP will be suitable for producing exemplars in the form of 3D delivery device structures for the release of encapsulated proteins.

3. IJP will allow controlled deposition of protein containing ink formulations, such that changes in spatial location of proteins and geometry will be able to be explored.

4.2 Methods for IJP Experiments

4.2.1 Ink Formulation Preparation

PEGDA was identified and selected as the monomer component to be used for formulation preparation. This was predominantly due to its well-researched and understood material properties, suitable with regards to biomedical applications. In addition, PEGDA is also widely used as a component capable of crosslinking, which is a required aspect for the IJP technique selected in this Chapter. Monomers with diacrylate functionalities have also been exploited in previous IJP literature for the successful encapsulation and release of small molecules through tuning formulations for fabricating 3D structures [105–107]. Formulation preparation stages are outlined in Section 3.3.1.1.

4.2.2 IJP Setup and Parameter Trials

A Dimatix DMP-2830 IJ printer was used with DMC-11610 printheads as outlined in Section 3.2.1.

4.2.3 Ink Characterisation

The specified ideal ink properties recommended for the selected Dimatix IJP setup, with the available cartridge and printhead type were the following [151]:

- Viscosity between 10 to 12 cP, but processable outside of this.
- Surface tension 32 to 34 mN/m
- Density, where specific gravity > 1 is optimal.
- Low volatility, where the boiling point > 100°C.
- pH between 4 to 9.
- Maximum particulate size of 1/100th of nozzle orifice.

Viscosity was characterised with a shear rate range from 1 s^{-1} to 1000 s^{-1} using a rheometer setup outlined in Section 3.4.1. Surface tension measurements for PEGDA 250 were obtained using DSA outlined in Section 3.4.2.

4.3 Results

4.3.1 IJP of PEGDA 250 and Effect of ALP Loading

PEGDA 250 was selected initially for its suitable properties for IJP, with a Z value of 3.40 determined from the density (1.11 g/mL), shear viscosity (8.3 ± 0.2 cP) surface tension (33.96 ± 0.20 mN/m). Z values between 1 and 10 are deemed ideal for jetting. Firstly, a single droplet array grid was printed to measure the mean droplet diameter, as shown in Figure 4.4(a), which was determined to be 65.5 ± 1.1 µm (n = 10). Hence, a droplet spacing of 2/3 of the diameter (44 µm, 577 DPI) was selected and inputted into the Dimatix software and represented a corresponding sabre angle of 10.0°. This setup selection for jetting allowed for adequate overlapping of droplets leading to consistent line formation during deposition at 25°C and 28 V with a printhead height of 1 mm when producing a 1 x 1 mm square pattern printed for 1 layer and 10 layers, as shown in Figure 4.4(b)(c) respectively. This demonstrated that PEGDA 250 with the selected parameters was able to be jetted in a reliable and repeatable manner, as shown by progressive drop watcher imaging of individual droplet nozzles jetting in Figure 4.5(a-d). This includes

the stages of jetting involving droplet formation, ejection, flight and finally deposition at the print platform surface. Jetting allowed for the production of 100-layer 5 x 5 mm square printed samples, as shown in Figure 4.6(a) and the fabrication of a 40 x 2 x 2 mm implant exemplar (based off the NEXPLANON® contraceptive implant dimensions), as shown in Figure 4.6(b).

a　　　　　　　**b**　　　　　　　**c**
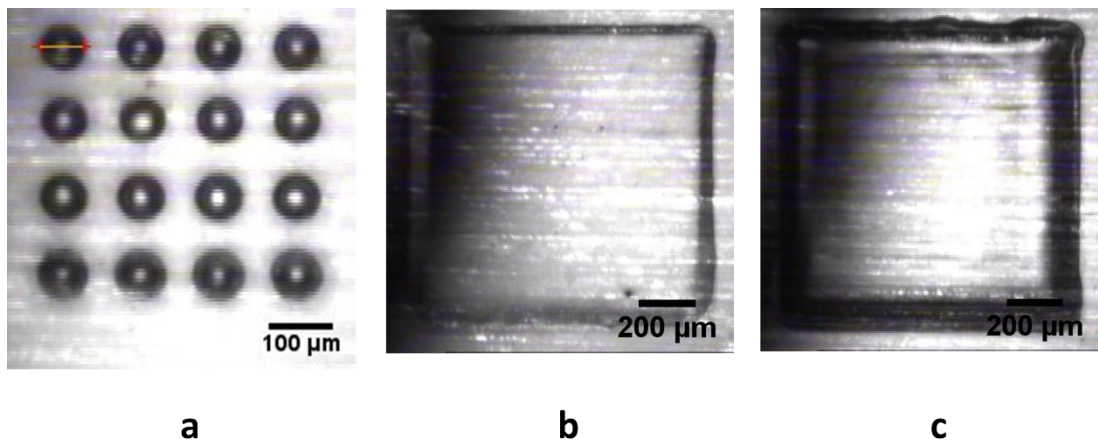
Figure 4.4: (a) Single droplet array grid used to determine droplet diameter and indicate the required droplet spacing, (b) 1-layer 1 x 1 mm square pattern deposition and (c) 5-layer 1 x 1 mm square pattern deposition.
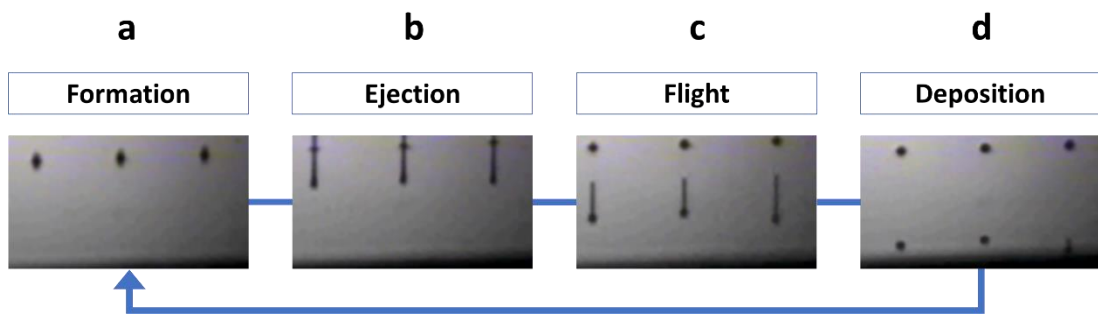
Figure 4.5: Drop watcher jetting images of associated droplet stages (a) formation, (b) ejection, (c) flight and (d) deposition for PEGDA 250.

Figure 4.6: Examples of IJP printed outcomes for (a) 100-layer 5 x 5 mm square patterns and (b) 40 x 2 x 2 mm implant exemplar. Ruler scale (cm).

Initially, an ALP addition of 10 mg/mL was proposed as it is desirable for final delivery devices fabricated to contain sufficient loading to increase the potential longevity of end release that can be achieved. Again, a single droplet array grid was used to establish the required printing parameters, as shown in Figure 4.7(a). The mean droplet diameter was determined to be 69.2 ± 1.9 µm (n = 10), from which a 46 µm droplet spacing (552 DPI) was selected with a corresponding sabre angle of 10.4°. Upon first observation, the introduction of ALP did not compromise the ability to jet droplets. However, the requirement for reliable jetting over a longer period, that allows for multiple layer deposition, presented problems. The printhead voltage applied was increased from 28 V to a maximum of 40 V, to generate a greater pressure gradient within the reservoir to improve droplet ejection. The frequency of cleaning cycles was increased to help maintain a clean nozzle plate. However, this did not prevent the issues experienced with Figure 4.7(b)(c) demonstrating deposition of a single layer and attempted printing of a 5 x 5 mm pattern, before jetting

stopped whilst attempting to reach a final structure Z height of 2 mm. The drop watcher function was used again to visualise the droplet formation and jetting, confirming ejection was less consistent leading to misfiring before partial and soon after complete blocking. Interestingly, accumulation on the left-hand side of the pattern potentially indicates the first ejection of each printhead swipe (left to right on the print platform) was successful, as indicated in Figure 4.7(d). It is then probable that nozzle jet orifices became blocked as the jets utilised became increasingly compromised, as shown in Figure 4.8(a-d). This contrasted the previously shown images of the progressive droplet stages for PEGDA 250 (no ALP additions) in Figure 4.5(a-d). Issues with nozzle maintenance associated with IJP protein loaded ink formulations has been noted in literature as a primary issue and is covered in a comprehensive review paper by Evans et al. [104]. To better understand the influence of the ALP additions it was decided to conduct rheological analysis.

a   b   c   d
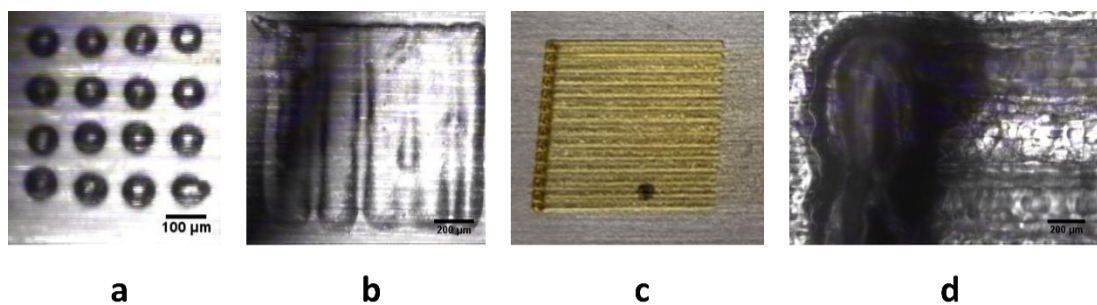
Figure 4.7: (a) Single droplet array grid used to determine droplet diameter and indicate the required droplet spacing, (b) 1-layer 1 x 1 mm square pattern deposition, (c) 5 x 5 mm printed pattern with accumulation on the left-hand side shown in (d).
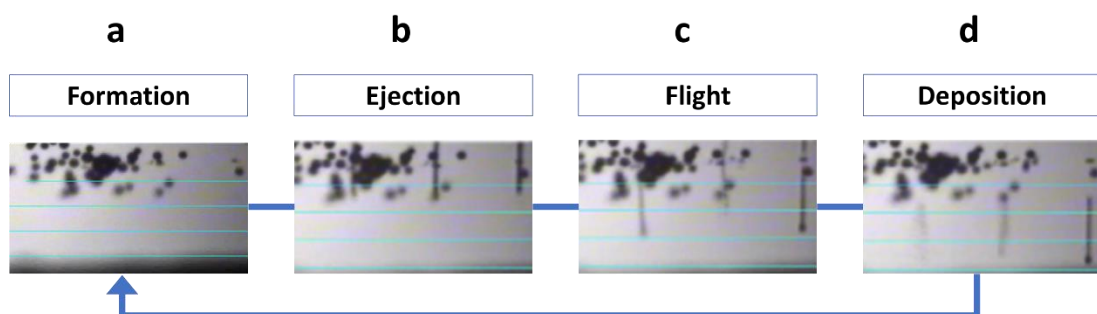
Figure 4.8: Drop watcher jetting images of associated droplet stages (a) formation, (b) ejection, (c) flight and (d) deposition for PEGDA 250 with 10 mg/mL ALP loading.

4.3.2 Influence of ALP Loading on Viscosity of PEGDA 250

Viscosity is a critical for ink selection for IJP, with the suggested range between 10 to 12 cP in relation to the printhead used. It was decided that the influence of ALP additions (0 to 25 mg/mL) to PEGDA 250 would be analysed by conducting rheology measurements over a range of shear rates (10 s^{-1} to 1000 s^{-1}) to determine differences in viscosity, as shown in Figure 4.9. Increasing ALP led to significant increases ($p < 0.0001$) at lower shear rates of 10 s^{-1} e.g. 3510.0 ± 683.0 cP at 25 mg/mL versus 9.9 ± 1.2 cP with no ALP addition. All formulations exhibited shear thinning properties, desirable for IJP, with the effect more profound at higher loadings e.g. 25 mg/mL. At a shear rate of 1000 s^{-1} values ranged from 8.3 ± 0.2 cP to 27.5 ± 0.4 cP with increasing ALP loading. During the IJP process it was anticipated that high enough shear rates would be experienced such that viscosity of the PEGDA 250 ink with ALP would be applicable. It is possible shear rates imparted onto the formulations during jetting may not be consistent across individual nozzles or fluctuates e.g. during idle periods between layers or cleaning cycles. Also, the results suggest that PEGDA 250 was not suitable for ALP incorporation and that the protein was not fully in solution, compromising jetting. Table 4.1 summarises the viscosity values for each ALP loading at shear rates of 10, 100 and 1000 s^{-1}. Surface tension ranged between 31.37 ± 0.55 mN/m and 34.46 ± 0.02 mN/m as listed in Table 4.2.
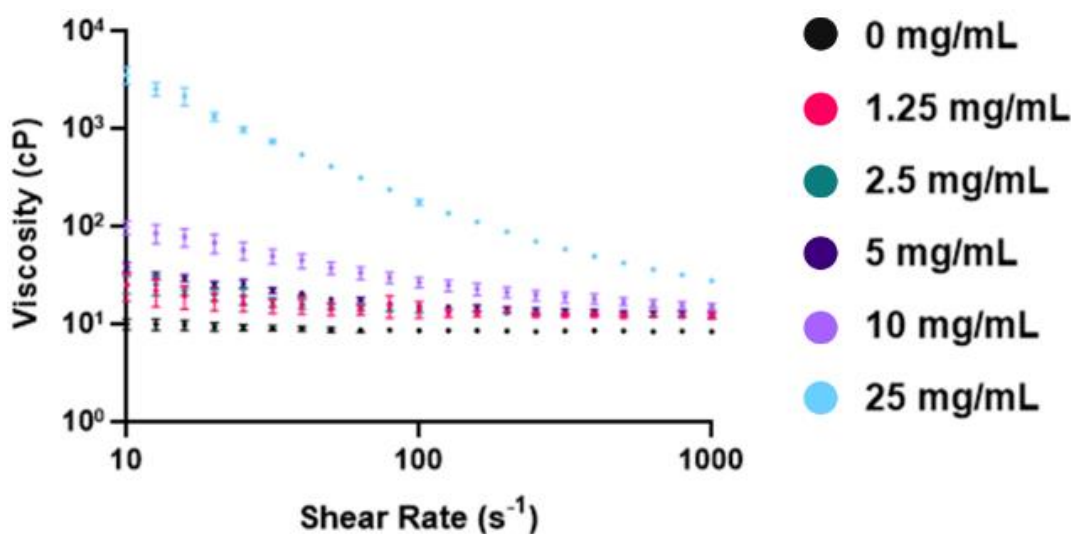
Figure 4.9: Shear rate vs viscosity for PEGDA 250 with ALP additions ranging from 0 to 25 mg/mL. Results denote mean ± S.D. (n = 3).

Table 4.1: Overview of viscosity values for PEGDA 250 with additions of ALP (0 to 25 mg/mL) at shear rates of 10, 100 and 1000 s^{-1}. Results denote mean ± S.D. (n = 3).

ALP Loading (mg/mL)	Viscosity at Shear Rate 10 s^{-1} (cP)	Viscosity at Shear Rate 100 s^{-1} (cP)	Viscosity at Shear Rate 1000 s^{-1} (cP)
0 (control)	9.9 ± 1.2	8.5 ± 0.3	8.3 ± 0.2
1.25	24.7 ± 7.7	14.1 ± 2.7	12.0 ± 0.6
2.5	25.1 ± 5.1	13.6 ± 0.6	12.0 ± 0.3
5	38.0 ± 3.8	15.1 ± 0.5	12.3 ± 0.9
10	96.5 ± 15.0	26.6 ± 3.2	15.0 ± 1.1
25	3510.0 ± 683.0	175.0 ± 11.3	27.5 ± 0.4

Table 4.2: Overview of surface tension values for PEGDA 250 with additions of ALP (0 to 25 mg/mL). Results denote mean ± S.D. (n = 5).

ALP Loading (mg/mL)	Surface Tension (mN/m)
0 (control)	33.96 ± 0.20
1.25	32.33 ± 0.80
2.5	31.37 ± 0.55
5	34.71 ± 0.03
10	34.26 ± 0.02
25	34.46 ± 0.02

4.3.3 IJP of PBS:PEGDA 575 Formulations

PEGDA 250 is not miscible in water so a decision was made to use PEGDA 575 within a PBS component (pH ~7.4). The use of a buffer was selected firstly in an attempt to improve solubility of the ALP in solution and provide conditions suitable for maintaining protein stability. A formulation of PEGDA 575 in PBS at 20% (*w/v*) was trialled, with the use of LAP as a photoinitiator at 1% (*w/v*), as it is water soluble and used previously in 3D printing for healthcare applications [164,165]. Individual droplet arrays were not able to be deposited due to evaporation occurring before they could be measured. It was decided that droplet spacing would be increased gradually for a 1 x 1 mm square pattern until an appropriate setting was established, as shown in Figure 4.10(a-d). Droplet spacings of 30, 38 and 42 μm were deemed too close together such that droplets coalesced prematurely forming larger droplets. In comparison, a droplet spacing of 60 μm allowed deposition of individual droplet lines in close proximity. This corresponded with a sabre angle of 13.7° and DPI of 423. These settings were then used to produce a 1 x 1 mm square pattern of multiple layers (5, 10, 20 and 50), as shown in Figure 4.11(a-d). The printed patterns were improved in comparison to ALP in PEGDA 250, however problems of droplet stability were still evident as the number of layers increased leading to compounding of deposition irregularities.

a **b** **c** **d**
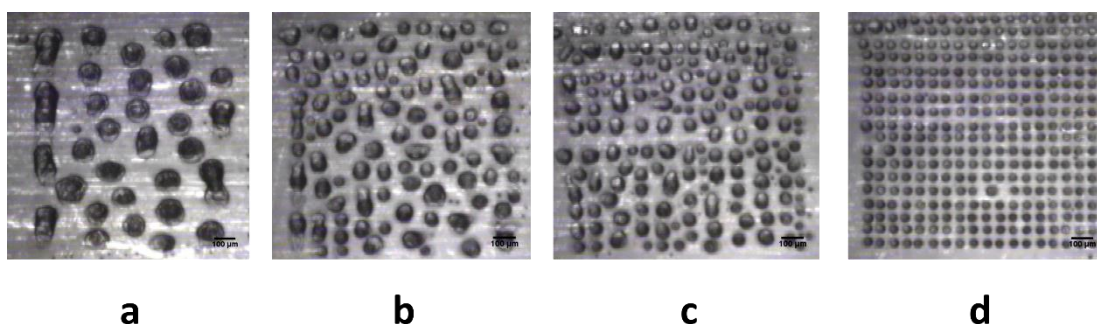
Figure 4.10: Droplet spacing trials of (a) 30 μm, (b) 38 μm, (c) 42 μm and (d) the selected spacing of 60 μm that prevented premature droplet coalescence for IJP of PEGDA 575 20% (*w/v*) in PBS.
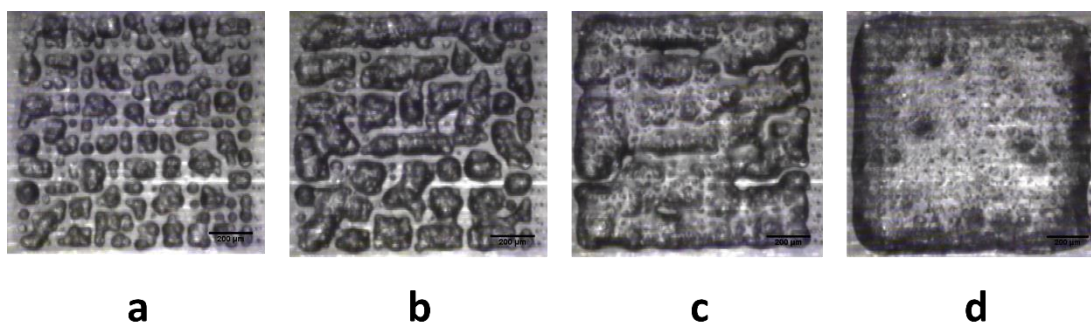
Figure 4.11: 1 x 1 mm square pattern printed with a droplet spacing of 60 µm for (a) 5, (b) 10, (c) 20 and (d) 50 layers through IJP of PEGDA 575 20% (*w/v*) in PBS.

4.3.4 IJP of MQ Ultrapure Water:PEGDA 575 Formulations

The previous trials of PEGDA 575 in PBS buffer were printable, however deposition was not consistent enough to allow fabrication of samples that required enough layers to form a 3D mm size structure e.g. 100+ layers. It was theorised that the salts present in the PBS buffer solution could be precipitating out of solution and residing as debris at the nozzle jet interface, adding to challenges the addition of ALP already seemed to present. Therefore, the same formulation of PEGDA 575 20% (*w/v*) was prepared in MQ ultrapure water for comparison. This led to improvements of jetting on a single layer basis, shown in Figure 4.12(a) using the same settings (60 µm droplet spacing, sabre angle of 13.7° and DPI of 423). This resulted in improved droplet stability that allowed reliable deposition and printing of a 1 x 1 mm pattern for 10 and 20 layers, as shown in Figure 4.12(b)(c). However, challenges occurred again as the number of layers was increased to 50 and 100, as shown in Figure 4.12(d)(e) respectively. A similar observation was made as was seen previously for PEGDA 250 with ALP loading, whereby droplet deposition appeared possible at the start of each layer of printing with material accumulation on the left-hand side of the pattern prior to nozzle blocking over time. This is evident when comparing images of deposition in Figure 4.12(b-e).
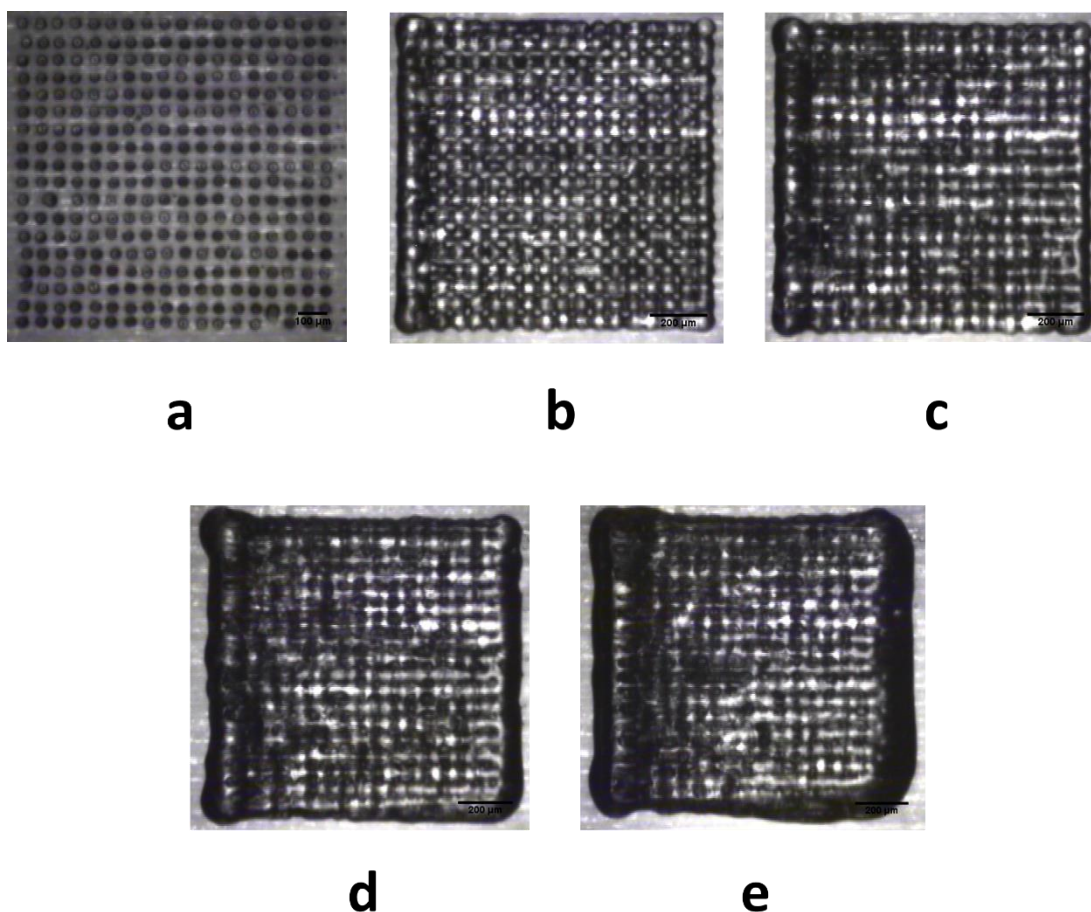
Figure 4.12: (a) Deposition using a droplet spacing of 60 µm and (b-e) a 1 x 1 mm square pattern printed with 10, 20, 50 and 100 layers respectively through IJP of PEGDA 575 20% (*w/v*) in MQ ultrapure water.

4.3.5 IJP of MQ Ultrapure Water:Glycerol:PEGDA 575 Formulations

The addition of glycerol has been used previously in IJP as a humectant, viscosity modifier and can be a protein structure stabiliser e.g. IJP attempts of LYZ containing formulations [108]. It has also been used previously to prevent protein aggregation and inhibit protein unfolding [166,167]. In the case of the ALP used in this work, the corresponding supplier data sheet stated relative activity is highly retained in 50% (*w/v*) glycerol solutions over the period of weeks at 37°C and months/years at 5°C, confirming it may be a suitable addition for ALP containing formulations. It was also proposed that introducing glycerol to the PEGDA 575 20% (*w/v*) in MQ ultrapure water formulation could limit evaporation and prevent the drying out of protein containing ink

formulations on the nozzle aperture. In doing so, this would aim to minimise the impact of debris accumulation from protein precipitating out of solution during printing that compromises jetting stability during droplet formation and ejection.

A formulation of PEGDA 575 20% (*w/v*) and glycerol 20% (*w/v*) in MQ ultrapure water was printed. Initially achieving droplet deposition was challenging with poor consistency and repeatability as documented in Figure 4.13(a-c). The selection of a 42 µm droplet spacing (sabre angle of 9.5° and DPI of 607) jetted at 25°C and 28 V provided less variance but full coverage for a 1 x 1 mm pattern was not achieved. The increase in layers deposited did allow the pattern to be realised e.g. square formation after 10, 20 and 50 layers in Figure 4.14(a-c). A larger pattern of 5 x 5 mm was also attempted but jetting challenges persisted. A splashing effect was also observed and became more profound as layers deposited increased, as shown in Figure 4.15(a-d) for 10, 50, 100 and 200 layers respectively. Ultimately, blocking of nozzles still occurred and the introduction of glycerol presented new difficulties in trying to achieve successful IJP for an ALP containing formulation.

a **b** **c**
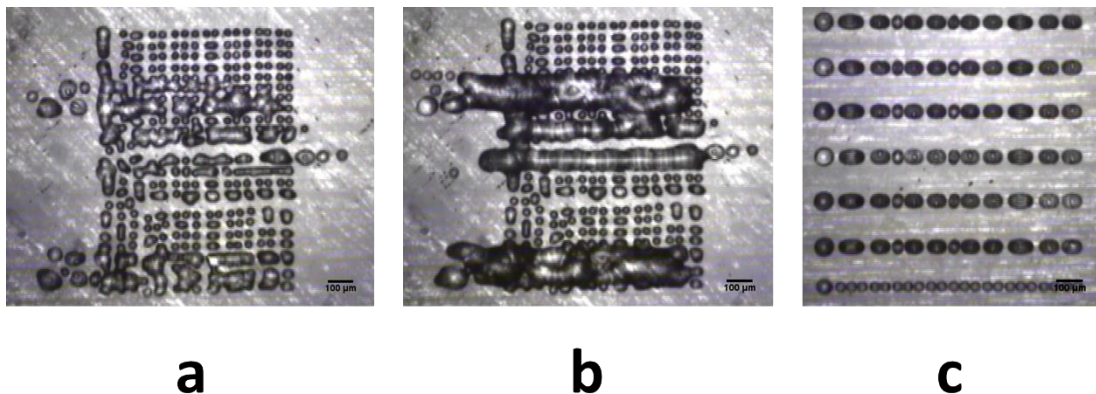
Figure 4.13: (a)(b) Examples of initial inconsistent and variable jetting and cartridge leaking and (c) use of a 42 µm droplet spacing for printing a formulation of PEGDA 575 20% (*w/v*) and glycerol 20% (*w/v*) in MQ ultrapure water.
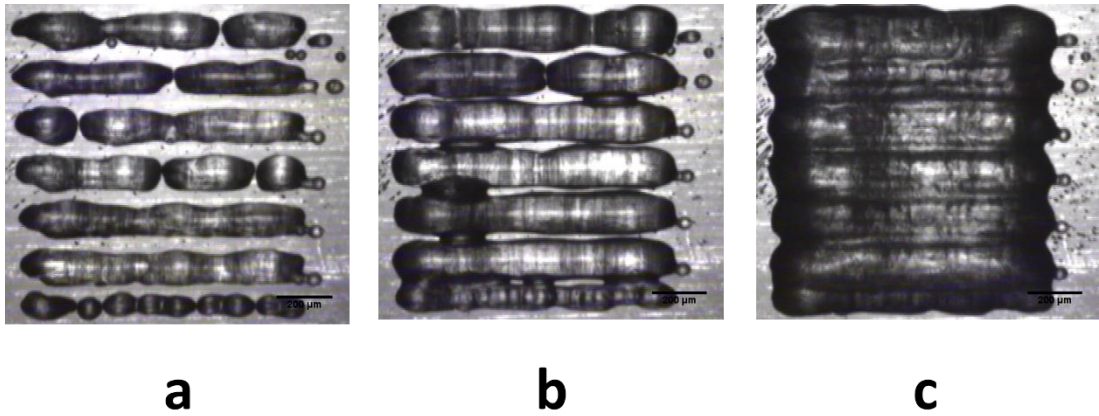
Figure 4.14: A 1 x 1 mm square pattern printed with (a) 10, (b) 20 and (c) 50 layers using a formulation of PEGDA 575 20% (*w/v*) and glycerol 20% (*w/v*) in MQ ultrapure water.
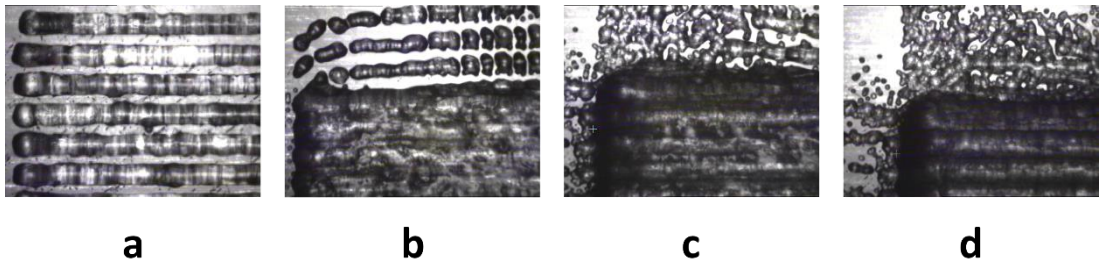
Figure 4.15: A 5 x 5 mm square pattern printed with (a) 10, (b) 50 and (c) 100 and (d) 200 layers using a formulation of PEGDA 575 20% (*w/v*) and glycerol 20% (*w/v*) in MQ ultrapure water, showing a splashing effect is observed with increasing layer count.

4.4 Discussion

IJP was identified as a potential method for processing ink formulations with a model protein incorporated for encapsulation within a fabricated 3D structure, which would then be intended for an *in vitro* release study. The reasoning for exploring IJP included the previous success documented for small molecule release applications and advantages of non-contact droplet deposition with μm resolutions for high degree of control over deposition to aid in controlling biomacromolecule delivery [105–107]. Also, the research to date of IJP larger molecule biologics has been less explored and is in its relative infancy, naturally prompting further research to be conducted.

61

Low Mn PEGDA was selected for formulation with suitable photoinitiator additions to rapidly crosslink under UV light during IJP. The initial use of PEGDA 250, whilst printable alone, did not allow for suitable ALP loading due to solubility issues, as indicated by viscosity measurements with 0 to 25 mg/mL loading. It was decided a formulation would be prepared utilising PBS and water miscible PEGDA 575. However, the salts present in the buffer solution have potential to come out of solution during printing (nozzle open time) due to ejection pulses that produce the successive individual droplets. This has been a reported problem in literature where jetting of aqueous inks requires frequent cleaning of printhead nozzles [104,168]. A similar issue could potentially be occurring with protein adsorption onto the printhead. Furthermore, charge changes associated with the protein and the piezo-electric head, used to actuate the nozzles, could have an impact on the ability of an ink to be jetted successfully. The combination of these effects occurring simultaneously led to the accumulation of debris onto the nozzle plate. This in turn contributed to detrimental jetting performance over the time observed through wayward droplet ejection, misfires and ultimately blocking.

The issue of protein adsorption is a net result of complex interactions between that of materials selected, solvents, protein(s) encapsulated and printing equipment [104]. This includes dipole and induced dipole moments, hydrogen bond forming and electrostatic forces. Losses due to adsorption on the printhead is problematic for IJP with protein therapeutics that are costly [104]. Blockages are also not desirable in early-stage printing trials due to the associated cost implications of replacing the printhead repeatedly. Over time the ink resting within the print cartridge may phase-separate as there is an inability to further mix the formulation during printing. Hence, ink homogeneity and even distribution of the protein component in solution cannot be ensured. In theory, the nominal size of ALP shouldn't have had an impact, as this is significantly smaller than orifice of the printhead utilised. Potential aggregation may occur through formulation and IJP printhead interaction.

MQ ultrapure water was used to replace the PBS component. This led to improved jetting performance but was only feasible for lower layer height prints (droplet arrays or µm layers) before jetting issues or nozzles fully blocked and

the overall jetting reliability ultimately compromised for further printing. Importantly, this presents issues in printing a sufficient dimensional depth for an implantable long-term bioactive delivery device e.g. 2 mm Z height. This could provide reasoning as to why IJP of biologics to date has predominantly covered use for microarrays, immunoassays, thin film production and biosensors rather than mm scale long-term delivery devices [166,169,170].

To combat the issues of formulations drying out during printing, it was decided that a humectant, glycerol, would be added. Glycerol additions can be used as a viscosity modifier and protein protectant, but its use must still be assessed in relation to any impact on biological activity on a case-by-case basis [166,171,172]. Difficulties were still presented, with issues compounded as the layers deposited increased and nozzles blocked, although the time taken until this occurred was extended. Ultimately, formulating for the printing process rather than for the benefit of the protein(s) being encapsulated could present problems. In the case of IJP, adjusting viscosity or jetting performance by using diluents and surfactants may allow successful droplet deposition but could impact end delivery device success if the protein(s) encapsulated are compromised. Samples for release quantification in these early-stage trials were not able to be produced so this aspect could not be assessed and as such IJP did not satisfy the proposed hypotheses in this thesis.

4.5 Conclusions

Overall, the limitations of the IJP setup used in this section aligned with piezoelectric IJP literature and provided an initial insight into why IJP for biomacromolecules is currently not widely reported. However, attempts at IJP larger bioactives is still relatively new and it could be possible that foreseeable improvements in technology would allow for processing into end application delivery devices e.g. enhanced printhead stability and methods of maintaining nozzle interfaces. For example, the reported use of a MicroFab microjet MJ-AT-01–60 with a considerably increased diameter of 60 μm and DOD single jet dispensing was able to process PBS formulations with glucose oxidase (160 kDa), similar to the nominal size of ALP, at 3% (*w/v*) [173]. Whilst single dispensing limits scalability and use of larger nozzle orifices would likely reduce the possible print fidelity, it does show that IJP approaches could have

future potential in processing kDa biological containing formulations. However, it was decided that alternative printing modalities would be explored for their suitability.

Chapter 5 Optimisation of Digital Light Processing (DLP) Printing for Encapsulation and Release of Model Proteins

5.1 Introduction

VP processes operate by lowering a build platform into a vat of photopolymer resin where directed light exposure solidifies the resin via photopolymerisation [112]. Reactive UV-curable resins comprised of a monomer, oligomer or combination are required. Photoinitiator additions, which photodegrade under irradiation from the light source during printing, produce free radicals to initiate photopolymerisation to achieve crosslinked 3D structures [165,174]. Photoabsorber additions can be added to control cure depth and the processing parameter window [165,174]. Post-processing, e.g. support structure removal, removal of excess resin or UV treatment, must be well managed to prevent shrinkage and loss of feature accuracy [115].

Figure 5.1(a) represents a vector scanning laser-based process whereby galvanometers on the XY axes deflect a UV beam using a mirror movement, dictated by an inputted design file. Between each layer a recoating wiper blade passes over the build surface to ensure it is level. Setup considerations include top up or top down orientation and support structures if required [112,174]. DLP represented in Figure 5.1(b), uses photomask projections created from voxel-based patterns. Individual layer patterns are defined and projected with the corresponding pixel light intensity allowing selective photopolymerisation of a resin [112,174].

Following the introductory trials of IJP and the challenges encountered, DLP printing was proposed as an alternative light-based AM processing technique to explore. Previous literature into DLP based 3D printing has been assessed for medical applications as a potential tool for biological research including drug screening, disease modelling, tissue repair and tissue regeneration [175–178]. Also, VP printing modalities, such as DLP, have been cited for advantages in fabricating delivery devices e.g. printing of PEGDA/gelatin methacrylate (GelMA) formulations with transforming growth factor-beta 1 (TGF-β 1) nanospheres encapsulated for release over 21 days leading to

enhanced chondrogenic development of mesenchymal stem cells (MSCs) in cartilage-regeneration applications [179]. Another example includes sequential release of vascular endothelial growth factors (VEGFs) and platelet derived growth factor (PDGFs) from core-shell DLP printed hydrogels over 28 days [180].
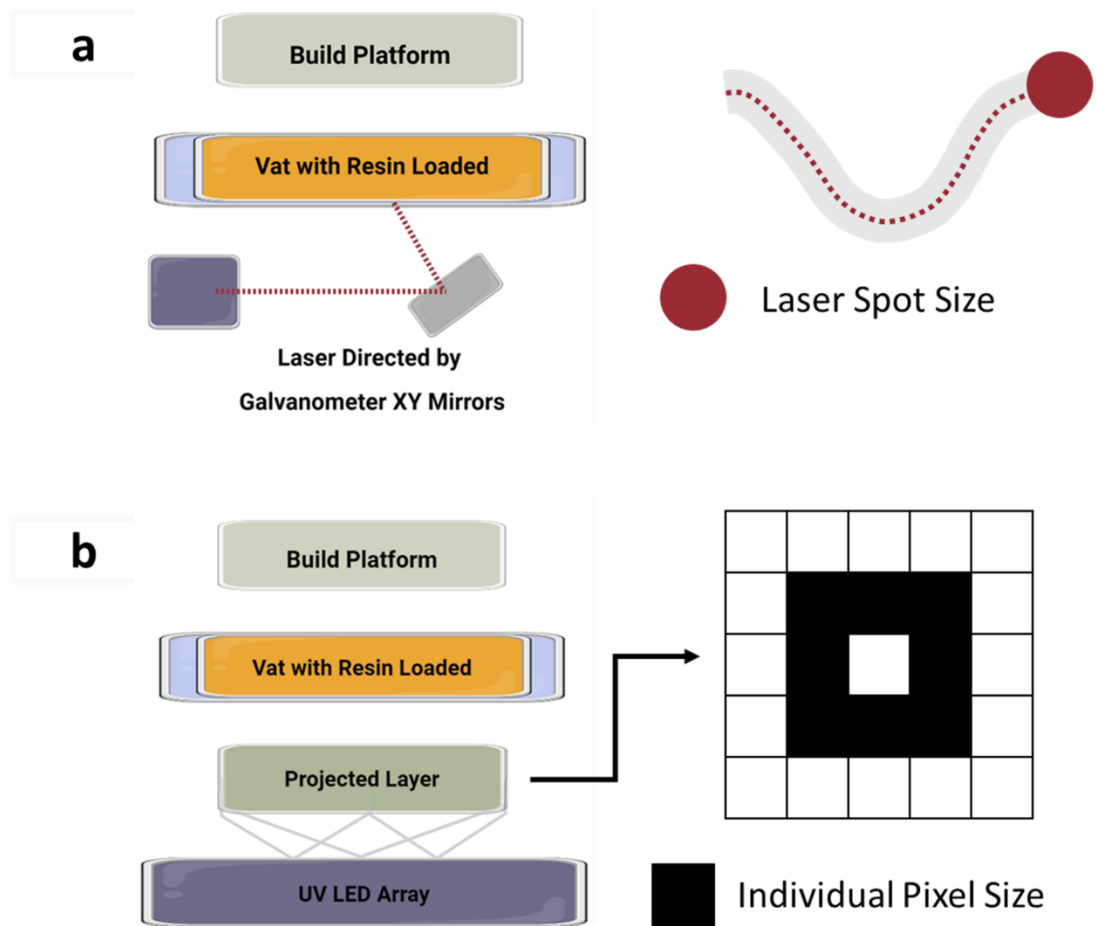
Figure 5.1: Simplified schematics of SLA printing process setups for (a) laser-based tracing with resolution dictated by laser spot size and (b) DLP projection with resolution dictated by individual pixel size. Created with Biorender.com.

Rationale for DLP selection included:

- Avoiding the requirement for formulations to pass through an orifice, which was found to be a dominating issue regarding nozzle blockages due to debris accumulation over time when processing a protein loaded ink.

- DLP techniques are typically capable of processing higher viscosities, in comparison to IJP, and could allow exploration of a wider materials library and protein loading capability for controlling end release characteristics.

- DLP techniques allow for typically faster build times, which permits multiple early-stage trials with different formulations and design changes to be explored and evaluated for success in shorter timeframes.

This section aims to show the implementation of a DLP printer system to determine the influence of ink formulation and printing parameter setup on the ability to fabricate a delivery device. Particular importance has been placed on finding materials and protocols that allow for incorporation of model proteins during formulation as well as the associated swelling properties, theoretical matrix mesh size approximations and any corresponding release characteristics observed.

This has been explored through chain-growth (CG) crosslinked formulations for encapsulation and attempted release of model proteins; lysozyme (LYZ, 14 kDa), bovine serum albumin (BSA, 66 kDa) and alkaline phosphatase (ALP, 160 kDa) outlined in Section 2.2. Similar photopolymerised PEGDA based formulations allowed for a comparison in the suitability of the printing process with the previous IJP work shown.

5.1.1 Chapter Hypotheses

1. DLP will be able to process PEGDA based formulations, with CG polymerisation a suitable mechanism of crosslinking to utilise for fabrication of 3D structures initiated by UV light.

2. The ability of DLP to process higher viscosity ink formulations will allow for a range of Mn PEGDAs to be explored to modulate the end polymer matrix characteristics.

3. Increasing the selected Mn of PEGDA will correspond with increases in both swelling and theoretical matrix mesh size calculated. A relationship

will be able to be generated between these characteristics and the associated release of encapsulated model proteins.

4. Calculated theoretical matrix mesh sizes will form an appropriate basis for indicating if release of encapsulated model proteins is observed. For example, matrix mesh size < protein size will lead to protein entrapment and matrix mesh size > protein size will correspond with release.

5.2 Methods for DLP Printing Experiments

5.2.1 Formulation Preparation

Table 5.1 outlines the outlines formulations prepared in PBS with 0.5% (*w/v*) LAP in respect to total formulation and 0.1% (*w/w*) tartrazine relative to PEGDA content for DLP printing, as mentioned in Chapter 3.3.1.2. Formulation characteristics including monomer Mn, monomer% (*v/v*) or (*w/v*) and protein loading implemented have been explored. Formulation codes have been used for reference throughout this results Chapter e.g. "chain-growth formulation one" is denoted as CG–F1. LYZ, BSA and ALP were encapsulated at 1 mg/mL, with further BSA work conducted with 5 mg/mL.

Table 5.1: Overview of CG formulations prepared, coded for reference purpose.

Formulation Code	Formulation
CG–F1	**PEGDA 575** 50% (*v/v*)
CG–F2	**PEGDA 700** 50% (*v/v*)
CG–F3	**PEGDA 1000** 20% (*w/v*)
CG–F4	**PEGDA 4000** 20% *(w/v)*
CG–F5	**PEGDA 8000** 20% (*w/v*)
CG–F6	**PEGDA 10,000** 20% (*w/v*)

5.2.2 Pre-Print Characterisation

PEGDA of varying Mn were characterised using GPC and ^{1}H NMR and the viscosity of formulations established following the methods outlined in Sections 3.4.3, 3.4.4 and 3.4.1 respectively. Assessment of stirring speed and duration, as well as the influence of UV exposure, on protein activity was conducted with ALP in PBS and use of a Pierce™ PNPP substrate kit as described in Sections 3.3.2, 3.3.3 and 3.4.8.2. An example standard curve for PNP product is shown in Appendix: Supplementary Information Figure S.1.

5.2.3 DLP Printing and Establishing Polymer Matrix Properties

Formulations (CG–F1 to CG–F6) were DLP printed using an Anycubic Photon Mono, described further in Section 3.2.2, and imaged with optical microscopy and SEM detailed in Sections 3.4.5 and 3.4.6. Matrix properties were calculated using the equations stated in Section 3.4.7. For each condition and time point the result presented is the mean of three samples ± S.D.

5.2.4 Experimental Setup for Controlled *In Vitro* Release Studies

Three model proteins of LYZ, BSA and ALP were incorporated into each of the formulations and DLP printed to produce 10 x 10 x 2 mm samples. Samples were added to 3 mL of PBS solution (pH 7.4) at 37°C in scintillation vials and sampled hourly for the first four hours and at days 1, 2, 3, 7, 10 and 14 and then weekly, or until no significant elution was detected, as outlined in Section 3.4.8.1. Total protein release was quantified using the PBS media from sample containing vials and a Bradford total protein assay, as outlined in Section 3.4.8.3. An example standard curve for BSA is shown in Appendix: Supplementary Information Figure S.2. For each condition and respective time point, the result presented is the mean of three samples ± S.D.

5.3 Results

5.3.1 Pre-Print Characterisation

5.3.1.1 GPC Analysis of PEGDA Materials

GPC analysis was used as a characterisation method to provide confirmation of the Mn, Mw and PDI in regard to the range of PEGDA materials sourced. PDI describes the range of the MW distribution, whereby a value of 1 represents a sample that is monodisperse and higher values polydisperse

[181]. Figure 5.2 shows differences in MW (g/mol) versus normalised differential weight fraction/differential log concentration (dW/dlogM) for the six different Mn PEGDA selected for use in this Chapter. Table 5.2 provides an overview of the associated Mn and Mw, whereby the values of each increased with increasing reported Mn from the supplier as was anticipated. The PDI for all PEGDA samples analysed was between 1.04 and 1.13, representing minimal differences between Mn and Mw.
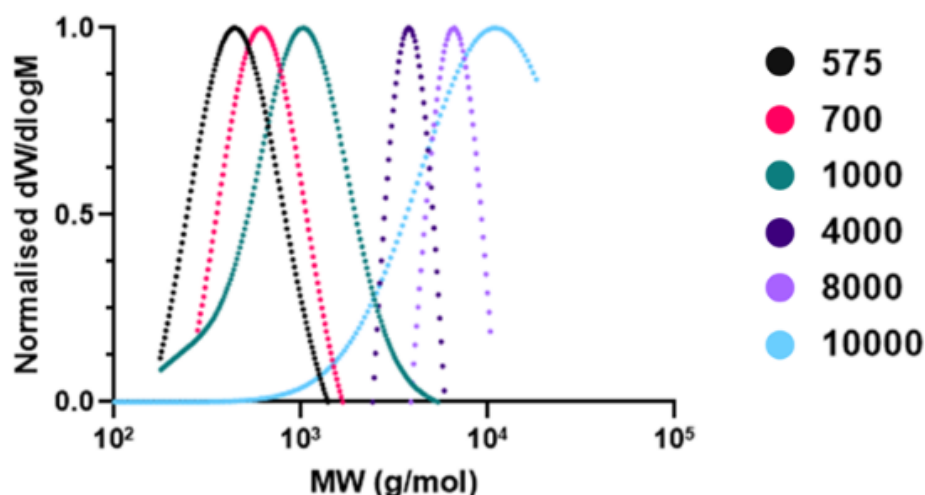
Figure 5.2: MW distribution (g/mol) versus normalised dW/dlogM for the range of PEGDA Mn selected, ranging from 575 to 10,000.

Table 5.2: Overview of the PEGDA range analysed by GPC for Mn, Mw and PDI.

GPC Analysis			
Reported PEGDA Mn	Mn	Mw	PDI
575	419	475	1.13
700	590	642	1.09
1000	985	1050	1.07
4000	3680	3846	1.05
8000	6539	6768	1.04
10,000	10231	10962	1.07

5.3.1.2 ^{1}H NMR Spectroscopy Analysis of PEGDA Materials

Further to the GPC analysis, NMR spectroscopy was conducted to provide further confirmation and compare differences in associated acrylate:EG ratios. The increase in Mn of the PEGDA analysed corresponded with an increase in the sum of the EG peaks and resulted in a reduction in acrylate:EG ratio. For example, these values for PEGDA 575 (CG–F1) were 18.9 and 0.1 and for PEGDA 10,000 (CG–F6) were 546.7 and 0.004 respectively. Table 5.3 summarises the results for CG–F1 to CG–F6, with the NMR spectra shown in Appendix: Supplementary Information Figure S.3.

Table 5.3: Overview of the PEGDA range analysed by ^{1}H NMR. *HOD peak at 4.7 ppm calibrated to a value of 10.0, with all spectra scaled identically for comparison. Values reported to 1 d.p or 1 s.f, where deemed appropriate.

^{1}H NMR Analysis*			
Reported PEGDA Mn	Sum of Acrylate Peaks	Sum of EG Peaks	Acrylate:EG Ratio
575	3.0	18.9	0.1
700	3.0	27.3	0.07
1000	3.0	46.7	0.04
4000	2.8	221.6	0.008
8000	3.1	507.8	0.004
10,000	3.2	546.7	0.004

5.3.1.3 Rheological Analysis

After the GPC and NMR confirmation of the sourced PEGDA materials, it was decided that the viscosity of the prepared formulations (CG–F1 to CG–F6) would be established. In the case of DLP printing, higher viscosity materials can typically be processed in comparison to IJP and was a primary factor in the decision to change to this printing modality. However, an understanding of viscosity must first be established as sufficient spreading within the printer vat

is required to ensure adequate layer adhesion, with shear rates most applicable between 1 to 100 s^{-1}. For the lower Mn PEGDA formulations (CG–F1 and CG–F2) the respective viscosity values were 92.5 ± 72.4 and 248.2 ± 232.6 cP at a shear rate of 10 s^{-1} and 11.6 ± 3.6 and 23.7 ± 3.2 cP at a shear rate of 100 s^{-1}, as shown in Figure 5.3. Formulations utilising 20% (*w/v*) monomer additions are compared in Figure 5.4, with the viscosity of CG–F3 and CG–F4 determined to be 33.1 ± 11.1 and 21.5 ± 3.2 cP at a shear rate of 10 s^{-1} respectively and 5.0 ± 1.4 and 7.9 ± 2.1 cP rate of 100 s^{-1}. In the context of the two highest Mn PEGDA formulations (CG–F5 and CG–F6) the viscosity values were 17.7 ± 3.1 and 23.3 ± 6.7 cP at a shear rate of 10 s^{-1} and 8.2 ± 0.1 and 13.6 ± 0.6 cP at a shear rate of 100 s^{-1}. Due to the low % (*w/v*) the differences in viscosity were not significant at lower shear rates e.g. 10 s^{-1}. All formulations prepared exhibited shear thinning properties, whereby increasing the shear rate from 10 to 1000 s^{-1} led to decreases in formulation viscosity.
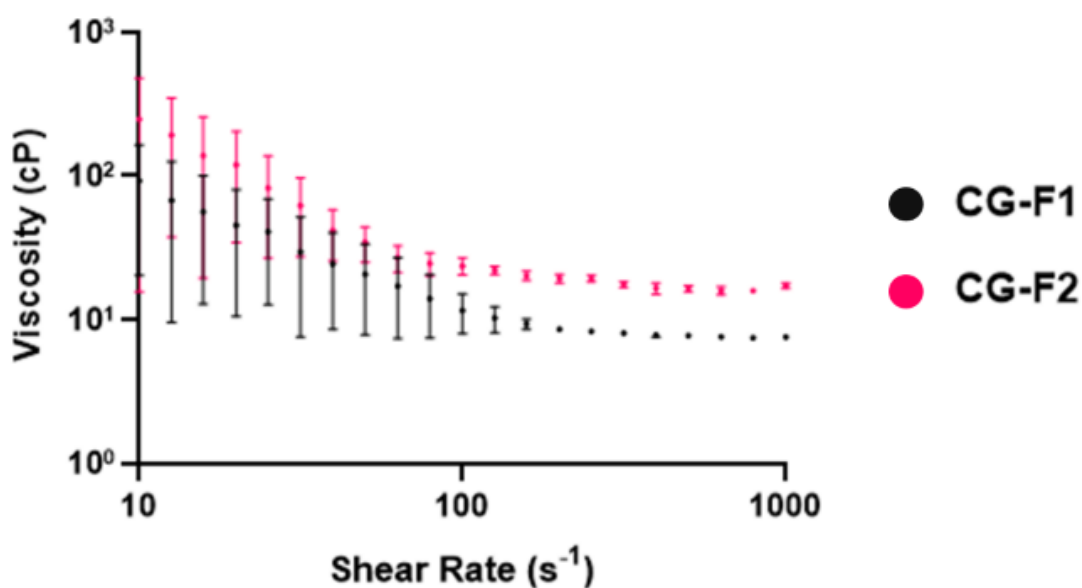
Figure 5.3: Shear rate vs viscosity for PEGDA 575 and PEGDA 700 50% (*v/v*) formulations (CG–F1 to CG–F2). Results denote mean ± S.D. (n = 3).
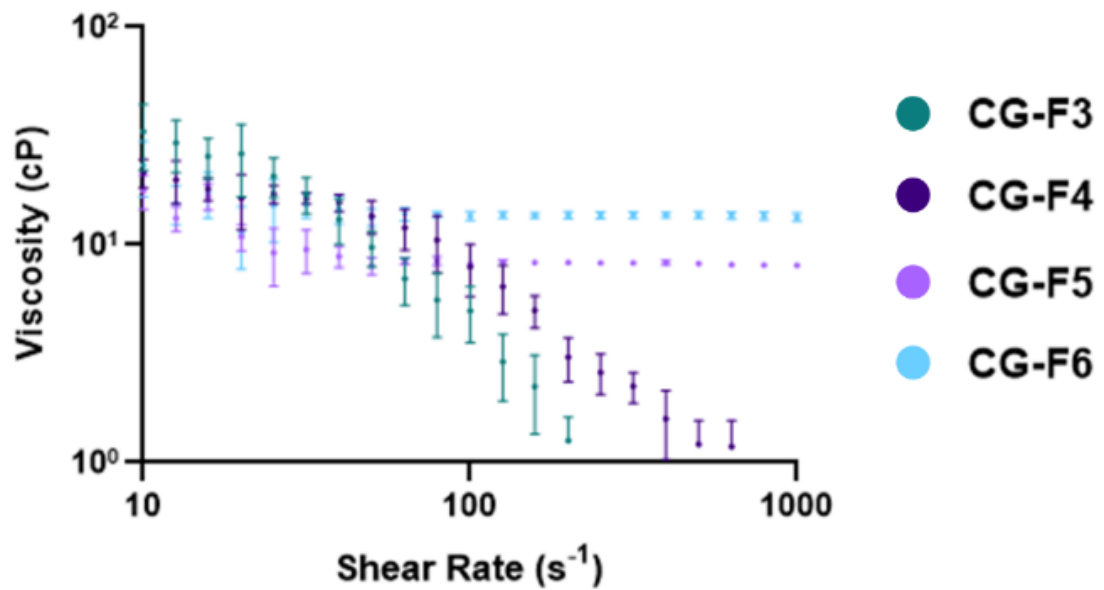
Figure 5.4: Shear rate vs viscosity for PEGDA 1000, 4000, 8000 and 10,000 20% (*w/v*) formulations (CG–F3 to CG–F6). Results denote mean ± S.D. (n = 3).

5.3.1.4 Influence of Stirring Speed and Duration on the Activity of a Model Protein (ALP)

The preparation of formulations for printing commonly requires the addition of materials in combination to form a homogenous solution. Hence, it was decided to assess the selected stirring speed and stirring duration during this preparation and the associated influence on the activity of a selected model protein, in this instance ALP. A stock solution of 20 µg/mL concentration ALP in PBS was prepared and a stirrer bar added to each vial of 20 mL. Figure 5.5 shows the corresponding ALP activity retention for each stirring speed (100, 200 and 300 RPM) and duration (5, 15 and 30 minutes) relative to a stock solution. Comparing the stock solution activity to each stir speed and duration condition there was no statistically significant difference. There was also no statistically significant difference within each individual stirring speed setting data set when comparing the three different durations selected. Hence, this indicates that the conditions trialled to simulate mixing of formulation constituents did not negatively impact the loaded model protein of ALP in PBS.
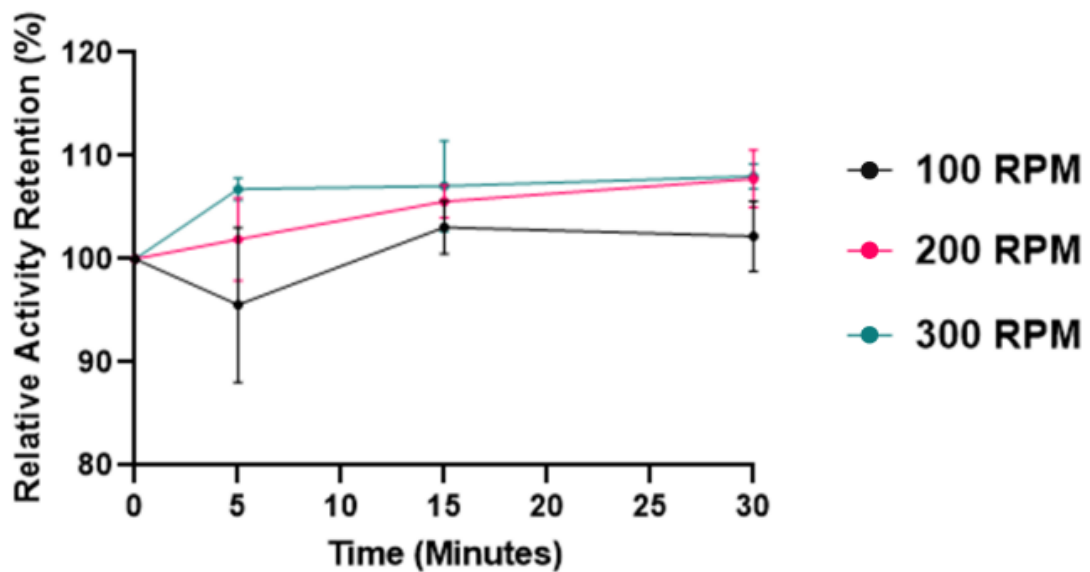
Figure 5.5: Relative ALP activity retention (%) in relation to stirring speeds of 100, 200 and 300 RPM and durations of 5, 15 and 30 minutes. Results denote mean ± S.D. (n = 3).

5.3.1.5 Influence of UV Exposure on the Activity of a Model Protein (ALP): UV Lamp and In-Situ Anycubic Photon Mono DLP Printer

DLP printing processes require selected ink formulations to be able to be crosslinked, ideally in a short time period, under light/UV exposure. Initially, to get a baseline understanding of any potential UV induced effect on activity, a UV lamp experiment setup was used. In this case, a stock solution of ALP in PBS (20 µg/mL) was prepared and the effect of continuous UV exposure compared versus UV exposure cycles with periodic rest intervals. For example, where exposure was turned on and off in 0.5-minute cycles until the desired total UV exposure period had been reached. Activity was quantified for the stock solution, to provide a pre-exposure value for comparison, and at each time point interval selected as shown in Figure 5.6. The continuous UV exposure experiment indicated ALP activity was initially well retained with no statistical difference from the stock solution, up until 1.5 minutes where $p < 0.01$. For all remaining time point data collected from 2 to 5 minutes $p < 0.0001$ when compared to the pre-exposed stock solution. Under the second experimental condition, where periods of 0.5 minutes of rest from UV

exposure were introduced, activity also showed no statistically significant decrease from the stock solution up until 2 minutes, where $p < 0.0001$. The use of on/off exposures retained higher activity that was significantly improved on the continuous test where $p < 0.01$ at 2.5 minutes and $p < 0.0001$ from 3.5 minutes onwards. Whilst not a standardised experimental test, this provided an initial indication as to how UV could possibly impact protein activity, in this case ALP, and provided the basis for further investigation. It is probable that a localised heat induced effect from the high-power UV light (1.5 W/cm^2) also contributed to activity loss [182].

Arguably, the most important information to determine is the impact of the DLP printing process. A continuous UV exposure test was carried out within the printer vat to determine if the Anycubic Photon Mono UV projection (1.2 – 1.4 mW/cm^2) would be appropriate. ALP activity was determined before and after continuous exposure for pre-selected time periods of 1, 5, 10 and 30 minutes. A decrease in activity retention was observed as UV exposure time was increased with values statistically different after 1 minute ($p < 0.05$), 5 minutes ($p < 0.01$), 10 minutes ($p < 0.01$) and finally 30 minutes ($p < 0.001$) where 84.6 ± 0.9% was retained. Figure 5.7 compares the UV exposure tests conducted with the UV lamp and in-situ DLP printer setup, showing the impact of exposure over longer time periods was less detrimental when simulating the printing process.
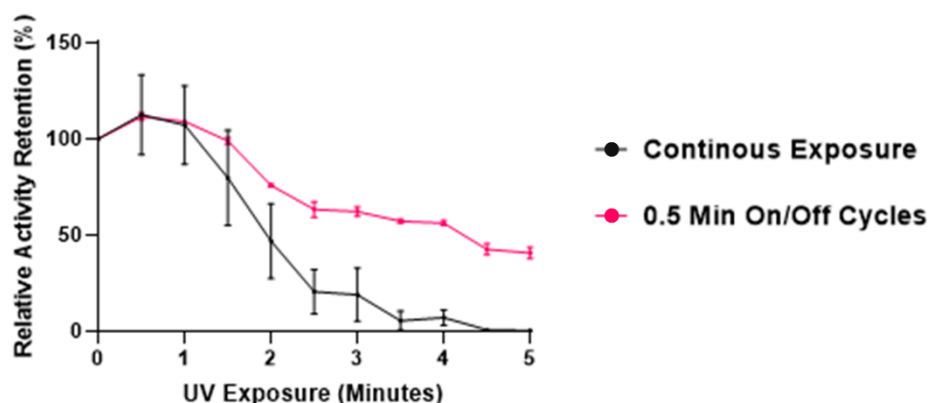
Figure 5.6: Relative activity retention (%) of ALP as a function of time under continuous or cycles of 0.5 min on/off UV lamp exposure. Results denote mean ± S.D. (n = 3).
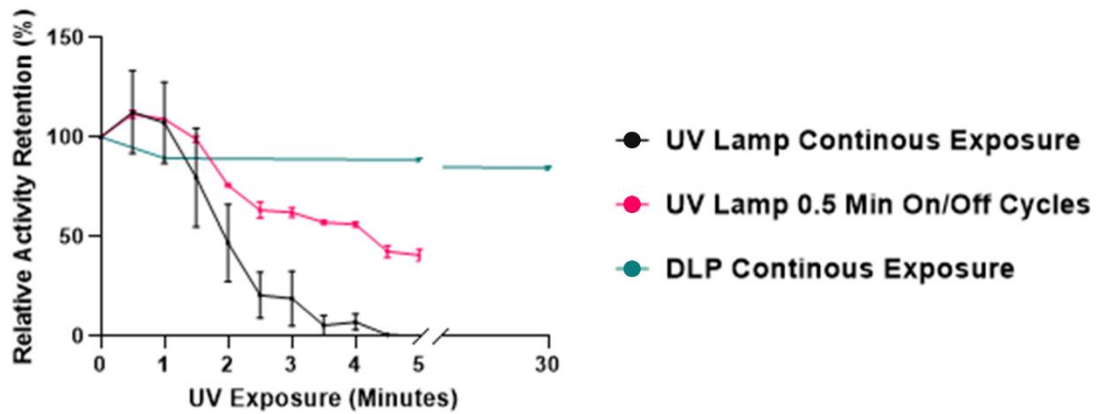
Figure 5.7: Comparison of relative activity retention (%) of ALP as a function of time under continuous or cycles of 0.5 min on/off UV lamp exposure versus the continuous exposure within the DLP printing setup. Results denote mean ± S.D. (n = 3).

Reasoning for this improved activity retention may include the less intense light source of the DLP printer and increased distance between UV source and the solution. Also, there is a fluorinated ethylene propylene (FEP) film sheet barrier between the UV source and solution and a higher quantity of solution in the vat (20 mL), as would be typical for printing use, compared to just 50 µL in the UV lamp syringe setup. The combination of the differences in experimental setup potentially allowed heat to be better dissipated. In contrast, a localised heat induced effect could have been potentially experienced from the UV lamp experiments, contributing to protein inactivation, rather than the effect of UV alone [182]. This would also provide explanation for why the periods of UV exposure rest in the on/off experiment helped retain activity even though the total time the solution experienced UV exposure at each time point was the same for the continuous UV exposure conditions. It is worth noting that during a printing cycle the periods of UV exposure are typically shorter, for example seconds per layer. In addition, between layer exposures there is a period of rest, where the UV light is not turned on as the build platform moves. Evaluating the effect of UV exposure by simulating conditions within the printer was beneficial to confirm the process alone corresponded with a significantly lower drop in activity (~20% of the pre-exposed value) even at extended periods e.g. 30 minutes.

This study considered the effect of UV on ALP freely in PBS, whereas in reality formulations prepared for printing require a photoinitiator addition. Under UV exposure photoinitiator components produce free radicals, which react with monomer components to initiate polymer chain reactions and crosslinking. Previous literature has shown that free radical interaction can negatively impact protein activity retention [183]. The extent of this would need to be determined on an individual basis for proteins of interest that are firstly encapsulated and then released to see if activity has been retained during formulation and throughout printing to final elution.

5.3.2 DLP Printing

5.3.2.1 Parameter Optimisation

Formulations based on PEGDA and PBS components were initially selected to provide a reasonable comparison to the formulations tried previously for IJP. This would indicate whether the change in printing technique had any improvement on processing these formulations. A particularly important parameter is the selection of the required UV exposure time, sufficient to crosslink the required material of the design inputted [184]. Optimisation is required to minimise over exposure whereby external areas outside the inputted design are crosslinked. Figure 5.8(a-c) shows the design file for a 10 x 10 x 2 mm pattern, an example of an overexposed print (no photoabsorber addition) and example of an optimised print aided by the addition of a photoabsorber. Introducing a photoabsorber allows an enhanced control over curing depth and minimises the chance of over exposure relative to the intended projected pattern layer. For this work, it was decided to select tartrazine, an FDA approved water soluble synthetic food dye, due to its high solubility (20 g/100 mL at 25°C in water) and non-toxicity (safe dosage up to 7.5 mg/kg bodyweight per day) which is a requirement for implants when regarding end patient use [185]. It was decided that tartrazine additions of 0.1% (*w/v*) relative to the PEGDA addition were suitable to control over exposure but still ensure adequate bonding to the build platform.

To ensure adhesion of the fabricated components to the top build platform, the Chitubox software used allows for the incorporation of extended bottom layer exposures. The principle being to provide a solid foundation for subsequent

77

layers to be photopolymerised until print completion. Additional parameters that can be controlled include movement distance and speed, ensuring the ink can be spread easily within the vat. Furthermore, the ability to use setups that allow faster build times are desirable for future scale up potential of the technology [176]. However, care must be taken to avoid physical detachment from the build platform, which can be caused by either inadequate adhesion or the platform movement speed selected being too fast and causing pulling-up separation [186].

For the swelling and release studies 10 x 10 x 2 mm samples were fabricated using the Anycubic Photon Mono DLP printer, with suitable exposure times established for each formulation (CG–F1 to CG–F6) documented in Table 5.4. An example of voxel patterning, dictated by projected layers of the inputted design, can be observed on the surface and the individual layer accumulation via optical and SEM imaging shown in Figure 5.9(a-c). These features align with past literature and is a characteristic well reported for projection DLP printed components [187,188].

a   **b**   **c**
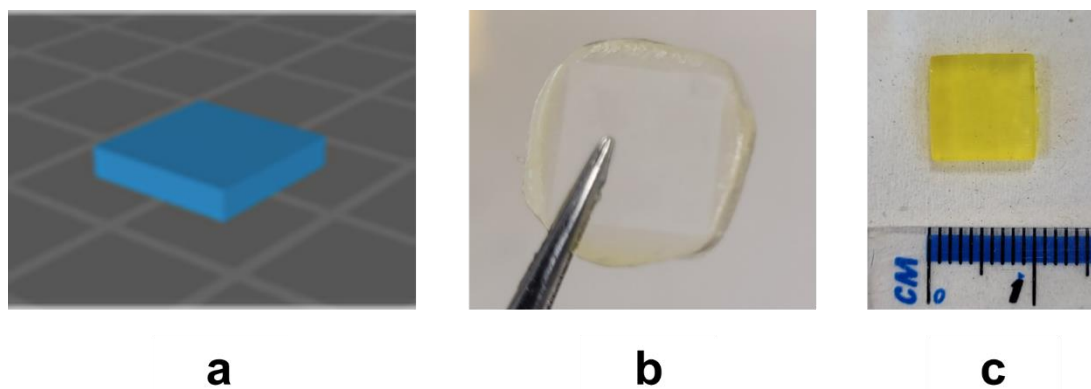
Figure 5.8: (a) Example design file of a 10 x 10 x 2 mm pattern, (b) example of an overexposed print (no photoabsorber addition) and (c) an optimised outcome aided by the addition of tartrazine.

Table 5.4: Overview of DLP printer settings utilised for each CG formulation, with corresponding Z height measurements. Results denote mean ± S.D. (n = 10).

Suitable Printing Parameters			
Formulation Code	Bottom Exposure (s) First 2 Layers	Normal Exposure (s)	Z Height (mm)
CG–F1	30	15	1.98 ± 0.02
CG–F2			1.99 ± 0.03
CG–F3	40	20	2.00 ± 0.04
CG–F4	45	22	2.00 ± 0.03
CG–F5	50	25	1.99 ± 0.03
CG–F6	70	35	1.97 ± 0.04

a   **b**   **c**
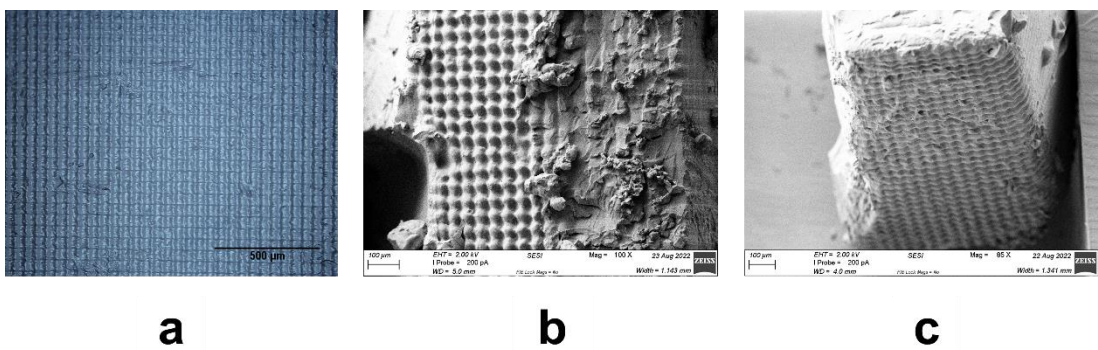
Figure 5.9: Imaging of the voxel patterning surface feature for DLP printed samples using (a) optical imaging and (b) SEM imaging. (c) SEM imaging used to show individual layers of a printed sample via the layer-by-layer build nature of the DLP process.

5.3.2.2 DLP 3D Printed Structures with Model Proteins (ALP, BSA and LYZ) Encapsulated

5.3.2.2.1 Swelling and Theoretical Matrix Mesh Size Approximations

Using the range of formulations prepared with increasing PEGDA Mn (CG–F1 to CG–F6), a study was conducted to determine the influence of the changes in sample composition on the resulting swelling and theoretical matrix mesh size. Firstly, swelling rate and swelling ratio were able to be calculated by tracking the mass of samples in the as printed state and swelled state. Figure 5.10 shows the associated swelling rate for each sample composition analysed and was primarily used to determine the point where no further swelling occurred, whereby after 24 hours (day 1) all samples had reached an equilibrium.

Swelling behaviour of the printed polymer network structure will correspond to the mass transfer of water into and out of the matrix, which in turn will influence the release of proteins encapsulated within a structure [189,190]. Swelling ratio, defined as the fractional weight increase due to water absorption, was compared for statistical difference and is shown in Figure 5.11. Swelling ratio ranged from 0.77 to 13.24 ± 0.23 and increased as PEGDA Mn was increased, as was hypothesised. There was no statistically significant difference between CG–F1 and CG–F2, however there was a statistically significant difference ($p < 0.0001$) each time the Mn of PEGDA was increased for the 20% (*w/v*) formulations (CG–F3 to CG–F6).

Theoretical matrix mesh size approximations were also determined and acted as a comparative tool for the printed sample sets. Values ranged from 3.3 Å to 83.5 ± 1.2 Å, with greater matrix mesh sizes calculated associated with the increased Mn of the PEGDA selected in formulations as shown in Figure 5.12. There was no significant difference between CG–F1 and CG–F2, but again there was a statistically significant difference ($p < 0.0001$) each time the Mn of PEGDA was increased from CG–F2 to CG–F6. The trend of increasing swelling ratio and theoretical matrix mesh size approximation values indicated that the two matrix properties were closely related. Hence, Figure 5.13 shows that the relationship between these two parameters is near linear (square of the correlation coefficient, $R^2 = 0.99$). A summary of the differences

in matrix characteristics for samples prepared using CG–F1 to CG–F6 is provided in Table 5.5. The properties assessed are dictated by material composition of the final 3D printed structures. PEGDA based formulations used in this Chapter were not expected to degrade or change significantly over the time frames that release would be quantified. Therefore, once samples were swelled in the PBS release media, it was deemed the matrix mesh size would not change significantly after reaching equilibrium.
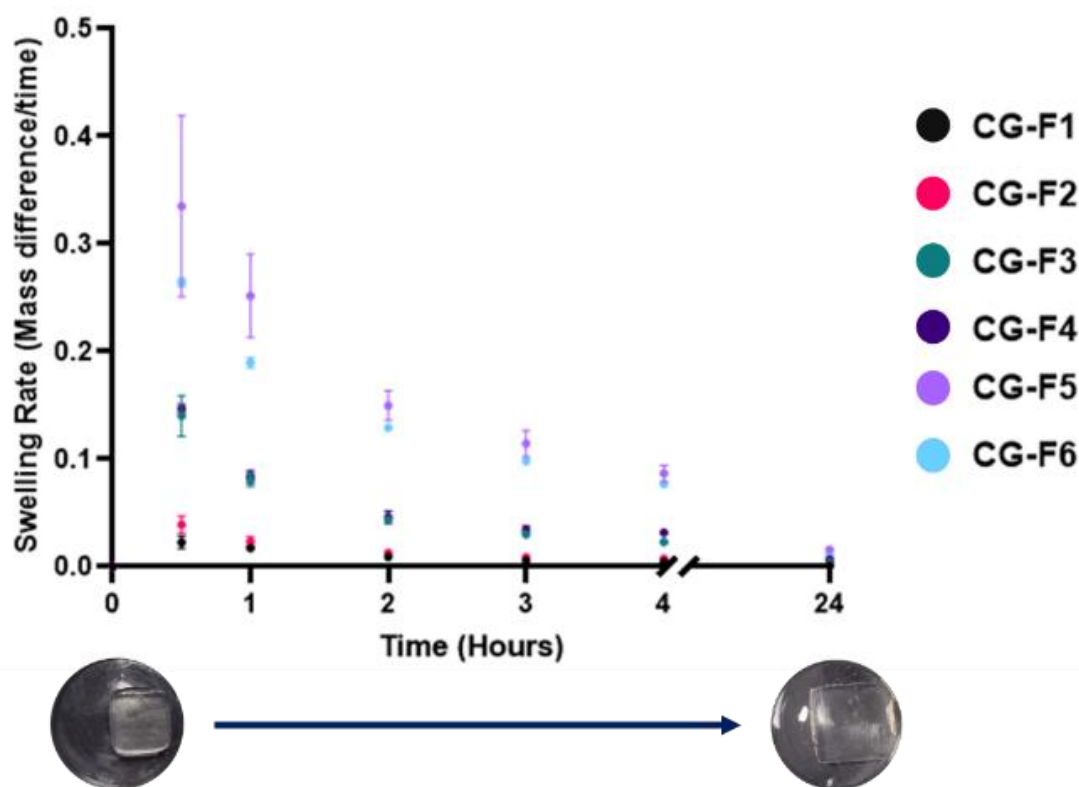
Figure 5.10: Tracking changes in swelling rate until swelled equilibrium for samples printed using CG–F1 to CG–F6. Results denote mean ± S.D. (n = 3).
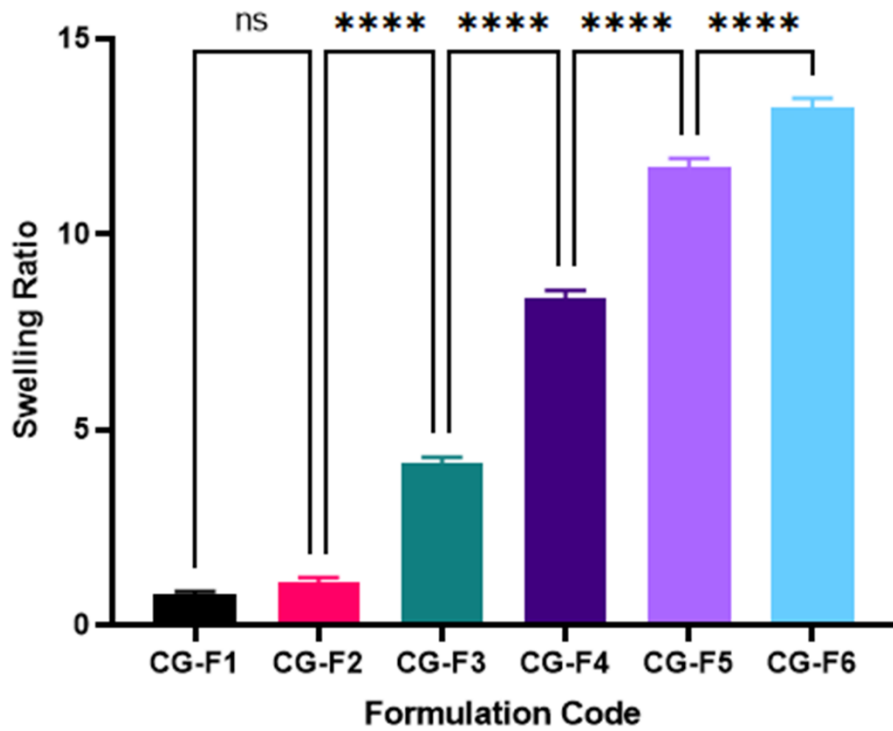
Figure 5.11: Associated swelling ratio comparisons after 1 day of swelling for samples printed using CG–F1 to CG–F6. Results denote mean ± S.D. (n = 3).
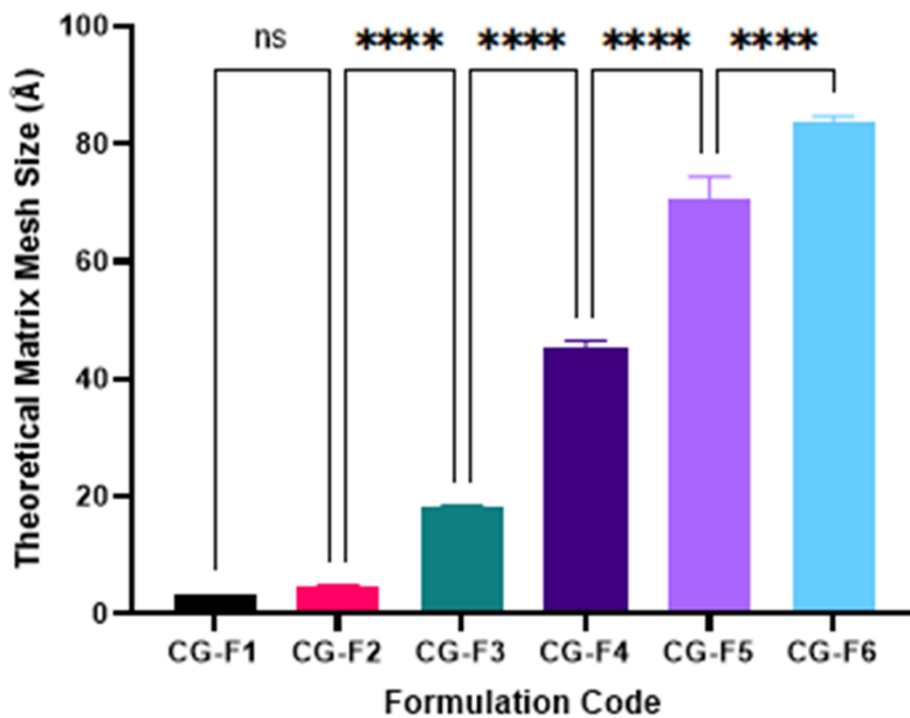
Figure 5.12: Associated theoretical matrix mesh size comparisons after 1 day of swelling for samples printed using CG–F1 to CG–F6.
Results denote mean ± S.D. (n = 3).
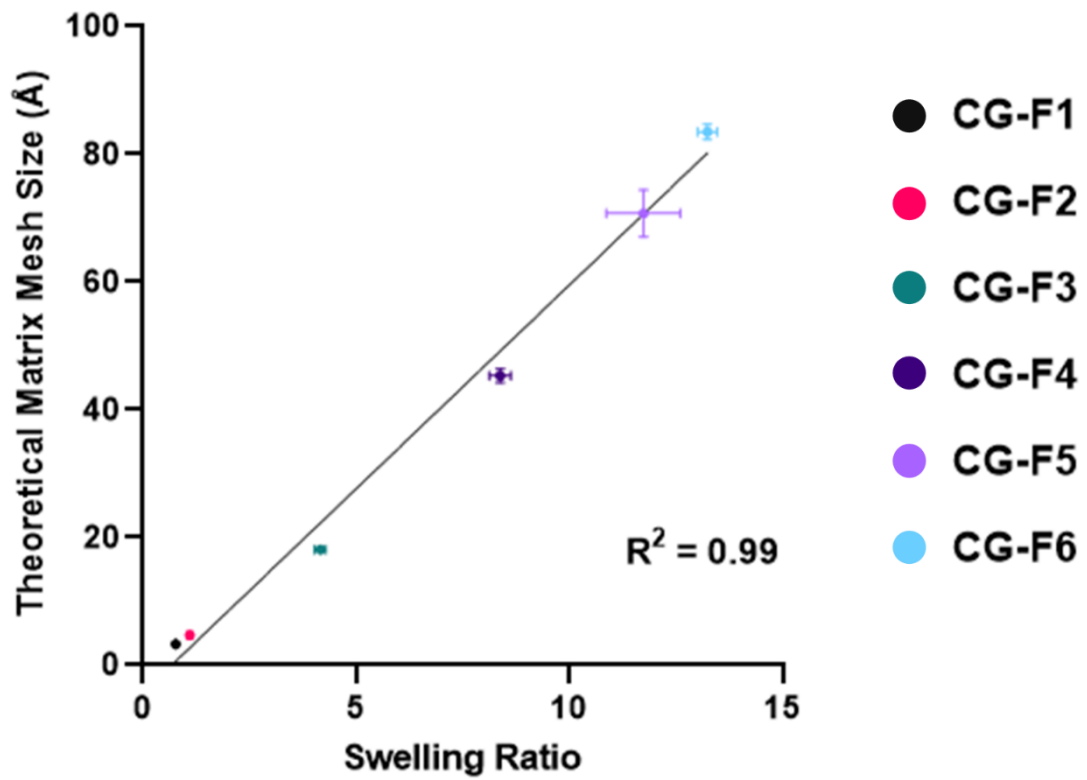
Figure 5.13: Correlation between matrix properties of swelling ratio and theoretical matrix mesh size using values determined for the range of printed samples comprised of CG–F1 to CG–F6. Results denote mean ± S.D. (n = 3).

Table 5.5: Overview of swelling ratio and theoretical matrix mesh size determined for samples printed using CG–F1 to CG–F6. Results denote mean ± S.D. (n = 3).

Summary of Matrix Characteristics			
Formulation Code	Swelling Ratio at Day 1	Theoretical Matrix Mesh Size As Printed (Å)	Theoretical Matrix Mesh Size As Swelled at Day 1 (Å)
CG–F1	0.77	3.0	3.3
CG–F2	1.10 ± 0.05	3.8 ± 0.2	4.7 ± 0.2
CG–F3	4.16 ± 0.13	12.7 ± 0.5	18.1 ± 0.5
CG–F4	8.38 ± 0.25	31.1 ± 0.7	45.3 ± 1.1
CG–F5	11.74 ± 0.87	21.4 ± 2.8	70.7 ± 3.7
CG–F6	13.24 ± 0.23	29.9 ± 1.2	83.5 ± 1.2

5.3.2.2.2 Model Protein Release from DLP 3D Printed Structures

Initially, a 1 mg/mL loading of each of the model proteins (LYZ, BSA and ALP) was selected and utilised in the six formulations prepared. It was hypothesised that matrix mesh sizes greater than the encapsulated protein would lead to release. There was no significant release detected in all cases from formulations CG–F1 to CG–F5, however for CG–F6 samples, with the highest Mn PEGDA 10,000 selected at 20% (*w/v*), managed to release LYZ and BSA in limited quantities. For example, release of LYZ was 17.6 ± 5.2% (35.2 ± 10.4 µg) achieved over 72 hours (3 days) before plateau and release of BSA was 13.3 ± 1.2% (26.6 ± 2.4 µg) in just 1 hour before no further elution as shown in Figure 5.14.
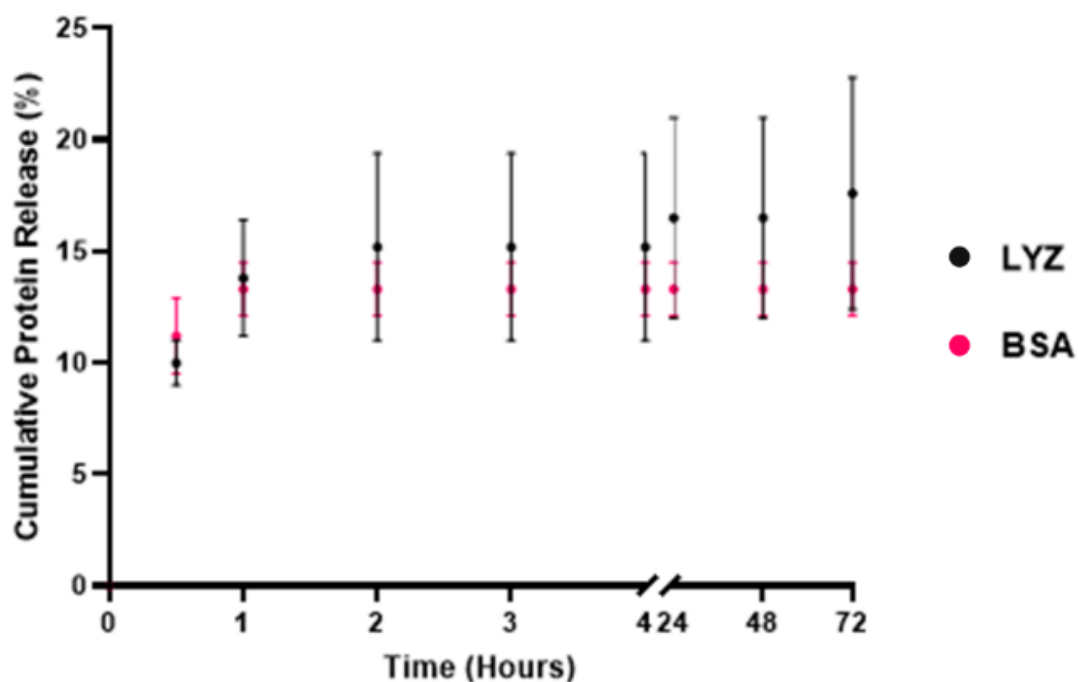
Figure 5.14: Cumulative release (%) of LYZ and BSA from CG–F6 printed samples with 1 mg/mL loading (200 µg per sample). Results denote mean ± S.D. (n = 3).

5.3.2.2.3 Influence of Model Protein Loading on BSA release

To determine the influence of model protein loading on release that could be achieved, formulations were prepared again and BSA was encapsulated at 5 mg/mL to allow comparison with release using 1 mg/mL. Increasing to the higher concentration of BSA meant the theoretical loading was 1000 µg per 10 x 10 x 2 mm sample printed and as such there was a higher likelihood of freely available protein able to be eluted. Hence, release was able to be achieved from a wider range of sample compositions of CG–F4 to CG–F6, as shown in Figure 5.15. Increased BSA release was able to be achieved from these 20% (*w/v*) formulations with increasing PEGDA Mn. Release was 17.9 ± 1.5%, 21.8 ± 1.5% and 25.8 ± 1.4% for CG–F4 to CG–F6 respectively, corresponding to 178.6 ± 15.4 µg, 217.7 ± 15.1 µg and 257.9 ± 13.6 µg. There was still no significant release detected from samples comprised of CG–F1 to CG–F3, even with the increased loading.
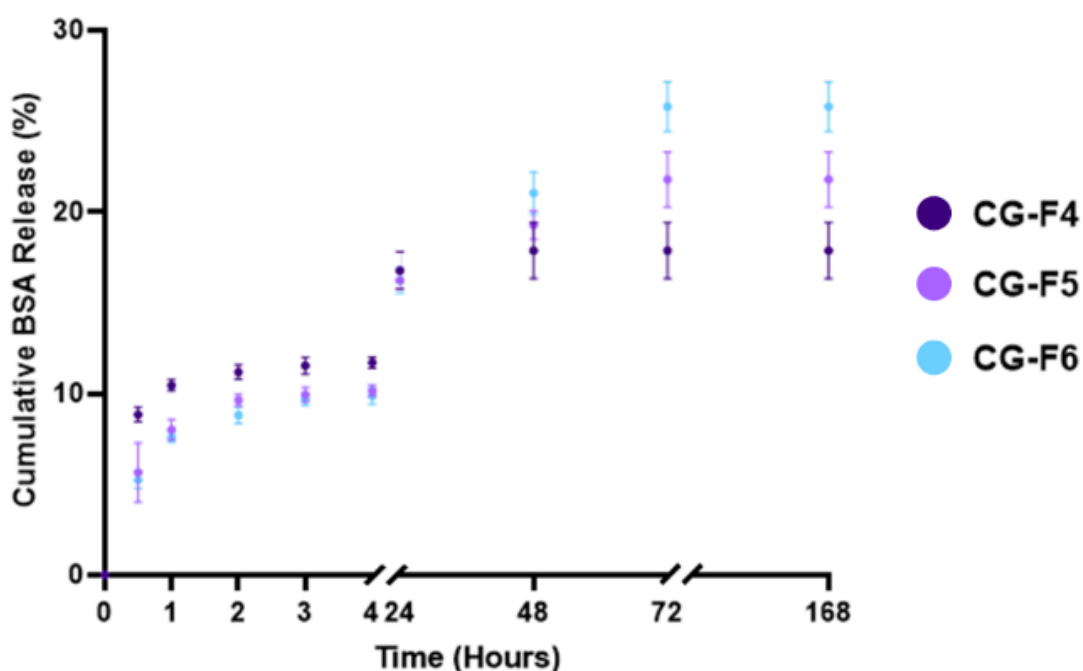
Figure 5.15: Cumulative release (%) of BSA from CG–F4 to CG–F6 printed samples with 5 mg/mL loading (1000 µg per sample). Results denote mean ± S.D. (n = 3).

5.4 Discussion

DLP was proposed as an alternative light-based 3D printing technique in this Chapter. This process negates the requirement for protein containing formulations to pass through a nozzle, which was problematic for IJP. In addition, higher viscosity formulations can be processed which expands the applicable material combinations that can be explored [112].

It was hypothesised DLP printing would be able to process formulations for fabrication of 3D structures initiated by UV light and the ability to process higher viscosity ink formulations would allow for a range of Mn PEGDAs to be explored to modulate the end polymer matrix characteristics. Hence, a range of PEGDA, with Mn from 575 to 10,000, were chosen and analysed with GPC and ^{1}H NMR spectroscopy to verify the properties of Mn, Mw and PDI of the sourced materials. Formulations prepared of CG–F1 and CG–F2 utilised lower Mn PEGDAs 575 and 700 at 50% (*v/v*) and CG–F3 to CG–F6 used PEGDA Mn 1000, 4000, 8000 and 10,000 respectively at 20% (*w/v*). Rheological

properties were also assessed with all formulations deemed appropriate for the DLP setup used.

Prior to printing, an influence of stirring study on ALP activity was conducted. No significant change was observed across all conditions (100, 200, 300 RPM at durations of 5, 15 and 30 minutes). The influence of UV exposure was also explored, with particular importance placed on the understanding effects of the DLP printing process. It was observed that activity of ALP in PBS solution after 30 minutes of continuous UV exposure was mostly retained (84.6 ± 0.9%). However, it was noted that the introduction of a photoinitiator required for sample fabrication leads to free radical generation, which has previously been reported to negatively impact activity of some proteins in literature and would need to be assessed if elution occurred [183].

Printing parameters were established, aided by the introduction of a photoabsorber component (tartrazine) at low concentrations to control depth of curing [165,174]. The production of samples comprised of CG–F1 to CG–F6 allowed swelling rate changes as well as swelling ratio and theoretical matrix mesh size approximations in the as printed and as swelled state at day 1 to be established. There was no significant difference in swelling ratio or matrix mesh size between CG–F1 and CG–F2, but a statistically significant difference each time the Mn of PEGDA was increased for the 20% (*w/v*) samples using CG–F3 to CG–F6. Increasing the selected Mn of PEGDA corresponded with increases in swelling and theoretical matrix mesh size approximations, which satisfied the hypothesis proposed. Additionally, a near-linear relationship was generated between these two matrix characteristics ($R^2 = 0.99$).

It was hypothesised that calculated theoretical matrix mesh size estimations would form an appropriate basis for indicating if release of encapsulated model proteins would be observed. For example, matrix mesh size < protein size will lead to protein entrapment and matrix mesh size > protein size will correspond with release. Initially, samples were printed with 1 mg/mL loading of LYZ, BSA and ALP (200 µg per sample). No release was detected for any of the three proteins from samples comprised of CG–F1 to CG–F5 formulations. CG–F6

samples allowed release of LYZ and BSA at respective quantities of 17.6 ± 5.2% (35.2 ± 10.4 µg) over 3 days and 13.3 ± 1.2% (26.6 ± 2.4 µg) in just 1 hour before plateau. Increasing the loading to 5 mg/mL (1000 µg per sample) allowed elution from a wider sample set (CG–F4 to CG–F6). Maximum BSA release achieved relative to total loading was 25.8 ± 1.4% (257.9 ± 13.6 µg) over 3 days. Reliance on increased bioactive loading for delivering desired quantities regarding end elution is not preferential, particularly for future ambitions of delivering higher-cost therapeutics for application-based delivery. Higher concentrations may also lead to aggregation that prevents release [191].

The largest protein from the selection, ALP, was not able to release from any of the formulations utilised. These results allow insight into challenges of achieving long-term release of bioactives from the 3D printed structures. Whilst matrix mesh approximations have provided a basis for comparison it is likely in reality there could be regions of the network that cause entrapment or more tortuous pathways for diffusion of the protein. In addition, there is potential for some inconsistencies between the theoretical prediction and reality that would account for matrix heterogeneity associated with CG polymerised networks [85]. Hence, low-cost experimental approaches that explore protein entrapment and release are necessary [192].

5.5 Conclusions

Overall, DLP printing allowed sample production for the analysis of matrix properties and associated protein release. However, the heterogeneity of PEGDA only CG polymerised networks, and reliance on sample swelling and diffusion alone as a mechanism for release of encapsulated proteins, was deemed insufficient. Subsequently, this prompted the proposal of alternative ideas that could be tried using DLP printing to work towards controlled long-term release for 1 to 3+ months in duration.

Formulations should be prepared that increase in swelling ratio and theoretical matrix mesh size through degradation of the polymer matrix, such that sustained release of encapsulated proteins is possible. For example, introducing degradable aspects into the existing PEGDA polymer chain.

Reliance on swelling, through changes in PEGDA Mn, and diffusion alone lead to limited release of the encapsulated model proteins.

Polymer networks produced via CG polymerisation have inherent heterogeneity, which likely leads to areas of the matrix causing entrapment of the encapsulated proteins [85]. As a result, pathways for their release may be more tortuous in nature. Instead, a progression towards mixed-mode (MM) or step-growth (SG) mechanisms of crosslinking may correspond with more homogenous polymer sample networks and opportunities for tuning structural characteristics [85,88]. The use of MM/SG polymerisation may result in faster rates of crosslinking and fabrication of structures, meaning the encapsulated proteins are exposed to shorter cumulative doses of UV light. Extended UV dosing was observed to decrease the activity of ALP, within formulations with a photoinitiator addition, and could be undesirable for other proteins.

Chapter 6 DLP Printing of Mixed-Mode (MM) Crosslinked Formulations using Hydrolytically Labile Macromers

6.1 Introduction

It was proposed that the synthesis of hydrolytically labile macromers, applicable for DLP printing, would allow production of samples that would degrade and lead to increased and extended release of encapsulated model proteins in relation to total loading. The rationale for this was to allow measurement of the influencing characteristics such as swelling, associated matrix mesh size and structural morphology through partial or full degradation of printed samples. Through a combination of degradation of the polymer network and diffusion of the encapsulated protein, it was anticipated that release would be able to be achieved over sustained periods as was intended. In addition, the continued use of PEGDA as the backbone, with degradable aspect variations now utilised, allowed for a direct comparison with the CG PEGDA formulations previously prepared in Chapter 5.

Importantly, through an experimental approach, the aim of this work has been to develop the overall fundamental understanding on factors that influence matrix mesh morphology in relation to any associated release. The selection of relatively low-cost materials with predominantly PEGDA, PBS, DTT and LAP have allowed for multiple formulation iterations to be explored, leading to a comprehensive discussion of the acquired results. The use of similar material combinations has been reported for use in extrusion printing with nano-silicates [193]. PEGDA-DTT macromers have also been assessed for adaptable mechanical and degradation properties for use in biomedical properties [152,194]. However, DLP printing has been explored to lesser extent with these material combinations, which are chemically suitable for UV photopolymerisation, and hence prompted the investigation in this Chapter.

6.1.1 Chapter Hypotheses

1. Formulations crosslinked via mixed-mode (MM) polymerisation mechanisms will be suitable for processing via DLP printing to produce implant exemplars that allow for assessing the release of encapsulated model protein(s).

2. The introduction of degradable aspects, in this case the synthesis and use of a PEGDA-DTT macromer, will lead to release of encapsulated model proteins through partial or full degradation of the DLP printed sample matrix.

3. Duration and rate of release will be able to be modulated through changes in both PEGDA-DTT polymer concentration and thiol (SH) to acrylate ratios selected for formulations.

6.1.2 Formulation Considerations

Formulations should be predominantly water-based or applicable for the model protein of interest to be soluble within, to maximise potential loading and homogenous distribution. Moreover, formulations should ideally be processable without, or with minimal, additional heat to avoid model protein(s) denaturing. This could limit applicable PEGDA-DTT formulations for the DLP printing process, particularly the SH:acrylate ratio selected when synthesising the macromers.

Adequate crosslinking components within the desired formulations must be ensured to allow fabrication of required replicates for analysis e.g. swelling, release, mechanical testing and imaging. Also, it is ideal if a low percentage of non-biodegradable components are used within formulations. Aspects that degrade over the time of intended release are preferred. For example, to minimise potential toxicity and allow easy elimination from the body.

6.2 Methods for DLP Printing Experiments

6.2.1 Formulation Preparation

Table 6.1 outlines formulations prepared in PBS with 0.5% (*w/v*) LAP with respect to total formulation and 0.1% (*w/w*) tartrazine relative to LAP for DLP printing, as mentioned in Chapter 3.3.1.2. Formulation characteristics include monomer Mn, monomer% (*v/v*) or (*w/v*), DTT additions in relation to SH:acrylate ratios and protein loading implemented. Formulation codes have been used for reference throughout this results chapter e.g. "mixed-mode formulation one" is denoted as MM–F1.

Table 6.1: Overview of MM PEGDA-DTT formulations prepared, coded for reference purpose.
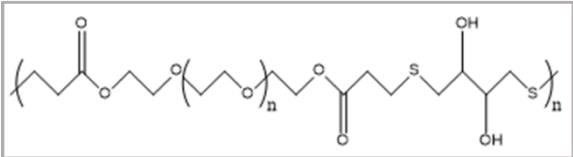
PEGDA-DTT		
Formulation Code	**Formulation**	**SH:Acrylate Ratio**
MM–F1	**PEGDA 575** 50% (*v/v*)	0.1
MM–F2		0.25
MM–F3		0.5
MM–F4		1
MM–F5	**PEGDA 700** 50% (*v/v*)	0.1
MM–F6		0.25
MM–F7		0.5
MM–F8		1
MM–F9	**PEGDA 575/4000 (1:1)** 10% (*w/v*)	0.25
MM–F10		0.5
MM–F11	**PEGDA 575/4000 (1:1)** 20% (*w/v*)	0.25
MM–F12		0.5

6.2.2 Pre-Print Characterisation

Prepared formulations were analysed with GPC to determine the influence of SH additions on MW distribution and PDI for MM–F1 to MM–F12, as outlined in Section 3.4.3. ^{1}H NMR spectroscopy was used, as outlined in Section 3.4.4, primarily to compare the decrease in acrylate signal associated with increasing DTT additions during functionalisation of PEGDA to form PEGDA-DTT, shown in Section 3.3.4. Rheological measurements were conducted using the method outlined in Section 3.4.1, to compare the effect of SH:acrylate ratios on viscosity for all formulations prepared.

6.2.3 DLP Printing

Formulations MM–F1 to MM–F12 were printed using an Ancyubic Photon Mono DLP printer, described further in Section 3.2.2. Table 6.2 summarises the geometries explored within this chapter, with geometry A (10 x 10 x 2 mm) sample design and 5 mg/mL protein loading utilised for the majority of the release study data presented.

Table 6.2: Overview of five geometries (A-E) explored for differences in SA/volume ratios to analyse for influences on release of BSA.

Geometrical Changes Explored					
Sample Design Code	Sample Design	Volume (V) (mm³)	Surface Area (SA) (mm²)	SA/V Ratio	Theoretical BSA Loading (µg)
Geometry A (block)		200	280	1.40	1000
Geometry B (window)		150	270	1.80	750
Geometry C (waffle)		168	312	1.86	840
Geometry D (snowflake)		164	332	2.02	820
Geometry E (rod)		100	208	2.08	500

6.2.4 Measuring Swelling Properties and Theoretical Matrix Mesh Size Approximations

Printed samples (geometry A) were used to determine changes in swelling ratio and theoretical matrix mesh size approximations over time in PBS media at 37°C. The properties of each were calculated using the equations shown in Section 3.4.7. For each condition and time point the result presented is the mean of three samples ± S.D.

6.2.5 Experimental Setup of Controlled *In Vitro* Release Studies

In vitro release studies for printed DLP samples was conducted as outlined in Section 3.4.8.1. For each condition and respective time point release value, the result presented is the mean of three samples ± S.D. Zero-order, first-order, Higuchi and Korsmeyer-Peppas release kinetic mathematical models, explained in Section 3.4.9, were used for fitting of quantified BSA release, where applicable.

6.2.6 Cryo-SEM Imaging

Sacrificial samples were printed and imaged at day 0 and after submersion in PBS at 37°C to allow a visual comparison of structural morphology before and after degradation, using the method stated in Section 3.4.6.

6.2.7 Mechanical Analysis

Compression testing was conducted using a texture analyser setup, as outlined in Section 3.4.10. Samples were compared in the as printed and as swelled state after 1 day in PBS at 37°C. For each condition and time point the result presented is the mean of three samples ± S.D.

6.3 Results

6.3.1 Initial Proof of Concept Trial Using As Cast PEGDA-DTT Samples for Encapsulation and Release of BSA

Initially, a proof of concept trial was proposed whereby an SH component would be introduced into the previously explored acrylate formulations. In this instance, a low-cost SH of DTT was used to synthesise a MM acrylate-SH macromer of PEGDA-DTT as outlined in Section 3.3.4.

Firstly, a formulation consisting of PEGDA 4000 20% (*w/v*), with an SH to acrylate ratio of 0.8:1, 0.5% (*w/v*) LAP of total formulation and 0.1% (*w/w*) tartrazine relative to LAP was prepared. A purposely high SH:acrylate ratio was chosen to clearly understand the influence and extent of the SH addition. During the preparation, it became evident after the 1 hour of synthesis that the addition of DTT contributes to an increase in formulation viscosity with the resultant ink not having the properties suitable for processing using the DLP printer selected. For example, the formulation was not able to be spread evenly within the printing vat when in contact with the build plate. Hence, it was decided to use the prepared formulation to create UV crosslinked as cast samples (in a mould), shown in Figure 6.1(a), to assess the influence of the DTT addition on subsequent degradation and thus potential release of BSA.

In Chapter 5, structures printed using formulations without degradable components were seen to release the encapsulated model proteins in limited quantities e.g. 13.3 ± 1.2% to 25.8 ± 1.4% of total BSA loaded. Release observed was also unsustained; 3 days before plateau and no further elution. In contrast, the addition of the DTT component into the PEGDA 4000 20% (*w/v*) formulation led to the complete degradation of the structure within 9 days in PBS, 37°C. Figure 6.1(b) shows that the as cast sample initially undergoes a period of swelling as observed previously with PEGDA only based samples. Initial signs of degradation were observed, to the point samples could not be handled without causing damage, at day 3 in Figure 6.1(c). This degradation corresponded with release of the encapsulated BSA, incorporated at a 1 mg/mL concentration relative to the overall formulation, with no further release detected after full degradation at day 9, shown in Figure 6.1(d)(e). This

confirmed that the addition of DTT led to structural changes that enabled a previously non-degradable PEGDA only formulation to be broken down.

Overall, this initial trial provided a promising insight into how changes in the structural morphology, in this instance through hydrolytic degradation and disruption of the polymer matrix, could lead to release of an incorporated model protein, BSA. Hence, this could be exploited to achieve controlled elution of protein in quantities not observed through the use of CG PEGDA only based formulations that relied on swelling and diffusion alone. Whilst beneficial to understand the effect of DTT addition on sample degradation, the formulation used for the as cast example was inappropriate for DLP printing and release was only achieved over a short time period of 9 days. Evident issues with viscosity, associated with the Michael addition of the DTT into the PEGDA chain, meant characterisation of the formulations would be required to determine suitable options for DLP printing. It has been shown previously that the synthesis of PEGDA-DTT, specifically the SH:acrylate ratio selected, has influence on the final macromer produced [195].
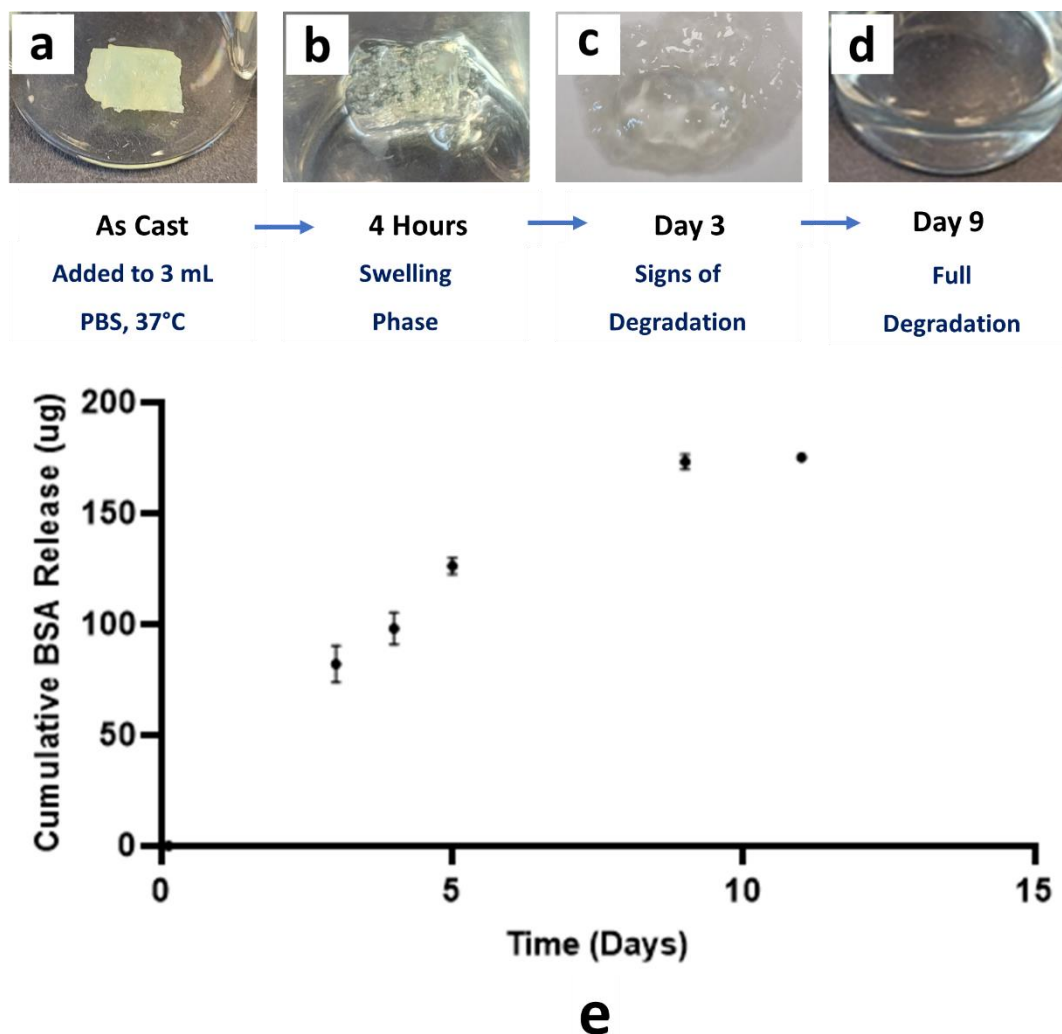
Figure 6.1: Stages of the PEGDA 4000 20% (*w/v*) 0.8 SH:acrylate sample state from (a) as cast, (b) swelling in PBS at 37°C after 4 hours, (c) signs of hydrolytic degradation at day 3 and (d) full degradation at day 9. (e) The associated cumulative BSA release during the period of swelling and degradation. Results denote mean ± S.D. (n = 3).

6.3.2 Pre-Print Characterisation

6.3.2.1 GPC Analysis of Synthesised PEGDA-DTT Macromers

GPC was conducted to determine the influence of DTT (SH component) additions to PEGDA (acrylate component) on the properties of the resulting PEGDA-DTT macromers. The analysis indicated that these macromers increased in overall Mn and Mw with selection of higher Mn PEGDA or PEGDA blends and increasing SH:acrylate ratios as demonstrated in Figure 6.2(a) for PEGDA 575 formulations (MM–F1 to MM–F4). For example, Mn ranged from 645 to 3210 g/mol and Mw from 933 to 12220 g/mol. The GPC analysis of the

PEGDA 575 reacted at SH:acrylate ratios of 0.1 to 1 indicated a 2.0 to 25.7-fold increase in polymer Mw of the PEGDA 575 monomer after completion of the reaction. This was anticipated due to the nature of Michael addition reactions and provided confirmation that the DTT addition into the PEGDA leads to chain elongation, where the SH aspects will act as the hydrolytically labile regions; this finding aligns well with past literature involving MM reactions [194–196]. The effect of increasing SH content on the synthesised macromer is also demonstrated in Figure 6.2(b) for the PEGDA 700 formulations (MM–F5 to MM–F8), with Mn and Mw ranging from 1051 to 5554 g/mol and 1420 to 14140 g/mol respectively. This corresponded with a 2.2 to 22.0-fold increase in polymer Mw of the PEGDA 700 monomer after completion of the reaction.

For the higher Mn formulations, PEGDA 575/4000 (1:1) 10% and 20% (*w/v*) (MM–F9 to MM–F12), a similar trend was observed as for the lower Mn PEGDA formulations. For example, Mn ranged from 696 to 865 g/mol and Mw from 1575 to 2488 g/mol. Variability is seen in the end macromer distribution, with two peaks at 613 ± 12 and 5965 ± 342 g/mol shown in Figure 6.2(c). This can be attributed to the DTT addition in relation to equal parts of low Mn PEGDA 575 and higher Mn PEGDA 4000 in the formulations.

Across the formulations it was shown that higher SH content in the PEGDA-DTT synthesis contributed to heterogenous populations of macromers. The PDI values determined indicated that MW distribution became more varied with increasing SH additions and for all formulations was higher than the PDI of their respective CG PEGDA formulations (Chapter 5). PDI is typically higher for SG crosslinked networks, which provides reasoning for the increase in PDI for MM formulations in comparison to CG only formulations. In the case of the PEGDA 575 formulations (MM–F1 to MM–F4), PDI increased from 1.45 to 3.81 and for the PEGDA 700 formulations (MM–F5 to MM–F8) PDI ranged from 1.35 to 2.55. For the higher MW formulations (MM–F9 to MM–F12), the PDI was between 2.26 to 2.88. Table 6.3 summarises the results gathered from GPC analysis for the different PEGDA-DTT formulations prepared, with the trend of increases in the associated Mn, Mw and PDI consistent for all formulations prepared when the SH:acrylate ratio is increased.
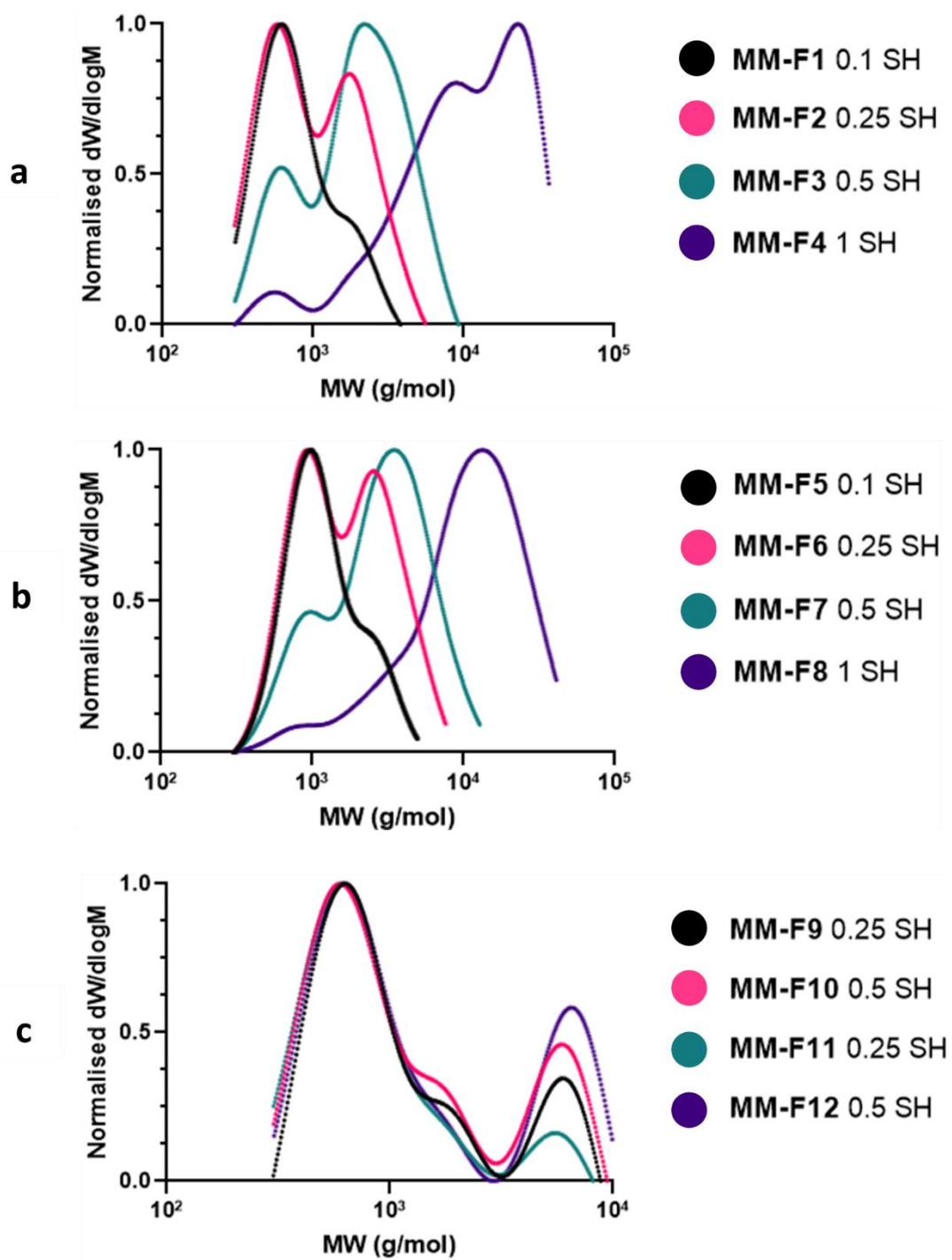
Figure 6.2: GPC analysis of the MW distribution (g/mol) versus normalised dW/dlogM for (a) PEGDA 575 formulations, (b) PEGDA 700 formulations and (c) PEGDA 575/4000 (1:1) formulations.

Table 6.3: Overview of formulations analysed by GPC for Mn, Mw and PDI.

GPC Analysis			
Formulation Code	Mn	Mw	PDI
MM–F1	645	933	1.45
MM–F2	751	1304	1.74
MM–F3	1178	2320	1.97
MM–F4	3210	12220	3.81
MM–F5	1051	1420	1.35
MM–F6	1381	2050	1.60
MM–F7	2074	3865	1.86
MM–F8	5554	14140	2.55
MM–F9	840	2105	2.51
MM–F10	823	2201	2.67
MM–F11	696	1575	2.26
MM–F12	865	2488	2.88

6.3.2.2 ^{1}H NMR Spectroscopy Analysis of PEGDA-DTT Macromers

The functionalisation of PEGDA to form PEGDA-DTT macromers was verified further by NMR spectroscopy. Figure 6.3 shows the representative spectra peaks for the PEGDA 575 based formulations and how acrylate peaks are minimised with increasing additions of DTT with 0.1:1, 0.25:1, 0.5:1 and 1:1 SH:acrylate ratios (MM–F1 to MM–F4). The decreasing acrylate signal associated with increase in SH indicates that the DTT addition in the reaction leads to increased consumption of the acrylate groups. The NMR spectra for formulations of PEGDA 700 (MM–F5 to MM–F8), PEGDA 575/4000 (1:1) SH:acrylate addition variations (MM–F9 to MM–F12) are shown in Appendix: Supplementary Information Figure S.5 and S.6 respectively. This confirmed

the findings from analysis of the PEGDA 575 formulations. Table 6.4 summarises the integrated peaks from NMR spectra gathered to compare differences in decreasing acrylate groups with increasing DTT addition.
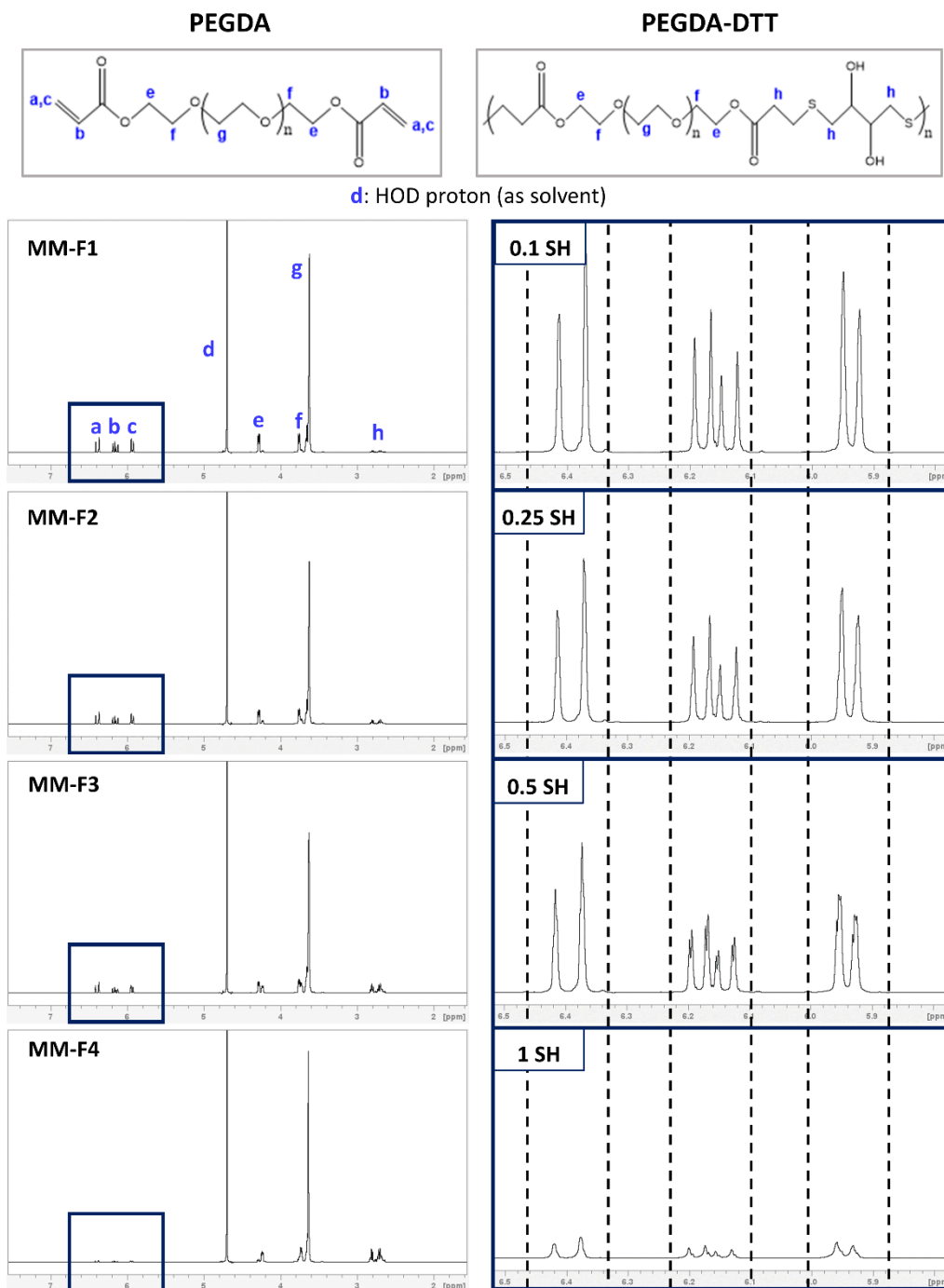
Figure 6.3: Representative NMR spectra for PEGDA 575 50% (*v/v*) formulations (MM–F1 to MM–F4), showing peak comparison and decreasing acrylate signal corresponding with increasing SH content. All spectra scaled identically.

Table 6.4: Overview of formulations analysed by ^{1}H NMR with peaks relative to the PEGDA-DTT macromer compared. *HOD peak at 4.7 ppm calibrated to a value of 10.0, with all spectra scaled identically for comparison. Values reported to 1 d.p or 1 s.f, where deemed appropriate.

^{1}H NMR Analysis*				
Formulation Code	Sum of Acrylate Peaks	Sum of EG Peaks	Acrylate:EG Ratio	DTT Peak
MM–F1	2.8	19.5	0.1	0.6
MM–F2	3.0	23.6	0.08	1.6
MM–F3	2.5	26.1	0.06	3.4
MM–F4	0.4	15.7	0.02	3.9
MM–F5	2.6	25.6	0.07	0.6
MM–F6	1.6	19.6	0.06	1.1
MM–F7	1.0	18.8	0.04	2.1
MM–F8	0.02	8.7	0.002	1.9
MM–F9	0.1	1.9	0.05	0.08
MM–F10	0.05	1.3	0.02	0.1
MM–F11	0.08	1.2	0.04	0.04
MM–F12	0.004	0.3	0.01	0.04

6.3.2.3 Rheological Analysis

The selection of DLP as a printing technique allows scope for higher viscosity formulations to be processed, as mentioned previously in Chapter 5 when transitioning from using IJP. However, across previous literature there is a suggested maximum viscosity of 5000 cP to ensure stable printing via sufficient spreading within the ink vat between each layer [197–199]. In addition, formulations that are too high in viscosity could lead to agglomeration and prevent flowability for recoating that could cause poor inter-layer adhesion

and unwanted air voids [200,201]. Ultimately, viscosity requirements must be applicable within the selected printing setup. For DLP printing, shear rates up to 100 s^{-1} are typically of most interest in relation to recoating and spreading of the ink formulation between layer solidification [202,203].

All formulations, as anticipated from the as cast trial and from the GPC and NMR data, were shown to increase in viscosity with increasing addition of the SH component (DTT). Figure 6.4 and Figure 6.5 show examples of the PEGDA 575 and PEGDA 700 50% (*v/v*) formulations prepared with SH:acrylate ratios ranging from 0.1:1 – 1:1. Viscosity increased for the PEGDA 575 SH:acrylate variations from 51.3 ± 3.4 cP to 1581.9 ± 836.2 cP at a shear rate of 10 s^{-1} and 24.2 ± 0.6 cP to 335.1 ± 64.9 cP at a shear rate of 100 s^{-1}. In the case of the PEGDA 700 SH:acrylate formulations viscosity ranged from 53.1 ± 3.4 cP to 1241.9 ± 305.4 cP (10 s^{-1}) and 22.2 ± 1.5 cP to 1037.7 ± 167.7 cP (100 s^{-1}).

Further to this, PEGDA 575/4000 blends at 10% and 20% (*w/v*), with 0.25 and 0.5 SH:acrylate ratios were analysed in Figure 6.6. Viscosity ranged from 100.2 ± 3.6 cP to 157.7 ± 19.5 cP (10 s^{-1}) and 38.6 ± 1.8 cP to 53.5 ± 6.9 cP (100 s^{-1}) for the 10% (*w/v*) SH:acrylate variations. For the 20% (*w/v*) SH:acrylate variations viscosity was between 880.2 ± 61.6 cP to 1061.4 ± 65.6 cP (10 s^{-1}) and 359.7 ± 41.9 cP to 420.3 ± 20.1 cP (100 s^{-1}).
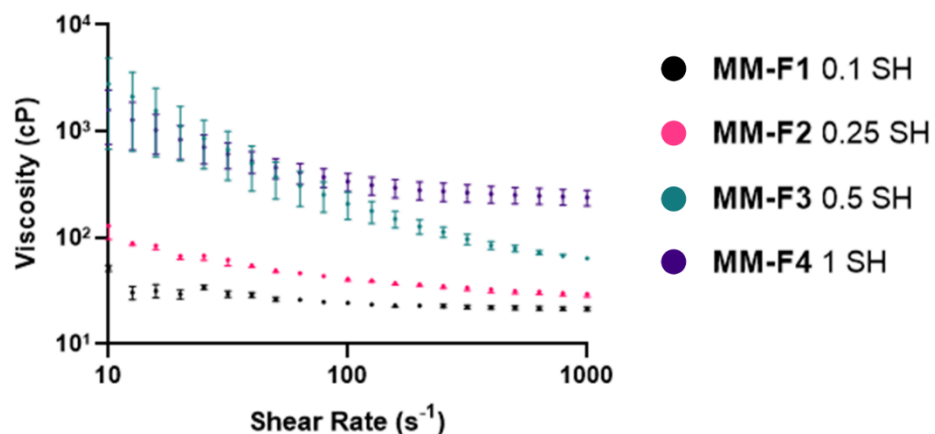
Figure 6.4: Shear rate vs viscosity for PEGDA 575 50% (*v/v*) formulations (MM–F1 to MM–F4). Results denote mean ± S.D (n = 3).
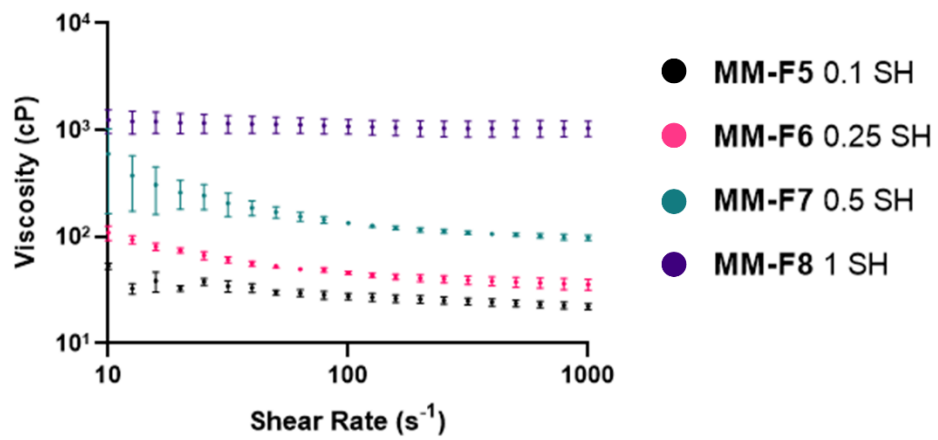
Figure 6.5: Shear rate vs viscosity for PEGDA 700 50% (*v/v*) formulations (MM–F5 to MM–F8). Results denote mean ± S.D (n = 3).
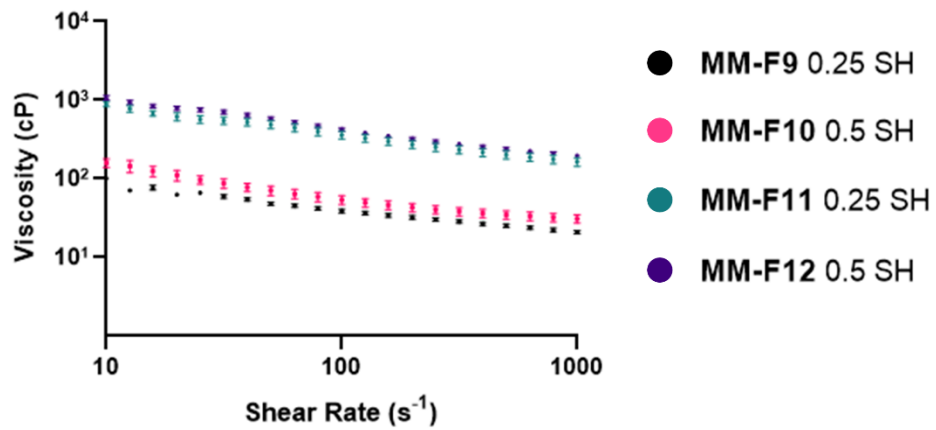
Figure 6.6: Shear rate vs viscosity for PEGDA 575/4000 (1:1) 10% and 20% (*w/v*) formulations (MM–F9 to MM–F12).
Results denote mean ± S.D (n = 3).

6.3.3 DLP Printing

6.3.3.1 Parameter Optimisation

Preparation of formulations that can be initiated via a MM polymerisation mechanism (a combination of CG and SG polymerisation instead of CG only), leads to faster crosslinking. This is due to reactions consisting of two monomer components with reactive groups and functionality to act as crosslinking sites during structure fabrication. It is also widely known that SG polymerisation results in more homogenous end polymer matrices, whereas CG formed networks are dictated by random free radical initiated chain propagation and termination [85,88].

A longer exposure time was adopted for the first two layers of the selected pattern to ensure adequate adhesion to the build platform and provides a foundation for the subsequent layers to be progressively formed in a reliable manner. For printing it was decided simple cuboid structures of 10 x 10 x 2 mm would be produced. This firstly allowed for optimisation of printing parameters relative to each individual formulation prepared. Secondly, this provided a construct that would be replicable for printing samples required for different analyses including matrix mesh size determination, imaging, release studies and mechanical testing. In this study, all print cycles were prepared with a 50 µm individual Z layer height, such that a 2 mm design would equate to 40 layers. Whilst decreasing the Z layer height further, such as 25 µm, may have improved the interlayer adhesion, the improvement may not have outweighed the increase in overall printing time and time of parts under UV, which may impact bioactives incorporated into formulations. A photoabsorber was also introduced into formulations to minimise undesirable crosslinking, such as that outside of the desired printing area, as explained in Chapter 5.

Table 6.5 compares the different time periods of UV exposure optimised for the range of formulations prepared. Determining suitable printing parameters, particularly the UV exposure, is an important aspect of sample fabrication. The addition of a photoabsorber, tartrazine in this case, helped control UV penetration and curing depth to widen applicable processing windows for printing. This in turn gives greater control over print accuracy relative to the

original design input desired; printed samples were measured in the Z direction (n = 10).

Table 6.5: Overview of printing settings utilised for each formulation with corresponding Z height measurements. Results denote mean ± S.D. (n = 10).

Suitable Printing Parameters			
Formulation Code	Bottom Exposure (s) First 2 Layers	Normal Exposure (s)	Z Height (mm)
MM–F1	4	2	2.10 ± 0.08
MM–F2			2.14 ± 0.06
MM–F3			2.15 ± 0.04
MM–F4			2.01 ± 0.08
MM–F5	4	2	2.09 ± 0.05
MM–F6			2.09 ± 0.06
MM–F7			2.07 ± 0.03
MM–F8			1.97 ± 0.11
MM–F9	20	10	2.01 ± 0.04
MM–F10			2.05 ± 0.08
MM–F11	16	8	2.00 ± 0.04
MM–F12			2.01 ± 0.03

Once printing parameters were established, samples were produced for the planned experimental work (swelling, release, imaging and compression testing). Figure 6.7(a-d) displays examples of printed samples of the prepared formulations for PEGDA 575 (MM–F1), 700 (MM–F5), 700 (MM–F8) and 575/4000 (1:1) (MM–F9) respectively. It should be noted that the PEGDA 700 formulation with 1:1 SH:acrylate ratio (MM–F8) was not easily processed within the DLP printed, with the viscosity of the formulation increasing quickly over time in the printing vat and when left without agitation led to gelation. Due to this, a limited number of samples were able to be produced for experimental work and sample use was prioritised for the release study. Hence, tracking of swelling over time (requiring 27 samples for the time period selected) was not able to be conducted for this formulation.
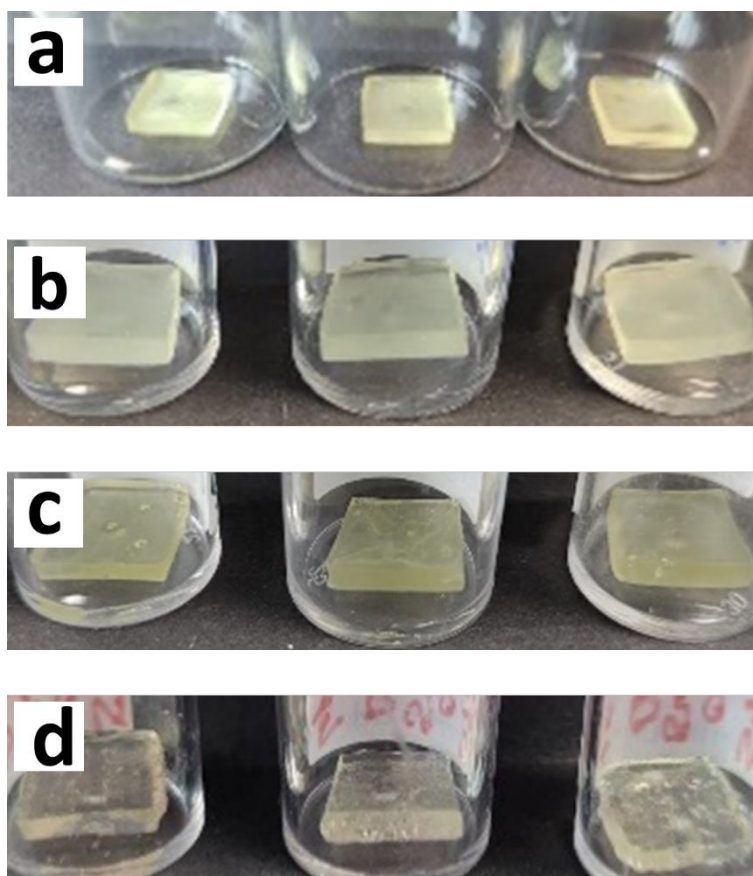
Figure 6.7: Examples of DLP printed 10 x 10 x 2 mm samples of
(a) MM–F1, (b) MM–F5, (c) MM–F8 and (d) MM–F9.

6.3.4 DLP Printed 3D Structures with a Model Protein (BSA) Encapsulated

6.3.4.1 Swelling Ratio and Theoretical Matrix Mesh Size

Swelling ratio and theoretical matrix mesh size is largely dictated by monomer Mn and end polymer concentration in a structure. Further to this, adjusting the DTT:PEGDA ratio in this chapter, and as such the SH:acrylate ratio, it was possible to change the number of hydrolytically labile sites in the printed samples. Increasing SH:acrylate content was expected to lead to greater regions of degradable aspects and hence increase the potential for the matrix mesh to be disrupted and broken down. Swelling was tracked over time to determine the influence of the DTT addition into the PEGDA chain on associated swelling ratio using Equation 3.3 and theoretical matrix mesh size using the equation of a straight line ($y = 0.6375x - 4.251$, $R^2 = 0.99$) established from Figure 5.13, with the results summarised in Table 6.6.

Table 6.6: Overview of the swelling ratio and theoretical matrix mesh size calculations used as comparative tool for MM–F1 to MM–F12. *Values reported to 2 d.p, ** values reported to 1 d.p. Results denote mean ± S.D. (n = 3).

Swelling and Theoretical Matrix Mesh Size			
Formulation Code	Swelling Ratio at Day 1 *	Theoretical Matrix Mesh Size As Printed (Å) **	Theoretical Matrix Mesh Size As Swelled at Day 1 (Å) **
MM–F1	1.05 ± 0.03	0.8	2.6 ± 0.2
MM–F2	1.02 ± 0.01	0.6 ± 0.1	2.4 ± 0.1
MM–F3	1.11 ± 0.02	0.2	3.0 ± 0.1
MM–F4	1.48 ± 0.02	Negligible	5.2 ± 0.1
MM–F5	1.37 ± 0.04	1.3	4.7 ± 0.2
MM–F6	1.49 ± 0.01	0.8 ± 0.1	5.4
MM–F7	1.75 ± 0.03	1.9 ± 0.1	7.1 ± 0.2
MM–F8	Formulation not analysed; samples prioritised for release.		
MM–F9	10.67 ± 0.17	41.4 ± 0.3	63.9 ± 1.1
MM–F10	11.24 ± 0.36	39.4 ± 1.0	67.5 ± 2.3
MM–F11	6.27 ± 0.34	19.6	35.8 ± 2.2
MM–F12	7.05 ± 0.47	18.1 ± 0.2	40.8 ± 3.0

Figure 6.8(a) shows the change in swelling ratio for PEGDA 575 50% (*v/v*) formulations (MM–F1 to MM–F4), with the most obvious change occurring in the first 24 hours when the samples are taking up water and swelling. After 1 day, swelling ratios ranged from 1.02 ± 0.01 to 1.48 ± 0.02. MM–F4 showed a statistically significant difference ($p < 0.0001$) to all formulations. Statistical difference was also observed comparing MM–F3 and MM–F2 ($p < 0.01$) as well as between MM–F3 and MM–F1 ($p < 0.05$). After day 1, variation in swelling ratio was only significant for MM–F4 ($p < 0.05$).

Theoretical matrix mesh size calculated ranged from 2.4 ± 0.1 Å to 5.2 ± 0.1 Å after swelling for 1 day, shown in Figure 6.8(b). Statistical difference was determined between MM–F1 and MM–F3 ($p < 0.05$) and MM–F1 and MM–F4 ($p < 0.0001$). Differences were also shown between MM–F2 and MM–F3 ($p < 0.01$), MM–F2 and MM–F4 ($p < 0.0001$) as well as MM–F3 and MM–F4 ($p < 0.0001$). No significant difference in calculated mesh size formulation was seen from day 1 onwards in the case of each individual formulation. The results compared across the four formulations indicated the SH:acrylate ratio implemented, acting as the singular variable factor, has a significant impact on the final matrix properties of the printed samples. It also supports the rationale that increasing the number of hydrolytically labile areas within a polymer network, and their subsequent degradation in the PBS solution, aligns with increases in the theoretical matrix mesh size. It has also provided one way to compare the changes occurring from the as printed and swelled state of printed samples of different compositions.
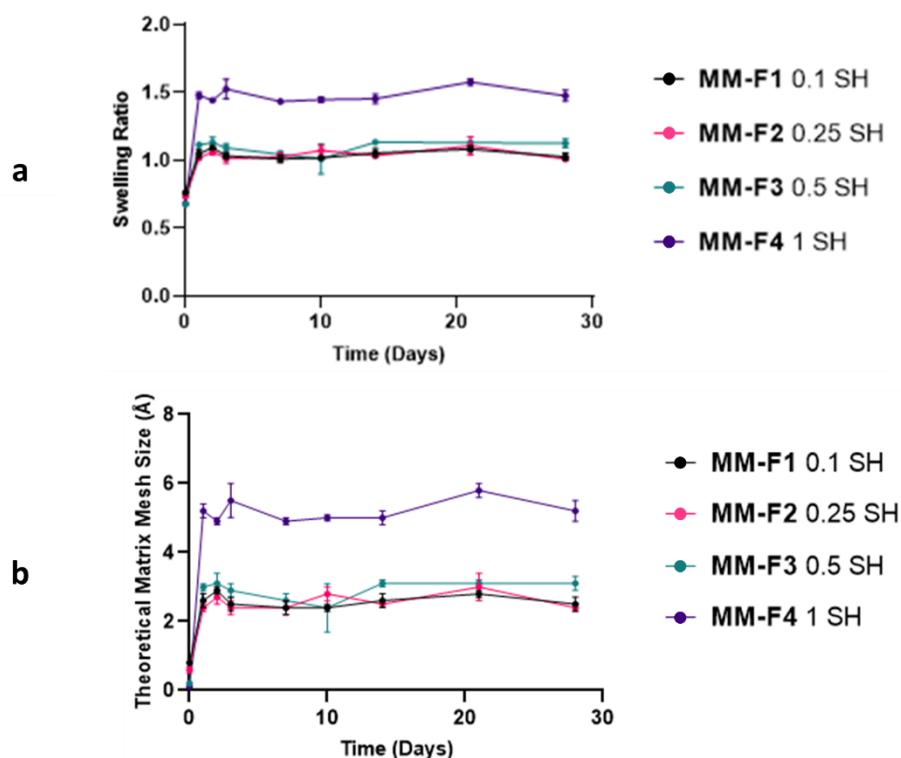
Figure 6.8: Changes in (a) swelling ratio and (b) theoretical matrix mesh size over time for PEGDA 575 50% (*v/v*) formulations (MM–F1 to MM–F4). Results denote mean ± S.D. (n = 3).

Figure 6.9(a) shows the change in swelling ratio with time for PEGDA 700 50% (*v/v*) formulations (MM–F5 to MM–F7), ranging from 1.37 ± 0.04 to 1.75 ± 0.03 after 1 day of swelling. Increased swelling ratios, related to increases in SH:acrylate ratio utilised, were again shown in this sample set. Statistical difference was seen between MM–F5 and MM–F6 ($p < 0.01$), MM–F5 and MM–F7 ($p < 0.0001$) and MM–F6 and MM–F7 ($p < 0.0001$). After day 1, swelling ratio variation was significant in MM–F5 ($p < 0.01$) and MM–F7 samples ($p < 0.05$). As mentioned previously, the reduced number of samples able to be prepared with MM–F8 were prioritised for the release assay studies and hence changes in swelling were not tracked.

Theoretical matrix mesh size calculated for MM–F5 to MM–F7 ranged from 4.7 ± 0.2 Å to 7.1 ± 0.2 Å after 1 day of swelling, as shown in Figure 6.9(b). Statistically significant differences were observed between MM–F7 and MM–F6 ($p < 0.0001$), MM–F7 and MM–F5 ($p < 0.0001$) as well as MM–F6 and MM–F5 ($p < 0.01$). Variation was deemed significant from day 1 to 28 for

MM–F5 (p < 0.01) and MM–F7 (p < 0.05) in the case of tracking each formulation individually. Overall, the associated swelling ratio and theoretical matrix mesh size, as swelled, was higher than the PEGDA 575 equivalent e.g. evaluating MM–F3 versus MM–F7 shows a statistically significant difference for both matrix attributes analysed (p < 0.0001). From these results, it can be seen that a singular change in selected PEGDA Mn, combined with the introduction of increasing SH component, led to different end properties in the polymer matrix of the sample printed.
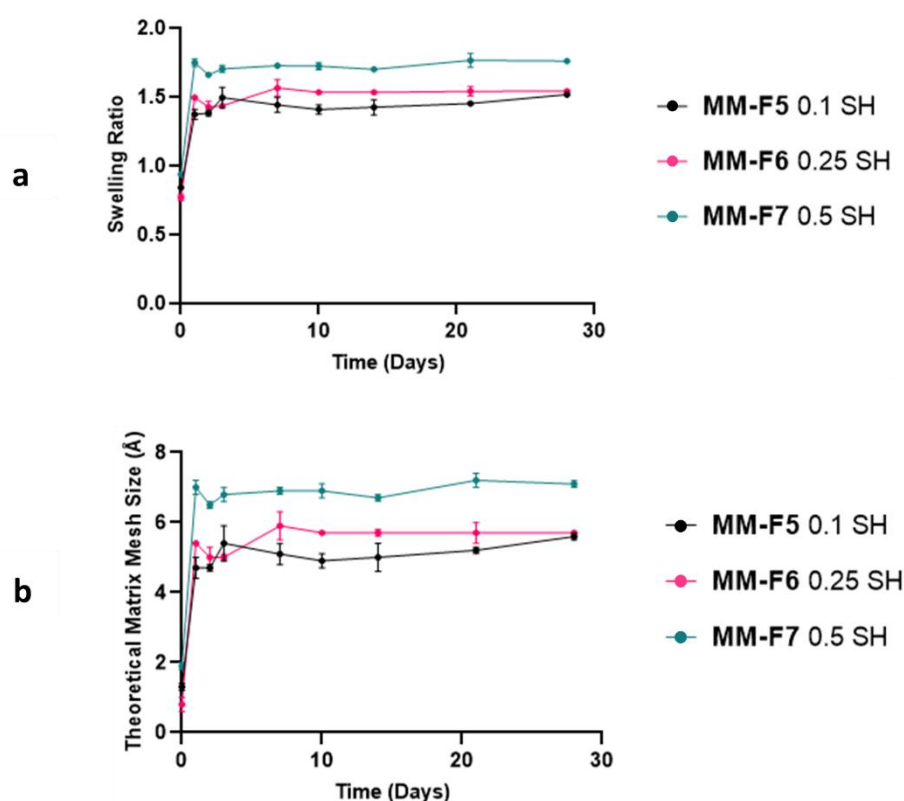
Figure 6.9: Changes in (a) swelling ratio and (b) theoretical matrix mesh size over time for PEGDA 700 50% (*v/v*) formulations (MM–F5 to MM–F7). Results denote mean ± S.D. (n = 3).

A higher PEGDA Mn blend of PEGDA 575/4000 (1:1) was prepared with two SH:acrylate ratios, that were applicable regarding their viscosity for DLP printing and allowed for further comparisons. Figure 6.10(a) firstly shows the change in swelling ratio for PEGDA 575/4000 (1:1) 10% (*w/v*) formulations

(MM–F9 to MM–F10) with values of 10.67 ± 0.17 and 11.24 ± 0.36 reported respectively after 1 day of swelling and were not statistically different. From day 1 onwards, individual variance in swelling ratio was only significant for MM–F9 ($p < 0.01$).

Theoretical matrix mesh sizes at the same time point for these formulations was determined to be 63.9 ± 1.1 Å and 67.5 ± 2.3 Å and not statistically different, as shown in Figure 6.10(b). A significant difference was observed for both matrix properties, compared to formulations MM–F1 to MM–F7 ($p < 0.0001$) at the same time point. Increases in calculated matrix characteristics is likely due to a combination of factors. Predominantly the reduction in polymer content in the formulation, 50% (*v/v*) to 10% (*w/v*), alongside a higher Mn PEGDA blend led to increased starting chain length, which have been further elongated with the addition of DTT when synthesising the PEGDA-DTT macromer. Sample handling and weighing became progressively more difficult of due to the hydrolytic degradation that occurred causing breakdown of the sample structures into smaller fragments.

Due to the significant effect on the printed matrix, achieved through a PEGDA 575/4000 (1:1) blend and lowering the polymer content in the formulation to 10% (*w/v*), it was decided to also consider a 20% (*w/v*) of the same PEGDA blend with the same SH:acrylate ratios of 0.25 and 0.5 (MM–F11 and MM–F12). Figure 6.10(a) shows the swelling ratio changes, which after 1 day were 6.27 ± 0.34 and 7.05 ± 0.47 respectively and were not statistically different from each other. Both values were significantly lower than that of MM–F9 and MM–F10 ($p < 0.0001$).

Significantly lower values ($p < 0.0001$) were also calculated for the theoretical matrix mesh size, whereby MM–F11 and MM–F12 were 35.8 ± 2.2 Å and 40.8 ± 3.8 Å respectively after 1 day of swelling but were not statistically different from each other, summarised in Figure 6.10(b). Values did not vary significantly over the remaining days tracked. To note, MM–F11 and MM–F12 samples were still significantly different for both attributes analysed compared to that of the lower Mn PEGDA formulations MM–F1 to MM–F7.

In this study, Peppas-Merrill theoretical matrix mesh principles have been implemented and have acted as a comparative tool between the formulations prepared. This has allowed for the evaluation of selected formulation changes in relation to final matrix properties. These characteristics are later linked with quantitative release of encapsulated model proteins alongside cryo-SEM imaging and compression testing in Sections 6.3.4.2 – 6.3.4.8.
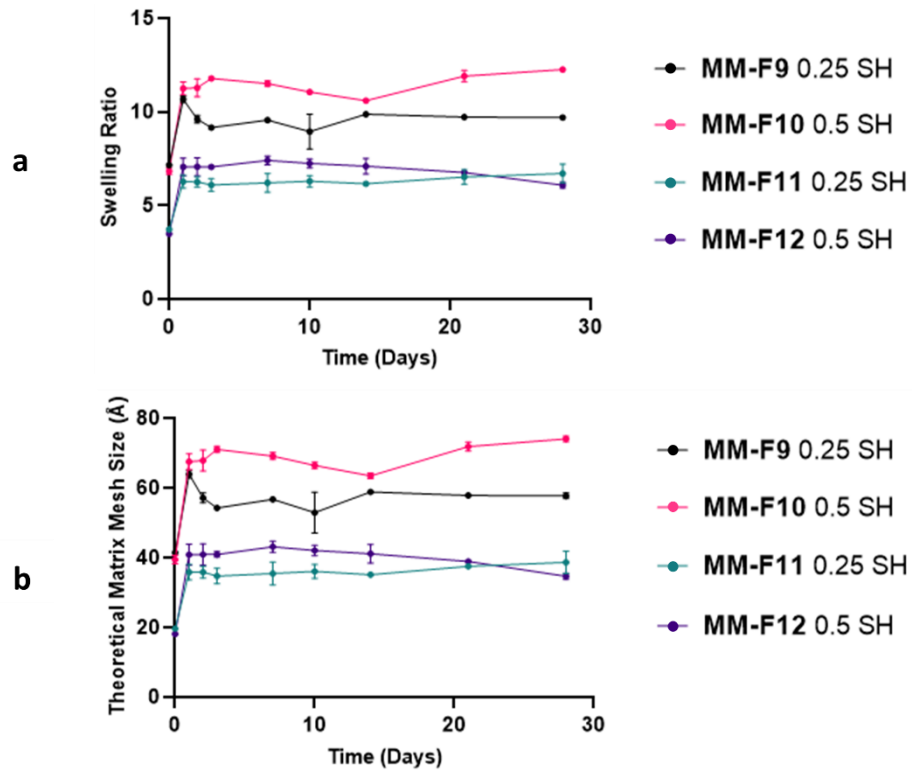
Figure 6.10: Changes in (a) swelling ratio and (b) theoretical matrix mesh size over time for PEGDA 575/4000 (1:1) 10% and 20% (*w/v*) formulations (MM–F9 to MM–F12). Results denote mean ± S.D. (n = 3).

6.3.4.2 BSA Release from DLP 3D Printed Structures using PEGDA-DTT Macromers

Using the printed structures prepared through optimisation of printing exposure settings, it was possible to conduct the necessary *in vitro* release study under simulated conditions for subcutaneous implantation (pH 7.4 at 37°C) [57]. It was also decided that the loading of BSA would be increased from 1 mg/mL to 5 mg/mL, with 1000 µg encapsulated per 10 x 10 x 2 mm sample. The reasoning behind this was to allow for longer periods of release to be studied, as was shown to influence the amount released from the CG–F6 samples in Chapter 5.

Figure 6.11 shows the cumulative BSA release for samples prepared using the different PEGDA 575 50% (*v/v*) based formulations with varying DTT additions, and thus SH:acrylate ratio. For MM–F1 to MM–F4, the increase in SH content in the formulation corresponded with increased % of BSA release, ranging from 8.3 ± 1.1% of total BSA loading for MM–F1 to 22.8 ± 10.1% for MM–F4. In addition, these low levels of release were observed over relatively short periods before plateau and no further release between 7 and 28 days. However, protein was released compared to the equivalent PEGDA 575 CG formulations explored previously where no significant release was detected. Also, the S.D. between samples prepared using MM–F4 was not desirable.

Formulations with PEGDA 700 at 50% (*v/v*) with the same SH:acrylate ratios (MM–F5 to MM–F8) allowed for comparisons to be made in the two sets of lower PEGDA Mn formulations. Similar issues were presented that were observed with the PEGDA 575 formulations. Initial release of the encapsulated BSA was achieved but again was not sustained, apart from for MM–F8 where release of the total loaded BSA was achieved over 56 days. However, it must be noted again that this formulation had issues with gelation during printing and approximations of matrix mesh size were not calculated. Arguably, the matrix was suitable to allow for release and it can be inferred that it would be greater than those calculated for MM–F1 to MM–F7. Increases in the DTT SH addition again led to increased durations of BSA release being observed between 7 and 56 days from MM–F5 to MM–F8 respectively. Figure 6.12(a)(b) displays the information reported for these formulations.
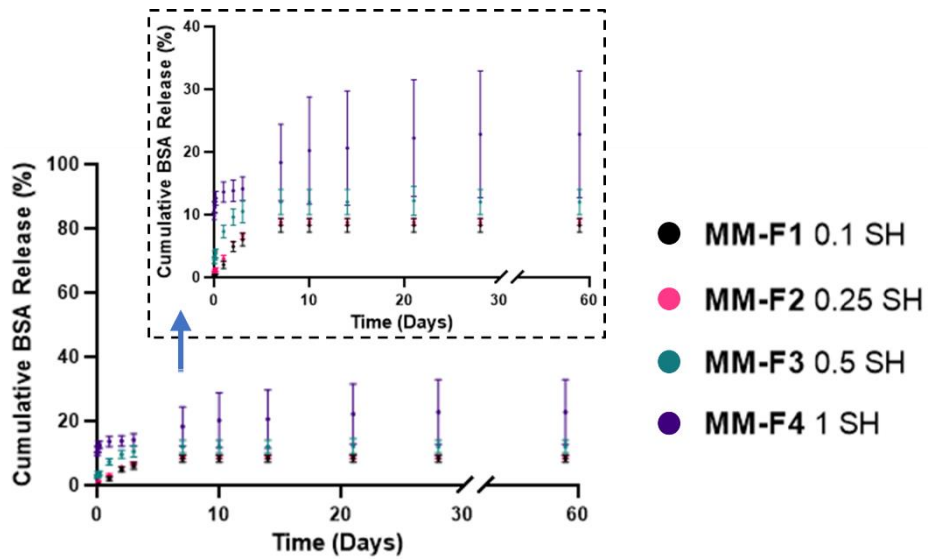
Figure 6.11: Cumulative BSA release profiles obtained from printed samples comprised of PEGDA 575 50% (*v/v*) formulations (MM–F1 to MM–F4). Results denote mean ± S.D. (n = 3).
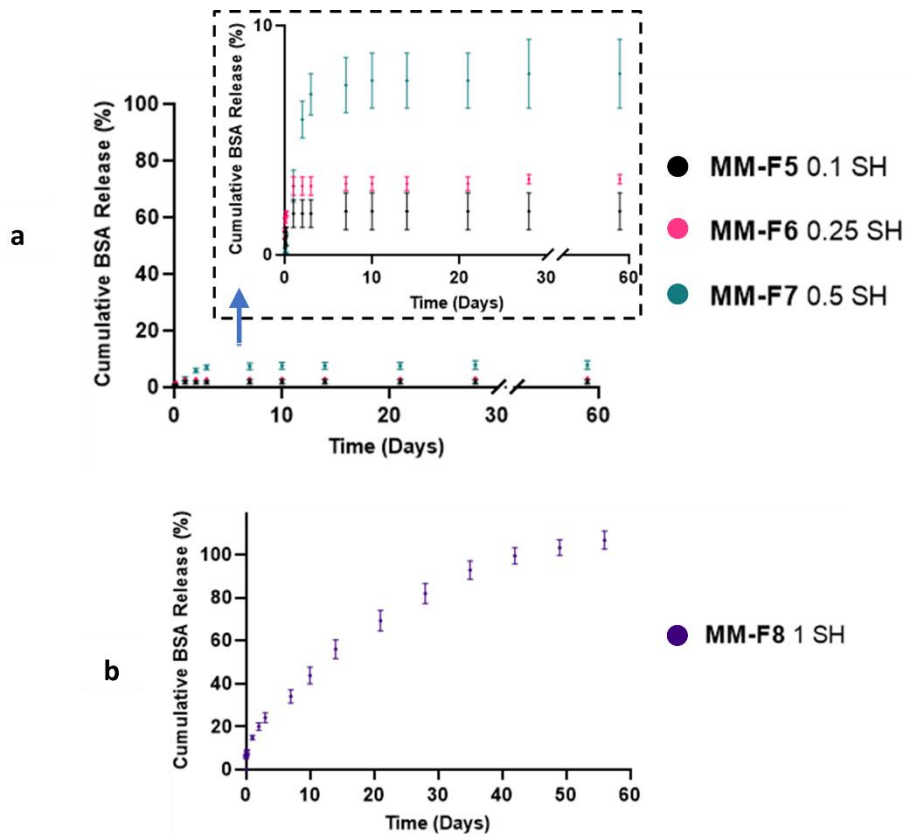
Figure 6.12: Cumulative BSA release profiles obtained from printed samples comprised of (a) PEGDA 700 50% (*v/v*) formulations (MM–F5 to MM–F7) and (b) MM–F8. Results denote mean ± S.D. (n = 3).

It was shown previously in Section 6.3.1 using as-cast samples, that a higher starting Mn PEGDA and addition of DTT resulted in sample breakdown and release of BSA within 9 days. Hence, to try and achieve further release it was proposed that the higher Mn PEGDA 575/4000 (1:1) blend at lower polymer concentrations could be utilised. Figure 6.13 shows the graph plot for the combined results of the printed blends at 10% and 20% (*w/v*) with 0.25 and 0.5 SH:acrylate ratios to allow for comparison. To summarise, release of BSA through these changes was able to be achieved lasting 70 days (MM–F10), 91 days (MM–F12), 105 days (MM–F9) and 112 days (MM–F11). Starting theoretical matrix mesh size determined previously for the PEGDA 575/4000 (1:1) 10% (*w/v*) (MM–F10) in the as printed state was similar to that of the swelled state of the PEGDA 575/4000 (1:1) 20% (*w/v*) (MM–F12). This reinforces the influence of changing initial monomer% (*w/v*) on matrix characteristics in relation to the rate and duration of BSA release. Therefore, a balance between these factors and changing the Mn of the backbone monomer can significantly change delivery and could be modulated and tuned as desired through these variations in composition. To determine the mechanism(s) of the BSA release achieved it was decided that the assay data collected would be applied to a range of release kinetic mathematical models, documented in Section 6.3.4.3.

Importance of the initial PEGDA Mn selected was highlighted in the lower Mn formulation printed samples (PEGDA 575 and 700 variations, MM–F1 to MM–F8) where in most cases, barring MM–F8, the BSA loaded was predominantly entrapped. In comparison, the PEGDA 575/4000 blend variations (MM–F9 to MM–F12) allowed full elution over extended periods of up to ~3+ months. The concentration of polymer volume fraction in the printed samples contributed to this difference, reducing from 50% (*v/v*) to 20% and 10% (*w/v*). Although release was able to be modulated, a particular limitation of utilising PEGDA-DTT macromers is the corresponding increase in the overall chain Mn and Mw as shown in Section 6.3.2.1. This can provide complications with viscosity, whereby a PEGDA 575/4000 (1:1) 0.8 SH:acrylate formulation could not be printed within the DLP setup. This formulation's degradation and release duration was also not desirable in the

context of achieving extended release (weeks/months) of BSA. However, delivery of larger bioactive components from a 3D printed construct may necessitate the need for larger matrix mesh sizes, which would require the use of higher Mn PEGDA blends and/or increased DTT additions in relation to SH:acrylate ratios.
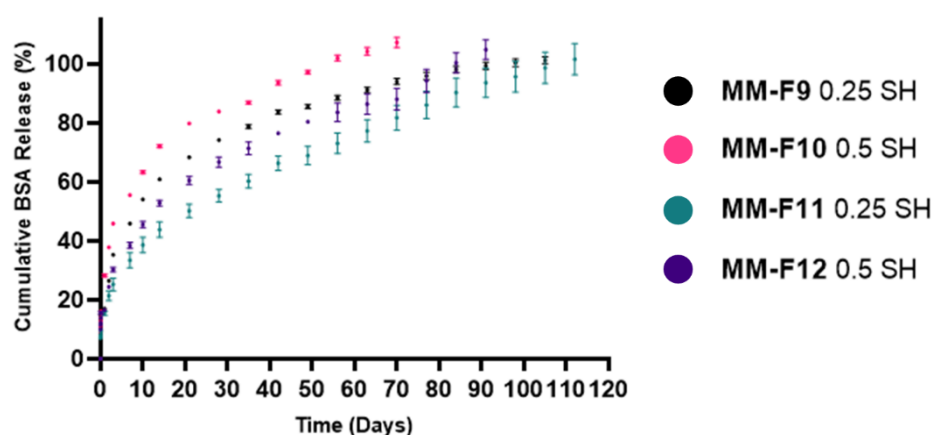
Figure 6.13: Cumulative BSA release profiles obtained from printed samples comprised of PEGDA 575/4000 (1:1) 10% and 20% (*w/v*) formulations (MM–F9 to MM–F12). Results denote mean ± S.D. (n = 3).

6.3.4.3 Fitting of Release Kinetic Mathematical Models

The release mechanisms for the printed samples studied for BSA release were evaluated further by applying release kinetic models. This included zero-order, first-order, Higuchi and Korsmeyer-Peppas with comparisons made between the models using the square of the correlation coefficient (R^2) summarised for best fit in Table 6.7. In this section, PEGDA 575:4000 (1:1) 10% and 20% (*w/v*) (MM–F9 to MM–F12) have been evaluated.

6.3.4.3.1 Zero-Order

Attaining zero-order release was deemed a common industrial objective in Chapter 2.3. Consistent regular dosing throughout the entirety of the delivery device release can be beneficial in achieving therapeutic benefit with minimal side effect [62,204]. Figure 6.14(a) displays the application of the zero-order model to formulations MM–F9 to MM–F12, using linear regression and R^2 values reported as 0.804, 0.810, 0.918 and 0.893 respectively. Whilst this

model was not the best fit compared to the other models applied, it is interesting to note that from day 28, 10, 2 and 7, for the same formulations respectively, onward release remained near constant with $R^2 > 0.95$, as shown in Figure 6.14(b). The increase in polymer blend% (*w/v*) and decrease in SH:acrylate content minimised the period of time until BSA release became more constant and sustained.
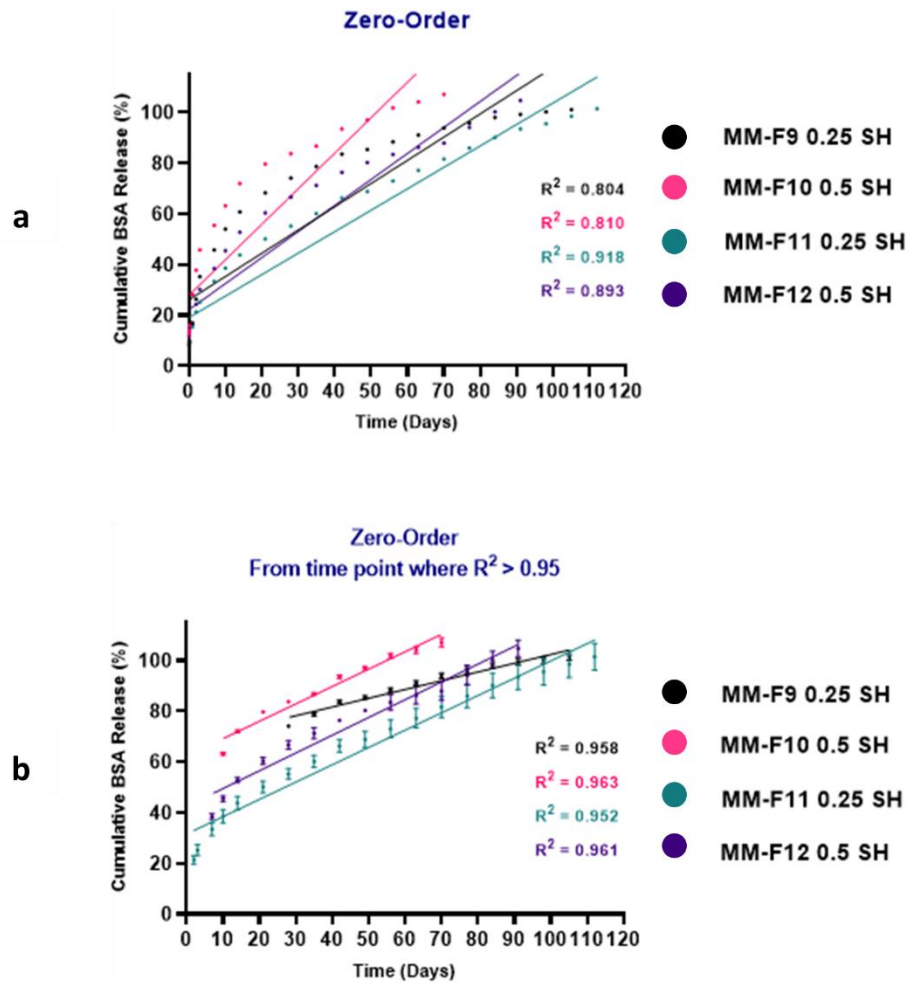
Figure 6.14: (a) Zero-order release kinetics for MM–F9 to MM–F12 and (b) zero-order kinetics fitted from time points where $R^2 > 0.95$.

6.3.4.3.2 First-Order

For the release from MM–F9 and MM–F10 samples, the first-order model was deemed the best fit out of the models applied. The R^2 values were 0.981 and 0.974 respectively, with all formulations shown in Figure 6.15. The rate of release is dictated by changes in concentration of the BSA with respect to

change in time and could explain why the initial rate of release in the first few days of release is higher than later on in the time period assessed.
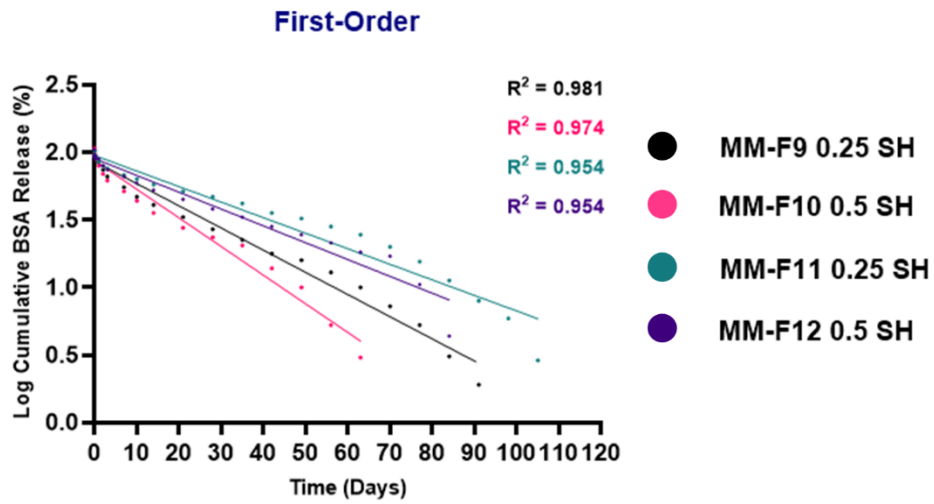
First-Order

Figure 6.15: First-order release kinetics for MM–F9 to MM–F12, with the associated R^2 values.

6.3.4.3.3 Higuchi

The Higuchi model assumes that the initial concentration of a loaded bioactive in the printed sample is higher than the bioactive solubility. For the release from MM–F11 and MM–F12 samples this was deemed the best fit out of the models applied with R^2 values of 0.997 and 0.989 respectively, shown in Figure 6.16.
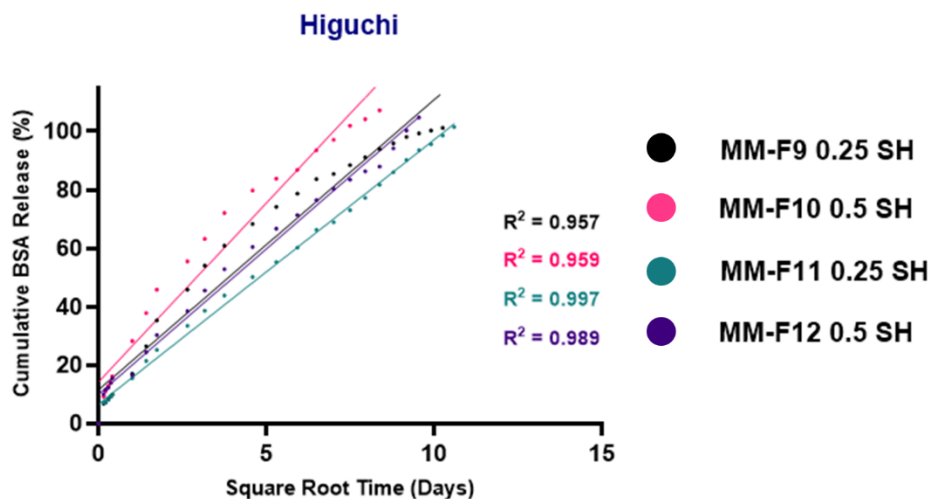
Higuchi

Figure 6.16: Higuchi release kinetics for MM–F9 to MM–F12, with the associated R^2 values.

6.3.4.3.4 Korsmeyer-Peppas

The Korsymeyer-Peppas model can typically be applied when the mechanism of release is less understood or when multiple mechanisms may contribute, such as a combination of diffusion and degradation. It has also been reported previously that the fit should be applied for the first 60% of cumulative release [205,206]. Figure 6.17 shows the application Korsmeyer-Peppas release kinetic model to the formulations with R^2 values for MM–F9 and MM–F10 0.974 and 0.936 respectively, with corresponding n values between 0.5 and 1 of 0.621 and 0.501. This suggested release occurs through non-Fickian transport, which can be attributed to a combination of diffusion and erosion. For these samples, this could be associated with the initial swelling period alongside disruption of the lower % (*w/v*) polymer matrix through hydrolytic degradation of the PEGDA-DTT macromers utilised. For MM–F11 and MM–F12, R^2 values were 0.982 and 0.970 respectively with n values < 0.5; 0.462 and 0.426. This suggests release was governed by Fickian diffusion and that the process of diffusion of the BSA was driven by the concentration gradient between sample and release media.
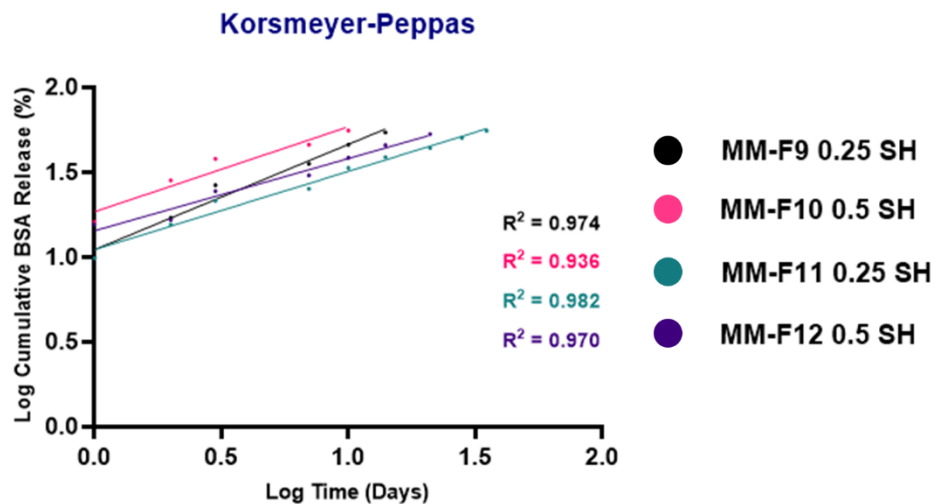
Figure 6.17: Korsmeyer-Peppas release kinetics for MM–F9 to MM–F12, with the associated R^2 values.

Table 6.7: Overview of R^2 and n values for release kinetic models of zero-order, first-order, Higuchi and Korsmeyer-Peppas (MM–F9 to MM–F12).

Fitting of Release Kinetic Models to MM–F9 to MM–F12				
Formulation Code	Zero-Order	First-Order	Higuchi	Korsmeyer-Peppas
MM–F9	0.804	**0.981**	0.957	0.974 n = 0.621
MM–F10	0.810	**0.974**	0.959	0.936 n = 0.501
MM–F11	0.918	0.954	**0.997**	0.982 n = 0.462
MM–F12	0.893	0.954	**0.989**	0.970 n = 0.426

6.3.4.4 Cryo-SEM Imaging for Visual Comparison of DLP Printed Samples

Matrix mesh size calculations indicated that morphological changes occur within the printed PEGDA-DTT samples. For example, calculated values in all cases increased after swelling. For this analysis, sacrificial samples of the PEGDA 575/4000 (1:1) blends at 10% and 20% (*w/v*) (MM–F9 to MM–F12) were printed. Imaging at both day 0 (as printed) and then hydrolytically degraded has provided a visual confirmation of matrix disruption. The influence of the higher Mn blend at lower concentrations with adequate SH:acrylate additions showed structural changes after hydrolytic degradation. Figure 6.18(a-d) shows examples of samples in the as printed state prior to their degraded state in Figure 6.18(e-h). This confirms the findings and differences reported previously regarding the swelling ratio and theoretical matrix mesh size, which were statistically significantly different to the lower Mn PEGDA formulations. For formulations MM–F9 to MM–F12 the ability to create more open and disrupted polymer matrix networks, achieved through degradation once swelled, led to sustained BSA release. This mechanism of achieving release is promising for implantable devices, particularly for long-term delivery applications where there is potential to avoid the requirement for

implant extraction after elution ends. Cryo-SEM imaging has aided in demonstrating the effect of changes in formulation composition related to comparative matrix characteristics, and importantly release characteristics.
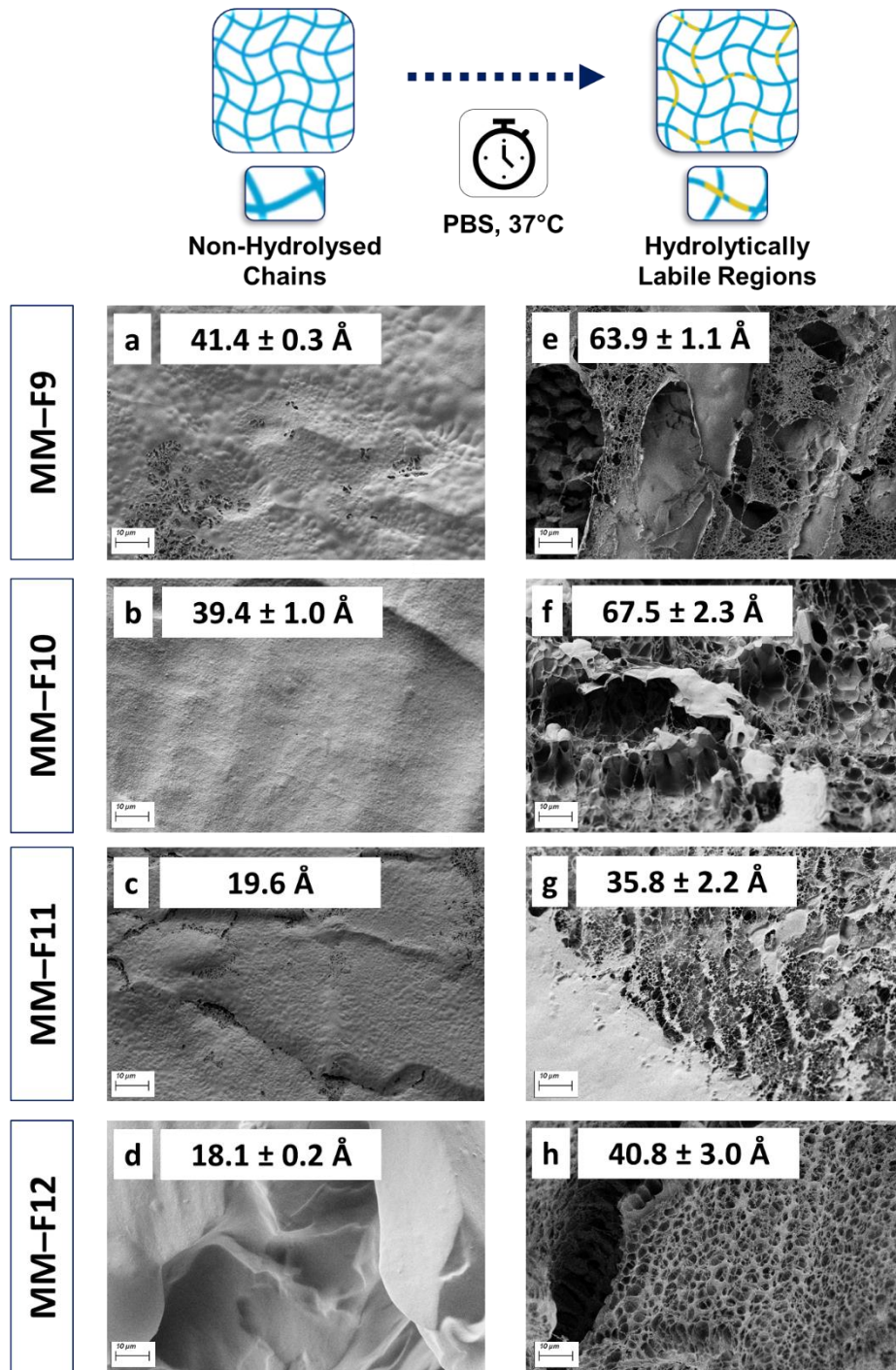
Figure 6.18: Cryo-SEM imaging of MM–F9 to MM–F12 samples in the as printed state (a-d) and degraded state (e-h) with the corresponding theoretical matrix mesh size calculated at day 1. Results denote mean ± S.D. (n = 3). Scale bar 10 µm.

6.3.4.5 Texture Analyser Compression Testing for Mechanical Comparison of DLP Printed Samples

A texture analyser was used to provide a mechanical properties comparison between samples DLP printed with the formulations prepared within this chapter. Samples were evaluated for their compressive Young's modulus in the as printed state and, if applicable, after swelling in PBS at 37°C for 1 day.

Figure 6.19(a) compares the PEGDA 575 50% (*v/v*) formulations with increasing SH:acrylate ratios (MM–F1 to MM–F4) in the as printed state. Significant differences applicable have been shown, with the general trend being a decrease in compressive Young's modulus with increasing SH:acrylate content and ranged from 22.5 ± 0.3 to 16.5 ± 1.7 kPa. Figure 6.19(b) shows the compressive modulus for MM–F4 decreased significantly ($p < 0.01$) from 16.5 ± 1.7 kPa in the as printed state to 13.3 ± 0.3 kPa when swelled. This is likely due to increased hydrolytically labile regions and aligns with greater changes established in theoretical matrix mesh size. This led to increased release of BSA when comparing to the other PEGDA 575 based formulations. For MM–F1 to MM–F3 the difference in compressive modulus between the as printed and swelled sample state was not significant.

Figure 6.20(a) compares the compressive modulus determined for the PEGDA 700 50% (*v/v*) formulations (MM–F5 to MM–F8) in the as printed state. The same trend of decreasing Young's modulus with increased SH:acrylate ratio continued, ranging from 20.2 ± 0.4 to 9.9 ± 0.2 kPa in the as printed state. Similarly, to the PEGDA 575 formulations, negligible differences were observed for SH:acrylate ratios from 0 – 0.5 (MM–F5 to MM–F7). However, MM–F8 with an SH:acrylate ratio of 1:1 corresponded with a statistically significant decrease in compressive modulus ($p < 0.0001$) as shown in Figure 6.20(b). This potentially provides reasoning why samples fabricated using MM–F8 were able to achieve release of BSA for a significantly longer period (56 days) than the other PEGDA 700 based formulations.
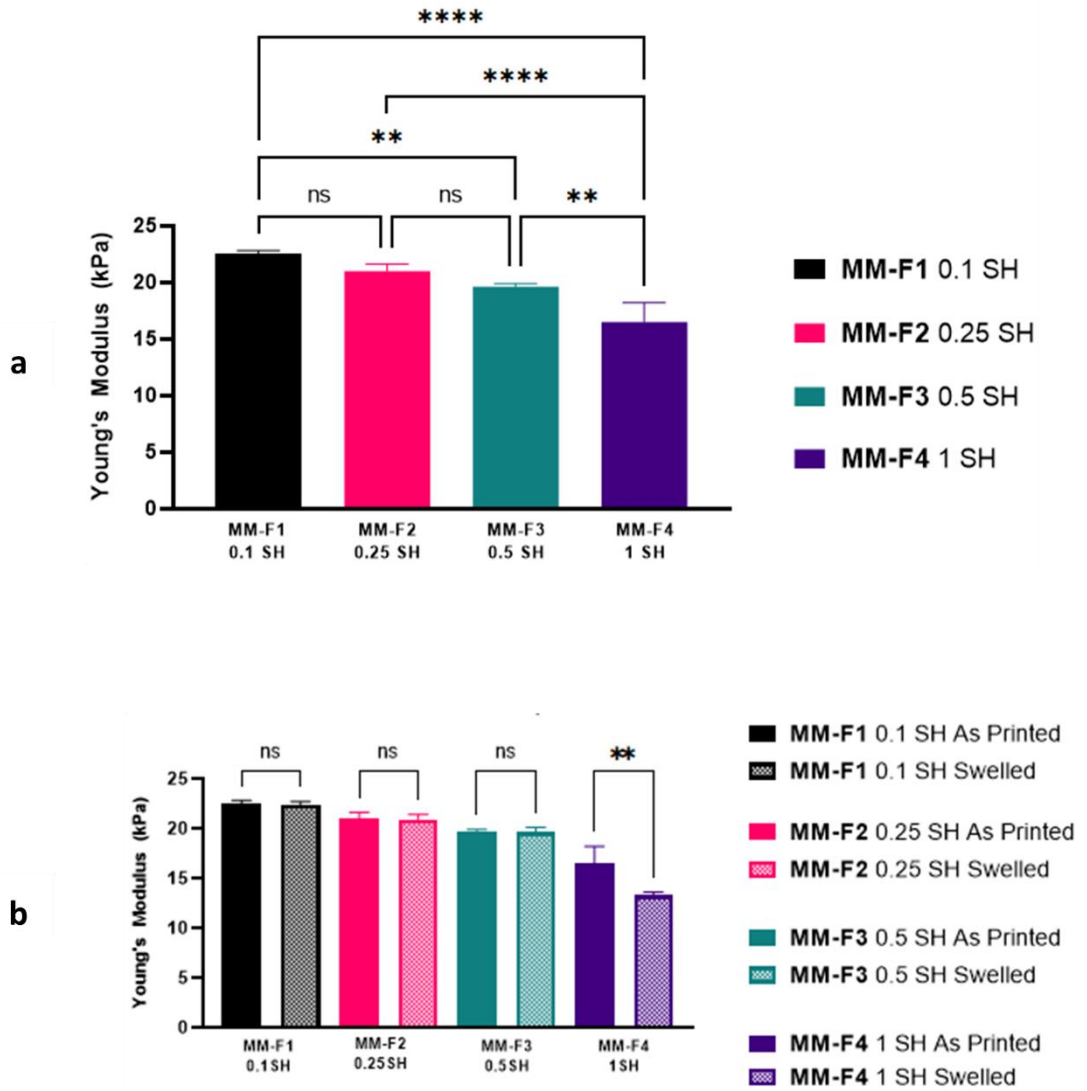
Figure 6.19: (a) Compressive Young's modulus values for PEGDA 575 50% (*v/v*) samples (MM–F1 to MM–F4) in the as printed state and (b) comparisons between as printed and swelled state. Results denote mean ± S.D. (n = 3).
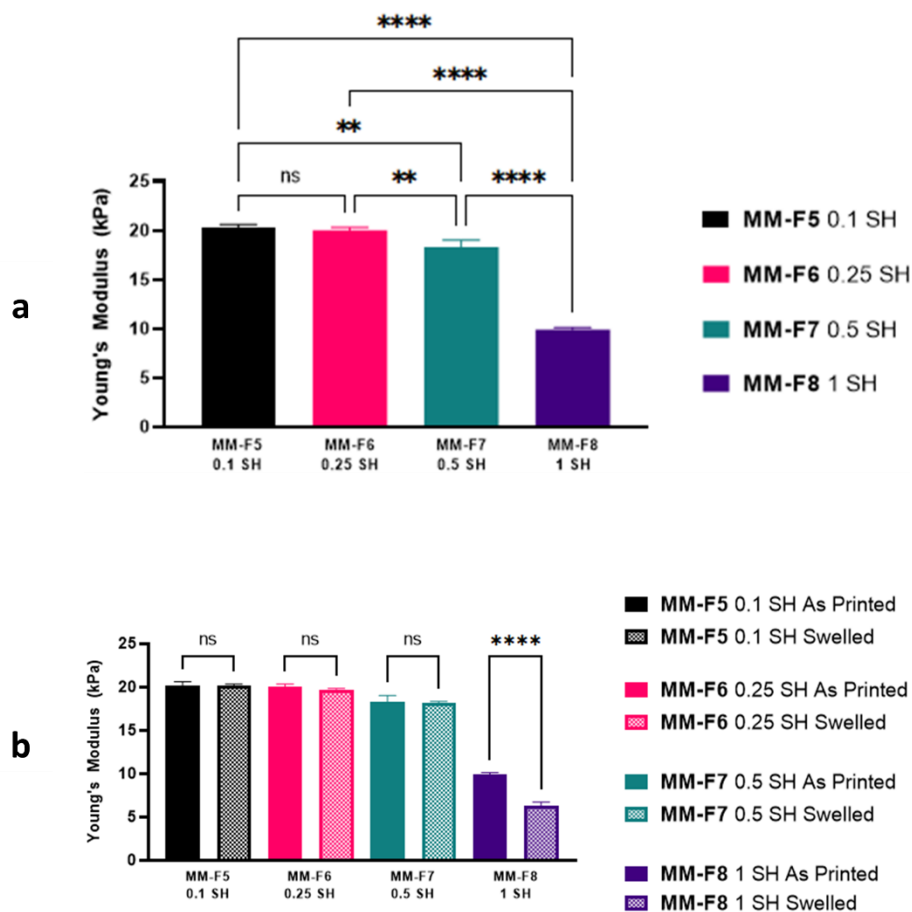
Figure 6.20: (a) Compressive Young's modulus values for PEGDA 700 50% (*v/v*) samples (MM–F5 to MM–F8) in the as printed state and (b) comparisons between as printed and swelled state. Results denote mean ± S.D. (n = 3).

Differences between the 10% and 20% (*w/v*) PEGDA 575/4000 (1:1) formulations (MM–F9 to MM–F12) in the as printed state are shown in Figure 6.21(a), where MM–F11 was statistically significantly different. This was also the case when comparing the as printed state to the swelled state with the Young's modulus decreasing from 5.8 ± 0.6 to 4.4 ± 0.3 kPa ($p < 0.001$) in Figure 6.21(b). The other samples did not show any significant difference between as printed and swelled. Overall MM–F9 to MM–F12 prepared with lower monomer% (*w/v*) are weaker mechanically in both the as printed and swelled state when compared to that of PEGDA 575 and 700 formulations with higher monomer content, 50% (*v/v*) versus 10% and 20% (*w/v*). This information provides additional reasoning for why increased theoretical matrix mesh sizes were calculated, leading to release of BSA (70 to 112 days).
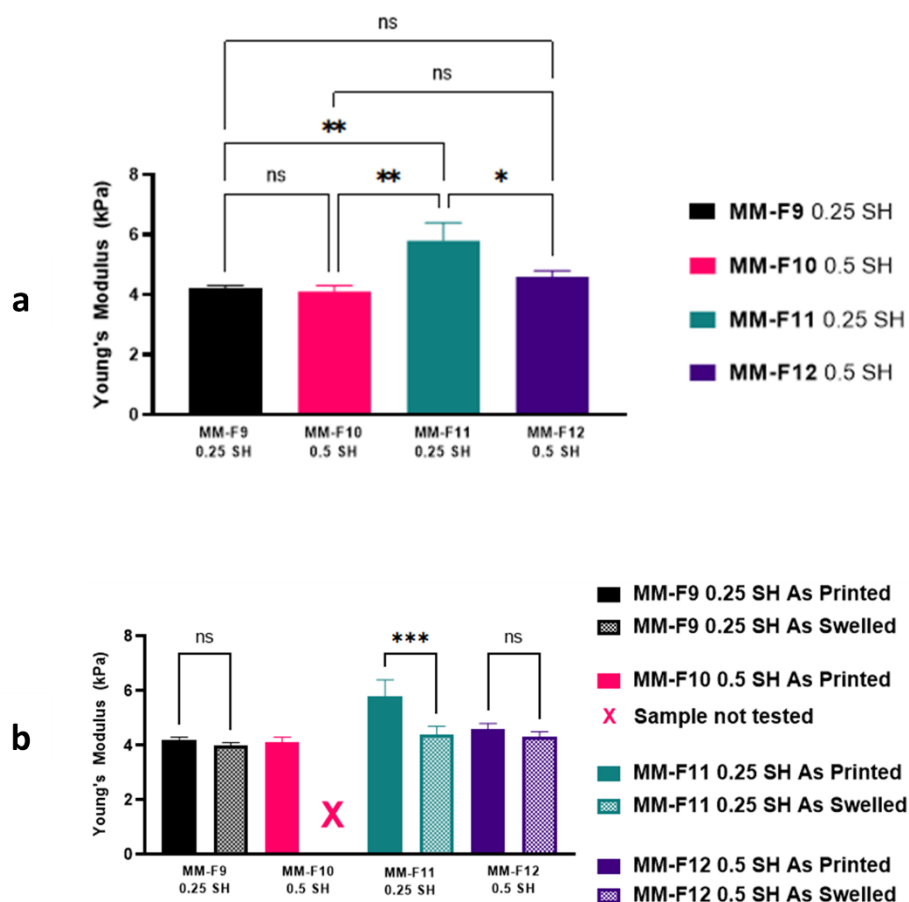
Figure 6.21: (a) Compressive Young's modulus values for PEGDA 575/4000 (1:1) 10% and 20% (*w/v*) samples (MM–F9 to MM–F12) in the as printed state and (b) comparisons between as printed and swelled state. Results denote mean ± S.D. (n = 3).

For clinical end applications, a balance between mechanically suitable structures for implantation and desirable delivery characteristics in-situ is required. These two ideal attributes are, in the case of the PEGDA work shown, inversely related. For example, the lower Mn PEGDA with higher % (*w/v*) in formulations and lower SH:acrylate ratios corresponded with higher compressive Young's modulus but largely had limited and unsustained release. On the other hand, higher Mn PEGDA formulations with low % (*w/v*) and increased SH:acrylate ratios led to extended release but compromised the compressive Young's modulus. Appendix: Supplementary Information Table S.8 provides a summarised table of values reported. Surrounding tissue will impart a combination of compressive and tensile loads onto the implanted hydrogels [130]. The selection of formulation, and the resulting end

implantable structure, would be dependent on the implantation site and application. The work contained within this section has highlighted factors that must be evaluated further, addressed in Chapter 7.

6.3.4.6 Influence of Loading (1, 2.5 and 5 mg/mL) on BSA Release

After establishing the release associated with variation in formulation composition prepared for DLP printing and making associations with structural characteristics, it was decided to conduct a study to check the effect of protein loading. Again, BSA was utilised as the model protein for comparison. The previous composition of a PEGDA 575/4000 (1:1) 10% (*w/v*) blend with a 0.5 SH:acrylate ratio (MM–F10) and 5 mg/mL BSA loading achieved release over an extended time frame of 70 days.

Figure 6.22(a) shows the cumulative release (%) profiles seen for each loading scenario and Figure 6.22(b) cumulative release (µg). Loading of 1, 2.5 and 5 mg/mL of BSA corresponded with a theoretical loading of 200, 500 and 1000 µg per printed sample of 10 x 10 x 2 mm. BSA release periods ranged from 14 to 70 days, with time of release extended with an increase in µg BSA encapsulated within a structure. Higher loading corresponds with a higher probability of freely available BSA to be released, which is exemplified particularly at the initial stages of the release e.g. days 0 to 7. From the results, there could be potential to produce delivery devices with a gradient of bioactive loading concentration through multi-material printing. For example, more central areas of an implant could be loaded with a higher protein concentration than the outer region. This would help minimise initially higher uncontrolled rates of release and shorten the time period until more constant rates are achieved.
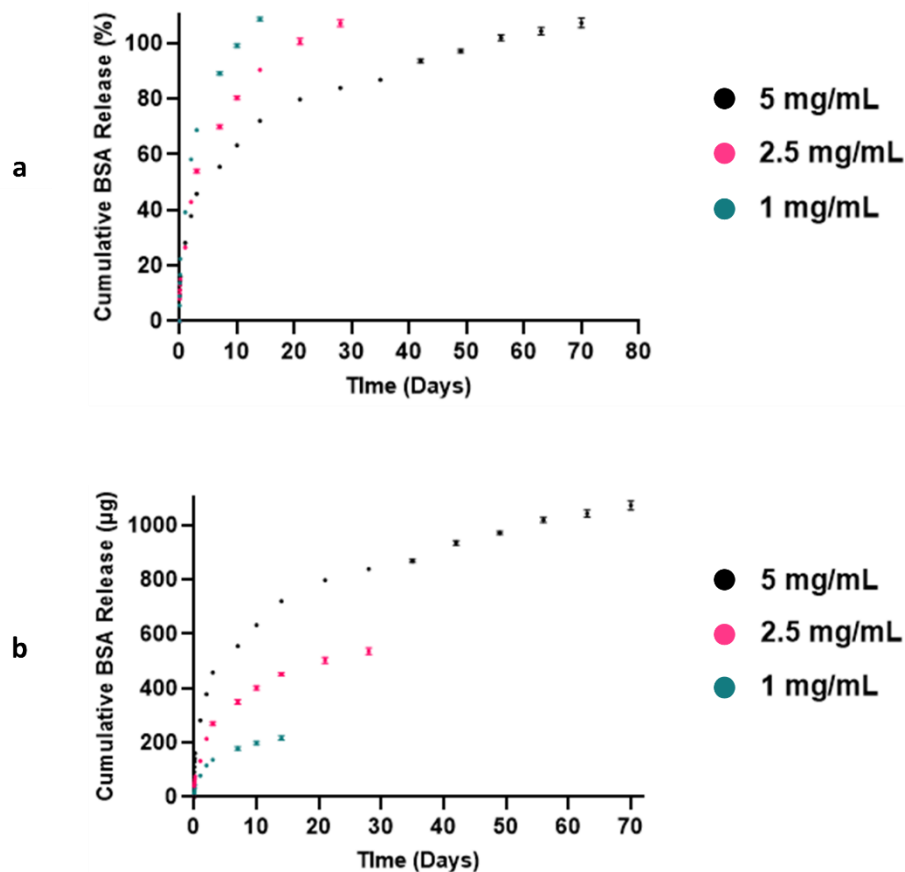
Figure 6.22: (a) Cumulative release (%) and (b) cumulative release (µg) of BSA for each loading of scenario of 1, 2.5 and 5 mg/mL released from PEGDA 575/4000 (1:1) 10% (*w/v*) 0.5 SH samples (MM–F10). Results denote mean ± S.D. (n = 3).

6.3.4.7 Influence of Geometry of DLP Printed Samples on BSA Release

As indicated within the literature review, the use of 3D printing has advantages of being able to easily change geometries and the ability to print different geometries within the same printing cycle [112]. Sections 6.3.1 to 6.3.4.6 provide narrative for the development of formulations suitable for DLP printing and the progression towards achieving release of BSA over sustained periods. This was successful and it was decided that changes in surface area to volume (SA/V) ratio would be explored, as this has seen previous success for tuning release of small molecule APIs. It was also proposed that increased SA would allow greater contact between the printed structure and the PBS release media it was releasing into and increase interaction with the hydrolytically labile regions of the polymer matrix [207].

Results from the previous sections in this chapter utilised geometry A (block). Four additional geometries (B–E) were prepared using PEGDA 575/4000 (1:1) 20% (*w/v*) 0.5 SH:acrylate (MM–F12) with 5 mg/mL BSA loading, as outlined previously in Section 6.2.3 Table 6.2. Examples of the design patterns and printed outcomes are shown in Figure 6.23.

Geometry A (block)	Geometry B (window)	Geometry C (waffle)	Geometry D (snowflake)	Geometry E (rod)
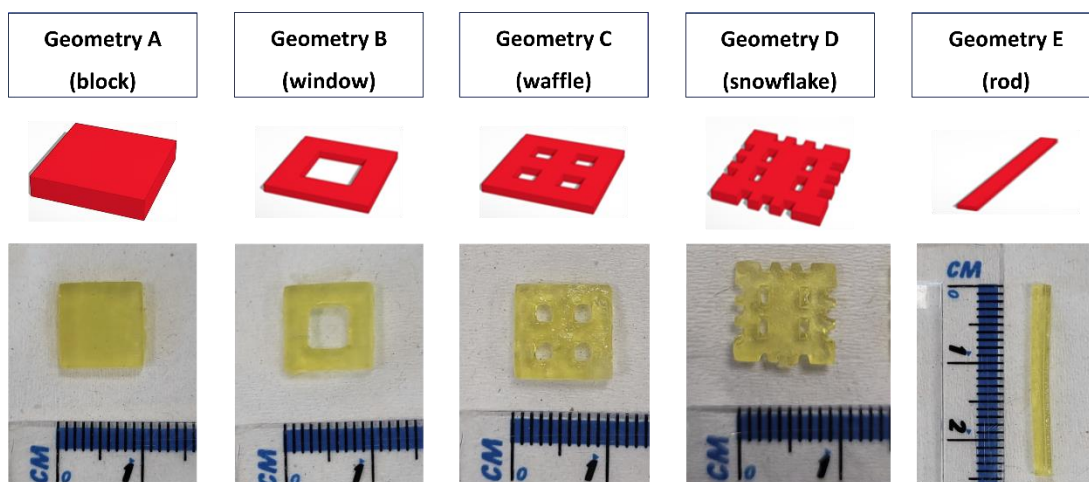
Figure 6.23: Examples of the design patterns for geometries A to E and the respective printed outcomes using MM–F12.

Figure 6.24(a) shows the associated cumulative BSA release as a % of total theoretical loading and Figure 6.24(b) shows the cumulative release in terms of µg quantity for the geometries A-E prepared. The previously assessed geometry A (block) with a SA/V ratio of 1.40 acted as a basis for comparison. It was observed that geometry E (rod shape) with the highest SA/V ratio of 2.08 corresponded with the fastest release rates. Due to its smaller volume, total release of the BSA encapsulated with 5 mg/mL loading was achieved over 42 days. For the samples produced with geometry A (block), the rate of release of total loaded BSA (%) remained the longest in duration (91 days).
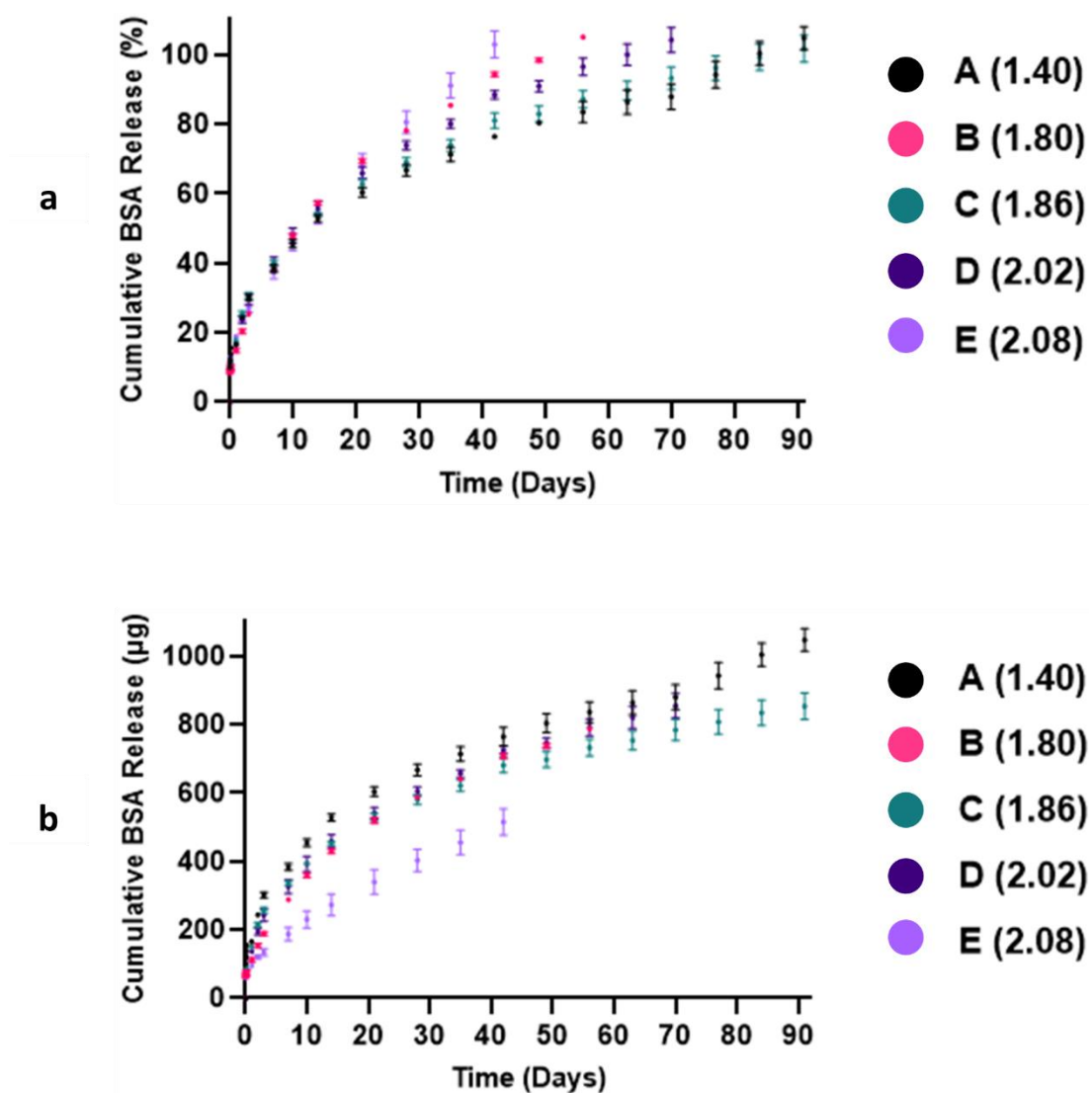
Figure 6.24: (a) Cumulative release (%) and (b) cumulative release (µg) of BSA from geometries A-E (SA/V ratio) printed using PEGDA 575/4000 (1:1) 20% (*w/v*) 0.5 SH (MM–F12). Release for the control samples (10 x 10 x 2 mm) acted as a reference point. Results denote mean ± S.D. (n = 3) and values in brackets denote the respective SA/V calculated for each geometry.

6.3.4.8 DLP Printed 3D Structures with a Model Protein (ALP) Encapsulated

6.3.4.8.1 ALP Release from DLP 3D Printed Structures

Important factors in achieving and controlling release from the PEGDA-DTT based formulations have been explored primarily using BSA. However, as mentioned previously in Section 2.3, understanding how proteins with different properties could be released was also an industrial desire. This could allow further relationships to be made connecting formulation compositions, matrix mesh properties and delivery approaches adopted.

In Chapter 5 LYZ and BSA were able to be released in limited quantities in relation to theoretical loading from the sampled printed with the highest Mn CG PEGDA formulation. However, there was no significant release detected using ALP, the largest nominal size model protein proposed. Hence, since BSA release had been achieved and modulated from printed samples using MM formulations it was decided it may be possible to release ALP from the same structures. Also, the associated PNPP activity assay would help provide an insight into activity retention or loss during preparation and fabrication stages. In a wider context, this aimed to feed into overall ambitions to understand release characteristics for a comprehensive model protein database.

The use of ALP, with a greater nominal size of (~160 kDa, 150 Å) compared to that of BSA (~66 kDa, 70 Å), naturally presents more challenges with release. It is desirable to understand the influence of biomacromolecule size in relation to entrapment or release on an individual basis as well as in the context of multi-bioactive delivery systems. Figure 6.25 shows the release of BSA and ALP from the same formulation (MM–F10), with 5 mg/mL loading. It was anticipated that larger polymer matrix mesh sizes would be required to allow for sustained elution of the ALP. MM–F10 was selected due to the printed samples having the highest calculated theoretical matrix mesh size out of the MM formulations prepared. It is clear that the extent of ALP release possible was considerably less (56.6 ± 1.6% of total loaded) from the same structure composition and ultimately plateaued after 21 days.
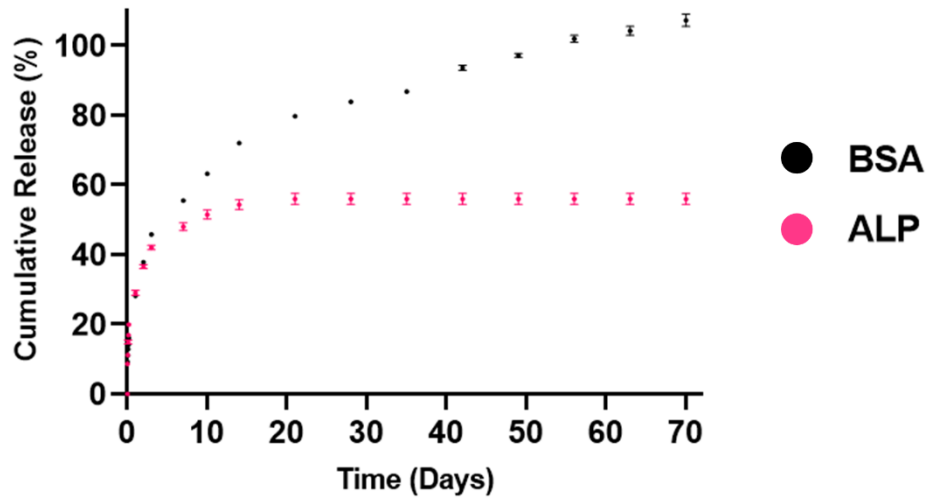
Figure 6.25: Comparison of the cumulative release (%) achieved for BSA and ALP encapsulated within samples printed using PEGDA 575/4000 (1:1) 10% (*w/v*) 0.5 SH (MM–F10). Results denote mean ± S.D. (n = 3).

6.3.4.8.2 Establishing Activity Retention of ALP Eluted

For quantifying ALP activity, a PNPP activity assay was used. This importantly allowed for assessing the activity retention regarding formulation preparation, DLP printing of samples and end ALP elution. Figure 6.26 shows the µmol PNP/min/µg ALP values regarding the different time point sample intervals assayed in respect to the total protein release, which was conducted more regularly on day 1 (0.5, 1, 2, 3, 4 and 24 hours) before measurements taken on day 2, 3, 7, 10, 14 and 21.
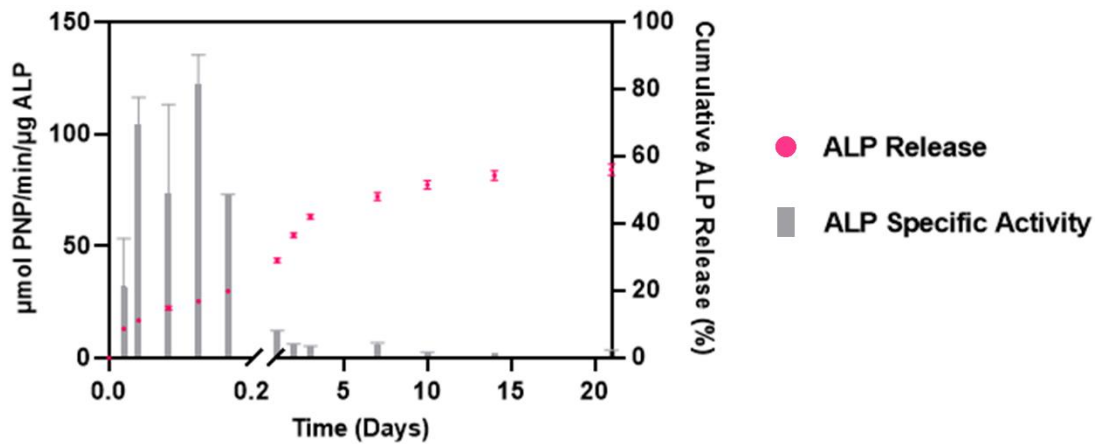
Figure 6.26: ALP activity quantification represented in µmol PNP/min/µg ALP in regard to respective release over 21 days. Results denote mean ± S.D. (n = 3).

6.4 Discussion

In this chapter, progression has been made from utilising formulations for DLP printing with a purely CG based mechanism of crosslinking towards MM SH:acrylate polymerisation. It was observed that the process of Michael addition of DTT (SH component) into the PEGDA (acrylate component) chain led to the synthesis of hydrolytically labile PEGDA-DTT macromers. It was theorised that the introduction of degradable aspects would lead to release of encapsulated model proteins, through partial or full degradation of the polymer matrix. Previous literature has shown that higher MW PEGDA, increased SH:acrylate ratio implemented and lower % (*v/v* or *w/v*) implemented correspond with more significant decreases in mechanical properties over time [152,195]. Therefore, this was exploited in an effort to achieve and tune release of an encapsulated protein from DLP 3D printed structures.

This concept was proven firstly by samples created using a PEGDA 4000 20% (*w/v*) 0.8 SH:acrylate formulation. However, this formulation was too viscous to be DLP printed. As cast samples were instead made and BSA was released during degradation over 9 days, supporting the rationale that SH groups would be hydrolytically labile. Due to the viscosity issues, pre-print characterisation of prepared formulations was conducted using GPC, ^{1}H NMR spectroscopy and rheological analysis. Increasing the SH:acrylate ratio overall led to increases in overall Mn, Mw and DPI for MM formulations and minimising of acrylate NMR peaks, aligning with previous literature [194–196]. All formulations (MM–F1 to MM–F12) satisfied the theory that mixed-mode (MM) polymerisation mechanisms would be suitable for DLP printing to produce implant exemplars and allowed for assessing the release of encapsulated model protein(s) from 3D structures.

It was also theorised that the duration and rate of release would be able to be modulated through changes in both PEGDA-DTT polymer concentration and SH:acrylate ratios selected. Quantifiable differences in matrix properties were established by comparing swelling ratio and theoretical matrix mesh approximations using Peppas-Merrill principles [130,156,157]. It was shown that the implementation of PEGDA-DTT macromers can significantly impact the final printed samples and thus release e.g. total BSA release ranging from

70 to 112 days for samples prepared with PEGDA 575/4000 (1:1) blend formulations (MM–F9 to MM–F12). Decreasing the selected PEGDA % (*w/v*) whilst increasing the PEGDA Mn and SH:acrylate ratio corresponded with greater swelling ratios and theoretical matrix mesh size that contribute to faster rates of release. Increasing protein loading also led to increased release and allowed longer periods of delivery. Nominal protein size also influences release e.g. total BSA release in 70 days compared to 56.6 ± 1.6% ALP release over 21 days from samples printed using the same formulation. Release profiles were fitted, where applicable, to release kinetic mathematical models and the best fit reported to indicate the mechanism of release. The influence of formulation on modulating release was prioritised in this thesis, but a preliminary study was conducted with five different sample geometries of varying SA/V ratios. Further work is needed to establish the effect of design changes.

The activity of ALP release was quantified but was near negligible, meaning there are further factors that need to be taken into consideration to protect this model protein. This must also be addressed for encapsulation of other potential bioactives within similar light-based printing modalities and formulations. Whilst the generation and utilisation of free radicals under UV irradiation for MM crosslinking mechanisms is typically less than that of CG polymerisation, it is likely that this could still be impacting on the ALP activity [183]. Therefore, lower concentrations of the photoinitiator could be trialled but printing parameters would need to be optimised further and may prevent sufficient crosslinking that allows part fabrication. Instead, the exploration of purely SG formulations presents a natural progression due to the enhanced rate of crosslinking that can be achieved with lower photoinitiator additions e.g. 0.05% (*w/v*) LAP; a 10-fold decrease on the LAP used for the formulations in this chapter. For example, the use of thiol-ene chemistries such as PEG-norbornene (PEG-NB) with PEG-SH or enzymatically degradable peptide-SH linkages [192]. However, time restrictions to formulate compositions suitable for DLP processing meant that this was outside the scope of this thesis.

6.5 Conclusions

The use of low-cost materials and an inexpensive DLP setup has allowed for a range of MM PEGDA-DTT formulations to be prepared and printed. Fundamental aspects that dictate entrapment or release in relation to matrix properties have been evaluated. This included the selection of the starting PEGDA/blend MW, % (*v/v* or *w/v*), SH:acrylate ratio implemented, protein loading (mg/mL) and nominal size. Differences in swelling and theoretical matrix mesh size calculated for low MW PEGDA (575 and 700 Mn) 50% (*v/v*) (MM–F1 to MM–F8) formulations versus formulations comprised of a PEGDA 575/4000 (1:1) blend at 10 and 20% (*w/v*) (MM–F9 to MM–F12) gave reasoning for release characteristics found. Visual differences were confirmed through cryo-SEM imaging in the as printed state and degraded state to provide further validation.

Release of BSA (66 kDa, 70 Å) from DLP 3D printed structures was able to be achieved for a duration of 3+ months, identified as an industrial need alongside new strategies in satisfying controlled and long-term release in Section 2.3. This contrasts the CG-based formulation sample results from Chapter 5 whereby release was limited in both duration and quantity in relation to total protein loading. Results gathered through using model proteins in this thesis has initiated work towards the potential generation of a novel AM "toolbox" guide whereby higher-cost protein therapeutics with similar characteristics may be able to be delivered with similar formulations and manufacturing approaches.

Chapter 7 Discussion and Conclusions

7.1 Discussion

This thesis considers firstly the identification of suitable printing modalities that facilitate processing of biomacromolecule containing formulations, explored in Chapter 4 to 6. Low-cost model proteins of varying size were selected, which included lysozyme (LYZ, 14 kDa), bovine serum albumin (BSA, 66 kDa) and alkaline phosphatase (ALP, 160 kDa). Proteins were encapsulated during printing and allowed for investigation into the factors that govern release of proteins from 3D printed constructs, quantified *in vitro*. There is an opportunity to suggest that viable approaches established with model proteins could be later adopted for higher cost biological therapeutics with similar characteristics.

Inkjet printing (IJP) was proposed due to previous success documented for processing small molecule (Da) containing formulations, with a high degree of control in deposition via non-contact droplet formation [105–107]. PEG was identified as a suitable material for biomedical applications (hydrophilic, non-toxic and non-immunogenic), with the diacrylate derivative, PEGDA, allowing for crosslinking under UV with the necessary photoinitiator addition [128,129,208]. Diluent components of PBS and MQ ultrapure water were used in the formulations prepared to allow improved solubility of ALP, which was not suitable in PEGDA alone and increased viscosity with increased loading concentration. Protein loaded formulations led to jetting issues due to the accumulation of debris on the nozzle jet interface likely resulting from the protein incorporated and salts in the PBS precipitating out of solution during droplet ejection. To combat this a humectant, glycerol, was added as previously exploited [166,171,172]. This increased the time until nozzle jet blocking occurred, but issues were still prevalent. Challenges encountered aligned with past literature and provided explanation as to why attempts at biomacromolecule processing via IJP have been less reported [104,168]. This could also provide explanation to why IJP has been predominantly used for microarrays, immunoassays, thin film production and μm size biosensors rather than mm scale sustained release delivery devices [166,169,170].

DLP printing was proposed as an alternative to IJP. The main rationale for this was the avoidance of the requirement for formulations to pass through an orifice and the ability to process higher viscosity formulations, which widens the applicable materials library [197–199]. A low-cost Anycubic photon mono was utilised, with a range of PEGDA Mn selected (575 to 10,000 g/mol) for use in formulations prepared for printing via chain-growth (CG) polymerisation. Samples were able to be fabricated and the use of DLP printing satisfied the technique identification and encapsulation aspect of industrial aim 1. It was anticipated that increases in PEGDA Mn would correspond with an increase in swelling ratio and theoretical matrix mesh size, which was calculated using Peppas-Merrill principles [130,156,157]. Whilst release of LYZ and BSA was achieved from the higher Mn PEGDA formulations at 20% (*w/v*) (CG–F4 to CG–F6), reliance on swelling and diffusion alone meant release was limited, even when protein loading was increased from 1 to 5 mg/mL.

In Chapter 6, it was proposed that the incorporation of a degradable component into formulations, to disrupt and breakdown the printed polymer matrices, when swelled, would allow sustained release. PEGDA-DTT macromers with varying SH:acrylate ratios were synthesised and allowed fabrication of samples via DLP printing using a mixed-mode (MM) polymerisation mechanism [195]. Significant changes in swelling ratio and theoretical matrix mesh size approximations were established when comparing the as printed and swelled (hydrolytically degraded) sample state. The quantified values were used as a means for comparison between sample sets and were validated by visual imaging using cryo-SEM. Release rate and duration was modulated through changes in the PEGDA-DTT compositions, suitable for DLP, and validated industrial aim 1. Decreasing the PEGDA content in a formulation whilst increasing the PEGDA Mn and SH:acrylate ratio contributed to firstly achieving total BSA release, and the ability to tune delivery. Samples comprised of a PEGDA Mn 575/4000 blend at 10% and 20% (*w/v*) with 0.25 and 0.5 SH:acrylate ratios allowed the delivery period to be adjusted between 70 to 112 days. This satisfied industrial aim 3 for long-term and controlled protein release over 1 to 3+ months. Differences in release profiles were related to previously established polymer matrix properties and

release kinetic models, to check the mechanism of release as deemed important to identify in industrial aim 2. This confirmed that higher swelling ratios and increased matrix mesh sizes, in relation to the printed structures after degradation in PBS at 37°C, corresponded with total release of the BSA loaded.

Understanding the effect of different biomacromolecule properties, e.g. nominal size, on end release characteristics is important in the wider context of delivering biological therapeutics. A preliminary study encapsulating ALP within the MM formulations provided an initial validation of industrial aim 4. However, a wider library of model proteins is required to inform future decisions regarding the best protocols to adopt for delivering a diverse range of biological therapeutics, which was an identified industrial ambition. The consolidation of multiple bioactives within one dosage form or compartmentalised within implantable devices for autonomous controlled release has promise to improve patient adherence to treatment plans by minimising the self-administering burden and enhancing therapeutic benefit [209,210].

The work presented in this thesis has demonstrated the feasibility of utilising a 3D printing method, DLP, for encapsulation and subsequent release of biomacromolecules that can be modulated through changes in formulation decisions. Establishing the requirements for printing and influence of matrix properties in relation to protein delivery from 3D printed structures was prioritised. Importantly, the over-arching framework, developed through an experimental approach, has been successful in highlighting the dominating factors governing end release characteristics. The implementation of DLP has shown the flexibility and novelty that 3D printing approaches can allow. This is particularly beneficial in the development of biological therapeutics and the optimisation of strategies for their delivery. On-demand manufacturing could also allow for flexible dose adjustments and thus personalised medication plans.

7.2 Future Work Proposed

The suggested work in this section focuses on areas of the thesis that were not able to be addressed due to time restrictions and would be recommended to investigate further.

In the first instance, the implementation of model proteins with a range of attributes to compare differences in associated release was planned. A decision was made to prioritise BSA to allow for progression to be made in terms of comparing the effect of formulation changes in end fabricated sample structure, and ultimately influence of this on the release profile. However, expansion of the model protein library, with different physiochemical properties, was an identified industrial desire. The DLP process used in this thesis appears to be feasible for encapsulating biomacromolecules within photopolymerised formulations for subsequent release and analysis. Process suitability for bioactives, such as protein therapeutics, should be considered on a case-by-case basis.

Dithiothreitol (DTT) was used for a proof of concept study in Chapter 6, but the modification of synthesised SH:acrylate macromers with different SH components could also be considered e.g. use of enzymatically degradable linkages. Additionally, progression towards SG polymerisation-based formulations has promise to achieve more homogenous crosslinked networks with greater flexibility in property tuning and faster rates of crosslinking using lower photoinitiator additions e.g. 0.05% (*w/v*) instead of 0.5% (*w/v*). For example, PEG-Norbornene (PEG-NB) functionalities with a degradable SH component would meet this criteria [192,211,212]. Minimising free radical production could also benefit activity retention of biologics incorporated [183]. For this thesis, SG functionalities were not explored due to the associated costs of commercially supplied materials in relation to the quantities needed for multiple DLP printing trials. Instead, understanding key intrinsic properties (swelling and theoretical matrix mesh size) of printed PEGDA based samples was prioritised to build data relationships between different sample compositions for understanding what governs release from 3D printed constructs.

Focus was placed on identifying a suitable AM technique capable of processing protein containing formulations and understanding the effect of formulation changes on delivery device fabrication and *in vitro* release. The influence of changes in geometry was only briefly explored through variations in SA/V ratio in Chapter 6.3.4.7. Other areas to consider would be the use of loading gradients, such as lower loading/no loading in outer regions of a device to minimise faster release in the early phase of delivery (day 0 to 3), or material gradients e.g. stiffer regions to prevent flex/breakage upon implantation. The ability to combine multiple bioactives within a singular delivery device with potentially different release profiles e.g. anti-inflammatory release followed by growth factor delivery, would also be highly beneficial. DLP systems with multi-material capability are becoming more established and could offer opportunities to refine biologic release through increasing delivery device functionality [178,213].

Technological advancements in AM/3D printing continue to occur, allowing for scope to have greater control over bioactive release to achieve desired dosing and maximise therapeutic benefits. A simple suggestion could be the adaption of a DLP printing setup to allow smaller scale material trials e.g. use of smaller vats and printing platforms to print with more expensive materials, which would also be beneficial when using higher-cost biological therapeutics at early-stage development. Alternatively, printing methods capable of processing higher viscosities, such as CAL systems, could be investigated [214,215]. This would extend the materials choices, and thus formulations that could be prepared and exploited to gain an enhanced regulation of end delivery. Also, the use of SG chemistries combined with this AM technique could allow for rapid on-demand fabrication of bioactive encapsulated structures for implantation.

A combination of experimental and modelling approaches, to understand release from 3D printed constructs, would also aid the continual progression towards end application use. Identifying applicable formulations and delivery device designs that allow the intended release of specific biological therapeutics, based upon known characteristics, would assist in the development of *in vitro in vivo* correlations. This has potential to eventually

reduce requirements to conduct costly experimental testing at the initial stages of delivery device development, which is desirable for industry. For example, creation of predictive models that identify suitable formulations dictated by properties of the encapsulated bioactive(s), final device structure requirement and end delivery profile(s) desired in relation to release rate and time frame.

Due to time restrictions, it was decided that one set of physiological conditions would be considered for the swelling and release studies. This was conducted at pH 7.4 and 37°C to simulate the upper arm subcutaneous tissue region [57]. However, a range of environmental conditions could be evaluated in relation to intended implantation sites and further experimental repeats would be required before progressing towards *in vivo* studies [216]. Further mechanical testing and physical manipulation could also be assessed. In this thesis, a compression test was deemed suitable to provide a comparison between samples in the as printed and swelled state. However, additional tests such as clinical manipulation (pushing, pulling and folding) could be considered in terms of requirements for administration [194].

7.3 Summarising Statement of Research Purpose and Novelty

To date, the majority of success for 3D printed therapeutic delivery devices has been previously seen for small molecule (Da) release but is not currently reflected for larger biomacromolecules (kDa). As a result, this prompts the exploration into the viability of 3D printing as a manufacturing route to address the delivery of challenging biomacromolecules. The novelty in the research proposed places focus on firstly the identification of a suitable AM technique that allows bioactive encapsulation during printing followed by parameter optimisation. Materials selection and formulations prepared must be able to be processed by the printing modality, but importantly allow for a defined level of control over desired end release characteristics. The intention behind this is to develop informed insight into how to harness manufacturing method(s) identified alongside requirements regarding formulation preparation and processing to produce a 3D printed biomacromolecule delivery device.

Fundamentally, the research in this thesis encompasses the primary influencing factors when processing biomacromolecules throughout the

required steps involved in delivery device fabrication using AM. This includes stages from initial addition to a formulation, printing and final elution. As a result, if these aspects can be better understood using a model protein(s) there is an opportunity to suggest that similar approaches could be adopted for higher cost protein therapeutics with similar characteristics. Ultimately, this development process could be conducted in the future for a library of different proteins to create novel formulations that are adapted to other biologics and be a first step in patient-centred drug delivery.

References

[1]   S. Mitragotri, P.A. Burke, R. Langer, Overcoming the challenges in administering biopharmaceuticals: Formulation and delivery strategies, Nat. Rev. Drug Discov. 13 (2014) 655–672. https://doi.org/10.1038/nrd4363.

[2]   J.M. Berg, J.L. Tymoczko, L. Stryer, Protein structure and function, in: Biochemistry, 5th ed., New York: W.H Freeman, 2002: pp. 41–67.

[3]   C.F. Van Der Walle, O. Olejnik, An overview of the field of peptide and protein delivery, in: Pept. Protein Deliv., Elsevier Inc., 2011: pp. 1–22. https://doi.org/10.1016/B978-0-12-384935-9.10001-x.

[4]   R. Bischoff, H. Schlüter, Amino acids: Chemistry, functionality and selected non-enzymatic post-translational modifications, J. Proteomics. 75 (2012) 2275–2296. https://doi.org/10.1016/j.jprot.2012.01.041.

[5]   A.K. Sieradzan, A.G. Lipska, E.A. Lubecka, Shielding effect in protein folding, J. Mol. Graph. Model. 79 (2018) 118–132. https://doi.org/10.1016/j.jmgm.2017.10.018.

[6]   C. Zhang, S.H. Kim, The anatomy of protein β-sheet topology, J. Mol. Biol. 299 (2000) 1075–1089. https://doi.org/10.1006/jmbi.2000.3678.

[7]   B. Alberts, A. Johnson, J. Lewis, M. Raff, K. Roberts, P. Walter, The shape and structure of proteins, in: Mol. Biol. Cell, 4th ed., New York: Garland Science, 2002.

[8]   S.-G. Chang, K.-D. Choi, S.-H. Jang, H.-C. Shin, Role of Disulfide Bonds in the Structure and Activity of Human Insulin, Mol. Cells. 16 (2003) 323–330.

[9]   P. Bork, E. V. Koonin, Protein sequence motifs, Curr. Opin. Struct. Biol. 6 (1996) 366–376. https://doi.org/10.1016/s0959-440x(96)80057-1.

[10]   A.D. Moore, Å.K. Björklund, D. Ekman, E. Bornberg-Bauer, A. Elofsson, Arrangements in the modular evolution of proteins, Trends Biochem. Sci. 33 (2008) 444–451.

https://doi.org/10.1016/j.tibs.2008.05.008.

[11]   D.S. Dimitrov, Therapeutic Proteins, Methods Mol. Biol. 899 (2012) 1.
        https://doi.org/10.1007/978-1-61779-921-1_1.

[12]   B. Leader, Q.J. Baca, D.E. Golan, Protein therapeutics: a summary
        and pharmacological classification, Nat. Rev. Drug Discov. 2007 71. 7
        (2008) 21–39. https://doi.org/10.1038/nrd2399.

[13]   L. Wang, N. Wang, W. Zhang, X. Cheng, Z. Yan, G. Shao, X. Wang, R.
        Wang, C. Fu, Therapeutic peptides: current applications and future
        directions, Signal Transduct. Target. Ther. 2022 71. 7 (2022) 1–27.
        https://doi.org/10.1038/s41392-022-00904-4.

[14]   E. Fang, X. Liu, M. Li, Z. Zhang, L. Song, B. Zhu, X. Wu, J. Liu, D.
        Zhao, Y. Li, Advances in COVID-19 mRNA vaccine development,
        Signal Transduct. Target. Ther. 7 (2022).
        https://doi.org/10.1038/s41392-022-00950-y.

[15]   J. Downing, R. Taylor, R. Mountain, B. Barr, K. Daras, T. Comerford,
        A.G. Marson, M. Pirmohamed, F. Dondelinger, A. Alfirevic,
        Socioeconomic and health factors related to polypharmacy and
        medication management: analysis of a Household Health Survey in
        North West Coast England, BMJ Open. 12 (2022) 54584.
        https://doi.org/10.1136/bmjopen-2021-054584.

[16]   Health Survey for England 2016 findings and trend tables, NHS Digital,
        Leeds, England, 2017.

[17]   M.T. Brown, J.K. Bussell, Medication Adherence: WHO Cares?, Mayo
        Clin. Proc. 86 (2011) 304. https://doi.org/10.4065/MCP.2010.0575.

[18]   Good for you, good for us, good for everybody: a plan to reduce
        overprescribing to make patient care better and safer, support the
        NHS, and reduce carbon emissions, Department of Health & Social
        Care, 2021.

[19]   J.L. England, G. Haran, Role of Solvation Effects in Protein
        Denaturation: From Thermodynamics to Single Molecules and Back,

Annu. Rev. Phys. Chem. 62 (2011) 257–277.
https://doi.org/10.1146/annurev-physchem-032210-103531.

[20] D.R. Canchi, A.E. García, Cosolvent Effects on Protein Stability, Annu.
Rev. Phys. Chem. 64 (2013) 273–293.
https://doi.org/10.1146/annurev-physchem-040412-110156.

[21] J.M. Berg, J.L. Tymoczko, L. Stryer, Catalytic strategies, in:
Biochemistry, 5th ed., New York: W.H Freeman, 2002: pp. 227–260.

[22] A.P. Golovanov, G.M. Hautbergue, S.A. Wilson, L.Y. Lian, A simple
method for improving protein solubility and long-term stability, J. Am.
Chem. Soc. 126 (2004) 8933–8939. https://doi.org/10.1021/ja049297h.

[23] R.M. Kramer, V.R. Shende, N. Motl, C.N. Pace, J.M. Scholtz, Toward a
molecular understanding of protein solubility: Increased negative
surface charge correlates with increased solubility, Biophys. J. 102
(2012) 1907–1915. https://doi.org/10.1016/j.bpj.2012.01.060.

[24] S.R. Trevino, J.M. Scholtz, C.N. Pace, Amino Acid Contribution to
Protein Solubility: Asp, Glu, and Ser Contribute more Favorably than
the other Hydrophilic Amino Acids in RNase Sa, J. Mol. Biol. 366
(2007) 449–460. https://doi.org/10.1016/j.jmb.2006.10.026.

[25] W. Jiskoot, T.W. Randolph, D.B. Volkin, C. Russell Middaugh, C.
Schöneich, G. Winter, W. Friess, D.J.A. Crommelin, J.F. Carpenter,
Protein Instability and Immunogenicity: Roadblocks to Clinical
Application of Injectable Protein Delivery Systems for Sustained
Release, J. Pharm. Sci. 101 (2012) 946–954.
https://doi.org/10.1002/jps.23018.

[26] G.M. Pauletti, S. Gangwar, T.J. Siahaan, J. Aubé, R.T. Borchardt,
Improvement of oral peptide bioavailability: Peptidomimetics and
prodrug strategies, Adv. Drug Deliv. Rev. 27 (1997) 235–256.
https://doi.org/10.1016/s0169-409x(97)00045-8.

[27] J. Renukuntla, A.D. Vadlapudi, A. Patel, S.H.S. Boddu, A.K. Mitra,
Approaches for enhancing oral bioavailability of peptides and proteins,

Int. J. Pharm. 447 (2013) 75–93.
https://doi.org/10.1016/j.ijpharm.2013.02.030.

[28]   C. Stillhart, K. Vučićević, P. Augustijns, A.W. Basit, H. Batchelor, T.R.
Flanagan, I. Gesquiere, R. Greupink, D. Keszthelyi, M. Koskinen, C.M.
Madla, C. Matthys, G. Miljuš, M.G. Mooij, N. Parrott, A.L. Ungell, S.N.
de Wildt, M. Orlu, S. Klein, A. Müllertz, Impact of gastrointestinal
physiology on drug absorption in special populations—An UNGAP
review, Eur. J. Pharm. Sci. 147 (2020) 105280.
https://doi.org/10.1016/j.ejps.2020.105280.

[29]   A. Bak, D. Leung, S.E. Barrett, S. Forster, E.C. Minnihan, A.W.
Leithead, J. Cunningham, N. Toussaint, L.S. Crocker, Physicochemical
and Formulation Developability Assessment for Therapeutic Peptide
Delivery—A Primer, AAPS J. 17 (2015) 144–155.
https://doi.org/10.1208/s12248-014-9688-2.

[30]   D.J. Drucker, Advances in oral peptide therapeutics, Nat. Rev. Drug
Discov. 19 (2020) 277–289. https://doi.org/10.1038/s41573-019-0053-
0.

[31]   S. Patil, A. Narvekar, A. Puranik, R. Jain, P. Dandekar, Formulation of
Therapeutic Proteins: Strategies for Developing Oral Protein
Formulations, in: John Wiley & Sons, Ltd, 2019: pp. 391–432.
https://doi.org/10.1002/9783527812172.ch12.

[32]   M.D. Del Curto, A. Maroni, L. Palugan, L. Zema, A. Gazzaniga, M.E.
Sangalli, Oral delivery system for two-pulse colonic release of protein
drugs and protease inhibitor/absorption enhancer compounds, J.
Pharm. Sci. 100 (2011) 3251–3259. https://doi.org/10.1002/jps.22560.

[33]   S. Alaei, H. Omidian, Mucoadhesion and Mechanical Assessment of
Oral Films, Eur. J. Pharm. Sci. 159 (2021) 105727.
https://doi.org/10.1016/j.ejps.2021.105727.

[34]   S. Hua, Advances in Nanoparticulate Drug Delivery Approaches for
Sublingual and Buccal Administration, Front. Pharmacol. 10 (2019).
https://doi.org/10.3389/fphar.2019.01328.

[35]   J.K.W. Lam, C.C.K. Cheung, M.Y.T. Chow, E. Harrop, S. Lapwood, S.I.G. Barclay, I.C.K. Wong, Transmucosal drug administration as an alternative route in palliative and end-of-life care during the COVID-19 pandemic, Adv. Drug Deliv. Rev. 160 (2020) 234–243. https://doi.org/10.1016/j.addr.2020.10.018.

[36]   M. Pandey, H. Choudhury, A. Abdul-Aziz, S.K. Bhattamisra, B. Gorain, T. Carine, T.W. Toong, N.J. Yi, L.W. Yi, Promising Drug Delivery Approaches to Treat Microbial Infections in the Vagina: A Recent Update, Polymers (Basel). 13 (2021) 1–65. https://doi.org/10.3390/polym13010026.

[37]   S. Srikrishna, L. Cardozo, The vagina as a route for drug delivery: A review, Int. Urogynecol. J. Pelvic Floor Dysfunct. 24 (2013) 537–543. https://doi.org/10.1007/s00192-012-2009-3.

[38]   E.D.B. Johansson, R. Sitruk-Ware, New delivery systems in contraception: Vaginal rings, Am. J. Obstet. Gynecol. 190 (2004). https://doi.org/10.1016/j.ajog.2004.01.056.

[39]   S.K. Bardal, J.E. Waechter, D.S. Martin, Pharmacokinetics, in: Appl. Pharmacol., Elsevier Health Sciences, 2011: pp. 17–34.

[40]   S.N. Economidou, D.A. Lamprou, D. Douroumis, 3D printing applications for transdermal drug delivery, Int. J. Pharm. 544 (2018) 415–424. https://doi.org/10.1016/J.IJPHARM.2018.01.031.

[41]   F.K. Aldawood, A. Andar, S. Desai, A Comprehensive Review of Microneedles: Types, Materials, Processes, Characterizations and Applications, Polymers (Basel). 13 (2021). https://doi.org/10.3390/POLYM13162815.

[42]   B. Chaulagain, A. Jain, A. Tiwari, A. Verma, S.K. Jain, Passive delivery of protein drugs through transdermal route, Artif. Cells, Nanomedicine, Biotechnol. 46 (2018) 472–487. https://doi.org/10.1080/21691401.2018.1430695.

[43]   M.N. Pastore, Y.N. Kalia, M. Horstmann, M.S. Roberts, Transdermal

patches: History, development and pharmacology, Br. J. Pharmacol.
172 (2015) 2179–2209. https://doi.org/10.1111/bph.13059.

[44] Y.C. Kim, C. Jarrahian, D. Zehrung, S. Mitragotri, M.R. Prausnitz,
Delivery Systems for Intradermal Vaccination, Intradermal Immun. 351
(2012) 77. https://doi.org/10.1007/82_2011_123.

[45] W.Y. Jeong, M. Kwon, H.E. Choi, K.S. Kim, Recent advances in
transdermal drug delivery systems: a review, Biomater. Res. 25 (2021)
1–15. https://doi.org/https://doi.org/10.1186/s40824-021-00226-6.

[46] P. Shrestha, B. Stoeber, Fluid absorption by skin tissue during
intradermal injections through hollow microneedles, Sci. Rep. 8 (2018)
13749. https://doi.org/10.1038/S41598-018-32026-9.

[47] M. Willihnganz, S.L. Gurevitz, B.D. Clayton, Parenteral administration:
intradermal, subcutaneous, and intramuscular routes, in: Elsevier Inc.
(Ed.), Clayton's Basic Pharmacol. Nurses, 18th ed., 2019: pp. 133–
143.

[48] A. Rzhevskiy, A. Popov, C. Pavlov, Y. Anissimov, A. Zvyagin, Y. Levin,
E. Kochba, Intradermal injection of lidocaine with a microneedle device
to provide rapid local anaesthesia for peripheral intravenous
cannulation: A randomised open-label placebo-controlled clinical trial,
PLoS One. 17 (2022).
https://doi.org/10.1371/JOURNAL.PONE.0261641.

[49] D.S. Hurst, A.B. McDaniel, Clinical Relevance and Advantages of
Intradermal Test Results in 371 Patients with Allergic Rhinitis, Asthma
and/or Otitis Media with Effusion, Cells. 10 (2021).
https://doi.org/10.3390/CELLS10113224.

[50] D. Patel, S.S. Zode, A.K. Bansal, Formulation aspects of intravenous
nanosuspensions, Int. J. Pharm. 586 (2020) 119555.
https://doi.org/10.1016/j.ijpharm.2020.119555.

[51] A.C. Anselmo, Y. Gokarn, S. Mitragotri, Non-invasive delivery
strategies for biologics, Nat. Rev. Drug Discov. 18 (2018) 19–40.

https://doi.org/10.1038/nrd.2018.183.

[52] R. Ferrari, M. Sponchioni, M. Morbidelli, D. Moscatelli, Polymer nanoparticles for the intravenous delivery of anticancer drugs: the checkpoints on the road from the synthesis to clinical translation, Nanoscale. 10 (2018) 22701–22719. https://doi.org/10.1039/C8NR05933K.

[53] K. Marulanda, A. Mercel, D.C. Gillis, K. Sun, M. Gambarian, J. Roark, J. Weiss, N.D. Tsihlis, M.R. Karver, S.R. Centeno, E.B. Peters, T.D. Clemons, S.I. Stupp, S.E. McLean, M.R. Kibbe, Intravenous Delivery of Lung-Targeted Nanofibers for Pulmonary Hypertension in Mice, Adv. Healthc. Mater. 10 (2021). https://doi.org/10.1002/ADHM.202100302.

[54] K. Long, Y. Yang, W. Lv, K. Jiang, Y. Li, A.C.Y. Lo, W.C. Lam, C. Zhan, W. Wang, Green Light-Triggered Intraocular Drug Release for Intravenous Chemotherapy of Retinoblastoma, Adv. Sci. 8 (2021) 2101754. https://doi.org/10.1002/ADVS.202101754.

[55] D.N. McLennan, C.J.H. Porter, S.A. Charman, Subcutaneous drug delivery and the role of the lymphatics, Drug Discov. Today Technol. 2 (2005) 89–96. https://doi.org/10.1016/j.ddtec.2005.05.006.

[56] A. V. Badkar, R.B. Gandhi, S.P. Davis, M.J. Labarre, Subcutaneous Delivery of High-Dose/Volume Biologics: Current Status and Prospect for Future Advancements, Drug Des. Devel. Ther. 15 (2021) 159. https://doi.org/10.2147/DDDT.S287323.

[57] I.R. Dubbelboer, E. Sjögren, Physiological based pharmacokinetic and biopharmaceutics modelling of subcutaneously administered compounds – An overview of in silico models, Int. J. Pharm. 621 (2022) 121808. https://doi.org/10.1016/j.ijpharm.2022.121808.

[58] H. Zhao, S. Xue, M.D. Hussherr, A.P. Teixeira, M. Fussenegger, Autonomous push button–controlled rapid insulin release from a piezoelectrically activated subcutaneous cell implant, Sci. Adv. 8 (2022) 4389. https://doi.org/10.1126/SCIADV.ABM4389.

[59] L. Li, G.J. Gatto, R.M. Brand, S.A. Krovi, M.L. Cottrell, C. Norton, A. van der Straten, L.M. Johnson, Long-acting biodegradable implant for sustained delivery of antiretrovirals (ARVs) and hormones, J. Control. Release. 340 (2021) 188–199. https://doi.org/10.1016/J.JCONREL.2021.10.021.

[60] E. Soliman, S. Ranjan, T. Xu, C. Gee, A. Harker, A. Barrera, J. Geddes, A narrative review of the success of intramuscular gluteal injections and its impact in psychiatry, Bio-Design Manuf. 1 (2018) 161–170. https://doi.org/10.1007/s42242-018-0018-x.

[61] S. Kempe, K. Mäder, In situ forming implants - An attractive formulation principle for parenteral depot formulations, J. Control. Release. 161 (2012) 668–679. https://doi.org/10.1016/j.jconrel.2012.04.016.

[62] A.D. Brunaugh, H.D.C. Smyth, R.O. Williams III, Modified Release Solid Oral Dosage Forms, in: Essent. Pharm., Springer, Cham, 2019: pp. 59–72. https://doi.org/10.1007/978-3-030-31745-4_4.

[63] T. Zambanini, R. Borges, J. Marchi, Bioactive glass/polymer composites for drug delivery, in: G. Kaur (Ed.), Clin. Appl. Biomater. State-of-the-Art Progress, Trends, Nov. Approaches, Springer International Publishing, 2017: pp. 287–312. https://doi.org/10.1007/978-3-319-56059-5.

[64] R. Kienitz, L. Kay, I. Beuchat, S. Gelhard, S. von Brauchitsch, C. Mann, A. Lucaciu, J.H. Schäfer, K. Siebenbrodt, J.P. Zöllner, S. Schubert-Bast, F. Rosenow, A. Strzelczyk, L.M. Willems, Benzodiazepines in the Management of Seizures and Status Epilepticus: A Review of Routes of Delivery, Pharmacokinetics, Efficacy, and Tolerability, CNS Drugs 2022 369. 36 (2022) 951–975. https://doi.org/10.1007/s40263-022-00940-2.

[65] J.E. Gibbs, D.W. Ray, The role of the circadian clock in rheumatoid arthritis, Arthritis Res. Ther. 15 (2013) 1–9. https://doi.org/10.1186/ar4146.

[66] C. Maderuelo, J.M. Lanao, A. Zarzuelo, Enteric coating of oral solid dosage forms as a tool to improve drug bioavailability, Eur. J. Pharm. Sci. 138 (2019). https://doi.org/10.1016/j.ejps.2019.105019.

[67] M.L. Bruschi, ed., Mathematical models of drug release, in: Strateg. to Modify Drug Release from Pharm. Syst., Woodhead Publishing, 2015: pp. 63–86. https://doi.org/10.1016/B978-0-08-100092-2.00005-9.

[68] S. Adepu, S. Ramakrishna, Controlled Drug Delivery Systems: Current Status and Future Directions, Molecules. 26 (2021). https://doi.org/10.3390/molecules26195905.

[69] M.L. Laracuente, M.H. Yu, K.J. McHugh, Zero-order drug delivery: State of the art and future prospects, J. Control. Release. 327 (2020) 834–856. https://doi.org/10.1016/J.JCONREL.2020.09.020.

[70] X.L. Zhou, J.T. He, H.J. Du, Y.Y. Fan, Y. Wang, H.X. Zhang, Y. Jiang, Pharmacokinetic and pharmacodynamic profiles of recombinant human erythropoietin-loaded poly(lactic-co-glycolic acid) microspheres in rats, Acta Pharmacol. Sin. 33 (2012) 137. https://doi.org/10.1038/aps.2011.157.

[71] C.M. Wells, M. Harris, L. Choi, V.P. Murali, F.D. Guerra, J.A. Jennings, Stimuli-Responsive Drug Release from Smart Polymers, J. Funct. Biomater. 10 (2019) 34. https://doi.org/10.3390/jfb10030034.

[72] C.K. Boughton, R. Hovorka, New closed-loop insulin systems, Diabetologia. 64 (2021) 1007–1015. https://doi.org/10.1007/s00125-021-05443-1.

[73] V.P. Torchilin, Passive and active drug targeting: Drug delivery to tumors as an example, in: M. Schäfer-Korting (Ed.), Handb. Exp. Pharmacol., 1st ed., Springer Berlin Heidelberg, 2010: pp. 3–53. https://doi.org/10.1007/978-3-642-00477-3_1.

[74] A. Geraili, M. Xing, K. Mequanint, Design and fabrication of drug-delivery systems toward adjustable release profiles for personalized treatment, View. 2 (2021) 20200126.

https://doi.org/10.1002/viw.20200126.

[75] B.L. Dargaville, D.W. Hutmacher, Water as the often neglected medium at the interface between materials and biology, Nat. Commun. 2022 131. 13 (2022) 1–10. https://doi.org/10.1038/s41467-022-31889-x.

[76] W.B. Liechty, D.R. Kryscio, B. V. Slaughter, N.A. Peppas, Polymers for Drug Delivery Systems, Annu. Rev. Chem. Biomol. Eng. 1 (2010) 149. https://doi.org/10.1146/annurev-chembioeng-073009-100847.

[77] R.A. Alshaikh, C. Waeber, K.B. Ryan, Polymer based sustained drug delivery to the ocular posterior segment: barriers and future opportunities for the treatment of neovascular pathologies, Adv. Drug Deliv. Rev. 187 (2022) 114342. https://doi.org/10.1016/j.addr.2022.114342.

[78] E. Holz, M. Darwish, D.B. Tesar, W. Shatz-Binder, A Review of Protein- and Peptide-Based Chemical Conjugates: Past, Present, and Future, Pharm. 2023, Vol. 15, Page 600. 15 (2023) 600. https://doi.org/10.3390/pharmaceutics15020600.

[79] F.C. Mackintosh, J. Kas, P.A. Janmey, Elasticity of Semiflexible Biopolymer Networks, Phys. Rev. Lett. 75 (1995).

[80] Y. Yu, Y. Chau, Formulation of in situ chemically cross-linked hydrogel depots for protein release: From the blob model perspective, Biomacromolecules. 16 (2015) 56–65. https://doi.org/10.1021/bm501063n.

[81] W. Wang, S.A. Sande, A dynamic light scattering study of hydrogels with the addition of surfactant: a discussion of mesh size and correlation length, Polym. J. 2015 474. 47 (2014) 302–310. https://doi.org/10.1038/pj.2014.114.

[82] N.R. Richbourg, N.A. Peppas, The swollen polymer network hypothesis: Quantitative models of hydrogel swelling, stiffness, and solute transport, Prog. Polym. Sci. 105 (2020).

https://doi.org/10.1016/j.progpolymsci.2020.101243.

[83]   Y. Akagi, T. Katashima, Y. Katsumoto, K. Fujii, T. Matsunaga, U. Il
       Chung, M. Shibayama, T. Sakai, Examination of the theories of rubber
       elasticity using an ideal polymer network, Macromolecules. 44 (2011)
       5817–5821. https://pubs.acs.org/doi/full/10.1021/ma201088r.

[84]   N.A. Peppas, P. Bures, W. Leobandung, H. Ichikawa, Hydrogels in
       pharmaceutical formulations, Eur. J. Pharm. Biopharm. 50 (2000) 27–
       46. https://doi.org/10.1016/s0939-6411(00)00090-4.

[85]   C.C. Lin, K.S. Anseth, PEG hydrogels for the controlled release of
       biomolecules in regenerative medicine, Pharm. Res. 26 (2009) 631–
       643. https://doi.org/10.1007/s11095-008-9801-2.

[86]   S. Lee, X. Tong, F. Yang, Effects of the poly(ethylene glycol) hydrogel
       crosslinking mechanism on protein release, Biomater. Sci. 4 (2016)
       405. https://doi.org/10.1039/c5bm00256g.

[87]   Y. Gu, J. Zhao, J.A. Johnson, Polymer Networks: From Plastics and
       Gels to Porous Frameworks, Angew. Chemie - Int. Ed. 59 (2020)
       5022–5049. https://doi.org/10.1002/anie.201902900.

[88]   M.W. Tibbitt, A.M. Kloxin, L.A. Sawicki, K.S. Anseth, Mechanical
       Properties and Degradation of Chain and Step-Polymerized
       Photodegradable Hydrogels, Macromolecules. 46 (2013) 2785.
       https://doi.org/10.1021/ma302522x.

[89]   S.K. Reddy, K.S. Anseth, C.N. Bowman, Modeling of network
       degradation in mixed step-chain growth polymerizations, Polymer
       (Guildf). 46 (2005) 4212–4222.
       https://doi.org/10.1016/j.polymer.2005.02.050.

[90]   G. Jahanmir, M.J. Abdekhodaie, Y. Chau, Stochastic Modeling of
       Degradation Behavior of Hydrogels, (2018).
       https://doi.org/10.1021/acs.macromol.8b00165.

[91]   H. Zhu, X. Yang, G.M. Genin, T.J. Lu, F. Xu, M. Lin, The relationship
       between thiol-acrylate photopolymerization kinetics and hydrogel

mechanics: An improved model incorporating photobleaching and thiol-Michael addition, J. Mech. Behav. Biomed. Mater. 88 (2018) 160–169. https://doi.org/10.1016/j.jmbbm.2018.08.013.

[92] M. Rooney, Continuous oral solid dose processing, in: T. Jacobs, A.A. Signore (Eds.), Good Des. Pract. GMP Pharm. Facil., 2nd ed., CRC Press, 2016: pp. 269–294.

[93] N.G. Türeli, A.E. Türeli, Upscaling and GMP production of pharmaceutical drug delivery systems, in: Drug Deliv. Trends, Elsevier, 2020: pp. 215–229. https://doi.org/10.1016/b978-0-12-817870-6.00011-0.

[94] M. Gamlen, P. Cummings, Pharmaceutical Development, in: J.P. Griffin, J. Posner, G.R. Barker (Eds.), Textb. Pharm. Med., 7th ed., Blackwell Publishing Ltd., Oxford, UK, 2013: pp. 32–41. https://doi.org/10.1002/9781118532331.

[95] L. Zema, G. Loreti, A. Melocchi, A. Maroni, A. Gazzaniga, Injection Molding and its application to drug delivery, J. Control. Release. 159 (2012) 324–331. https://doi.org/10.1016/j.jconrel.2012.01.001.

[96] D.A. Dean, Pharmaceutical Packaging Technology, in: D.A. Dean, E.R. Evans, I.H. Hall (Eds.), Pharm. Packag. Technol., CRC Press, 2005: pp. 185–228.

[97] H. Patil, R. V. Tiwari, M.A. Repka, Hot-Melt Extrusion: from Theory to Application in Pharmaceutical Formulation, AAPS PharmSciTech. 17 (2016) 20–42. https://doi.org/10.1208/s12249-015-0360-7.

[98] M.A. Repka, S. Majumdar, S.K. Battu, R. Srirangam, S.B. Upadhye, Applications of hot-melt extrusion for drug delivery, Expert Opin. Drug Deliv. 5 (2008) 1357–1376. https://doi.org/10.1517/17425240802583421.

[99] ISO/ASTM 52900:2021(en), Additive manufacturing — General principles — Fundamentals and vocabulary, 2021.

[100] S. Kyle, Z.M. Jessop, A. Al-Sabah, I.S. Whitaker, 'Printability'' of

Candidate Biomaterials for Extrusion Based 3D Printing: State-of-the-Art,' Adv. Healthc. Mater. 6 (2017). https://doi.org/10.1002/adhm.201700264.

[101] S.A. Khaled, J.C. Burley, M.R. Alexander, J. Yang, C.J. Roberts, 3D printing of five-in-one dose combination polypill with defined immediate and sustained release profiles, J. Control. Release. 217 (2015) 308–314. https://doi.org/10.1016/j.jconrel.2015.09.028.

[102] S. Ilkhanizadeh, A.I. Teixeira, O. Hermanson, Inkjet printing of macromolecules on hydrogels to steer neural stem cell differentiation, Biomaterials. 28 (2007) 3936–3943. https://doi.org/10.1016/J.BIOMATERIALS.2007.05.018.

[103] K. Zub, S. Hoeppener, U.S. Schubert, K. Zub, S. Hoeppener, U.S. Schubert, Inkjet Printing and 3D Printing Strategies for Biosensing, Analytical, and Diagnostic Applications, Adv. Mater. 34 (2022) 2105015. https://doi.org/10.1002/ADMA.202105015.

[104] S.E. Evans, T. Harrington, M.C. Rodriguez Rivero, E. Rognin, T. Tuladhar, R. Daly, 2D and 3D inkjet printing of biopharmaceuticals – A review of trends and future perspectives in research and manufacturing, Int. J. Pharm. 599 (2021) 120443. https://doi.org/10.1016/j.ijpharm.2021.120443.

[105] E.A. Clark, M.R. Alexander, D.J. Irvine, C.J. Roberts, M.J. Wallace, S. Sharpe, J. Yoo, R.J.M. Hague, C.J. Tuck, R.D. Wildman, 3D printing of tablets using inkjet with UV photoinitiation, Int. J. Pharm. 529 (2017) 523–530. https://doi.org/10.1016/j.ijpharm.2017.06.085.

[106] Y. He, R. Foralosso, G.F. Trindade, A. Ilchev, L. Ruiz-Cantu, E.A. Clark, S. Khaled, R.J.M. Hague, C.J. Tuck, F.R.A.J. Rose, G. Mantovani, D.J. Irvine, C.J. Roberts, R.D. Wildman, A Reactive Prodrug Ink Formulation Strategy for Inkjet 3D Printing of Controlled Release Dosage Forms and Implants, Adv. Ther. 3 (2020) 1900187. https://doi.org/10.1002/adtp.201900187.

[107] L. Ruiz-Cantu, G.F. Trindade, V. Taresco, Z. Zhou, Y. He, L.

Burroughs, E.A. Clark, F.R.A.J. Rose, C. Tuck, R. Hague, C.J. Roberts, M. Alexander, D.J. Irvine, R.D. Wildman, Bespoke 3D-Printed Polydrug Implants Created via Microstructural Control of Oligomers, ACS Appl. Mater. Interfaces. 13 (2021) 38969–38978. https://doi.org/10.1021/acsami.1c07850.

[108] T.T. Biswas, J. Yu, V.A. Nierstrasz, Effects of ink characteristics and piezo-electric inkjetting parameters on lysozyme activity, Sci. Rep. 9 (2019) 1–11. https://doi.org/10.1038/s41598-019-54723-9.

[109] B. Derby, Bioprinting: Inkjet printing proteins and hybrid cell-containing materials and structures, J. Mater. Chem. 18 (2008) 5717–5721. https://doi.org/10.1039/b807560c.

[110] X. Wang, M. Jiang, Z. Zhou, J. Gou, D. Hui, 3D printing of polymer matrix composites: A review and prospective, Compos. Part B Eng. 110 (2017) 442–458. https://doi.org/10.1016/j.compositesb.2016.11.034.

[111] A. Kjar, Y. Huang, Application of Micro-Scale 3D Printing in Pharmaceutics, Pharmaceutics. 11 (2019). https://doi.org/10.3390/pharmaceutics11080390.

[112] I. Gibson, D. Rosen, B. Stucker, Vat photopolymerization processes, in: Addit. Manuf. Technol., 2nd ed., Springer New York, 2015: pp. 63–103.

[113] J. Wang, A. Goyanes, S. Gaisford, A.W. Basit, Stereolithographic (SLA) 3D printing of oral modified-release dosage forms, Int. J. Pharm. 503 (2016) 207–212. https://doi.org/10.1016/j.ijpharm.2016.03.016.

[114] X. Xu, A. Goyanes, S.J. Trenfield, L. Diaz-Gomez, C. Alvarez-Lorenzo, S. Gaisford, A.W. Basit, Stereolithography (SLA) 3D printing of a bladder device for intravesical drug delivery, Mater. Sci. Eng. C. 120 (2021) 111773. https://doi.org/10.1016/j.msec.2020.111773.

[115] U. Detamornrat, E. Mcalister, A.R.J. Hutton, E. Larrañeta, R.F. Donnelly, The Role of 3D Printing Technology in Microengineering of

Microneedles, Small. 18 (2022) 2106392.
https://doi.org/10.1002/smll.202106392.

[116] S.N. Economidou, C.P.P. Reid, A. Uddin, J.F.C. Lamprou, D.
Douroumis, 3D printed microneedle patches using stereolithography
(SLA) for intradermal insulin delivery, (2019).
https://doi.org/10.1016/j.msec.2019.04.063.

[117] I. Gibson, D. Rosen, B. Stucker, Powder Bed Fusion Processes, in:
Addit. Manuf. Technol., 2nd ed., Springer New York, 2015: pp. 107–
145. https://doi.org/10.1007/978-1-4939-2113-3_5.

[118] N. Allahham, F. Fina, C. Marcuta, L. Kraschew, W. Mohr, S. Gaisford,
A.W. Basit, A. Goyanes, Selective Laser Sintering 3D Printing of Orally
Disintegrating Printlets Containing Ondansetron, Pharmaceutics. 12
(2020) 110. https://doi.org/10.3390/pharmaceutics12020110.

[119] F. Fina, A. Goyanes, S. Gaisford, A.W. Basit, Selective laser sintering
(SLS) 3D printing of medicines, Int. J. Pharm. 529 (2017) 285–293.
https://doi.org/10.1016/j.ijpharm.2017.06.082.

[120] A. Paolini, S. Kollmannsberger, E. Rank, Additive manufacturing in
construction: A review on processes, applications, and digital planning
methods, Addit. Manuf. 30 (2019) 100894.
https://doi.org/10.1016/j.addma.2019.100894.

[121] G. Turnbull, J. Clarke, F. Picard, P. Riches, L. Jia, F. Han, B. Li, W.
Shu, 3D bioactive composite scaffolds for bone tissue engineering,
Bioact. Mater. 3 (2018) 278–314.
https://doi.org/10.1016/j.bioactmat.2017.10.001.

[122] S. Stewart, J. Domínguez-Robles, R. Donnelly, E. Larrañeta,
Implantable Polymeric Drug Delivery Devices: Classification,
Manufacture, Materials, and Clinical Applications, Polymers (Basel). 10
(2018) 1379. https://doi.org/10.3390/polym10121379.

[123] Merck & Co. Inc., Highlights of Prescribing Information - NEXPLANON
(etonogestrel implant), Whitehouse Station, NJ 08889, USA, 2019.

https://www.accessdata.fda.gov/drugsatfda_docs/label/2020/021529s0
19s020lbl.pdf.

[124] S. Palomba, A. Falbo, A. Di Cello, C. Materazzo, F. Zullo, Nexplanon: The new implant for long-term contraception. A comprehensive descriptive review, Gynecol. Endocrinol. 28 (2012) 710–721. https://doi.org/10.3109/09513590.2011.652247.

[125] D. Mansour, Nexplanon®: What Implanon® did next, J. Fam. Plan. Reprod. Heal. Care. 36 (2010) 187–189. https://doi.org/10.1783/147118910793048629.

[126] R.R. Henry, D. Logan, T. Alessi, M.A. Baron, A randomized, open-label, multicenter, 4-week study to evaluate the tolerability and pharmacokinetics of ITCA 650 in patients with type 2 diabetes, Clin. Ther. 35 (2013). https://doi.org/10.1016/j.clinthera.2013.03.011.

[127] F.K. Knop, A. Brønden, T. Vilsbøll, Exenatide: pharmacokinetics, clinical use, and future directions, Expert Opin. Pharmacother. 18 (2017) 555–571. https://doi.org/10.1080/14656566.2017.1282463.

[128] M.S. Hamid Akash, K. Rehman, S. Chen, Natural and Synthetic Polymers as Drug Carriers for Delivery of Therapeutic Proteins, Polym. Rev. 55 (2015) 371–406. https://doi.org/10.1080/15583724.2014.995806.

[129] J.T. Peters, M.E. Wechsler, N.A. Peppas, Advanced biomedical hydrogels: molecular architecture and its impact on medical applications, Regen. Biomater. 8 (2021) 1–21. https://doi.org/10.1093/rb/rbab060.

[130] K. McAvoy, D. Jones, R.R.S. Thakur, Synthesis and Characterisation of Photocrosslinked poly(ethylene glycol) diacrylate Implants for Sustained Ocular Drug Delivery, Pharm. Res. 35 (2018) 1–17. https://doi.org/10.1007/s11095-017-2298-9.

[131] M. Labet, W. Thielemans, Synthesis of polycaprolactone: a review, Chem. Soc. Rev. 38 (2009) 3484–3504.

https://doi.org/10.1039/b820162p.

[132] A.A. Konta, M. García-Piña, D.R. Serrano, Personalised 3D Printed Medicines: Which Techniques and Polymers Are More Successful?, Bioeng. (Basel, Switzerland). 4 (2017). https://doi.org/10.3390/bioengineering4040079.

[133] M.A. Woodruff, D.W. Hutmacher, The return of a forgotten polymer—Polycaprolactone in the 21st century, Prog. Polym. Sci. 35 (2010) 1217–1256. https://doi.org/10.1016/j.progpolymsci.2010.04.002.

[134] S.K. Prajapati, A. Jain, A. Jain, S. Jain, Biodegradable polymers and constructs: A novel approach in drug delivery, Eur. Polym. J. 120 (2019) 109191. https://doi.org/10.1016/j.eurpolymj.2019.08.018.

[135] L. Yang, J. Li, W. Zhang, Y. Jin, J. Zhang, Y. Liu, D. Yi, M. Li, J. Guo, Z. Gu, The degradation of poly(trimethylene carbonate) implants: The role of molecular weight and enzymes, Polym. Degrad. Stab. 122 (2015) 77–87. https://doi.org/10.1016/j.polymdegradstab.2015.10.016.

[136] R. Censi, P. Di Martino, T. Vermonden, W.E. Hennink, Hydrogels for protein delivery in tissue engineering, J. Control. Release. 161 (2012) 680–692. https://doi.org/10.1016/j.jconrel.2012.03.002.

[137] M. Puertas-Bartolomé, A. Mora-Boza, L. García-Fernández, Emerging Biofabrication Techniques: A Review on Natural Polymers for Biomedical Applications, Polymers (Basel). 13 (2021). https://doi.org/10.3390/POLYM13081209.

[138] E. Troy, M.A. Tilbury, A.M. Power, J.G. Wall, Nature-Based Biomaterials and Their Application in Biomedicine, Polym. 2021, Vol. 13, Page 3321. 13 (2021) 3321. https://doi.org/10.3390/POLYM13193321.

[139] S. Antony, T.R. Anju, B. Thomas, Nature-Inspired Biomimetic Polymeric Materials and Their Applications, Handb. Biopolym. (2022) 1–31. https://doi.org/10.1007/978-981-16-6603-2_50-1.

[140] P.K. Sharma, M. Halder, U. Srivastava, Y. Singh, Antibacterial PEG-

Chitosan Hydrogels for Controlled Antibiotic/Protein Delivery, ACS Appl. Bio Mater. (2019) 5313–5322. https://doi.org/https://doi.org/10.1021/acsabm.9b00570.

[141] Y. Yang, H. Wu, Q. Fu, X. Xie, Y. Song, M. Xu, J. Li, 3D-printed polycaprolactone-chitosan based drug delivery implants for personalized administration, Mater. Des. 214 (2022) 110394. https://doi.org/10.1016/J.MATDES.2022.110394.

[142] L.J. White, G.T.S. Kirby, H.C. Cox, R. Qodratnama, O. Qutachi, F.R.A.J. Rose, K.M. Shakesheff, Accelerating protein release from microparticles for regenerative medicine applications, Mater. Sci. Eng. C. 33 (2013) 2578–2583. https://doi.org/10.1016/j.msec.2013.02.020.

[143] M. Fosset, D. Chappelet-Tordo, M. Lazdunski, Intestinal Alkaline Phosphatase. Physical Properties and Quaternary Structure, Biochemistry. 13 (1974) 24.

[144] H. Neumann, A. Lustig, The Activation of Alkaline Phosphatase by Effector Molecules: A Combined Kinetic and Hydrodynamic Study, Eur. J. Biochem. 109 (1980) 475–480. https://doi.org/10.1111/J.1432-1033.1980.TB04818.X.

[145] Sigma-Aldrich Product Information Sheet - Alkaline Phosphatase from Bovine Intestinal Mucosa, (2013).

[146] D. Fologea, B. Ledden, D.S. McNabb, J. Li, Electrical characterization of protein molecules by a solid-state nanopore, Appl. Phys. Lett. 91 (2007) 053901–1. https://doi.org/10.1063/1.2767206.

[147] Y. Li, J. Lee, J. Lal, L. An, Q. Huang, Effects of pH on the interactions and conformation of bovine serum albumin: Comparison between chemical force microscopy and small-angle neutron scattering, J. Phys. Chem. B. 112 (2008) 3797–3806. https://doi.org/10.1021/JP077392H.

[148] Sigma-Aldrich Product Information Sheet - Bovine Serum Albumin, (2020).

[149] M.P. Rogan, P. Geraghty, C.M. Greene, S.J. O'Neill, C.C. Taggart, N.G. McElvaney, Antimicrobial proteins and polypeptides in pulmonary innate defence, Respir. Res. 7 (2006) 1–11. https://doi.org/https://doi.org/10.1186/1465-9921-7-29.

[150] Sigma-Aldrich Product Information Sheet - Lysozyme from Chicken Egg White, (2022).

[151] FUJIFILM Dimatix Materials Printer DMP-2800 Series User Manual, (2010) #PM000040 Rev. 05.

[152] J. Feng, Y. Zheng, S. Bhusari, M. Villiou, S. Pearson, A. del Campo, Printed Degradable Optical Waveguides for Guiding Light into Tissue, Adv. Funct. Mater. 30 (2020) 2004327. https://doi.org/10.1002/adfm.202004327.

[153] G.A. Hudalla, T.S. Eng, W.L. Murphy, An approach to modulate degradation and mesenchymal stem cell behavior in poly(ethylene glycol) networks, Biomacromolecules. 9 (2008) 842–849. https://doi.org/10.1021/bm701179s.

[154] B. Derby, Inkjet Printing of Functional and Structural Materials: Fluid Property Requirements, Feature Stability, and Resolution, Annu. Rev. Mater. Res. 40 (2010) 395–414. https://doi.org/10.1146/annurev-matsci-070909-104502.

[155] W. Umrath, Cooling bath for rapid freezing in electron microscopy, J. Microsc. 101 (1974) 103–105. https://doi.org/10.1111/j.1365-2818.1974.tb03871.x.

[156] S. Lin, N. Sangaj, T. Razafiarison, C. Zhang, S. Varghese, Influence of Physical Properties of Biomaterials on Cellular Behavior, Pharm. Res. 28 (2011) 1422. https://doi.org/10.1007/s11095-011-0378-9.

[157] K.T. Campbell, K. Wysoczynski, D.J. Hadley, E.A. Silva, Computational-Based Design of Hydrogels with Predictable Mesh Properties, ACS Biomater. Sci. Eng. 6 (2020) 308. https://doi.org/10.1021/acsbiomaterials.9b01520.

[158] M.M. Bradford, A Rapid and Sensitive Method for the Quantitation of Microgram Quantities of Protein Utilizing the Principle of Protein-Dye Binding, Anal. Biochem. 72 (1976) 248–254. https://doi.org/10.1006/abio.1976.9999.

[159] R. Peppas, N, Korsmeyer, Dynamically swelling hydrogels in controlled release applications, in: Hydrogels Med. Pharm., 1987: pp. 109–136.

[160] Y. He, C.J. Tuck, E. Prina, S. Kilsby, S.D.R. Christie, S. Edmondson, R.J.M. Hague, F.R.A.J. Rose, R.D. Wildman, A new photocrosslinkable polycaprolactone-based ink for three-dimensional inkjet printing, J. Biomed. Mater. Res. - Part B Appl. Biomater. 105 (2017) 1645–1657. https://doi.org/10.1002/jbm.b.33699.

[161] R. Daly, T.S. Harrington, G.D. Martin, I.M. Hutchings, Inkjet printing for pharmaceutics - A review of research and manufacturing, Int. J. Pharm. 494 (2015) 554–567. https://doi.org/10.1016/j.ijpharm.2015.03.017.

[162] D. Soltman, V. Subramanian, Inkjet-printed line morphologies and temperature control of the coffee ring effect, Langmuir. 24 (2008) 2224–2231. https://doi.org/10.1021/la7026847.

[163] M. Anyfantakis, Z. Geng, M. Morel, S. Rudiuk, D. Baigl, Modulation of the coffee-ring effect in particle/surfactant mixtures: The importance of particle-interface interactions, Langmuir. 31 (2015) 4113–4120. https://doi.org/10.1021/acs.langmuir.5b00453.

[164] J.R. Choi, K.W. Yong, J.Y. Choi, A.C. Cowie, Recent advances in photo-crosslinkable hydrogels for biomedical applications, Biotechniques. 66 (2019) 40–53. https://doi.org/10.2144/btn-2018-0083.

[165] C. Yu, J. Schimelman, P. Wang, K.L. Miller, X. Ma, S. You, J. Guan, B. Sun, W. Zhu, S. Chen, Photopolymerizable Biomaterials and Light-Based 3D Printing Strategies for Biomedical Applications, Chem. Rev. 120 (2020) 10695. https://doi.org/10.1021/acs.chemrev.9b00810.

[166] M. Montenegro-Nicolini, V. Miranda, J.O. Morales, Inkjet Printing of Proteins: an Experimental Approach, AAPS J. 19 (2017) 234–243. https://doi.org/10.1208/s12248-016-9997-8.

[167] V. Vagenende, M.G.S. Yap, B.L. Trout, Mechanisms of protein stabilization and prevention of protein aggregation by glycerol, Biochemistry. 48 (2009) 11084–11096. https://doi.org/10.1021/bi900649t.

[168] A. Elkaseer, K. Jia, Y. Chen, K.J. Chen, J.C. Janhsen, O. Refle, V. Hagenmeyer, S.G. Scholz, Material jetting for advanced applications: A state-of-the-art review, gaps and future directions, Addit. Manuf. 60 (2022) 103270. https://doi.org/10.1016/j.addma.2022.103270.

[169] J.T. Delaney, P.J. Smith, U.S. Schubert, Inkjet printing of proteins, Soft Matter. 5 (2009) 4866. https://doi.org/10.1039/b909878j.

[170] A. Hussain, N. Abbas, A. Ali, Inkjet Printing: A Viable Technology for Biosensor Fabrication, Chemosens. 2022, Vol. 10, Page 103. 10 (2022) 103. https://doi.org/10.3390/chemosensors10030103.

[171] M. Montenegro-Nicolini, P.E. Reyes, M.O. Jara, P.R. Vuddanda, A. Neira-Carrillo, N. Butto, S. Velaga, J.O. Morales, The Effect of Inkjet Printing over Polymeric Films as Potential Buccal Biologics Delivery Systems, AAPS PharmSciTech. 19 (2018) 3376–3387. https://doi.org/10.1208/s12249-018-1105-1.

[172] A. Mahle, N. Dashaputre, P. DeShong, D.C. Stein, Catanionic Surfactant Vesicles as a New Platform for Probing Glycan–Protein Interactions, Adv. Funct. Mater. 28 (2018) 1706215. https://doi.org/10.1002/adfm.201706215.

[173] C.C. Cook, T. Wang, B. Derby, Inkjet delivery of glucose oxidase, Chem. Commun. 46 (2010) 5452–5454. https://doi.org/10.1039/c0cc00567c.

[174] G. Taormina, C. Sciancalepore, M. Messori, F. Bondioli, 3D printing processes for photocurable polymeric materials: technologies,

materials, and future trends, J. Appl. Biomater. Funct. Mater. 16 (2018) 151–160. https://doi.org/10.1177/2280800018764770.

[175] A. Bagheri, J. Jin, Photopolymerization in 3D Printing, ACS Appl. Polym. Mater. 1 (2019) 593–611. https://doi.org/10.1021/acsapm.8b00165.

[176] J. Zhang, Q. Hu, S. Wang, J. Tao, M. Gou, Digital Light Processing Based Three-dimensional Printing for Medical Applications, Int. J. Bioprinting. 6 (2020) 12–27. https://doi.org/10.18063/ijb.v6i1.242.

[177] H. Li, J. Dai, Z. Wang, H. Zheng, W. Li, M. Wang, F. Cheng, Digital light processing (DLP)-based (bio)printing strategies for tissue modeling and regeneration, Aggregate. (2022) e270. https://doi.org/10.1002/agt2.270.

[178] Y. Wu, H. Su, M. Li, H. Xing, Digital light processing-based multi-material bioprinting: Processes, applications, and perspectives, J. Biomed. Mater. Res. Part A. 111 (2023) 527–542. https://doi.org/10.1002/jbm.a.37473.

[179] W. Zhu, H. Cui, B. Boualam, F. Masood, E. Flynn, R.D. Rao, Z.Y. Zhang, L.G. Zhang, 3D bioprinting mesenchymal stem cell-laden construct with core–shell nanospheres for cartilage tissue engineering, Nanotechnology. 29 (2018) 185101. https://doi.org/10.1088/1361-6528/aaafa1.

[180] P. Wang, D. Berry, A. Moran, F. He, T. Tam, L. Chen, S. Chen, Controlled Growth Factor Release in 3D-Printed Hydrogels, Adv. Healthc. Mater. 9 (2020) 1900977. https://doi.org/10.1002/adhm.201900977.

[181] S.S. Rane, P. Choi, Polydispersity index: How accurately does it measure the breadth of the molecular weight distribution?, Chem. Mater. 17 (2005) 926. https://doi.org/10.1021/CM048594I/ASSET/IMAGES/MEDIUM/CM048594IE00001.GIF.

[182] P. Ruzza, C. Honisch, R. Hussain, G. Siligardi, Free radicals and ros induce protein denaturation by uv photostability assay, Int. J. Mol. Sci. 22 (2021). https://doi.org/10.3390/ijms22126512.

[183] J.D. McCall, K.S. Anseth, Thiol-ene photopolymerizations provide a facile method to encapsulate proteins and maintain their bioactivity, Biomacromolecules. 13 (2012) 2410–2417. https://doi.org/10.1021/bm300671s.

[184] R. Chaudhary, P. Fabbri, E. Leoni, F. Mazzanti, R. Akbari, C. Antonini, Additive manufacturing by digital light processing: a review, Prog. Addit. Manuf. 2022. (2022) 1–21. https://doi.org/10.1007/s40964-022-00336-0.

[185] F.Z. Ameur, N. Mehedi, C. Soler Rivas, A. Gonzalez, O. Kheroua, D. Saidi, Effect of tartrazine on digestive enzymatic activities: in vivo and in vitro studies, Toxicol. Res. 36 (2020) 159–166. https://doi.org/10.1007/s43188-019-00023-3.

[186] X. Wu, Q. Lian, D. Li, Z. Jin, Tilting separation analysis of bottom-up mask projection stereolithography based on cohesive zone model, J. Mater. Process. Technol. 243 (2017) 184–196. https://doi.org/10.1016/j.jmatprotec.2016.12.016.

[187] A. Luongo, V. Falster, M.B. Doest, M.M. Ribo, E.R. Eiriksson, D.B. Pedersen, J.R. Frisvad, Microstructure Control in 3D Printing with Digital Light Processing, Comput. Graph. Forum. 39 (2020) 347–359. https://doi.org/10.1111/cgf.13807.

[188] K. Mostafa, A.J. Qureshi, C. Montemagno, Tolerance Control Using Subvoxel Gray-Scale DLP 3D Printing, ASME Int. Mech. Eng. Congr. Expo. Proc. 2 (2018). https://doi.org/10.1115/imece2017-72232.

[189] J. Li, D.J. Mooney, Designing hydrogels for controlled drug delivery, Nat. Rev. Mater. 1 (2016). https://doi.org/10.1038/natrevmats.2016.71.

[190] L. Abune, Y. Wang, Affinity Hydrogels for Protein Delivery, Trends Pharmacol. Sci. 42 (2021) 300.

https://doi.org/10.1016/j.tips.2021.01.005.

[191] R. Vaishya, V. Khurana, S. Patel, A.K. Mitra, Long-Term Delivery of Protein Therapeutics, Expert Opin. Drug Deliv. 12 (2015) 415. https://doi.org/10.1517/17425247.2015.961420.

[192] M.S. Rehmann, K.M. Skeens, P.M. Kharkar, E.M. Ford, E. Maverakis, K.H. Lee, A.M. Kloxin, Tuning and predicting mesh size and protein release from step growth hydrogels, Biomacromolecules. 18 (2017) 3131. https://doi.org/10.1021/acs.biomac.7b00781.

[193] C.W. Peak, K. Abhay Singh, M. Adlouni, J. Chen, A.K. Gaharwar, Printing Therapeutic Proteins in 3D using Nanoengineered Bioink to Control and Direct Cell Migration, (2019). https://doi.org/10.1002/adhm.201801553.

[194] M. Parlato, S. Reichert, N. Barney, W.L. Murphy, Poly(ethylene glycol) Hydrogels with Adaptable Mechanical and Degradation Properties for Use in Biomedical Applications, Macromol. Biosci. 14 (2014) 687. https://doi.org/10.1002/mabi.201300418.

[195] S. Cereceres, Z. Lan, L. Bryan, M. Whitely, T. Wilems, N. Fabela, C. Whitfield-Cargile, E. Cosgriff-Hernandez, In Vivo Characterization of Poly(ethylene glycol) Hydrogels with Thio-β Esters, Ann. Biomed. Eng. 48 (2020) 953–967. https://doi.org/10.1007/s10439-019-02271-8.

[196] M. Parlato, A. Johnson, G.A. Hudalla, W.L. Murphy, Adaptable Poly(ethylene glycol) Microspheres Capable of Mixed-mode Degradation, (2013). https://doi.org/10.1016/j.actbio.2013.08.011.

[197] L. Strohmeier, H. Frommwald, S. Schlögl, Digital light processing 3D printing of modified liquid isoprene rubber using thiol-click chemistry, RSC Adv. 10 (2020) 23607. https://doi.org/10.1039/d0ra04186f.

[198] D.M. Shah, J. Morris, T.A. Plaisted, A. V. Amirkhizi, C.J. Hansen, Highly filled resins for DLP-based printing of low density, high modulus materials, Addit. Manuf. 37 (2021) 101736. https://doi.org/10.1016/j.addma.2020.101736.

[199] S. Pal, S.K. Asha, Biodegradable, Solvent-Free Photocrosslinkable PLLA Resin Formulations for Additive Manufacturing, Macromol. Chem. Phys. 223 (2022) 2200139. https://doi.org/10.1002/macp.202200139.

[200] W. Xu, S. Jambhulkar, Y. Zhu, D. Ravichandran, M. Kakarla, B. Vernon, D.G. Lott, J.L. Cornella, O. Shefi, G. Miquelard-Garnier, Y. Yang, K. Song, 3D printing for polymer/particle-based processing: A review, Compos. Part B Eng. 223 (2021) 109102. https://doi.org/10.1016/j.compositesb.2021.109102.

[201] J.W. Choi, G.J. Kim, S. Hong, J.H. An, B.J. Kim, C.W. Ha, Sequential process optimization for a digital light processing system to minimize trial and error, Sci. Rep. 12 (2022) 13553. https://doi.org/10.1038/s41598-022-17841-5.

[202] V.S.D. Voet, T. Strating, G.H.M. Schnelting, P. Dijkstra, M. Tietema, J. Xu, A.J.J. Woortman, K. Loos, J. Jager, R. Folkersma, Biobased Acrylate Photocurable Resin Formulation for Stereolithography 3D Printing, ACS Omega. 3 (2018) 1403–1408. https://doi.org/10.1021/acsomega.7b01648.

[203] D.A. Komissarenko, P.S. Sokolov, A.D. Evstigneeva, I.A. Shmeleva, A.E. Dosovitsky, Rheological and Curing Behavior of Acrylate-Based Suspensions for the DLP 3D Printing of Complex Zirconia Parts, Materials (Basel). 11 (2018). https://doi.org/10.3390/ma11122350.

[204] M.L. Laracuente, M.H. Yu, K.J. McHugh, Zero-order drug delivery: State of the art and future prospects, J. Control. Release. 327 (2020) 834–856. https://doi.org/10.1016/j.jconrel.2020.09.020.

[205] N.S. Heredia, K. Vizuete, M. Flores-Calero, V. Katherine Pazmiño, F. Pilaquinga, B. Kumar, A. Debut, Comparative statistical analysis of the release kinetics models for nanoprecipitated drug delivery systems based on poly(lactic-co-glycolic acid), PLoS One. 17 (2022). https://doi.org/10.1371/journal.pone.0264825.

[206] N.A. Peppas, Analysis of Fickian and non-Fickian drug release from

polymers, Pharm. Acta Helv. 60 (1985) 110–11.

[207] S.A. Chew, M.A. Arriaga, V.A. Hinojosa, Effects of surface area to volume ratio of PLGA scaffolds with different architectures on scaffold degradation characteristics and drug release kinetics, J. Biomed. Mater. Res. - Part A. 104 (2016) 1202–1211. https://doi.org/10.1002/jbm.a.35657.

[208] K. McAvoy, D. Jones, R.R.S. Thakur, Synthesis and Characterisation of Photocrosslinked poly(ethylene glycol) diacrylate Implants for Sustained Ocular Drug Delivery, Pharm. Res. 35 (2018) 1–17. https://doi.org/10.1007/s11095-017-2298-9.

[209] V.M. Vaz, L. Kumar, 3D Printing as a Promising Tool in Personalized Medicine, AAPS PharmSciTech. 22 (2021). https://doi.org/10.1208/s12249-020-01905-8.

[210] H.G. Yi, H. Kim, J. Kwon, Y.J. Choi, J. Jang, D.W. Cho, Application of 3D bioprinting in the prevention and the therapy for human diseases, Signal Transduct. Target. Ther. 2021 61. 6 (2021) 1–17. https://doi.org/10.1038/s41392-021-00566-8.

[211] P.M. Kharkar, M.S. Rehmann, K.M. Skeens, E. Maverakis, A.M. Kloxin, Thiol–ene click hydrogels for therapeutic delivery, ACS Biomater. Sci. Eng. 2 (2016) 165. https://doi.org/10.1021/acsbiomaterials.5b00420.

[212] S. Summonte, G.F. Racaniello, A. Lopedota, N. Denora, A. Bernkop-Schnürch, Thiolated polymeric hydrogels for biomedical application: Cross-linking mechanisms, J. Control. Release. 330 (2021) 470–482. https://doi.org/10.1016/j.jconrel.2020.12.037.

[213] J. Cheng, R. Wang, Z. Sun, Q. Liu, X. He, H. Li, H. Ye, X. Yang, X. Wei, Z. Li, B. Jian, W. Deng, Q. Ge, Centrifugal multimaterial 3D printing of multifunctional heterogeneous objects, Nat. Commun. 13 (2022). https://doi.org/10.1038/s41467-022-35622-6.

[214] B.E. Kelly, I. Bhattacharya, H. Heidari, M. Shusteff, C.M. Spadaccini,

H.K. Taylor, Volumetric additive manufacturing via tomographic reconstruction, Science (80-.). 363 (2019) 1075–1079. https://doi.org/10.1126/science.aau7114.

[215] D. Loterie, P. Delrot, C. Moser, High-resolution tomographic volumetric additive manufacturing, Nat. Commun. 2020 111. 11 (2020) 1–6. https://doi.org/10.1038/s41467-020-14630-4.

[216] F.P. Pons-Faudoa, A. Ballerini, J. Sakamoto, A. Grattoni, Advanced implantable drug delivery technologies: transforming the clinical landscape of therapeutics for chronic diseases, Biomed. Microdevices 2019 212. 21 (2019) 1–22. https://doi.org/10.1007/s10544-019-0389-6.

Appendix: Supplementary Information

Example of a PNP Product Curve for the ALP PNPP Activity Assay
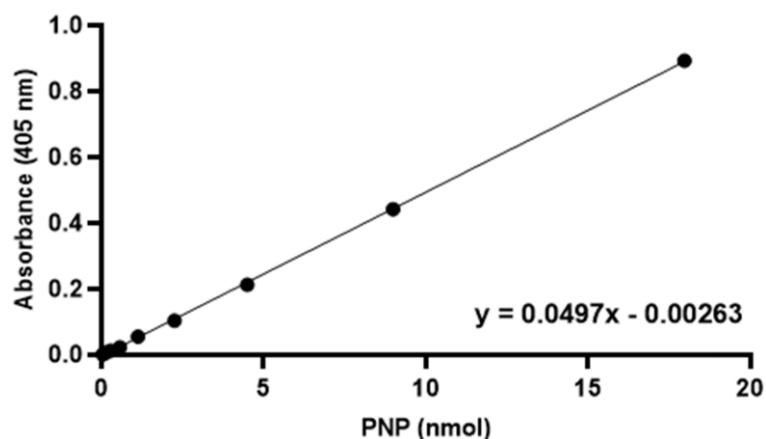
Figure S.1: Example standard curve for the ALP PNPP assay
($R^2 > 0.95$), where one absorbance value is equal to 20.02 ± 0.15.
Curve used to convert plate reader outputs (absorbance at 405 nm)
to known concentrations of PNP product.

Example of a Bradford Assay Standard Curve using BSA
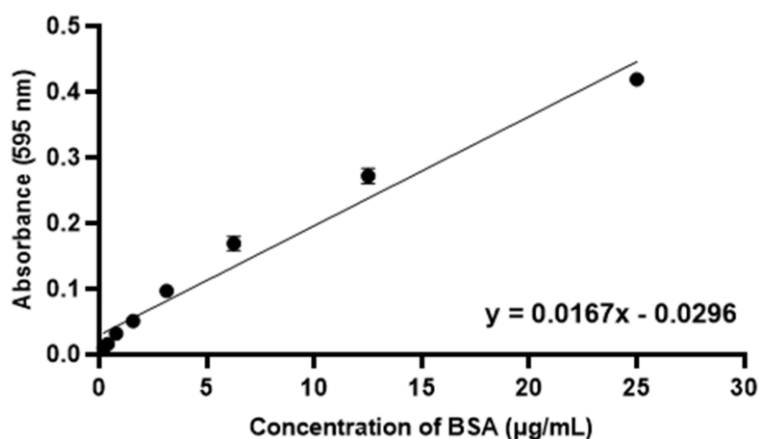
Figure S.2: Example standard curve for the Bradford
assay using a range of BSA concentrations ($R^2 > 0.95$).
Curve used to convert plate reader outputs (absorbance
at 595 nm) to a known concentration of BSA (µg/mL).
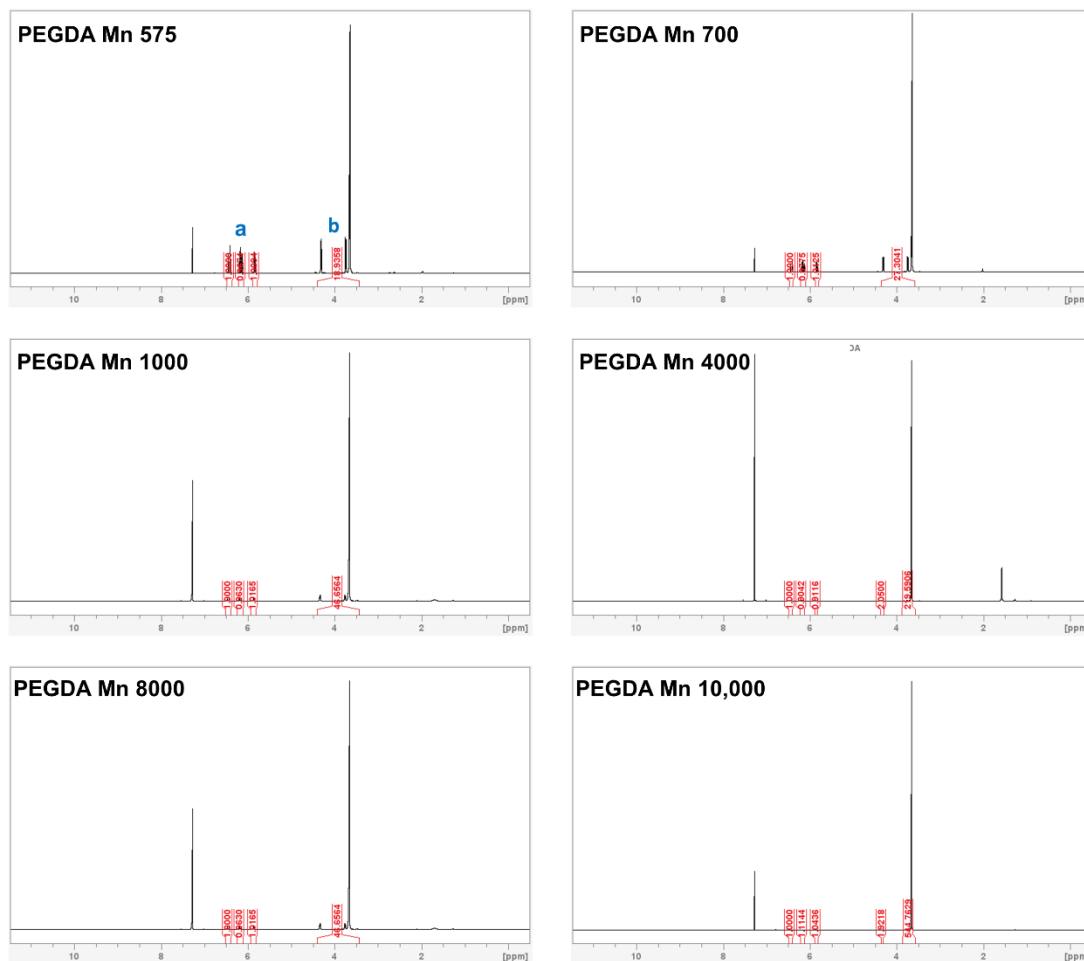
Figure S.3: NMR spectra prepared for the range of PEGDA used (Mn 575 to 10,000), allowing summation of the integrated peaks (acrylate and EG) for the corresponding values presented in Table 5.3.

Mass Swelling Data Collected for CG–F1 to CG–F6 to Calculate Swelling Ratio and Theoretical Matrix Mesh Size (Day 1 Example)

Table S.1: Raw data values, mass (g) for CG–F1 to CG–F6, used to calculate swelling ratio and theoretical matrix mesh size results presented in Table 5.5. Swelling ratio and theoretical matrix mesh size calculated using Equation 3.3 and Equation 3.8. *Values reported to 2 d.p, ** values reported to 1 d.p. Results denote mean ± S.D. (n = 3).

CG-F1 Raw Data			
Sample	Mass (g) As Printed	Mass (g) As Swelled Day 1	Mass (g) As Dried
A	0.423	0.440	0.248
B	0.475	0.493	0.279
C	0.441	0.464	0.263
Mean	0.446	0.466	0.263
Standard Deviation	0.022	0.022	0.013

CG-F1 Calculated Matrix Properties		
Sample	Swelling Ratio Day 1 *	Theoretical Matrix Mesh Size Day 1 (Å) **
A	0.78	3.3
B	0.77	3.3
C	0.76	3.3
Mean	0.77	3.3
Standard Deviation	Negligible	Negligible

CG-F2 Raw Data			
Sample	Mass (g) As Printed	Mass (g) As Swelled Day 1	Mass (g) As Dried
A	0.367	0.401	0.195
B	0.363	0.400	0.194
C	0.323	0.356	0.164
Mean	0.351	0.386	0.184
Standard Deviation	0.020	0.021	0.014

CG-F2 Calculated Matrix Properties		
Sample	Swelling Ratio Day 1 *	Theoretical Matrix Mesh Size Day 1 (Å) **
A	1.06	4.5
B	1.06	4.5
C	1.17	5.0
Mean	1.10	4.7
Standard Deviation	0.05	0.2

CG-F3 Raw Data			
Sample	Mass (g) As Printed	Mass (g) As Swelled Day 1	Mass (g) As Dried
A	0.304	0.399	0.079
B	0.306	0.394	0.077
C	0.308	0.415	0.078
Mean	0.306	0.402	0.078
Standard Deviation	0.002	0.009	0.001

CG-F3 Calculated Matrix Properties		
Sample	Swelling Ratio Day 1 *	Theoretical Matrix Mesh Size Day 1 (Å) **
A	4.03	17.6
B	4.13	17.9
C	4.33	18.7
Mean	4.16	18.1
Standard Deviation	0.13	0.5

CG-F4 Raw Data

Sample	Mass (g) As Printed	Mass (g) As Swelled Day 1	Mass (g) As Dried
A	0.383	0.542	0.057
B	0.409	0.569	0.059
C	0.406	0.557	0.062
Mean	0.399	0.556	0.059
Standard Deviation	0.012	0.011	0.001

CG-F4 Calculated Matrix Properties

Sample	Swelling Ratio Day 1 *	Theoretical Matrix Mesh Size Day 1 (Å) **
A	8.49	45.8
B	8.62	46.3
C	8.03	43.7
Mean	8.38	45.3
Standard Deviation	0.25	1.1

CG-F5 Raw Data			
Sample	Mass (g) As Printed	Mass (g) As Swelled Day 1	Mass (g) As Dried
A	0.237	0.608	0.050
B	0.206	0.630	0.045
C	0.288	0.635	0.052
Mean	0.244	0.624	0.049
Standard Deviation	0.034	0.012	0.003

CG-F5 Calculated Matrix Properties		
Sample	Swelling Ratio Day 1 *	Theoretical Matrix Mesh Size Day 1 (Å) **
A	11.1	67.2
B	12.97	75.8
C	11.14	69.1
Mean	11.74	70.7
Standard Deviation	0.87	3.7

CG-F6 Raw Data			
Sample	Mass (g) As Printed	Mass (g) As Swelled Day 1	Mass (g) As Dried
A	0.198	0.475	0.033
B	0.200	0.445	0.032
C	0.199	0.469	0.033
Mean	0.199	0.463	0.033
Standard Deviation	0.001	0.013	0.001

CG-F6 Calculated Matrix Properties		
Sample	Swelling Ratio Day 1 *	Theoretical Matrix Mesh Size Day 1 (Å) **
A	13.56	85.1
B	13.12	82.9
C	13.04	82.4
Mean	13.24	83.5
Standard Deviation	0.23	1.2

Data displayed for calculations regarding samples at Day 1. Full data set for each individual time point available on request.

Example of NMR Acrylate Peak Reduction with Increasing SH:Acrylate Ratios for MM–F5 to MM–F8
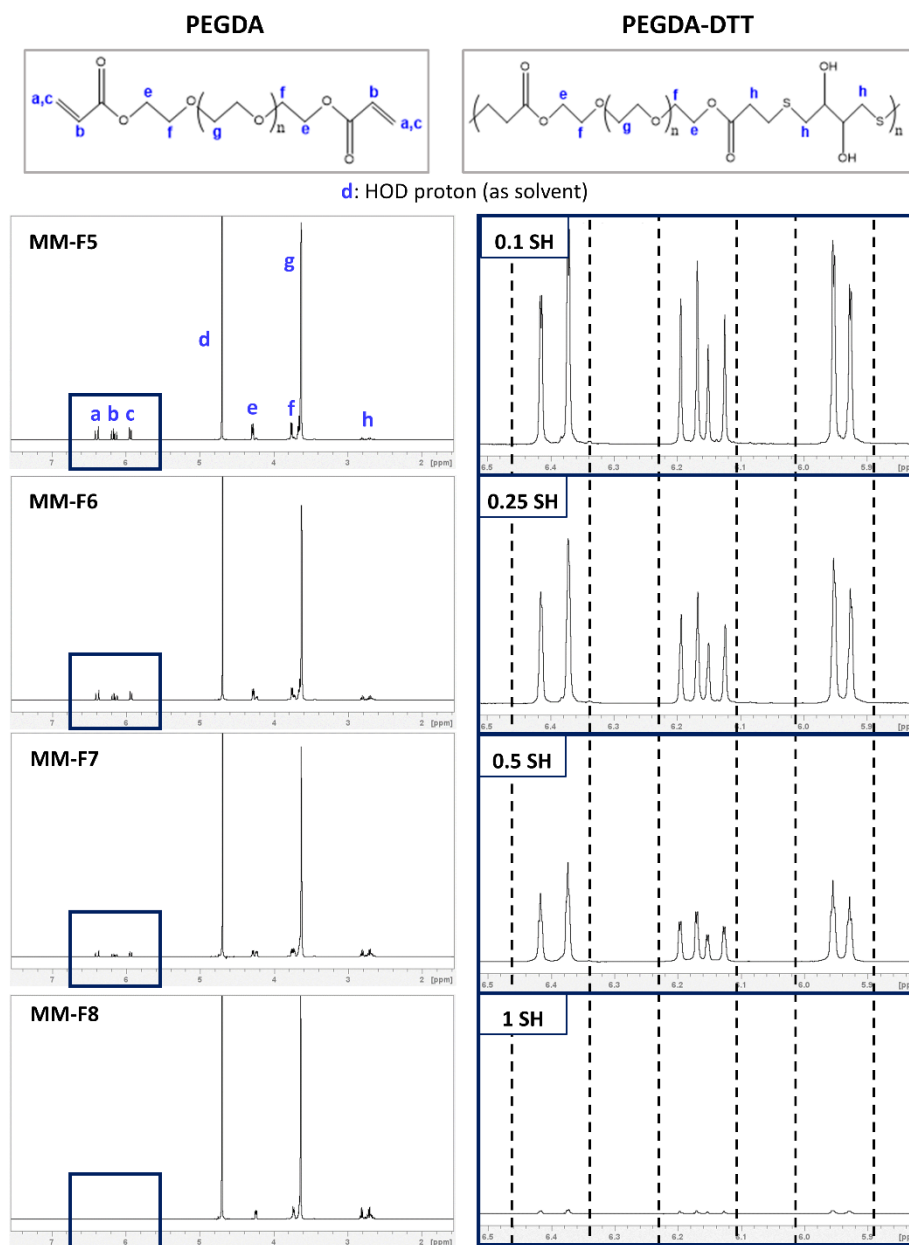
Figure S.4: Representative NMR spectra for PEGDA 700 50% (*v/v*) formulations (MM–F5 to MM–F8), showing peak comparison and decreasing acrylate signal corresponding with increasing SH content. All spectra scaled identically.

Example of NMR Acrylate Peak Reduction with Increasing SH:Acrylate Ratios for MM–F9 to MM–F12
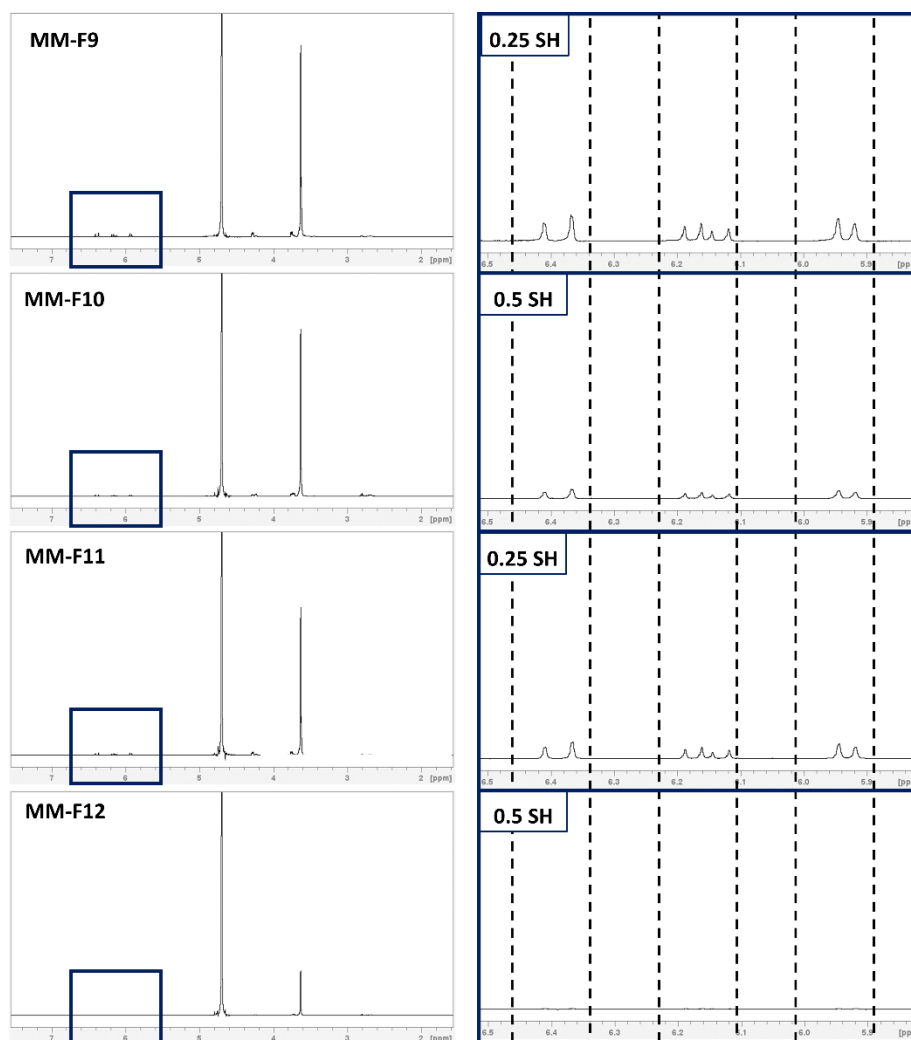
Figure S.5: Representative NMR spectra for PEGDA 575/4000 (1:1) 10% and 20% (*w/v*) formulations (MM–F9 to MM–F12), showing peak comparison and decreasing acrylate signal corresponding with increasing SH content. All spectra scaled identically.

Mass Swelling Data Collected for MM–F1 to MM–F12 to Calculate Swelling Ratio and Theoretical Matrix Mesh Size (Day 1 Example)

Table S.2: Raw data values, mass (g) for MM–F1 to MM–F12, used to calculate swelling ratio and theoretical matrix mesh size presented in Table 6.6. The equation of a straight line, shown in Figure 5.13 ($y = 0.6375x - 4.251$, $R^2 = 0.99$), was used to approximate matrix mesh sizes (y) using calculated swelling ratios (x). *Values reported to 2 d.p, ** values reported to 1 d.p. Results denote mean ± S.D. (n = 3).

MM-F1 Raw Data			
Sample	Mass (g) As Printed	Mass (g) As Swelled Day 1	Mass (g) As Dried
A	0.260	0.294	0.143
B	0.270	0.298	0.149
C	0.272	0.309	0.149
Mean	0.267	0.300	0.147
Standard Deviation	0.005	0.006	0.003

MM-F1 Calculated Matrix Properties		
Sample	Swelling Ratio Day 1 *	Theoretical Matrix Mesh Size Day 1 (Å) **
A	1.06	2.7
B	1.01	2.3
C	1.08	2.8
Mean	1.05	2.6
Standard Deviation	0.03	0.2

MM-F2 Raw Data			
Sample	Mass (g) As Printed	Mass (g) As Swelled Day 1	Mass (g) As Dried
A	0.279	0.307	0.153
B	0.281	0.317	0.156
C	0.279	0.310	0.154
Mean	0.280	0.312	0.154
Standard Deviation	0.001	0.004	0.001

MM-F2 Calculated Matrix Properties		
Sample	Swelling Ratio Day 1 *	Theoretical Matrix Mesh Size Day 1 (Å) **
A	1.01	2.3
B	1.04	2.5
C	1.01	2.4
Mean	1.02	2.4
Standard Deviation	0.01	0.1

MM-F3 Raw Data			
Sample	Mass (g) As Printed	Mass (g) As Swelled Day 1	Mass (g) As Dried
A	0.254	0.309	0.147
B	0.259	0.316	0.150
C	0.247	0.305	0.143
Mean	0.253	0.310	0.147
Standard Deviation	0.005	0.004	0.003

MM-F3 Calculated Matrix Properties		
Sample	Swelling Ratio Day 1 *	Theoretical Matrix Mesh Size Day 1 (Å) **
A	1.10	2.9
B	1.10	2.9
C	1.14	3.2
Mean	1.11	3.0
Standard Deviation	0.02	0.1

MM-F4 Raw Data			
Sample	Mass (g) As Printed	Mass (g) As Swelled Day 1	Mass (g) As Dried
A	0.263	0.355	0.145
B	0.276	0.375	0.151
C	0.267	0.366	0.146
Mean	0.269	0.366	0.147
Standard Deviation	0.006	0.008	0.003

MM-F4 Calculated Matrix Properties		
Sample	Swelling Ratio Day 1 *	Theoretical Matrix Mesh Size Day 1 (Å) **
A	1.45	5.0
B	1.49	5.2
C	1.50	5.3
Mean	1.48	5.2
Standard Deviation	0.02	0.1

MM-F5 Raw Data			
Sample	Mass (g) As Printed	Mass (g) As Swelled Day 1	Mass (g) As Dried
A	0.265	0.328	0.139
B	0.261	0.319	0.137
C	0.264	0.334	0.138
Mean	0.264	0.327	0.138
Standard Deviation	0.002	0.006	0.001

MM-F5 Calculated Matrix Properties		
Sample	Swelling Ratio Day 1 *	Theoretical Matrix Mesh Size Day 1 (Å) **
A	1.37	4.6
B	1.33	4.4
C	1.42	5.0
Mean	1.37	4.7
Standard Deviation	0.04	0.2

MM-F6 Raw Data			
Sample	Mass (g) As Printed	Mass (g) As Swelled Day 1	Mass (g) As Dried
A	0.270	0.356	0.142
B	0.272	0.363	0.146
C	0.262	0.354	0.142
Mean	0.268	0.357	0.143
Standard Deviation	0.004	0.004	0.002

MM-F6 Calculated Matrix Properties		
Sample	Swelling Ratio Day 1 *	Theoretical Matrix Mesh Size Day 1 (Å) **
A	1.50	5.5
B	1.49	5.4
C	1.50	5.5
Mean	1.49	5.4
Standard Deviation	0.01	Negligible

MM-F7 Raw Data			
Sample	Mass (g) As Printed	Mass (g) As Swelled Day 1	Mass (g) As Dried
A	0.272	0.337	0.136
B	0.282	0.380	0.140
C	0.264	0.376	0.137
Mean	0.273	0.378	0.137
Standard Deviation	0.007	0.002	0.002

MM-F7 Calculated Matrix Properties		
Sample	Swelling Ratio Day 1 *	Theoretical Matrix Mesh Size Day 1 (Å) **
A	1.78	7.3
B	1.71	6.8
C	1.75	7.1
Mean	1.75	7.1
Standard Deviation	0.03	0.2

MM-F9 Raw Data			
Sample	Mass (g) As Printed	Mass (g) As Swelled Day 1	Mass (g) As Dried
A	0.252	0.312	0.026
B	0.268	0.328	0.028
C	0.246	0.294	0.026
Mean	0.255	0.311	0.027
Standard Deviation	0.001	0.014	0.001

MM-F9 Calculated Matrix Properties		
Sample	Swelling Ratio Day 1 *	Theoretical Matrix Mesh Size Day 1 (Å) **
A	10.81	64.7
B	10.77	64.5
C	10.43	62.3
Mean	10.67	63.9
Standard Deviation	0.17	1.1

MM-F10 Raw Data			
Sample	Mass (g) As Printed	Mass (g) As Swelled Day 1	Mass (g) As Dried
A	0.215	0.292	0.023
B	0.219	0.272	0.022
C	0.210	0.256	0.022
Mean	0.215	0.273	0.022
Standard Deviation	0.004	0.015	0.001

MM-F10 Calculated Matrix Properties		
Sample	Swelling Ratio Day 1 *	Theoretical Matrix Mesh Size Day 1 (Å) **
A	11.64	70.1
B	11.30	67.9
C	10.77	64.5
Mean	11.24	67.5
Standard Deviation	0.36	2.3

MM-F11 Raw Data			
Sample	Mass (g) As Printed	Mass (g) As Swelled Day 1	Mass (g) As Dried
A	0.209	0.254	0.036
B	0.219	0.277	0.036
C	0.215	0.261	0.037
Mean	0.213	0.264	0.036
Standard Deviation	0.003	0.009	0.001

MM-F11 Calculated Matrix Properties		
Sample	Swelling Ratio Day 1 *	Theoretical Matrix Mesh Size Day 1 (Å) **
A	6.03	34.3
B	6.75	38.9
C	6.03	34.3
Mean	6.27	35.8
Standard Deviation	0.34	2.2

MM-F12 Raw Data			
Sample	Mass (g) As Printed	Mass (g) As Swelled Day 1	Mass (g) As Dried
A	0.218	0.309	0.036
B	0.222	0.300	0.039
C	0.231	0.313	0.040
Mean	0.224	0.307	0.038
Standard Deviation	0.005	0.006	0.002

MM-F12 Calculated Matrix Properties		
Sample	Swelling Ratio Day 1 *	Theoretical Matrix Mesh Size Day 1 (Å) **
A	7.71	45.1
B	6.70	38.6
C	6.74	38.8
Mean	7.05	40.8
Standard Deviation	0.47	3.0

Data displayed for calculations regarding samples at Day 1. Full data set for each individual time point available on request. MM–F8 formulation not analysed due to difficulties in producing samples, which were prioritised for the release study.

Compressive Young's Modulus Values for Samples Printed using MM–F1 to MM–F12

Table S.3: Overview of the compressive Young's modulus for samples comprised of MM–F1 to MM–F12 in the as printed and as swelled at day 1 state. Results denote mean ± S.D. (n = 3).

Formulation Code	Compressive Young's Modulus (kPa) As Printed	Compressive Young's Modulus (kPa) As Swelled at Day 1
MM–F1	22.5 ± 0.3	22.4 ± 0.3
MM–F2	21.0 ± 0.6	20.9 ± 0.5
MM–F3	19.6 ± 0.3	19.6 ± 0.5
MM–F4	16.5 ± 1.7	13.3 ± 0.3
MM–F5	20.2 ± 0.4	20.1 ± 0.2
MM–F6	20.0 ± 0.3	19.7 ± 0.1
MM–F7	18.3 ± 0.7	18.1 ± 0.2
MM–F8	9.9 ± 0.2	6.3 ± 0.4
MM–F9	4.2 ± 0.1	4.0 ± 0.1
MM–F10	4.1 ± 0.2	Not able to be tested.
MM–F11	5.8 ± 0.6	4.4 ± 0.3
MM–F12	4.6 ± 0.2	4.3 ± 0.2